

# PACIFIC EARTHQUAKE ENGINEERING RESEARCH CENTER

## **Generalized Hybrid Simulation Framework for Structural Systems Subjected to Seismic Loading**

**Tarek Elkhoraibi**

and

**Khalid M. Mosalam**

University of California, Berkeley

# **Generalized Hybrid Simulation Framework for Structural Systems Subjected to Seismic Loading**

**Tarek Elkhoraibi**

Department of Civil and Environmental Engineering  
University of California, Berkeley

**Khalid M. Mosalam**

Department of Civil and Environmental Engineering  
University of California, Berkeley

PEER Report 2007/101  
Pacific Earthquake Engineering Research Center  
College of Engineering  
University of California, Berkeley

July 2007

## ABSTRACT

A new hybrid simulation system (HSS), namely nees@berkeley, developed at the University of California, Berkeley (UCB), is presented in this study. Validation of the HSS is sought through testing steel cantilever columns with predictable structural response that is verifiable by purely numerical simulation of the experiment.

Two procedures are developed and implemented in the HSS with the aim of enhancing the accuracy and reliability of the pseudo-dynamic test results. The first procedure is a feed-forward error compensation scheme that aims at correcting the experimental systematic error in executing the displacement command signal. The second procedure employs mixed variables with mode switching between displacement and force controls. Two experimental test structures are considered in this study to demonstrate different aspects of the procedures developed in the HSS:

1. Reinforced concrete frames with and without unreinforced masonry infill walls, and
2. Wood shear walls of the first story of a two-story wood house over a garage.

The structural performance of the two test structures under seismic loading is evaluated using the developed HSS. The two test structures have the common feature of being large substructures of shaking table experiments and, accordingly, a comprehensive comparative study is conducted between the test results of the two testing methods.

## **ACKNOWLEDGMENTS**

This work made use of Pacific Earthquake Engineering Research Center Shared Facilities supported by the Earthquake Engineering Research Centers Program of the National Science Foundation under award number EEC-9701568.

The financial support for this project, provided by the National Science Foundation under NSF Contract No. CMS 0116005, is gratefully acknowledged. The reinforcing bars were donated by Mr. Thomas R. Tietz, former Western Regional Manager of the Concrete Reinforcing Steel Institute (CRSI).

# CONTENTS

<b>ABSTRACT</b> .....	<b>iii</b>
<b>ACKNOWLEDGMENTS</b> .....	<b>iv</b>
<b>TABLE OF CONTENTS</b> .....	<b>v</b>
<b>LIST OF FIGURES</b> .....	<b>ix</b>
<b>LIST OF TABLES</b> .....	<b>xv</b>
<b>1 INTRODUCTION</b> .....	<b>1</b>
1.1 General .....	1
1.2 Scope and Objectives .....	2
1.3 Contributions .....	4
1.4 Outline .....	4
<b>2 BACKGROUND</b> .....	<b>7</b>
2.1 Comparison of Experimental Methods .....	7
2.2 Development of HS Experimental Method.....	8
2.3 Integration Algorithms .....	10
2.4 HS of Stiff Structural Systems .....	13
2.5 Summary .....	14
<b>3 HYBRID SIMULATION SYSTEM</b> .....	<b>17</b>
3.1 HSS Overview.....	17
3.2 Structural Laboratory .....	18
3.2.1 Reconfigurable Reaction Walls (RRW).....	18
3.2.2 Actuators .....	21
3.3 ScramNet.....	21
3.4 Structural Test System .....	21
3.4.1 PIDF Control.....	22
3.4.2 Program Source in STS.....	23
3.5 xpc Target.....	25
3.6 Pacific Instruments Data-Acquisition System .....	27
3.7 MATLAB Environment.....	28
3.8 Operation Sequence in HSS .....	29

3.9	Validation of HSS .....	31
3.10	Summary .....	35
<b>4</b>	<b>TEST STRUCTURE A .....</b>	<b>37</b>
4.1	ST Test Structure .....	37
4.2	Strong Motion Selection .....	38
4.3	Physical Substructures in HS .....	42
4.4	RC Frame Design.....	44
4.5	Instrumentation .....	46
4.6	Construction and Material Properties.....	50
4.7	Experimental Setup Design.....	50
4.7.1	Reaction Wall Design and Actuator Selection.....	50
4.7.2	Setup on Strong Floor .....	54
4.8	Experimental Setup Implementation.....	54
4.8.1	Construction of RRW.....	55
4.8.2	Attachment of Actuator to RRW .....	55
4.8.3	Attachment of Test Substructures to Strong Floor.....	55
4.8.4	Installation of Loading Apparatus.....	58
4.9	HS Idealization of Test Structure.....	60
4.10	Governing Equations of Motion and Parameters.....	61
4.10.1	Mass Matrix .....	62
4.10.2	Damping Matrix.....	63
4.10.3	Stiffness Matrix.....	63
4.11	Initial Stiffness Estimation for Physical Substructures.....	64
4.12	RC Slab Stiffness Estimation.....	66
4.12.1	Theoretical In-Plane Stiffness of RC Slab .....	66
4.12.2	Experimental In-Plane Stiffness for RC Slab .....	67
4.13	Parameters of Equations of Motion.....	69
4.14	Integration Time-Step Estimation .....	71
4.15	Summary .....	72
<b>5</b>	<b>TEST STRUCTURE B.....</b>	<b>75</b>
5.1	ST Test Structure .....	75

5.2	Test Structure Design.....	76
5.3	Strong Motion Selection .....	77
5.4	Test Structure in HS.....	80
5.4.1	Idealization.....	80
5.4.2	Experimental Setup .....	80
5.4.3	Instrumentation .....	82
5.5	Governing Equation of Motion and Parameters.....	85
5.6	Summary .....	86
<b>6</b>	<b>NEW ADVANCES IN HYBRID SIMULATION.....</b>	<b>87</b>
6.1	Integration Algorithm in DC.....	87
6.2	Feed-Forward Error Compensation in DC.....	90
6.2.1	Test Rate .....	90
6.2.2	Error Prediction.....	91
6.2.3	Feed-Forward Error Compensation.....	93
6.3	Mixed-Variables Control in HS .....	95
6.3.1	FC Integration Algorithm.....	96
6.3.2	Extension to Mixed-Variables Control .....	98
6.4	Numerical Evaluation of FC Algorithm.....	102
6.5	Implementation Strategies of Mixed-Variables Control.....	105
6.5.1	Secant Stiffness Estimation.....	105
6.5.2	Mode-Switch Decision Implementation .....	108
6.5.3	Practical Iterative Solution.....	110
6.6	Summary .....	112
<b>7</b>	<b>APPLICATIONS OF DEVELOPED HYBRID SIMULATION PROCEDURES.....</b>	<b>113</b>
7.1	Feed-Forward Error Compensation.....	113
7.1.1	Calibration Parameter Evaluation .....	113
7.1.2	Experimental Results .....	116
7.2	Mixed-Variables Control .....	116
7.2.1	Structural States .....	117
7.2.2	Mode-Switch Decision Making .....	118
7.2.3	Experimental Results .....	121

7.3	Procedure Combination.....	122
7.4	Summary .....	125
<b>8</b>	<b>STRUCTURAL EVALUATION AND COMPARISONS.....</b>	<b>127</b>
8.1	Test Structure A: Phase S-1 .....	127
8.1.1	Force-Displacement Behavior.....	128
8.1.2	URM Infill Wall Contribution .....	132
8.2	Comparison to ST Experiment: Phase S-1.....	134
8.2.1	Force-Displacement Behavior.....	134
8.2.2	URM Infill Wall Contribution .....	143
8.3	Test Structure A: Phases S-2 and S-3 .....	147
8.4	Comparisons to ST Experiments: Phases S-2 and S-3.....	152
8.5	Contribution of Upper Stories.....	157
8.6	Test Structure B .....	165
8.6.1	Force-Displacement Behavior.....	165
8.6.2	Comparison to ST Experiment.....	168
8.7	Summary .....	172
<b>9</b>	<b>SUMMARY, CONCLUSIONS, AND FUTURE WORK.....</b>	<b>175</b>
9.1	Summary .....	175
9.2	Conclusions .....	176
9.3	Future Work .....	178
	<b>REFERENCES.....</b>	<b>181</b>
	<b>APPENDIX A: SPREADSHEET FOR CONFIGURING REACTION WALL.....</b>	<b>189</b>
A.1	Background .....	189
A.2	Application to Present Test Setup.....	190
	<b>APPENDIX B: EXACT SOLUTION FOR BILINEAR STIFFENING SDOF .....</b>	<b>195</b>
	<b>APPENDIX C: BOUC-WEN MODEL DESCRIPTION AND CALIBRATION.....</b>	<b>197</b>
C.1	Description.....	197
C.2	Calibration.....	199

## LIST OF FIGURES

Fig. 1.1	Overview of study program .....	3
Fig. 1.2	Overview of hybrid simulation experimental program .....	6
Fig. 3.1	Control room and HSS.....	18
Fig. 3.2	HSS architecture .....	19
Fig. 3.3	Concrete geometry of typical RRW unit (1"=25.4 mm) .....	20
Fig. 3.4	STS host PC.....	23
Fig. 3.5	PIDF controls of displacement (DC) and force (FC) in STS.....	24
Fig. 3.6	Available program sources in STS .....	24
Fig. 3.7	Function generator in STS .....	25
Fig. 3.8	Simulink model for xPC target.....	26
Fig. 3.9	Expansion of operation block in Simulink model for xPC target.....	27
Fig. 3.10	Calibration of sensors in the Pacific Instruments data-acquisition system.....	28
Fig. 3.11	Operation sequence in HS .....	30
Fig. 3.12	Steel specimens design and setup in structural laboratory .....	32
Fig. 3.13	Idealized model for HS validation structure.....	33
Fig. 3.14	Structural response of physical substructures $C_1$ (left) and $C_2$ (right).....	34
Fig. 3.15	Validation of HSS.....	34
Fig. 4.1	Five-story prototype and one-story ST structures (Hashemi and Mosalam 2007).....	38
Fig. 4.2	Response spectra with 5% damping for selected ground motions (Hashemi and Mosalam 2007).....	39
Fig. 4.3	Filtering of acceleration time history of ST output signal for TAR level 2 .....	41
Fig. 4.4	Chronological order of events for test structure A .....	42
Fig. 4.5	Test structures in HS.....	43
Fig. 4.6	Infilled frame reinforcement (bare frame is similar without URM infill wall and grade beam) (1'=304.8 mm, 1"=25.4 mm).....	45
Fig. 4.7	Design details of RC frames (1'=304.8 mm, 1"=25.4 mm).....	46
Fig. 4.8	Strain gages numbering on reinforcing steel bars in RC frames .....	47
Fig. 4.9	Numbered displacement transducers on URM infilled RC frame.....	48
Fig. 4.10	Accelerations at faster rate execution, LPB-9 at 20 times slower than real time .....	49

Fig. 4.11	Out-of-plane drift measurements in TAR-6 frame F2B, phase S-1.....	50
Fig. 4.12	Construction of RC frames .....	51
Fig. 4.13	Strength gain with time for concrete compressive strength of tested cylinders .....	52
Fig. 4.14	A 220-kip (979 kN) actuator mounted on RRW .....	53
Fig. 4.15	Design spreadsheet output for used RRW (1 ft = 304.8 mm, 1 kip = 4.448 kN) .....	54
Fig. 4.16	Test setup on strong floor for test structure A (1'=304.8 mm, 1"=25.4 mm, 1 kip = 4.448 kN).....	56
Fig. 4.17	Construction of RRW .....	57
Fig. 4.18	Installation of actuator at desired height.....	57
Fig. 4.19	Loading apparatus mounted on RC bare frame .....	58
Fig. 4.20	Details of loading apparatus for test structure A (1"=25.4 mm) .....	59
Fig. 4.21	Idealizations of test frame into a number of DOF .....	61
Fig. 4.22	Idealized test structure in phase S-1 (see Fig. 1.2) .....	61
Fig. 4.23	Mass allocation by tributary areas .....	62
Fig. 4.24	Pull-back test setup .....	65
Fig. 4.25	Restoring force versus lateral displacement of URM infilled RC frame from preliminary run (1 kip/in. = 0.175 kN/mm).....	66
Fig. 4.26	RC slab stiffness estimation (not to scale).....	67
Fig. 4.27	Differential drift in pseudo-dynamic test between F1I and F2B as function of theoretical in-plane stiffness of RC slab .....	68
Fig. 4.28	Differential drift in dynamic (ST) tests against applied maximum lateral displacement .....	69
Fig. 4.29	Mode shapes for test structure A in phase S-1 .....	70
Fig. 4.30	Comparison of response for TAR-2 using different integration time steps $\Delta t$ in HS .....	72
Fig. 5.1	Two-story wood house over garage on ST .....	76
Fig. 5.2	Wood house first-floor plan.....	77
Fig. 5.3	Wood house elevation views .....	78
Fig. 5.4	Design details of wood house .....	79
Fig. 5.5	Blocking used to brace shear-wall framing of test structure B.....	79
Fig. 5.6	Test setup and instrumentation on strong floor for test structure B (1'=304.8 mm, 1"=25.4 mm).....	81

Fig. 5.7	HS physical substructure for test structure B .....	82
Fig. 5.8	Loading frame for test structure B ( $l'=304.8$ mm, $l''=25.4$ mm).....	83
Fig. 5.9	Vertical force variation in post-tensioned steel rods in LPG-6 .....	84
Fig. 5.10	Displacement time history for preliminary test .....	84
Fig. 5.11	Sliding at base of shear walls in preliminary test .....	84
Fig. 5.12	Out-of-plane drift of north shear wall in preliminary test .....	85
Fig. 6.1	Flowchart of DC algorithm.....	89
Fig. 6.2	Correlation relationship between error $Er_i^{cc}$ and actuator velocity for test structure B.....	93
Fig. 6.3	Error remainder (difference between recorded and predicted error values) for test structure B.....	94
Fig. 6.4	Different lumped spring–mass systems.....	97
Fig. 6.5	Flowchart of FC algorithm .....	99
Fig. 6.6	Flowchart for integration algorithm with mixed-variables control without mode switch (DC for flexible DOF and FC for stiff DOF).....	100
Fig. 6.7	Flowchart for integration algorithm with mode switch between DC and FC for SDOF system.....	101
Fig. 6.8	Applied force and considered system for numerical evaluation of FC algorithm....	103
Fig. 6.9	Nonlinear elastic response using Menegotto-Pinto model ( $\theta = k_s/k_T$ ).....	103
Fig. 6.10	Parametric study of FC and DC algorithms using nonlinear elastic SDOF systems.....	105
Fig. 6.11	Schematic representation of secant stiffness estimation at time step $i+1$ and iteration $j$ .....	107
Fig. 6.12	Example results from test structure B for estimation of secant stiffness.....	107
Fig. 6.13	Mode-switch decision-making scheme.....	109
Fig. 6.14	Considered stiffening bilinear elastic system for numerical evaluation.....	110
Fig. 6.15	Parametric study of mode-switch algorithm using bilinear elastic SDOF systems.....	111
Fig. 7.1	Correlation relationship between error $Er_i^{cc}$ and actuator velocity.....	115
Fig. 7.2	Feed-forward error compensation results .....	117
Fig. 7.3	Typical force-deformation response for test structure B .....	118

Fig. 7.4	FC/DC mode-switch criteria for application example (test structure B).....	119
Fig. 7.5	Mode-switch decision-making scheme for test structure B.....	120
Fig. 7.6	Results of mixed-variables algorithm with mode switch for HS on test structure B.....	123
Fig. 7.7	Results of mixed-variables algorithm with mode switch for HS on test structure A .....	124
Fig. 7.8	Possible incorporation of two developed procedures in HS.....	124
Fig. 8.1	Total base shear versus lateral displacement for test structure A, phase S-1, TAR-2 to TAR-6 (1 kip/in.= 0.175 kN/mm).....	130
Fig. 8.2	Total base shear versus lateral displacement for test structure A, phase S-1, DUZ-7 to DUZ-9-2 (1 kip/in.= 0.175 kN/mm) .....	131
Fig. 8.3	Cracking patterns of URM infill wall in test structure A, phase S-1.....	131
Fig. 8.4	Contribution of URM infill wall and RC frames to restoring forces.....	133
Fig. 8.5	Total base shear versus lateral displacement comparisons for test structure A, phase S-1 (1 kip/in.=0.175 kN/mm) .....	136
Fig. 8.6	DUZ-7 comparisons for test structure A, phase S-1.....	138
Fig. 8.7	Cracking patterns developed in URM infill wall in HS and ST experiments (shaded areas indicate dislocated parts of wall) .....	139
Fig. 8.8	Deformation of URM infill wall and bounding RC frame .....	140
Fig. 8.9	Peak global responses in HS and ST experiments.....	141
Fig. 8.10	Displacement time histories for TAR-6.....	142
Fig. 8.11	Total base shear time histories for TAR-6.....	142
Fig. 8.12	URM infill wall contributions to restoring forces in HS and ST experiments .....	143
Fig. 8.13	Shear force versus shear strain of URM infill wall .....	145
Fig. 8.14	Estimation of shear strain from diagonal measurements ( $\Delta_1$ and $\Delta_2$ ).....	145
Fig. 8.15	URM infill wall sliding on bottom interface with respect to surrounding RC frame, TAR-6.....	146
Fig. 8.16	Observed damage in RC frame at beginning of phase S-2.....	147
Fig. 8.17	Peak lateral displacement and peak total base shear for phases S-2 and S-3 .....	148
Fig. 8.18	Total base shear versus lateral displacement for test structure A, phase S-2 for level LPB-9-2[2] (1 kip/in.=0.175 kN/mm) .....	149

Fig. 8.19	Observed damage at end of phase S-2.....	150
Fig. 8.20	Total base shear versus lateral displacement for test structure A, phase S-3 for level LPB-9-5[3] (1 kip/in.=0.175 kN/mm) .....	151
Fig. 8.21	Observed damage at end of phase S-3.....	151
Fig. 8.22	Rotation measurement in RC column-to-footing joint.....	152
Fig. 8.23	Top (beam-to-column) and bottom (column-to-footing) joint rotations for east column .....	153
Fig. 8.24	East column deformed shape at end of phase S-3, LPB-10[3].....	154
Fig. 8.25	Peak lateral displacement and peak total base shear relationships for test structure A, phase S-2.....	155
Fig. 8.26	Peak lateral displacement and total base shear relationships for test structure A, phase S-3.....	156
Fig. 8.27	Comparison of observed damage between HS and ST table test structures at end of phase S-3.....	157
Fig. 8.28	Schematic representation of test structures for quantifying the contribution of upper stories.....	158
Fig. 8.29	Idealized computational models of test structures for quantifying contribution of upper stories .....	160
Fig. 8.30	Restoring force versus lateral displacement of first-story URM infilled frame .....	162
Fig. 8.31	Evaluated fundamental frequencies of vibration in TAR-2 for different structural systems.....	163
Fig. 8.32	Evaluated fundamental frequencies of vibration in DUZ-8 for different structural systems.....	164
Fig. 8.33	Spectral acceleration of applied strong motions (5% damping ratio) for quantifying contribution of upper stories .....	165
Fig. 8.34	Total base shear versus lateral displacement for HS for test structure B (1 kip/in.=0.175 kN/mm).....	167
Fig. 8.35	Framing-to-sheathing connection schematic of local deformation .....	168
Fig. 8.36	Deformed shape of wood shear walls at peak lateral displacement .....	168
Fig. 8.37	Total base shear versus first-story lateral displacement for test structure B for LPG-4 (ST experiment).....	169
Fig. 8.38	Displacement time-history comparison for test structure B for LPG-4.....	170

Fig. 8.39	Total base shear time-history comparison for test structure B for LPG-4.....	170
Fig. 8.40	Displacement time-history comparison for test structure B for LPG-6.....	171
Fig. 8.41	Total base shear time-history comparison for test structure B for LPG-6.....	171
Fig. 8.42	Displacement time history for test structure B for third (last) repetition of LPG-6 (ST experiment).....	172
Fig. A.1	Design spreadsheet input for RRW design.....	191
Fig. A.2	Design spreadsheet output for used RRW (1 kip = 4.448 kN, 1 ft = 30.48 mm) .....	192
Fig. A.3	Frequency calculation of seven-unit high (210 in. (5334 mm)) RRW .....	193
Fig. B.1	Considered SDOF system.....	195
Fig. B.2	Typical displacement response of bilinear stiffening undraped SDOF system.....	196
Fig. C.1	Example of Bouc-Wen model including pinching .....	199
Fig. C.2	Bouc-Wen model calibration — TAR-2.....	200
Fig. C.3	Bouc-Wen model calibration — DUZ-8 .....	201

## LIST OF TABLES

Table 3.1	Actuator characteristics in nees@berkeley .....	21
Table 3.2	Evaluated parameters for validation of HSS .....	33
Table 4.1	Ground motion specifications (1 in. = 25.4 mm) .....	38
Table 4.2	Scale factors for different levels of input ground motions .....	40
Table 4.3	Physical substructures in HS .....	43
Table 4.4	Concrete compressive strength of tested cylinders .....	52
Table 4.5	Expected load and displacement requirements of substructures in test structure A .....	52
Table 4.6	Pull-back test results for substructures of test structure A .....	65
Table 4.7	Values of parameters used in RC slab in-plane stiffness estimation.....	67
Table 4.8	Estimated parameters for test structure A in phase S-1 .....	70
Table 4.9	Natural frequencies and periods for test structure A in phase S-1 .....	71
Table 5.1	Loma Prieta 1989, Los Gatos station strong motion (LPG).....	80
Table 5.2	Scale factors for different levels of input ground motion (fault normal) except as noted.....	80
Table 5.3	Estimated parameters for HS of test structure B .....	86
Table 6.1	Varied parameters for numerical evaluation of FC algorithm .....	104
Table 6.2	Varied parameters for numerical evaluation of mode-switch and iterative approach .....	112
Table 7.1	Calibration parameters for feed-forward error compensation procedure, Eq. 6.17 .....	114
Table 8.1	Tangent stiffness evaluation for test structure A, phase S-1 .....	129
Table 8.2	URM infill wall contribution to total restoring force .....	134
Table 8.3	Tangent stiffness comparisons for test structure A, phase S-1 .....	137
Table 8.4	Parameters for quantifying of contribution of upper stories .....	161
Table 8.5	Estimated natural periods (sec) for 3 DOF and 15 DOF systems .....	161
Table 8.6	Natural periods $T_n$ and corresponding spectral accelerations $S_A$ .....	164
Table B.1	Parameters for bilinear stiffening undamped SDOF system.....	196
Table C.1	Bouc-Wen model calibration parameters .....	199

# 1 Introduction

## 1.1 GENERAL

Experimental testing methods continue to benefit from technological advances. The George E. Brown, Jr. Network for Earthquake Engineering Simulation (NEES) was created by the National Science Foundation with the purpose of promoting research and education in earthquake engineering. In particular, at the University of California, Berkeley (UCB), a new hybrid simulation system (HSS), *nees@berkeley*, was established with major facilities for conducting pseudo-dynamic (online) experiments. The experimental program in the present study was designed for the purpose of developing the hybrid simulation (HS) testing method as a powerful tool for testing structural systems with an emphasis on hybrid systems, which include flexible and stiff structural elements.

Unreinforced masonry (URM) infill walls are commonly incorporated in buildings constructed in seismic and non-seismic regions, but their effect on the structural response of the structural system is often neglected during the design process. While this assumption may be valid when considering gravity loads, the lateral load resistance of these URM infill walls has a major effect on the response of the infilled systems, e.g., reinforced concrete (RC) frames, under seismic loading. The structural behavior of an infilled system is characterized by its hybrid nature due to the interaction between stiff elements (infill walls) and flexible elements (bounding frames). Although many research activities have been conducted on frames with infill walls (Mosalam 1996a, b, Mosalam et al. 1997a–e and Mosalam et al. 1998), the behavior of these structural systems under seismic loading is not yet well understood, and further experimental and computational studies are still needed. Moreover, understanding the behavior of these structural systems beyond the failure of one or more contributing elements, e.g., the URM infill wall, to the

lateral load resistance is crucial for the evaluation of structural systems experiencing progressive collapse under severe dynamic loading, e.g., due to earthquakes.

Timber structures, especially low-rise residential buildings, represent about 80% of the U.S. market. The seismic vulnerability of these structures was demonstrated during recent earthquakes in California. In particular, wood-frame buildings with an open front due to tuck-under parking are characterized by a “soft” (weak) first story. During the 1994 Northridge earthquake, 24 of the 25 fatalities that were caused by building damage occurred in wood-frame buildings. Moreover, half or more of the \$40 billion in property damage was related to wood-frame construction. In addition to the soft first story characterizing buildings with tuck-under parking, their usually asymmetric configuration in plan and irregularity in elevation may bring about torsional effects when subjected to ground motions (Mosalam et al. 2002; Mosalam and Mahin 2007). The assessment of the structural performance of this type of buildings under dynamic loading is therefore of great importance and is needed to identify the weaknesses and possible methods of enhancing the resistance to earthquake loading.

## **1.2 SCOPE AND OBJECTIVES**

The overall study program, outlined in Figure 1.1, is designed for the purpose of addressing a number of structural engineering problems. The topics in boxes 1–2, 4–6, 10, 14, and 16 are considered in Hashemi and Mosalam (2007) and focus on RC structures with URM infill walls looking to understand their structural response in terms of the interaction between infill walls and their bounding frames. Moreover, the damage and collapse mechanism is evaluated in Hashemi and Mosalam (2007), with the aim of developing representative computational models of URM infill walls and conducting reliability analysis on this type of structures. The topics in boxes 8–9, 13, and 15 are considered in Talaat and Mosalam (forthcoming 2007) and focus on the progressive collapse of structures and modeling their behavior by improving constitutive material and damage models and developing element removal algorithms, having the RC frame structure with URM infill wall as one of the main applications. The scope of this report is focused on tasks in boxes 3, 7, 11–12, and 17–18 in Figure 1.1. The detailed hybrid simulation framework designed to investigate these specific tasks is outlined at the end of this chapter in Figure 1.2.

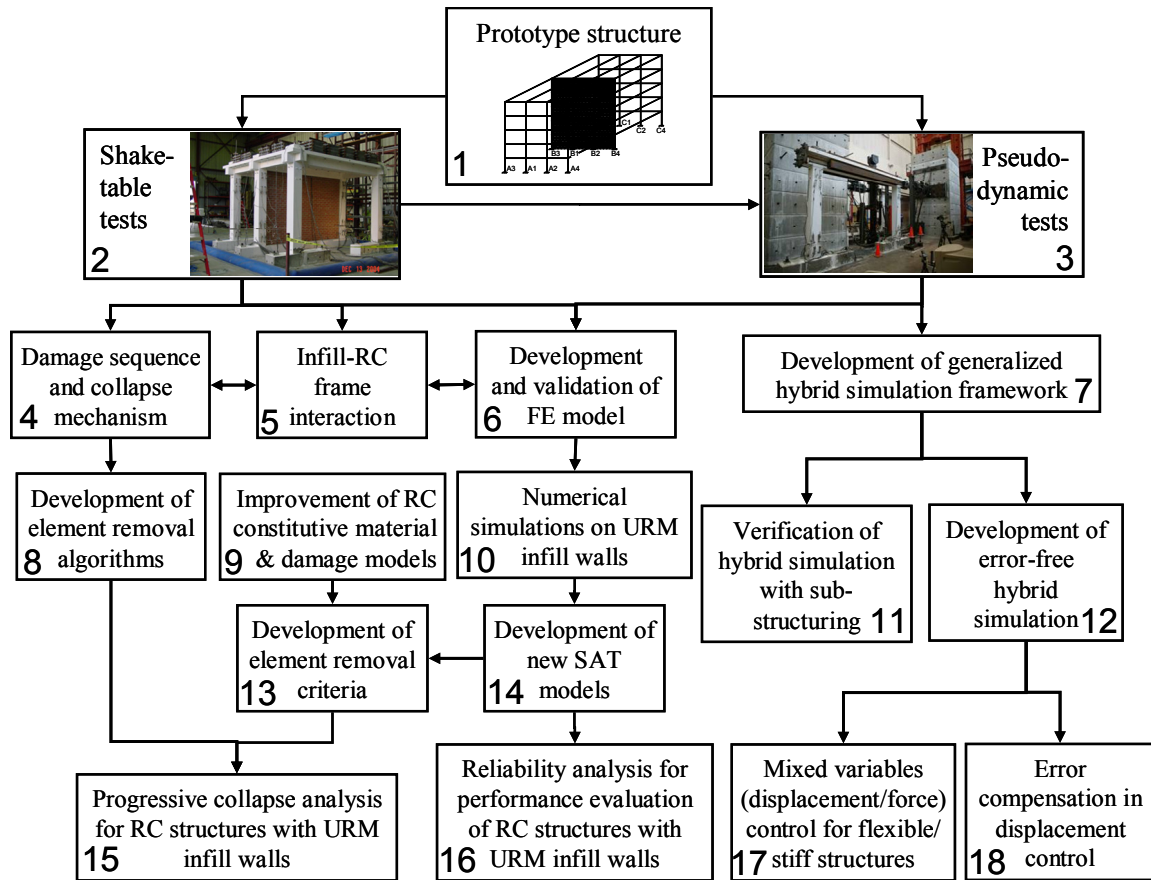


**Fig. 1.1 Overview of study program.**

The understanding of URM infilled RC systems is sought using HS in phases S-1, S-2, and S-3, as illustrated in Figure 1.2. Moreover, the idealizations, assumptions, and approximations inherent in the HS approach using the substructuring technique are evaluated by drawing a comparison with truly dynamic (shaking-table) benchmark experiments performed on a similar test structure. The potential of pseudo-dynamic experimentation is explored further through the development of a number of procedures aimed at increasing the accuracy of the execution of the experiment. First, the test rate, its implications on the test results, the experimental error evaluation and possible feed-forward compensation procedure are investigated in phase P-1 in Figure 1.2. Second, the possibility of performing pseudo-dynamic experiments in mixed-variables (displacement and force) control with mode-switching capabilities between the two control modes is explored in phase P-2, as depicted in Figure 1.2. These procedures are aimed at developing an error-free HS framework applicable to flexible/stiff structures and implemented in the *nees@berkeley* HSS. The developed procedures are performed on two different experimental test structures, namely:

1. RC frames with and without URM infill wall (test structure A in this report and referred to as test structure II in Elkhoraibi and Mosalam (2007)) as substructures of a five-story infilled RC building; and
2. Wood shear walls (test structure B in this report and referred to as test structure I in Elkhoraibi and Mosalam (2007)) of the first story of a two-story wood house-over-garage.

### 1.3 CONTRIBUTIONS

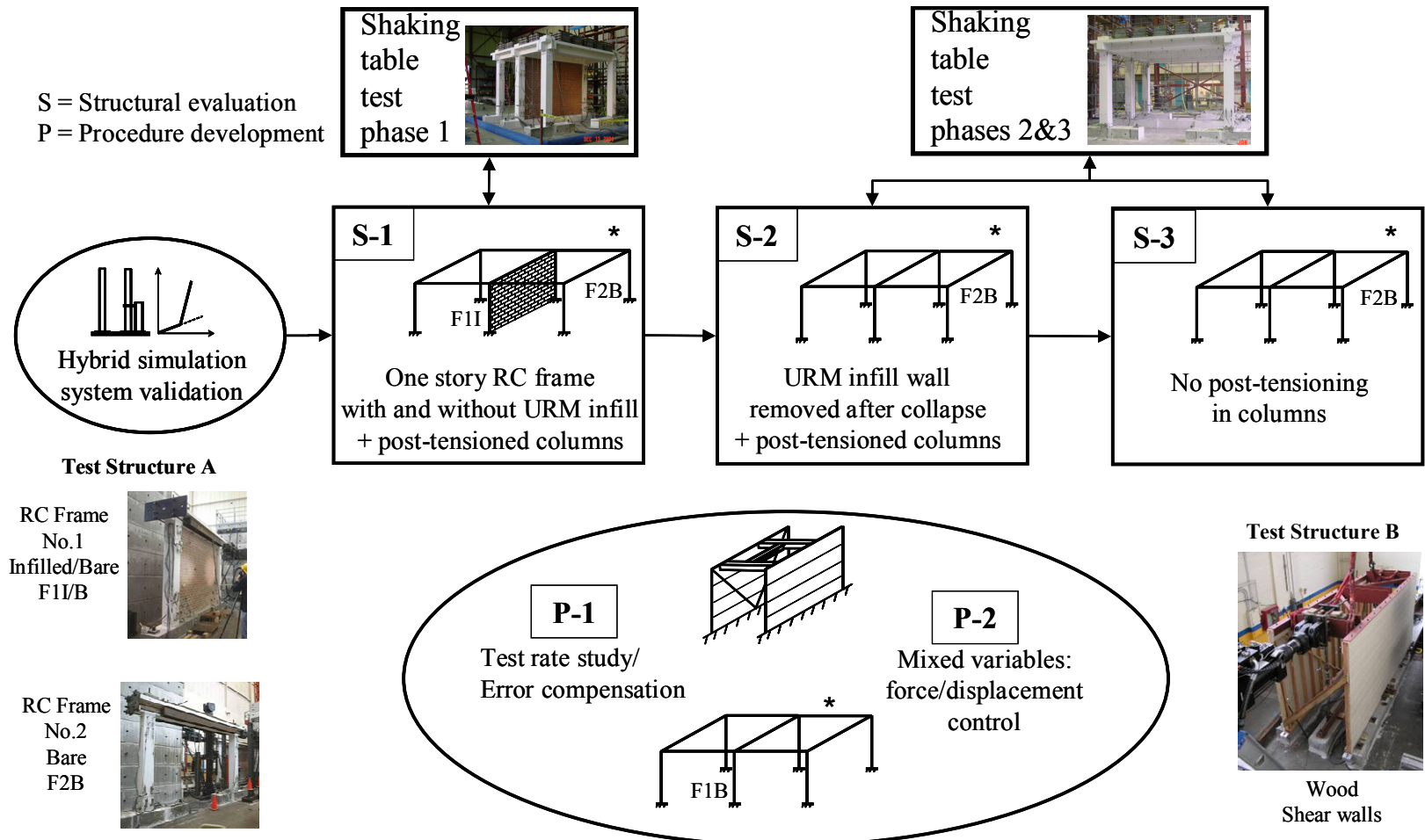
This study aims toward developing a generalized error-free hybrid simulation framework implemented within the *nees@berkeley* test facility. Accordingly, the following are regarded as the main contributions toward this goal:

- A novel implicit force-control algorithm is derived based on the  $\alpha$ -method and a numerical parametric study is conducted to evaluate its validity and accuracy.
- Mixed-variables (displacement and force) control is implemented within the hybrid simulation system with experimental validations on test structures exhibiting flexible/stiff behaviors.
- A comprehensive comparative study is conducted between the truly dynamic (shaking table) and the pseudo-dynamic (hybrid simulation) testing methods through the testing of identical structures using both experimental methods.

### 1.4 OUTLINE

The report is organized into nine chapters. Chapter 1 discusses the motivation of the study, its scope, objectives, and major contributions, with an overview of the different phases of the experimental program. A comparison between shaking-table (ST), quasi-static, and pseudo-dynamic experimental methods is presented in Chapter 2 with a special emphasis on the pseudo-dynamic method, discussing its advantages and limitations, as well as the numerical-integration algorithms associated with this type of hybrid simulation approach. The HSS at UCB *nees@berkeley*, is presented in Chapter 3, and a description of the operation sequence of the system is included, as well as a validation experiment conducted on the newly installed HSS. The design, construction, and instrumentation of the two test structures considered in this study

along with the design of their experimental setups are presented in Chapters 4 and 5 for test structures A and B, respectively. In these chapters, the development of the idealized lumped-mass model for each test structure and the estimation of key parameters in the governing equations of motion are discussed in addition to other estimated parameters such as the numerical-integration time step. In Chapter 6, the algorithmic formulation of the numerical solution of the governing equations of motion and the implementation of the displacement control (DC) algorithm are illustrated. Moreover, a procedure allowing for a feed-forward compensation of the experimental error of the displacement command execution is developed. A novel implicit force-control (FC) algorithm is derived and evaluated by a numerical parametric study. The implementation of this FC algorithm in the HSS, with mode switch between force and displacement control, is considered and several implementation strategies are developed. The FC algorithm is extended to a mixed formulation where FC may be used for certain degrees of freedom of the test structure and DC for others. Chapter 7 presents the implementation and results of the two procedures developed in Chapter 6 (phases P-1 and P-2 in Fig. 1.2) on test structures A and B. The structural evaluation of test structure A (phases S-1, S-2, and S-3 in Fig. 1.2) and that of test structure B, as well as the comparison of HS and ST experiments are discussed in Chapter 8. Finally, a summary, major conclusions, and future extensions are presented in Chapter 9.



\* Labeled frames are the physically modeled ones in the hybrid simulation experiments

**Fig. 1.2 Overview of hybrid simulation experimental program.**

## 2 Background

In this chapter, different experimental methods of structures subjected to dynamic loading, particularly those due to ground motion caused by earthquakes, are compared and the HS, i.e., pseudo-dynamic experimental method, is described. The development of the method is summarized and the integration algorithms used to solve the governing equations of motion of test structures are presented. HS of stiff structures in particular is examined.

### 2.1 COMPARISON OF EXPERIMENTAL METHODS

Structures subjected to seismic loading exhibit complex behavior, and several experimental techniques are employed to simulate their response. Purely numerical simulations are based on assumptions concerning the properties of materials and the behavior of structural elements, which are inherently uncertain. Experimental techniques are therefore needed to validate the accuracy of numerical simulation models. These techniques are divided into three main categories: (1) ST experiments, (2) quasi-static experiments, and (3) pseudo-dynamic experiments, also known as the online experiments, or HS.

In the ST experiments, the test structure is placed on the seismic simulator that is then subjected to a recorded strong motion by means of dynamic actuators. While this experimental technique is truly dynamic, the size of the ST and the capacity of the dynamic actuators, responsible for applying the strong motion, put limitations on the size of the test structure, the amplitude of the applied motion, and the accuracy of its implementation. If a small-scale specimen is used, similitude problems occur and the interpretation of the results becomes difficult. Note that other dynamic experimental techniques, such as the effective force method, are developed for the purpose of real-time experiments (Dimig et al. 1999; Shield et al. 2001; Wu et al. 2007) to alleviate the limitations associated with ST experiments.

The quasi-static experiments use static actuators to load the test structure at low speed with a prescribed load (displacement) time history. This allows testing larger structures than those that can be tested on the ST under large amplitudes of motion with high fidelity to the selected input pattern of loads or displacements. However, the equivalent static load or displacement needs to be defined prior to testing, e.g., by a series of loading/unloading (sinusoidal) cycles or by numerically solving the equations of motion using step-by-step numerical-integration algorithms (see Section 2.3) in the case of a defined seismic excitation with assumed structural parameters that are not entirely known in advance. In particular, while mass and damping may be estimated with reasonable accuracy, the stiffness of a test structure exhibiting nonlinear behavior changes as the loading progresses and causes the restoring forces and deformations to change accordingly. Thus, in general, the calculated loading history to be applied in quasi-static experiments may not correspond to the actual response of the test structure if it were tested dynamically.

HS experiments use the governing equations of motion of an equivalent lumped-mass system of the test structure to solve for the equivalent static load or displacement, but do so interactively during the experiment by using the readily available (online) force and deformation information from the test structure. At each integration time step, the displacement is applied on the test structure and its corresponding restoring-force feedback is measured and used to solve the next integration time step. This technique inherits the advantages of quasi-static experiments as well as implementing a much more accurate loading history by benefiting from these online measurements (feedbacks) and simulations.

## **2.2 DEVELOPMENT OF HS EXPERIMENTAL METHOD**

Since the first development introduced in Takanashi et al. (1975), the pseudo-dynamic method proved to be a versatile experimental approach and has benefited from technologically improved hardware and developed integration algorithms and techniques. A U.S.-Japan Cooperative Earthquake Research Program in the 1980s provided impetus for further development, with significant research efforts in the U.S. occurring primarily at UCB (Shing and Mahin 1983, 1984, 1985, 1987a, b; Shing et al. 1984) and the University of Michigan, Ann Arbor (McClamroch et al. 1981; Hanson and McClamroch 1984). Much of this research focused on accuracy

verification of this test method and the investigation into the control of certain experimental intricacies affecting the pseudo-dynamic test.

Comparative testing of pseudo-dynamic and ST methods by Yamazaki et al. (1989) revealed concerns regarding loading-rate effects and experimental errors. Takanashi and Nakashima (1987) and Mahin et al. (1989) provide summaries of the early development of the pseudo-dynamic testing in both Japan and the U.S., respectively, and identify needs for improved control of hydraulic actuators to limit the inevitable experimental errors. Loading-rate effects have largely been tolerated compared to uncertainties in small-scale ST tests. However, in some cases of velocity-dependent behavior, real-time HS is of interest and several research activities have studied that aspect by performing real-time pseudo-dynamic testing (Nakashima 2001; Magonette 2001) and by developing integration algorithms suitable for high-speed testing (Bonelli and Bursi 2004).

Perhaps one of the most important features of HS is substructuring (Dermitzakis and Mahin 1985; Gawthrop et al. 2005). In this technique, the test structure is divided into physically modeled and numerically simulated substructures. The numerical simulation is assigned to elements of the structure with well-understood behavior and the physical modeling is reserved for the more complex structural elements. Geographically distributed testing is another attractive feature in the HS testing method that is based on substructuring (Pinto et al. 2002; Mosqueda 2003; Pan et al. 2006; Takahashi and Fenves 2006). In Mosqueda (2003), a bridge is tested with the columns physically modeled, whereas the deck, which is expected to behave as a rigid connecting body, is numerically simulated. Furthermore, experimental and computational substructures are tested in different laboratories (sites) where data exchange between different simulation sites is achieved via the Internet.

Large-scale pseudo-dynamic experiments have been performed on stiff structures including masonry walls. A major pseudo-dynamic testing program at the University of California, San Diego, has been conducted on a five-story full-scale reinforced masonry test building. Two significant innovations that evolved during this research include the “soft-coupling” to improve actuator control and the “generalized sequential displacement method” to generalize pseudo-dynamic testing beyond a single ground motion (Seible et al. 1994a,b, 1996). At Cornell University, pseudo-dynamic testing has been conducted for the first time on a two-story infilled steel frame (Mosalam 1996a, 1997c, 1998) and on a two-story infilled RC frame (Buonopane 1997).

## 2.3 INTEGRATION ALGORITHMS

Numerical-integration algorithms, used to solve the equations of motion, play a major role in HS. A variety of algorithms exist and may be classified into explicit and implicit methods. Explicit formulations predict the displacement to be imposed on the test structure as a function of the information already available from the previous time steps. On the other hand, implicit formulations require information from the current time step to satisfy the kinematic conditions imposed on the test structure and the dynamic equilibrium governed by the equations of motion at the end of the time step; hence an iterative approach is needed. Most of the first-generation HS testing and research focused on the use of explicit time-integration algorithms (Shing and Mahin 1985). The intention of using HS tests to study the nonlinear seismic behavior of structures led to an avoidance of implicit techniques. With varying tangent stiffness at each time step, implicit solutions would require iterations unless reliable prediction of this continuously changing stiffness is made. Such iterations must be imposed on the test structure and therefore may introduce unrealistic loading/unloading cycles, one of the drawbacks of quasi-static testing meant to be avoided with pseudo-dynamic testing.

At this point, let us introduce the governing equations of motion for an idealized lumped-mass multiple-degree-of-freedom (MDOF) system subjected to an excitation force vector  $\mathbf{P}$  as follows:

$$\mathbf{M}\ddot{\mathbf{u}} + \mathbf{C}\dot{\mathbf{u}} + \mathbf{K}\mathbf{u} = \mathbf{P} \quad (2.1)$$

where the MDOF system is described by the mass matrix  $\mathbf{M}$ , damping matrix  $\mathbf{C}$ , restoring-force vector  $\mathbf{R} = \mathbf{K}\mathbf{u}$  with  $\mathbf{K}$  as the stiffness matrix of the structure, and the acceleration, velocity, and displacement vectors are denoted  $\ddot{\mathbf{u}}$ ,  $\dot{\mathbf{u}}$  and  $\mathbf{u}$ , respectively. Notice that the structure is idealized into a finite number of degrees of freedom (DOF) with lumped masses, which is an assumption not necessarily applicable for every structure (Shing et al. 1996).

Newmark's numerical-integration method (Newmark 1959) is presented below as the most common integration algorithm in structural dynamics. At time  $t_{i+1}$ , the equations of motion are discretized as follows:

$$\mathbf{M}\ddot{\mathbf{u}}_{i+1} + \mathbf{C}\dot{\mathbf{u}}_{i+1} + \mathbf{K}\mathbf{u}_{i+1} = \mathbf{P}_{i+1} \quad (2.2)$$

This is supplemented with the following expressions for the discretized displacement and velocity vectors,

$$\mathbf{u}_{i+1} = \mathbf{u}_i + \Delta t \dot{\mathbf{u}}_i + \Delta t^2 (1/2 - \beta) \ddot{\mathbf{u}}_i + \beta \Delta t^2 \ddot{\mathbf{u}}_{i+1} \quad (2.3)$$

$$\dot{\mathbf{u}}_{i+1} = \dot{\mathbf{u}}_i + \Delta t (1 - \gamma) \ddot{\mathbf{u}}_i + \Delta t \gamma \ddot{\mathbf{u}}_{i+1} \quad (2.4)$$

where  $\Delta t$  is the time step and  $\beta$  and  $\gamma$  are parameters of integration. Making use of  $\mathbf{R}_{i+1} = \mathbf{K}\mathbf{u}_{i+1}$ , Equation (2.4) and Equation (2.2) are used to estimate the acceleration vector as follows:

$$\ddot{\mathbf{u}}_{i+1} = [\mathbf{M} + \Delta t \gamma \mathbf{C}]^{-1} \{ \mathbf{P}_{i+1} - \mathbf{R}_{i+1} - \mathbf{C} [\dot{\mathbf{u}}_i + \Delta t (1 - \gamma) \ddot{\mathbf{u}}_i] \} \quad (2.5)$$

The application of the above algorithm in the context of pseudo-dynamic experimentation starts by applying an explicit version of Equation (2.3) to find the predicted displacement, and after its application on the test structure, the corresponding restoring-force vector  $\mathbf{R}_{i+1}$  is measured. This predictive step is subsequently corrected in an iterative manner using Equations (2.4)–(2.5) to satisfy equilibrium in Equation (2.2). Based on the values of the parameters  $\beta$  and  $\gamma$ , the method is defined as an average acceleration approach ( $\beta = 1/4$  and  $\gamma = 1/2$ ) or a linear acceleration approach ( $\beta = 1/6$  and  $\gamma = 1/2$ ). Both of these approaches are implicit in nature since the displacement at time  $t_{i+1}$ , i.e.,  $\mathbf{u}_{i+1}$ , is a function of the unknown acceleration  $\ddot{\mathbf{u}}_{i+1}$ . Note that the factor  $\gamma$  introduces artificial numerical damping in the system if taken to be greater than one half (Dermitzakis and Mahin 1985). The application of explicit integration is limited by certain conditional stability limits. If  $\beta = 0$  in the Newmark's numerical-integration method, the method becomes explicit and combined with  $\gamma = 1/2$ , the method reduces to the central difference method. As an example, the condition of convergence for the central difference method is  $\Delta t \leq 2/\omega_n$  where  $\omega_n$  is the largest natural frequency of the structure (Chopra 2000). For MDOF systems, as  $\omega_n$  increases, this condition of convergence may prove to be a major limitation, especially when considering the effect of experimental errors. This situation is very complicated due to the fact that the experimental errors increase with reduced time steps and may develop into spurious higher-mode response (Shing and Mahin 1983). For the purpose of controlling the spurious growth of experimental errors in higher-frequency modes, Shing and

Mahin (1983) suggested a modified Newmark explicit method employing artificial numerical damping with the modal damping ratio increasing proportionally with  $\Delta t \omega_n$ .

One of the most recognized numerical-integration algorithms was introduced in Hilber et al. (1977) and Hughes (1983) as the modified Newmark implicit  $\alpha$ -method. In this algorithm, the equations of motion are written in the following form:

$$\mathbf{M}\ddot{\mathbf{u}}_{i+1} + \mathbf{C}\dot{\mathbf{u}}_{i+1} + (1 + \alpha)\mathbf{R}_{i+1} - \alpha\mathbf{R}_i = \mathbf{P}_{i+1} \quad (2.6)$$

The displacement and velocity vectors are computed from Equations (2.3) and (2.4), respectively. The introduced parameter  $\alpha$  adds dissipation in the form of artificial damping to the MDOF system and is related to the original parameters in Newmark's numerical-integration method  $\beta$  and  $\gamma$  by  $\beta = (1 - \alpha)^2 / 4$  and  $\gamma = 1/2 - \alpha$ . If  $\alpha = 0$ , no numerical damping is introduced and the method reduces to the average acceleration method. This implicit method leads to the following relationships:

$$\mathbf{u}_{i+1} = \mathbf{u}_i + \Delta t \dot{\mathbf{u}}_i + \Delta t^2 (1/2 - \beta) \ddot{\mathbf{u}}_i + \beta \Delta t^2 [\mathbf{M} + \gamma \Delta t \mathbf{C}]^{-1} \{ \mathbf{P}_{i+1} + \alpha \mathbf{R}_i - \mathbf{C} \dot{\mathbf{u}}_i - \mathbf{C} (1 - \gamma) \Delta t \ddot{\mathbf{u}}_i - (1 + \alpha) \mathbf{R}_{i+1} \} \quad (2.7)$$

Notice that the right hand side of the above equation is explicit except for the restoring-force vector  $\mathbf{R}_{i+1}$ .

Based on the implicit-explicit method developed by Hughes et al. (1979), Nakashima et al. (1990) developed an operator-splitting (OS) scheme where the stiffness of the structure is split into experimental and numerical parts. This method allows the implementation of an explicit algorithm for the physical substructure and an implicit algorithm for the computational substructure. Moreover, the operator-splitting scheme ensures an unconditionally stable numerical solution if the nonlinearity of the physical substructure is of the softening type. Novel approaches such as the state-space procedure based on the interpolation of the discrete excitation signals for piecewise convolution integral are combined with the operator-splitting scheme (Wang et al. 2001). Recent developments include integration algorithms allowing a reliable real-time implementation of HS (Darby et al. 2001).

## 2.4 HS OF STIFF STRUCTURAL SYSTEMS

While for flexible behavior, displacement commands can be implemented with adequate accuracy under DC, it may be preferable in some stiffer states of behavior of the test structures (large force increments corresponding to small displacement increments) to switch to FC. With this possibility, the force commands are controlled during these stiff states with better accuracy than those of the corresponding displacement commands if executed under the more-conventional DC. Such concerns were previously addressed by several researchers. Thewalt and Mahin (1987 and 1995) implemented the modified Newmark implicit  $\alpha$ -method with a creative approach, making use of the available restoring-force information during the displacement command implementation within the same time step in an analog form. The displacement command  $\mathbf{u}_{i+1}$  is calculated in analog form by an addition of the explicit part of Equation (2.7) converted from digital to analog and an analog function for the implicit part involving  $\mathbf{R}_{i+1}$ . This signal is applied on the test structure while continuously being updated by the measured analog signal value of  $\mathbf{R}_{i+1}$  following Equation (2.7). This hybrid solution has the advantage of employing implicit integration methods without the need for iterations or for estimation of the tangent stiffness. Furthermore, Thewalt and Mahin (1987 and 1995) proposed an extension to their hybrid method to solve the equations of motion for force instead of displacement. In this approach, and rearranging Equation 2.7, the equations of motion can be solved for the restoring forces as follows:

$$\begin{aligned} \mathbf{R}_{i+1} = & \frac{1}{\beta\Delta t^2(1+\alpha)} [\mathbf{M} + \gamma\Delta t\mathbf{C}] \{ \mathbf{u}_i + \Delta t\dot{\mathbf{u}}_i + \Delta t^2(1/2 - \beta)\ddot{\mathbf{u}}_i - \mathbf{u}_{i+1} \} \\ & + \frac{1}{(1+\alpha)} \{ \mathbf{P}_{i+1} + \alpha\mathbf{R}_i - \mathbf{C}\dot{\mathbf{u}}_i - \mathbf{C}(1-\gamma)\Delta t\ddot{\mathbf{u}}_i \} \end{aligned} \quad (2.8)$$

This approach offers the possibility of conducting the pseudo-dynamic test in FC or by a mixed formulation in mixed-variables control, which would have the potential of eliminating some problems incorporated with testing stiff structures.

Sieble et al. (1994a, b and 1996) used elastomeric pads to develop the method of soft-coupling, which increases the DC accuracy hindered by limited actuator displacement resolution, especially in the case of stiff DOF. While this technique provides an interesting solution, it is not ideal for DOF experiencing mixed stiff and flexible behaviors, or for higher amplitudes of loads,

where the technique used to install the pads, employing a friction connection, becomes highly nonlinear and may affect the control accuracy especially at these higher load amplitudes.

Pan (2004) and Pan et al. (2005) tested a high-damping rubber bearing under seismic loading using mixed displacement-force control to apply the bearing axial load. Force control was used for loading in compression, which is associated with a high stiffness, and DC was used for loading in tension, which is associated with a much lower stiffness. The force command in the former case was calculated as the product of the calculated displacement command and a predetermined constant stiffness, assuming elastic response in compression. While this solution is suitable for a linear elastic structure, for a structure with nonlinear stiffness, the solution is not valid.

## 2.5 SUMMARY

Different experimental methods developed for the simulation of structural behavior under seismic loading are compared, with a focus on the advantages and disadvantages of the hybrid simulation testing. The development of hybrid simulation is summarized in terms of its earlier development, the problems it encounters, and the major efforts conducted to overcome these obstacles. The hybrid simulation testing method for testing the seismic performance of structures offers a number of advantages, summarized as follows:

- Allows testing larger-scale test structures than on the shaking table.
- Allows testing physical substructures experimentally while modeling other parts of the structure numerically.
- Offers the possibility of running simulations slower than real time to allow better monitoring of structural degradation.
- Offers the possibility of geographically distributed testing.

On the other hand, the hybrid simulation testing method faces some problems:

- Testing stiff structural systems remains a challenge.
- Rate-sensitive materials need to be tested in real or close to real time, although several efforts have been made in that regard.

To lay out the foundation of the hybrid simulation method, the equations of motion of a structural system subjected to dynamic loading are presented. Newmark's numerical-integration

method is presented as an example of the most widely used numerical-integration algorithms to solve the equations of motion during hybrid simulation. Finally, the development of new integration algorithms and novel techniques intended for the implementation in hybrid simulation are discussed including the treatment of stiff structural systems.

## 3 Hybrid Simulation

The HSS at *nees@berkeley.edu* consists of several components interconnected to allow for an efficient implementation of the online experimental technique with flexibility in designing the test setup. This chapter presents the different components of this particular HSS, its inner and interconnecting structures, and the testing possibilities such a system may offer. The newly installed GSS is then validated for the purpose of ensuring its proper functionality. For this validation, a pseudo-dynamic experiment is designed with a numerically reproducible structural behavior of the test specimens where experimental results using the HSS are validated against pure numerical simulation.

### 3.1 HSS OVERVIEW

The main components of the HSS used in the present study are shown in Figure 3.1. Each component is described in terms of its function and connections with the other constituents of the system. The main components are as follows:

1. Structural laboratory
2. ScramNet
3. Structural Test System (STS)
4. xPC target
5. Pacific Instruments data-acquisition system
6. MatLab environment

The architecture of the HSS is illustrated further in figure 3.2, where data exchange is identified. A detailed description of each component is presented in subsequent sections.

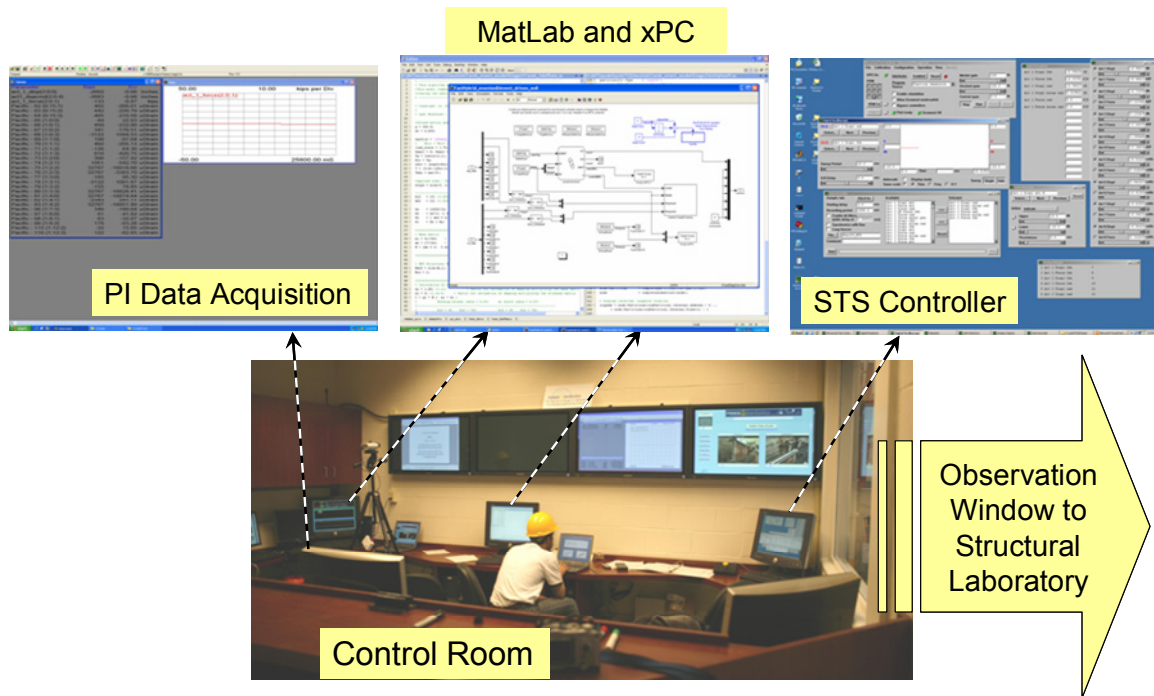


**Fig. 3.1 Control room and HSS.**

## **3.2 STRUCTURAL LABORATORY**

The structural laboratory provides the experimental site for testing the specimens using reconfigurable reaction walls (RRW). It includes the strong floor as well as the necessary hydraulic actuator system for loading the experimental substructures.

### **3.2.1 Reconfigurable Reaction Walls (RRW)**

The RRW is constructed by assembling a number of precast high-strength RC units of box-section type. These units are post-tensioned using high-strength steel rods to work in unison as a single or multiple reaction system fixed to the laboratory strong floor. The stiffness and fundamental frequencies of the RRW are evaluated experimentally for the configuration used in this study and confirmed for no possible interaction with the dynamics of the studied test structures (Mosalam and Elkhoraibi 2004). Upon assembling the RRW units, actuators are

attached to the test structures and reacted against the RRW. The concrete geometric details for a typical RRW unit in plan, elevation and side views are shown in Figure 3.3.

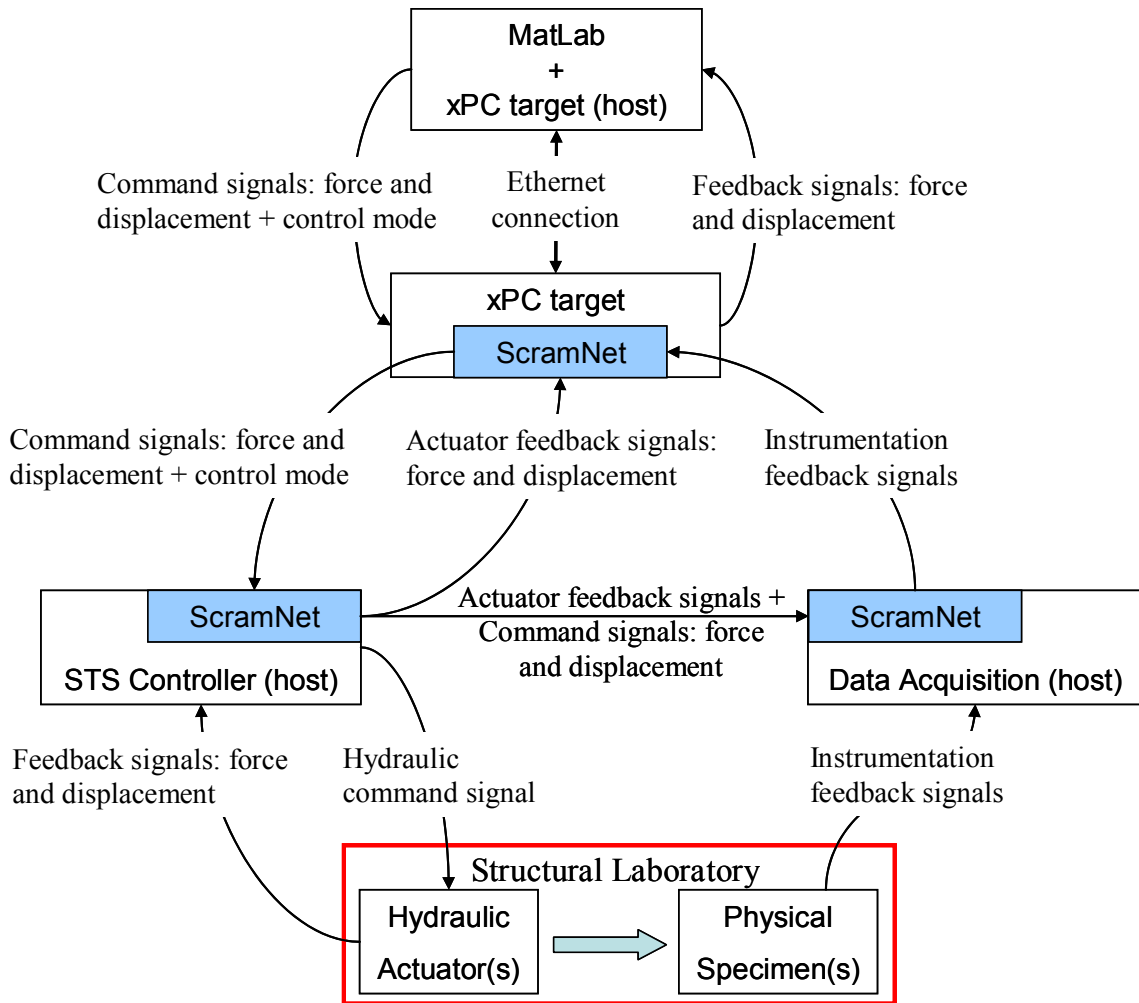


**Fig. 3.2 HSS architecture.**

The required number of RRW units to assemble for each reaction wall is determined based on the height of the load application point on the test structure. The structural properties of the assembled reaction wall are evaluated using a design spreadsheet where the reaction wall is checked for sliding, lateral displacement, and shear and tension limits specified by the user. In case of dynamic loading, the modal frequencies of the assembled reaction wall are also estimated. If any of the limits are not met, the user is able to choose a different reaction wall configuration by changing the height and/or the orientation of the weak and strong directions of the RRW units, or stiffening it with additional adjacent RRW units. Appendix A includes an

example for configuring the RRW used in the present study making use of the developed design spreadsheet.

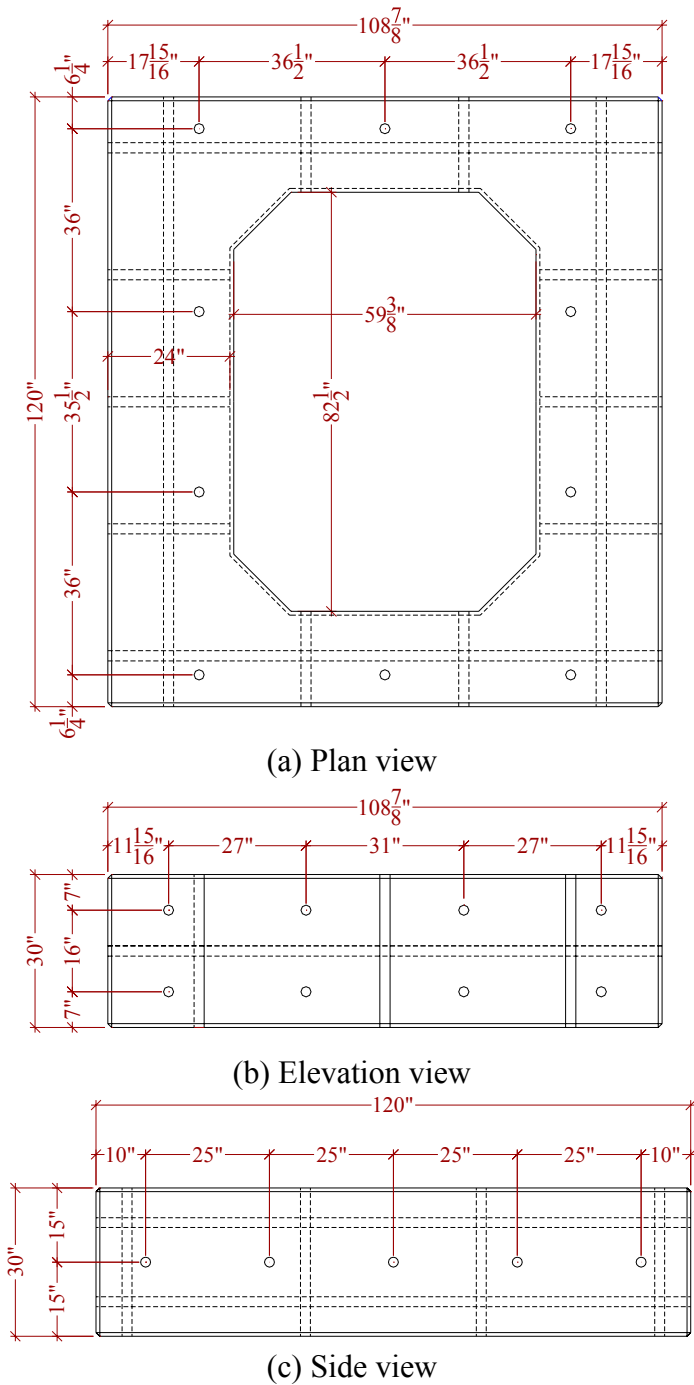


**Fig. 3.3 Concrete geometry of typical RRW unit (1"=25.4 mm).**

### 3.2.2 Actuators

Seven MTS actuators are available as *nees@berkeley* equipment to use with the RRW for testing different types of specimens. Based on the available actuator characteristics, as shown in Table 3.1, the intended loading configuration and the anticipated structural performance of the test structure, the user is able to select the most appropriate actuator(s) to be used in the experiment. In the present study, two dynamic actuators for test structure A and one actuator for test structure B in the top row of Table 3.1 (with high-force capacity and medium-stroke capacity) are used.

**Table 3.1 Actuator characteristics in nees@berkeley.**

Type	Compression/Tension capacity [kip (kN)]	Static/Dynamic stroke [in. (mm)]	Maximum velocity [in./sec <sup>2</sup> (mm/sec <sup>2</sup> )]	Quantity
Dynamic	220/220 (979/979)	22/20 (558/508)	20 (508)	2
Dynamic	150/150 (667/667)	42/40 (1067/1016)	20 (508)	2
Static	328/216 (1459/961)	72 (1829)	0.75 (19)	3

### 3.3 ScramNet

ScramNet is a real-time communications network, based on a replicated shared memory concept (Systran 2000). Each processor on the network has access to its own local copy of saved memory that is shared over a high-speed, serial ring network. The network is optimized for high-speed data transfer among multiple real-time computers, all solving portions of the same real-time problem. A ScramNet card is installed on each of the machines in question. ScramNet is used in the present study as a link between the different components of the HSS (Fig. 3.2). It holds data available at all times for all involved parties and is updated in real time.

### 3.4 STRUCTURAL TEST SYSTEM

The Structural Test System (STS) software is provided by MTS (2003). It is a digital control system designed to serve as the interface for the hybrid controller hardware, which serves as a link between the physical laboratory (servo-valves, actuators, and test specimens) and the computational laboratory (xPC target and MATLAB environment). The system includes the closed feedback control loop that controls the actuator(s) and insures proper execution of the

command signals. This is performed using PIDF control as discussed in the following section. STS also has the responsibility of converting digital command signals into analog signals and conversely analog feedback signals into digital signals made available in real time through ScramNet at interrupts of 1024 Hz, i.e., at time steps of  $\delta t = 1/1024$  sec. Moreover, STS provides means for filtering feedback signals when needed.

An important feature of the STS software is that all the parameters defined for a specific test setup are saved in a settings (\*.set) file, which is selected and invoked every time the system is turned on. This allows the reuse of the same setting of a particular experiment for other experiments. Another application in STS, namely the “Data Recorder,” allows recording the data obtained during the test, e.g., force feedback signals, through the STS controller (Fig. 3.4). Limit detectors are available for each actuator as a safety measure in case the actuator surpasses the maximum set limits in force or position among other parameters that may be monitored. Moreover, the STS controller provides viewing options in the form of an oscilloscope to monitor feedback and command signals while the test is in progress, as well as various window displays of digital values of parameters of interest, such as setpoints, which are the controller mode and command signals of each actuator.

### **3.4.1 PIDF Control**

A controller uses a target command and a sensor feedback to control the servo-valve feeding the hydraulic actuators. The main objective of the PIDF control is to provide a highly responsive system to implement the command signals accurately while ensuring stability. Inaccurate control increases the error and phase lag between the command and feedback signals.

The MTS controller uses a group of gain controls, namely: proportional (P), integral (I), derivative (D), and feed forward (F). The P gain increases the system response, while the I gain increases the system accuracy during static (low-frequency) operation and maintains the mean level at high-level operation. The D gain improves the dynamic stability for high P gain. Finally, the F gain increases the system accuracy during high-frequency operation.

While DC is tuned without the need for a specimen, FC tuning requires the installation of a specimen to provide the necessary force feedback. Figure 3.5 illustrates the windows used to define and tune the actuator controller in displacement and force modes.

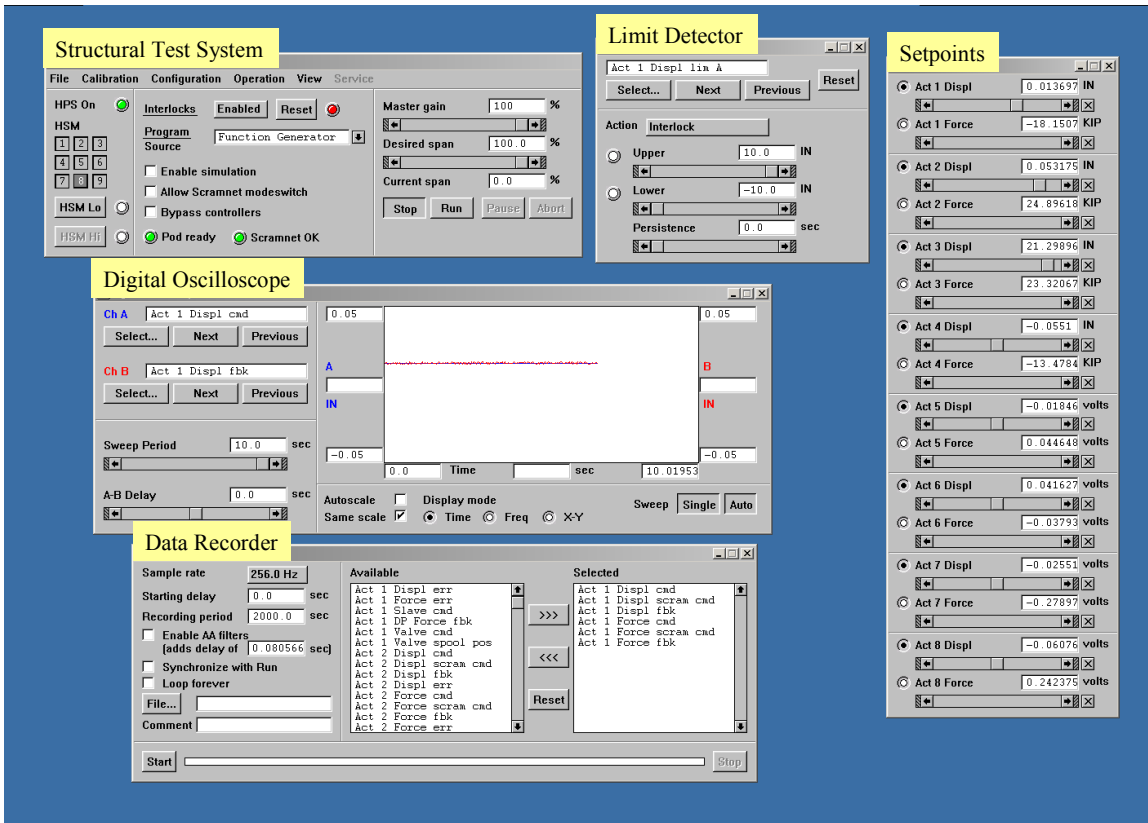
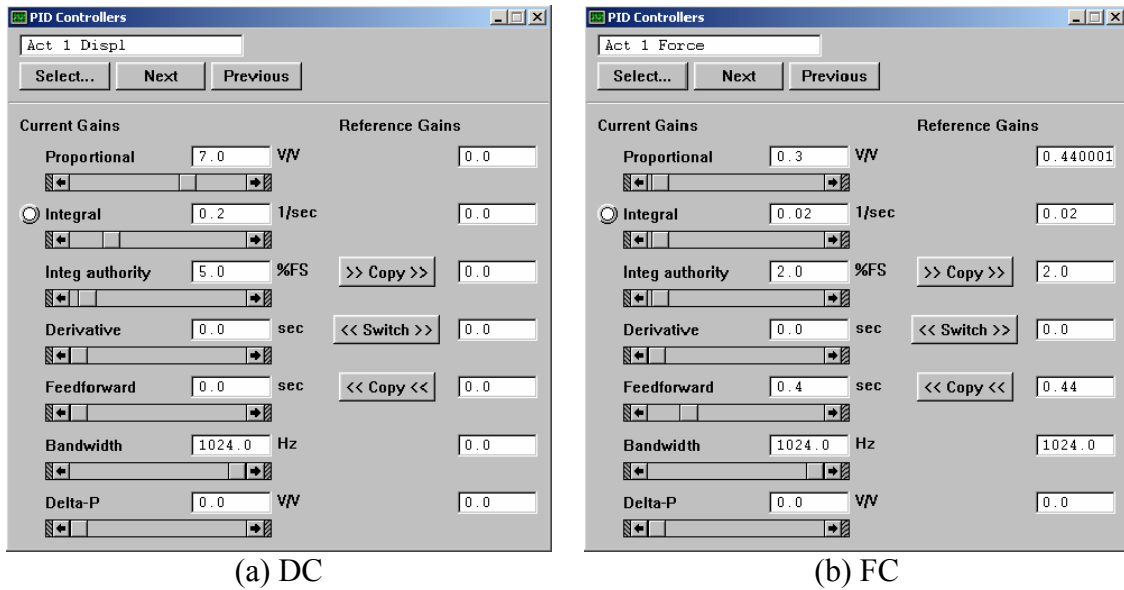


Fig. 3.4 STS host PC.

### 3.4.2 Program Source in STS

STS has a number of “Program Sources” available (Fig. 3.6) that define the source of the command signal transmitted to the PIDF controller. The available program sources are:

**Function Generator:** creates a cyclic signal characterized by its amplitude, frequency, and form (square, triangular, or sinusoidal) (Fig. 3.7). A different function form may be chosen for each actuator in DC or FC with its corresponding amplitude and frequency. This source is suitable for the pre-test phase and may be used to tune the actuators, or to warm up the hydraulic actuator system before an actual test run.



**Fig. 3.5 PIDF controls of displacement (DC) and force (FC) in STS.**

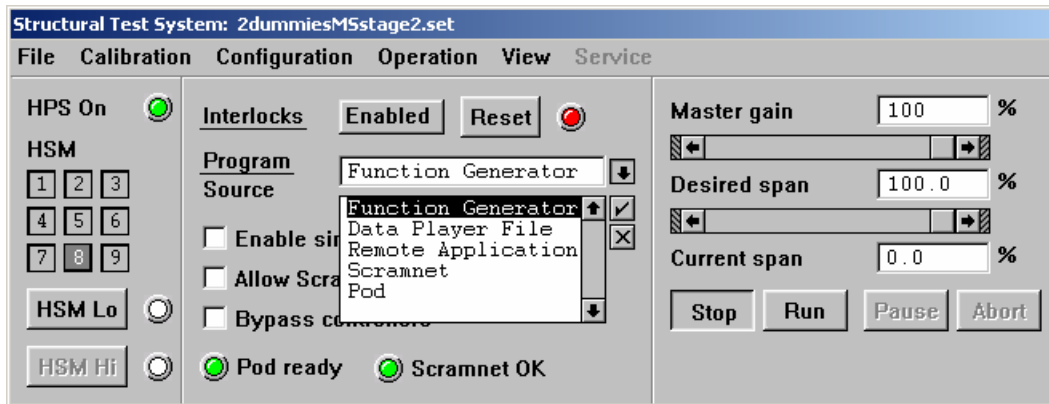


**Fig. 3.6 Available program sources in STS.**

**Data Player File:** used for applying a previously recorded load sequence.

**Remote Application:** provides the possibility of sending target commands from an outer source through Ethernet connection.

**ScramNet:** transmits the command signals from xPC target, discussed in the next section, to STS in real time where STS updates its memory at 1024 Hz. This source is used for the present HS. Discussion on ScramNet has been previously presented in Section 3.3.

**Pod:** allows the actuators to be controlled manually through a mobile pod available on the structural laboratory, which gives the user control over the actuator(s) to a high degree of accuracy (within thousandths of an inch), while observing the test structure and actuator. This is mainly used for the attachment of the actuator to the test structure.

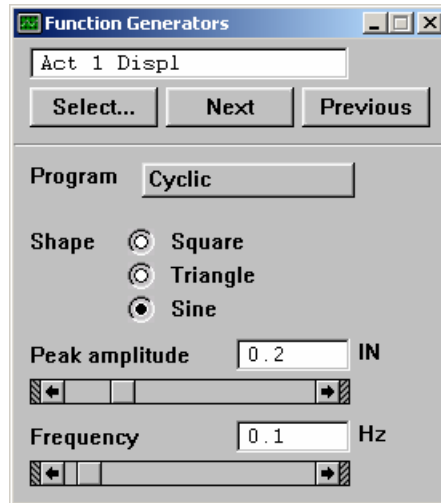


**Fig. 3.7 Function generator in STS.**

### 3.5 xPC TARGET

xPC target is a solution for prototyping, testing, and deploying real-time systems using standard PC hardware. It is an environment that uses a target PC, separate from a host PC, for running real-time applications. In the present study, xPC target is used as a link, running compiled Simulink models and operating in real time, between the STS controller and the MATLAB environment, discussed in Section 3.7. It is programmed on the host PC using MATLAB, Simulink, and Stateflow. The information exchanged between the two entities, namely STS controller and the MATLAB environment, includes feedback signals and control modes. In Figure 3.8, the left block represents the input parameters transmitted from STS to xPC, while the right block represents the output parameters sent from xPC to STS. The middle block is the mask for the operations performed by xPC using the input signals to produce the output signals and is expanded in Figure 3.9. The upper and lower lines, on the left hand side of the figure, are the displacement feedback and force feedback signals, respectively, of the eight actuators that may be incorporated in the model. Two actuators are used in this case and a series of operations is performed including the exchange of information with the MATLAB environment. The set of output (displacement command) signals is assembled at the vertical line, on the right-hand side of the figure, and passed to the STS controller through ScramNet.

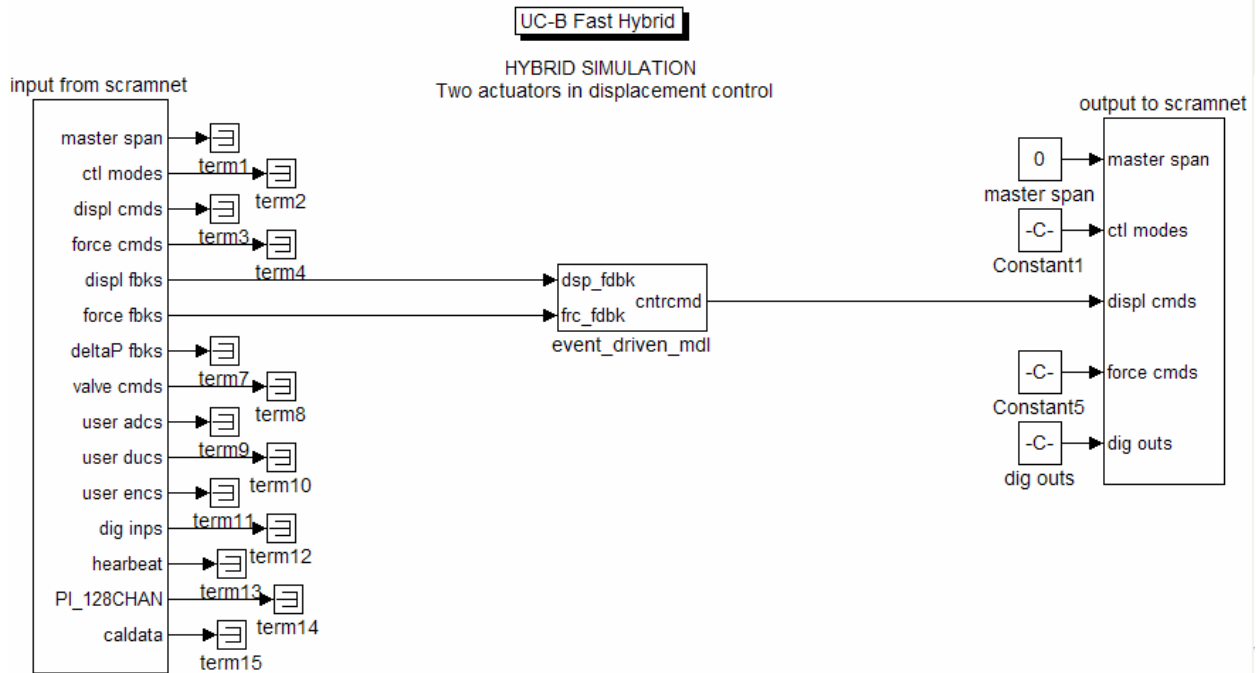


**Fig. 3.8 Simulink model for xPC target.**

Once the MATLAB environment computes the required information such as command values at the end of each integration time step as well as control modes, i.e., displacement or force in mixed-variables control discussed in Chapter 6, this information is transmitted to the xPC target. These signals are transformed into real-time interrupts (1024 Hz) in the Simulink model, which is linked to the STS controller in real time through ScramNet. The transformation is performed through a process of extrapolation/interpolation, as described in Section 3.8, where a variety of extrapolation and interpolation protocols are available. One of these protocols, namely the third-degree Lagrange polynomial (Mosqueda 2003), is used in the present study. This protocol ensures that the velocity of the actuator, dictated by the predicted target for extrapolation, closely matches the velocity implied by the calculated target displacement from an explicit integration algorithm in the same time step, thus causing the least disturbance possible to the motion of the actuators. This protocol, however, is not suitable for an implicit integration algorithm, where the iterations within the same integration time step do not necessarily follow the expected velocity pattern and where the displacement increments in one iteration may be in the opposite direction to the previous ones (same for velocities). In this case, and to avoid unrealistic loading/unloading cycles that may be caused by an erroneous predicted target for extrapolation, a linear interpolation from the current state to the new command is preferred. At

the end of the time step, as soon as the desired command is executed by the PIDF controller, the feedback signals corresponding to the implemented command are transferred to the MATLAB environment. Finally, xPC target offers an environment where the real-time data are available for special procedures such as computations related to the estimation of the secant stiffness, as discussed in Chapter 6.

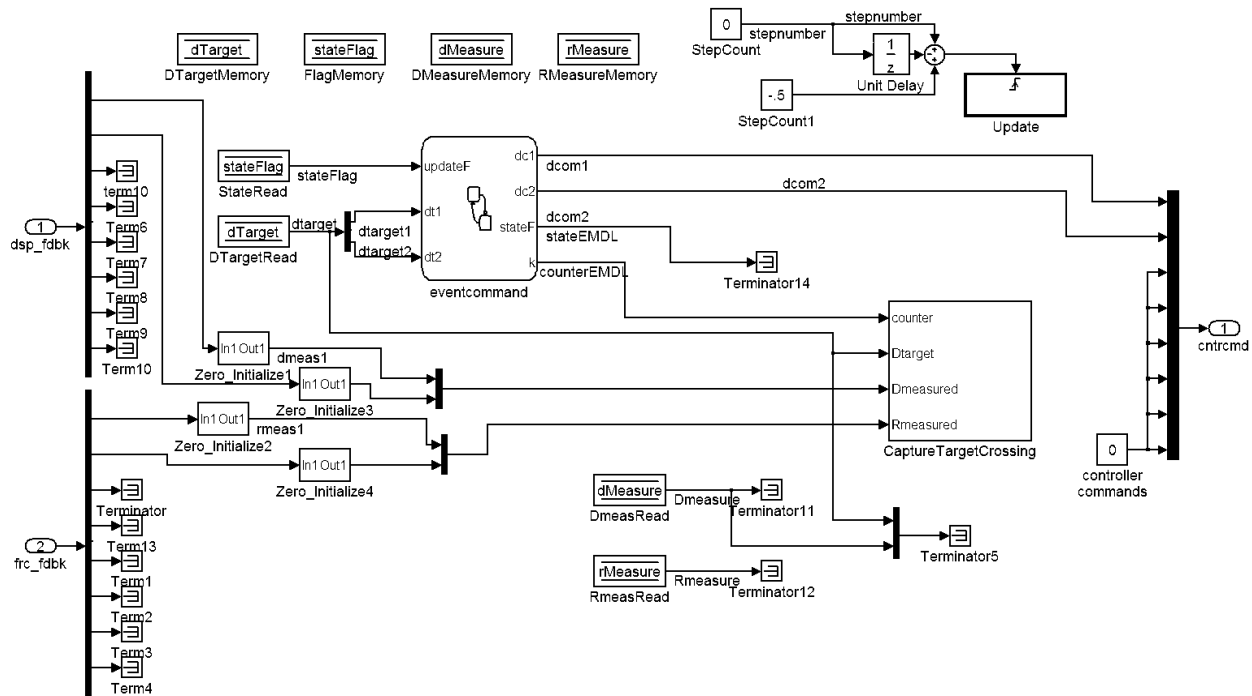


**Fig. 3.9 Expansion of operation block in Simulink model for xPC target.**

### 3.6 PACIFIC INSTRUMENTS DATA-ACQUISITION SYSTEM

The Pacific Instruments data-acquisition system is a receiver and compiler of all the information available from the instruments installed on the test structure. The software that runs the hardware interface on the host computer for the purpose of data acquisition is PI660 (Pacific Instruments 2004). The system has a capacity of 128 channels at a maximum sampling rate of 50 kHz. Sixteen additional channels are provided for STS feedback signals. High-pass filters, at the desired cut-off frequency, are provided for all channels. The acquired information is stored on the Pacific Instruments host PC for extraction after the completion of the test and is available on

ScramNet during the online experiment in real time for possible use within the online calculations.

The calibration process of all the instruments is performed through the interactive interface provided by the Pacific Instruments software (Fig. 3.10). Each horizontal line (row) represents a channel and its information is displayed in the respective columns, such as the type of instrument, the engineering unit used and the status, to indicate the completion of the calibration process, of voltage (V), and engineering unit (EU) calibrations that relate V output signals to measured quantities in EU. The system also provides a number of real-time viewing options including oscilloscopes and tables in engineering units.

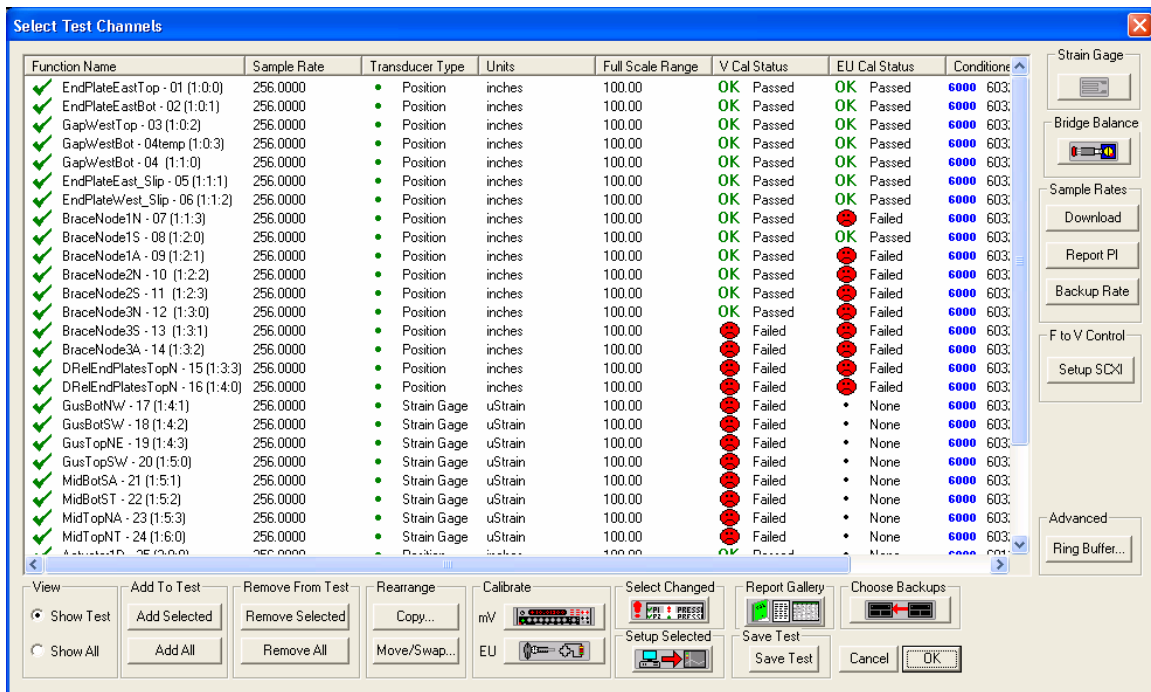


Fig. 3.10 Calibration of sensors in Pacific Instruments data-acquisition system.

### 3.7 MATLAB ENVIRONMENT

MATLAB is used in the test setup for the present study as the main site for the HS calculations. An Ethernet connection links the PC operating MATLAB to the xPC target. Therefore, MATLAB has access to the STS controller feedback information available through xPC target, as well as the Pacific Instruments data-acquisition information through ScramNet (Fig. 3.2). The

HS numerical-integration algorithm is programmed in the MATLAB environment together with numerical substructuring computations and the live displays for monitoring while online experiments are in progress.

It is worthy to note that MATLAB is not the only environment available in the HSS to run and control xPC target applications. A similar connection may be established with a C/C++ environment through the xPC target application program interface where other programs such as OpenSees (Open source for earthquake engineering simulation) (Mazzoni et al. 2006) may be used to replace MATLAB (Fenves et al. 2004; Schellenberg et al. 2007).

### 3.8 OPERATION SEQUENCE IN HSS

The operation sequence during the  $i$ -th numerical-integration time step with time-step duration  $t_d$  is discussed. Based on a prediction/correction scheme, using polynomial extrapolation/interpolation, designed to keep the actuators in continuous motions (Nakashima and Masaoka 1999; Mosqueda 2003), the sequence in Figure 3.11 is as follows:

- $D_{i-1}$  marks the end of execution, by the hydraulic system, of the command signal from the previous time-step number  $i-1$ . At this point, xPC target starts an extrapolation process of the command signals and continues communicating with STS by sending and receiving command and feedback signals, respectively.
- At  $A_i$ , a new integration time step begins where MATLAB receives the feedback from the previous time step through xPC target. This feedback is the latest received by xPC from STS and is used by MATLAB to calculate the next command signal.
- Between  $A_i$  and  $B_i$ , MATLAB performs its calculations and xPC continues extrapolating commands to send to STS keeping the actuators in continuous motions.
- At  $B_i$ , MATLAB is ready with the command signals for step number  $i$ , which are subsequently sent to xPC target.
- At  $C_i$ , xPC receives the target commands and immediately stops extrapolating and starts interpolating toward the current commands. Concurrently, MATLAB performs other tasks, e.g., calculations related to substructuring or data displays.

- At  $D_i$ , the actuators reach the commands of time step  $i$  ending interpolation and starting extrapolation in xPC target for the next time step  $i+1$  and then repeating the above sequence.
- Throughout the online experiment, xPC target is constantly sending command values to STS at time intervals  $\delta t = 1/1024$  sec, whether deduced by extrapolation or by interpolation, and receiving feedbacks. Provided that the time needed to reach  $C_i$  from  $D_{i-1}$  is small compared with  $t_d$ , each time step is performed in the prescribed  $t_d$ . However, in case of a delay in one or more of the steps in the previously discussed operation, the hydraulic system goes into a “slow” mode, i.e., slower than the prescribed  $t_d$  to reach the target command signals, followed by a system “hold” mode if needed for long delays, causing the experiment to run slower than desired (Mosqueda 2003).

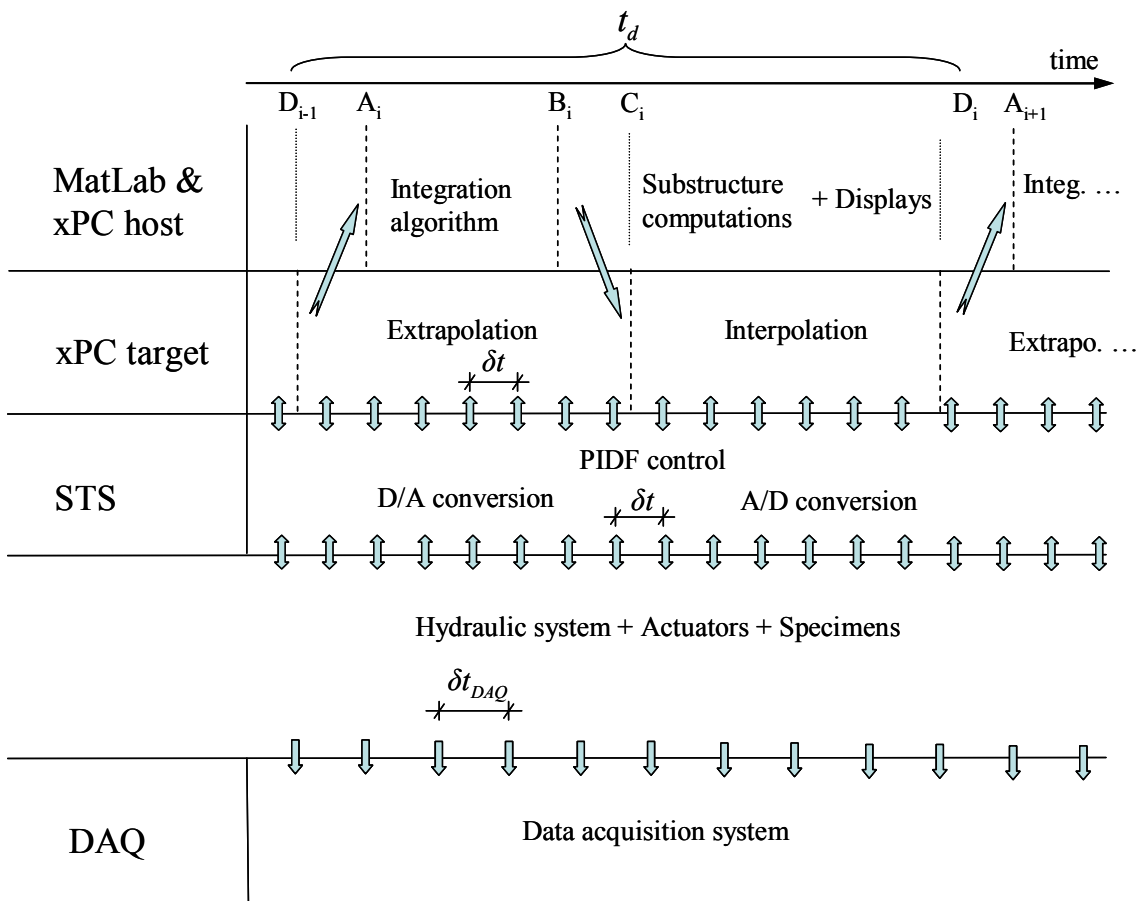


**Fig. 3.11 Operation sequence in HS.**

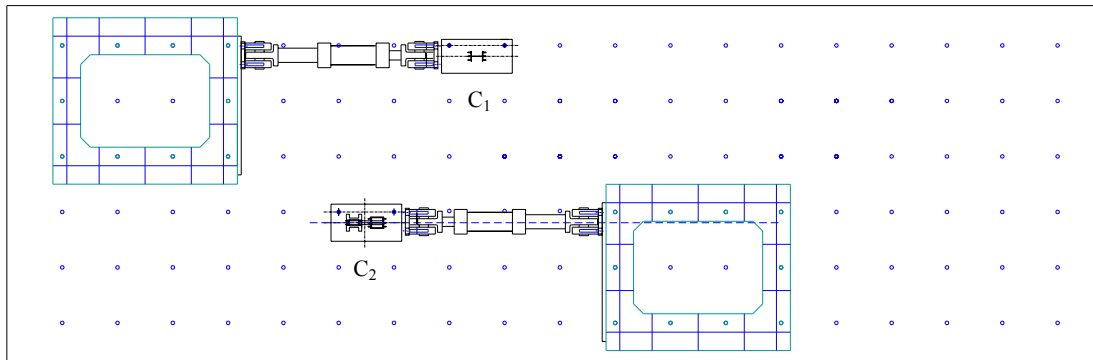
The data-acquisition is operating in parallel to the previously discussed sequence. In this operation, data are extracted from the instruments installed directly on the test structure or in the attached actuators at the selected sampling rate with time interval  $\delta t_{DAQ}$ , not necessarily the same as  $\delta t$ . However, this data-acquisition system information is readily available online for all components of the HSS through ScramNet.

### 3.9 VALIDATION OF HSS

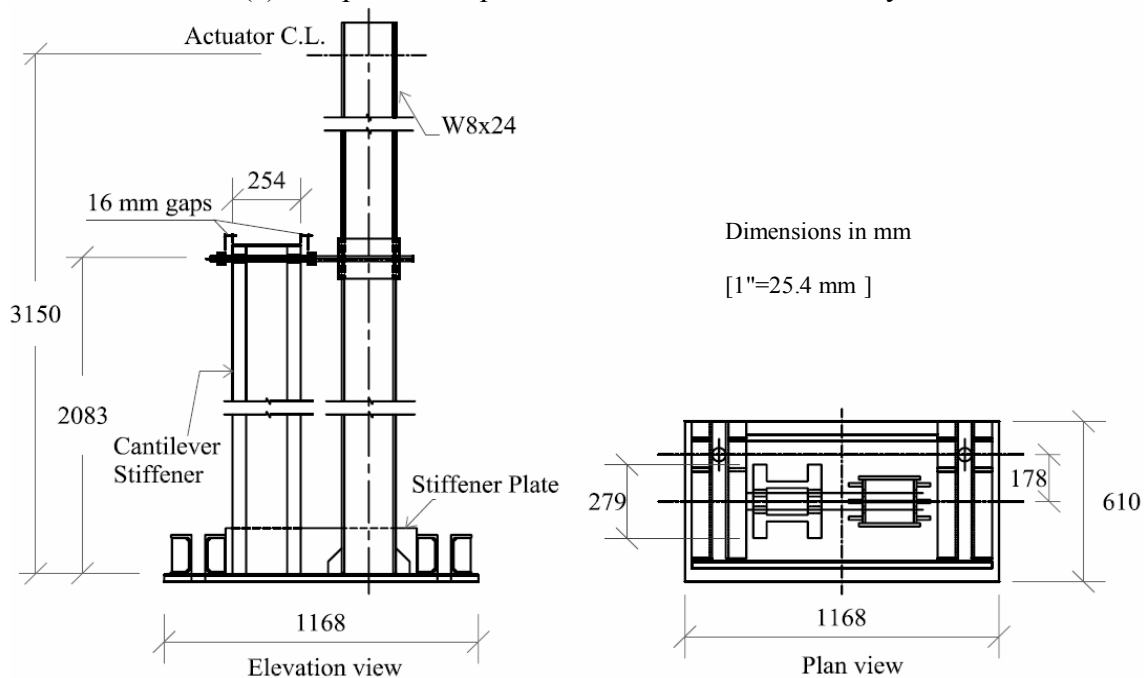
To evaluate the performance of the HSS, an online (pseudo-dynamic) experiment is designed with a numerically reproducible structural behavior of the test structure where test results can be validated against pure numerical simulation. Two steel cantilever columns,  $C_1$  and  $C_2$ , constitute the two physical substructures and are installed on the strong floor and connected to the same actuators used in the experimental program of the present study (Fig. 3.12(a)). Column  $C_1$  is designed to behave linearly and is tested in its elastic range. Column  $C_2$  is the same as  $C_1$  but is stiffened by a shorter cantilever adjacent to it when an adjustable initial gap closes in the push or pull loading directions. The design details are shown in Figure 3.12(b). Accordingly, the validation test structure is a coupled two-DOF system (Fig. 3.13) with linear and stiffening bilinear behaviors for  $C_1$  and  $C_2$ , respectively (Fig. 3.14), with a fundamental natural period of 0.31 sec. The structural parameters used for the online HS of the two columns are summarized in Table 3.2. A numerically simulated linear spring with high stiffness ( $k_l$ ) connects the two DOF of  $C_1$  and  $C_2$  in parallel, thus forcing them to be fully coupled, i.e., subjecting them to similar displacement time history.

Although the linear spring is of high stiffness ( $k_l$ ), the difference in the displacement between the two DOF is not to be entirely neglected and was a subject of study in itself. That is, the HS validation system is intended to mimic the system of test structure A in phase S-1 (see Fig. 1.2), where the RC bare frame is expected to be relatively flexible when compared to the URM infilled one, Chapter 4. An RC slab connects the RC frames and is analogous to the linear high-stiffness numerical spring ( $k_l$ ) used in the validation experiment. Moreover, the same numerical-integration algorithm implemented for the simulation of test structure A is used in the present validation experiment. The experiment therefore, not only serves to validate the HSS, but

also serves as a trial run on a system similar to that in phase S-1 for test structure A (see Fig. 1.2), and inspects the potential problems that may arise during the HS experiment of test structure A, whether in the numerical-integration algorithm or in the simulation of a two-DOF system exhibiting stiff and flexible behaviors.



(a) Setup of steel specimens in structural laboratory



(b) Cantilever  $C_2$  with bilinear behavior ( $C_1$  is similar but without cantilever stiffener)

**Fig. 3.12 Steel specimens design and setup in structural laboratory.**

**Table 3.2 Evaluated parameters for validation of HSS.**

Parameter	Value
Linear stiffness, $k_{C_1}$ [kip/in. (kN/mm)]	0.613 (3.50)
Initial stiffness, $k_{C_2}^I$ [kip/in. (kN/mm)]	0.536 (3.06)
Secondary stiffness, $k_{C_2}^S$ [kip/in. (kN/mm)]	2.011 (11.48)
Connecting stiffness, $k_l$ [kip/in. (kN/mm)]	1650 (289.0)
Stiffness ratio, $k_{C_2}^S/k_{C_2}^I$	3.75
Mass for $C_1$ ( $m_{C_1}$ ) [kip-sec <sup>2</sup> /in. (kN-sec <sup>2</sup> /mm)]	0.0017 (0.0096)
Mass for $C_2$ ( $m_{C_2}$ ) [kip-sec <sup>2</sup> /in. (kN-sec <sup>2</sup> /mm)]	0.0011 (0.0061)
Damping ratio (%)	5
Numerical-integration time step (sec)	0.01

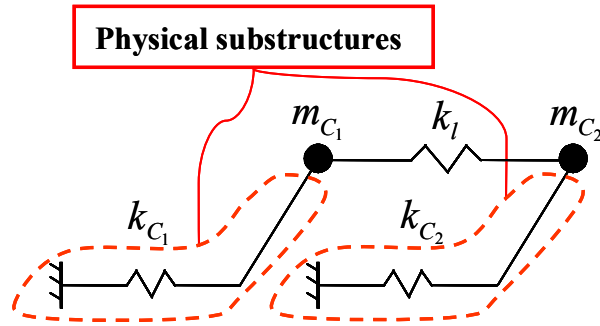


**Fig. 3.13 Idealized model for HS validation structure.**

The two DOF validation test structure is excited by the strong motion, Northridge, Tarzana station, 1994 earthquake scaled to 17% of the original record described in Table 4.1. Using the evaluated stiffness of the columns from the test results (Fig. 3.14), pure numerical simulation validates the experimental results with good accuracy, as illustrated in Figure 3.15, where representative numerical samples are shown along the displacement time history with a maximum error of 6.8%, relative to the peak recorded displacement.

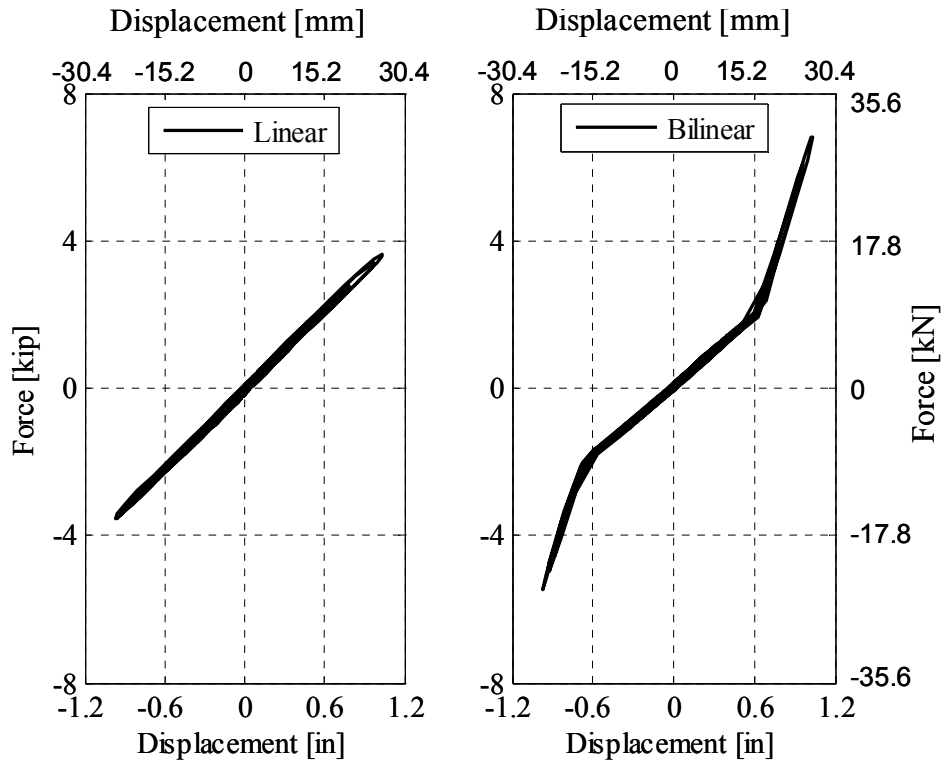


Fig. 3.14 Structural response of physical substructures  $C_1$  (left) and  $C_2$  (right).

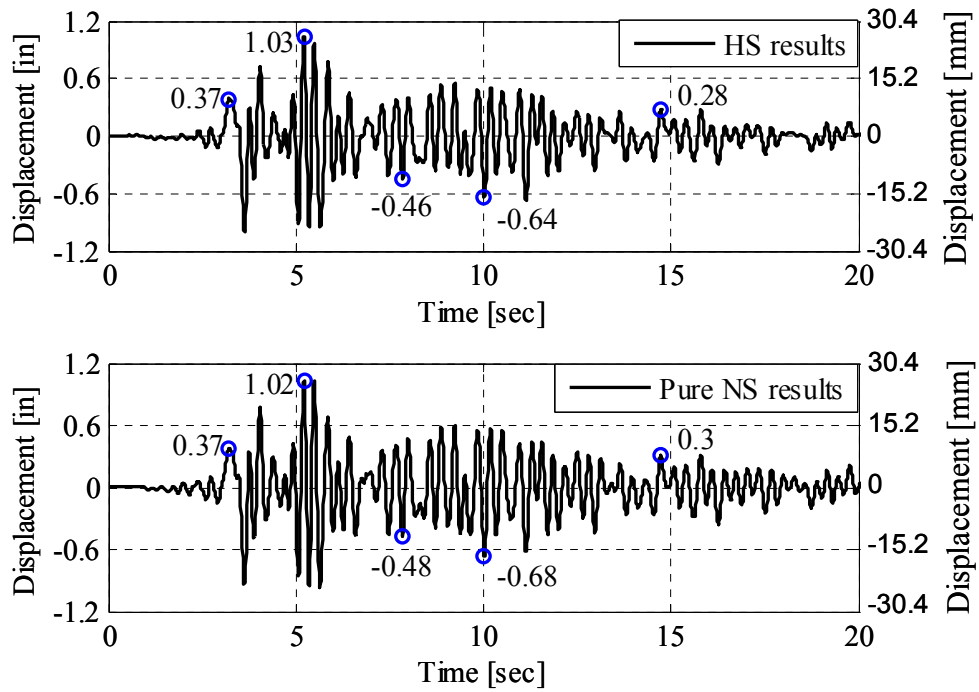


Fig. 3.15 Validation of HSS.

### 3.10 SUMMARY

The hybrid simulation system developed as part of *nees@berkeley* at the University of California, Berkeley, is presented. The components of the hybrid simulation system used in the present study are identified and described each in terms of its function and interconnection with the other components. The operation sequence of the hybrid simulation system during one numerical-integration time step of a generic online experiment is presented. Finally, a steel cantilever test structure is physically tested in a hybrid simulation setting and the results are validated against a pure numerical simulation. From this validation exercise, functionality of the newly installed hybrid simulation system is judged to be accurate and reliable.

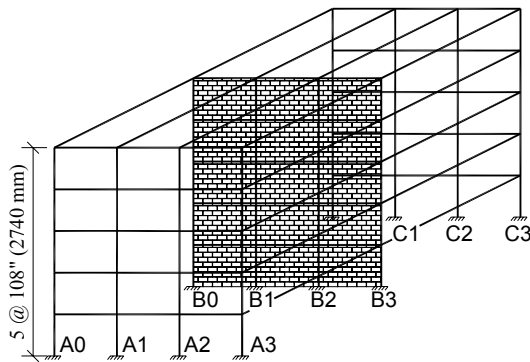
## 4 Test Structure A

The first test structure presented in this chapter consists of two large substructures of an ST experiment conducted at UCB. The ST test structure is briefly presented along with the selection of the strong motions applied during different phases of the experiment. This chapter describes the physical substructures including design, construction, and instrumentation. In addition, the test setup is discussed in terms of its design and assembly as a means of demonstrating the functionality of *nees@berkeley*. Moreover, the development of the computational part of the HS for this test structure is discussed. This includes the idealization of the test structure, the formulation of the governing equations of motion, and the estimation of some key parameters in these equations.

### 4.1 ST TEST STRUCTURE

A hypothetical five-story prototype structure with RC frames and URM infill walls is considered. The URM infill walls are assumed in the interior frames (Fig. 4.1(a)). The ST experiment is carried out on a reduced-scale one-story RC moment-resisting frame structure with URM infill wall on the seismic simulator test facility of UCB. The three-fourths-scale test structure represents the first-story middle bays of the prototype structure. The structure is designed based on the requirements of ACI318-02 (2002) and NEHRP recommendations (BSSC 2000) in seismic regions (Fig. 4.1(b)). As in the prototype structure, the URM infill wall of the ST test structure is constructed in the interior frame only. Moreover, a computationally determined additional mass is placed on the RC slab of the ST test structure with the objective of matching the base shear of this test structure with that of the prototype building when subjected to the design-level ground motion (Hashemi and Mosalam 2006, 2007). This additional mass and the mass of the ST test structure itself represent the total mass considered numerically in the HS experiments corresponding to the ST experiments. To simulate the effect of the upper stories of

the prototype building on the RC columns of the tested first-story structure, post-tensioning through concentric rods in all columns is included in the structures tested on the ST and using HS. Three test phases are performed as outlined in Figure 1.2. These three phases are reproduced on an identical test structure in the HS experiments. Therefore, the ST experiment serves as a benchmark for the HS experimental approach.



(a) Hypothetical five-story prototype structure



(b) One-story ST test structure

**Fig. 4.1 Five-story prototype and one-story ST structures (Hashemi and Mosalam 2007).**

## 4.2 STRONG MOTION SELECTION

In the test phases of structure evaluation, denoted by “S” in Figure 1.2, to compare with the parallel ST tests, the same strong motions as those used in the ST tests are adopted in the HS. Table 4.1 describes the strong motions selected for test structure A where PGA, PGV, and PGD refer to peak ground acceleration, velocity, and displacement, respectively. These ground motions are intended to be unidirectional in the direction parallel to the URM infill wall of the test structure (longitudinal direction).

**Table 4.1 Ground motion specifications (1 in. = 25.4 mm).**

Ground Motion	Station	Direction	PGA (g)	PGV (in./sec)	PGD (in.)
Northridge, CA, 1994 (TAR)	Tarzana	090	1.570	36.23	5.13
Düzce, Turkey, 1999 (DUZ)	Lamont	N	0.762	12.97	0.75
Loma Prieta, CA, 1989 (LPB)	Bran	000	0.426	17.43	2.28

Figure 4.1 shows the 5% damping acceleration response spectra for the three strong motions together with the NEHRP design spectrum. Each ground motion is scaled to generate different levels of intensity as listed in Table 4.2. The scaling is based on the average spectral acceleration of the selected ground motions over the range that the period of the test structure is expected to vary during the experiments, and the NEHRP design spectrum for a site with mapped spectral response acceleration at 1 sec,  $S_1 = 0.65g$ , and at short periods,  $S_s = 1.60g$ , and site class D with 5% damping. Level 1 is selected as a very small amplitude motion to check the performance of the data-acquisition system. Levels 2 and 3 are selected as low-intensity level motions while level 4 corresponds to the design level spectrum and level 6 corresponds to the maximum considered earthquake spectrum. Levels 7 and up are selected to achieve higher demands on the test structure considering the limits of the ST. The ground motion records are also compressed in time by a factor of  $\sqrt{3/4}$  to account for the 3/4 length scale of the test structure. In this way the frequency content of the record at the natural period of the undamaged test structure is the same as the prototype first-story substructure, i.e., without scaling.

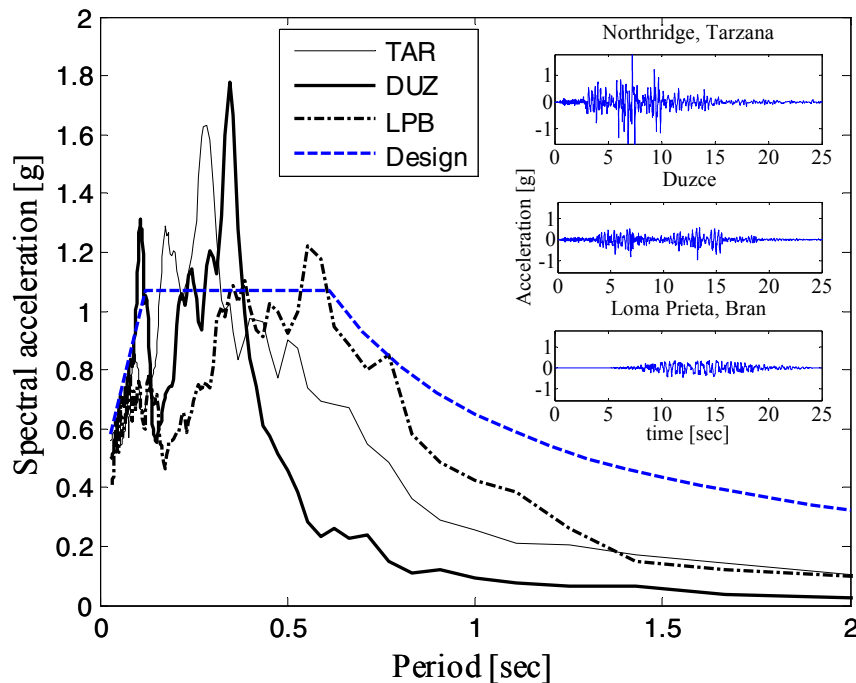


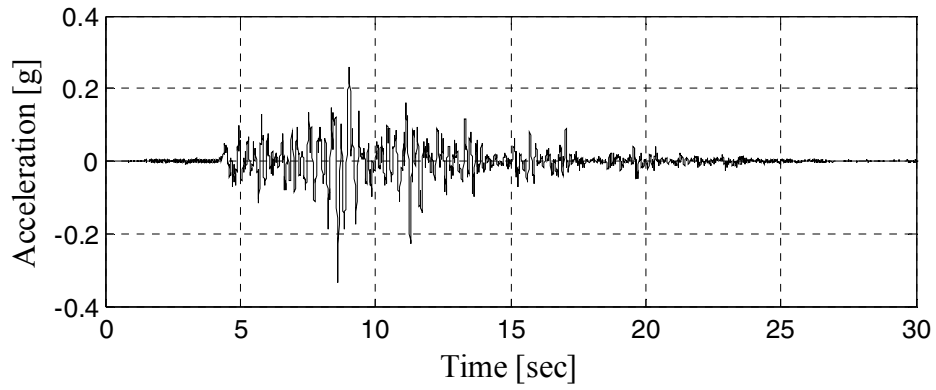
**Fig. 4.2 Response spectra with 5% damping for selected ground motions (Hashemi and Mosalam 2007).**

**Table 4.2 Scale factors for different levels of input ground motions.**

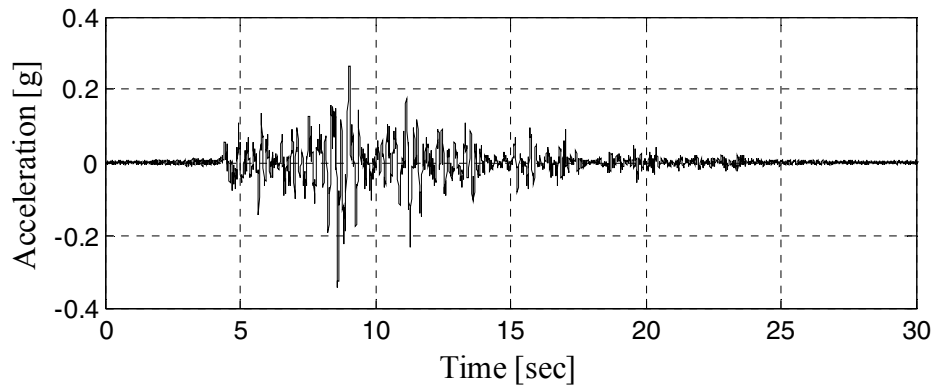
Level	1	2	3	4	6	7	8	9	10
Northridge, CA, 1994 (TAR)	0.05	0.17	0.23	0.39	0.59	-	-	-	-
Düzce, Turkey, 1999 (DUZ)	-	-	-	-	-	1.50	2.00	2.53	-
Loma Prieta, CA, 1989 (LPB)	-	0.31	0.44	0.67	1.00	1.50	1.95	2.19	3.29

Since the ST is not capable of exactly reproducing the input strong motions, the accelerations are measured on the table during each ST run and this measured (output) response of the table is applied in the HS rather than the original scaled input motion to the table. Moreover, the recorded acceleration time histories included high-frequency content (>25 Hz), introduced mainly by the electrical noise in the connecting cables when recording the output signals. Since these frequencies are too high to have any structural significance during the dynamic experiment on the test structure, a low-pass filter is applied to eliminate these high frequencies, while preserving the recorded lower frequencies (Fig. 4.3).

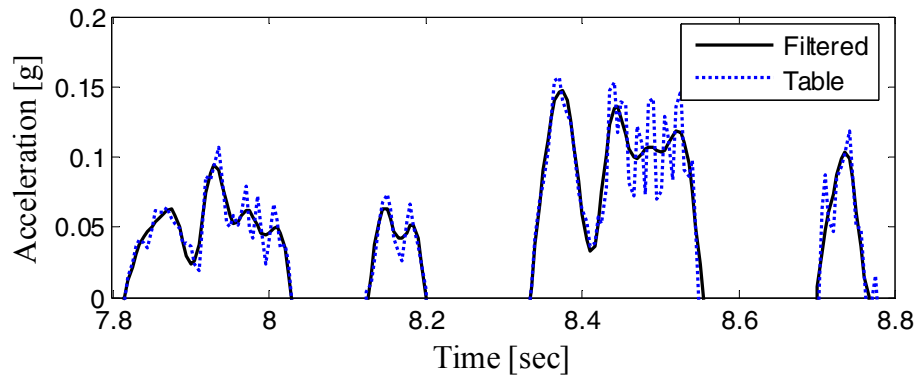
The diagram in Figure 4.4 illustrates the chronological order of the strong motions applied in each of the three structural evaluation phases of test structure A. Note that each event is labeled by the name of the strong motion, e.g., TAR in Table 4.1, followed by the intensity level, e.g., 2 in Table 4.2. The last two digits if present designate the repetition number of that level and the phase number between brackets, respectively. These two numbers are omitted if their value is one, e.g., TAR-4-2[2] designates the second repetition of TAR strong motion at intensity level 4 in phase 2 of the experiments, while TAR-2 designates the first run of TAR at intensity level 2 in phase 1 of the experiments.



(a) ST output time history



(b) Filtered signal time history



(c) Zoomed in part of time histories

**Fig. 4.3 Filtering of acceleration time history of ST output signal for TAR level 2.**

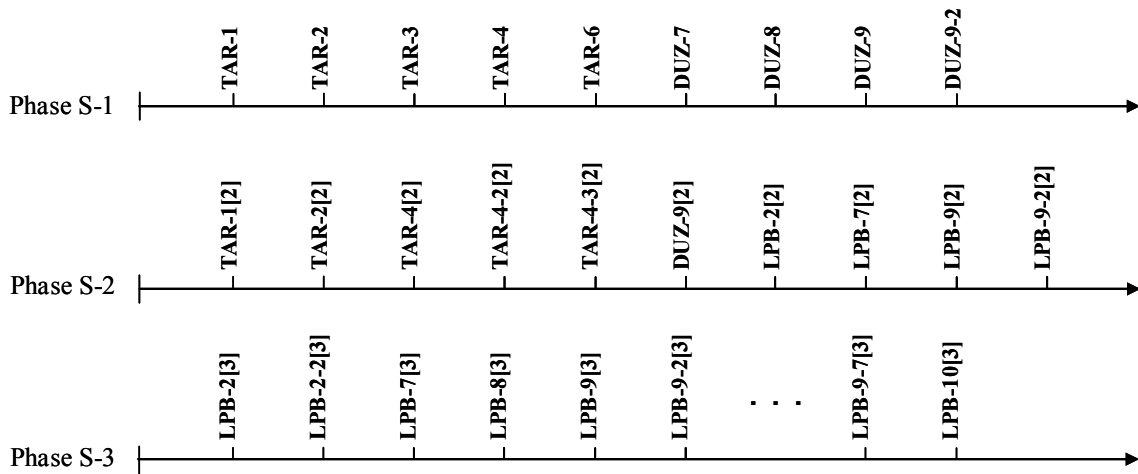


**Fig. 4.4 Chronological order of events for test structure A.**

### 4.3 PHYSICAL SUBSTRUCTURES IN HS

Each test structure in the outlined phases of the HS experimental program (Fig. 1.2) consists of physically tested substructure(s) using the hydraulic system and a numerically simulated substructure. The physical substructures used in all experiments are two  $\frac{3}{4}$ -scale RC frames with fixed footings to the strong floor of the structural laboratory. The first frame is infilled using URM wall, this is denoted F1I (frame no. 1 infilled). The second frame is not infilled and is denoted F2B (frame no. 2 bare). After the collapse of the URM infill wall, F1I is used for further testing after the complete removal of the collapsed URM infill wall and in this form is denoted F1B (frame no. 1 bare). Note that the URM infill wall protected the members of the bounding RC frame as discussed in subsequent chapters. This allowed the reuse of the RC frame of F1I as F1B after removal of the URM infill wall. All columns of the test frames are post-tensioned using concentric high-strength steel rods to account for the effect of the upper stories of a prototype building (Hashemi and Mosalam 2006). In later phases of testing, some of the experiments are conducted without the post-tensioning. The RC frames are then denoted F1BU and F2BU (frames no. 1 and 2 bare without post-tensioning). Table 4.3 summarizes the different states of the tested frames.

**Table 4.3 Physical substructures in HS.**

Frame Notation	Description
F1I	RC frame No. 1, infilled using URM wall
F1B	RC frame No. 1, after collapse and removal of the URM infill wall
F2B	RC frame No. 2, no infill is present, i.e., bare
F1BU	RC frame No. 1, same as F1B after removal of the column post-tensioning
F2BU	RC frame No. 2, the column post-tensioning of F2B is removed

The test structures used in the experiments are categorized as follows, based on the intended purpose of the experiments for the different phases as shown in Figure 1.2:

- Test structure in **S-1**: Three one-bay RC frames are connected with a RC slab at the level of the top beams (Fig. 4.5(a)). The URM infill wall is constructed inside the middle frame without any additional connection to the surrounding frame other than cement mortar. Frames F1I and F2B represent the physical substructures; the response of the remaining outer frame (identical to F2B because of symmetry) and the connecting RC slab are numerically modeled. The modeling details are discussed in subsequent sections.
- Test structure in **S-2**: This phase follows heavy damage of the URM infill wall and its removal. The test structure is the same as the one in S-1, with the exception that the URM infill wall is absent. Only frame F2B is used as the physical substructure, while the remaining two bare frames (identical to F2B from the stiffness point of view) and the connecting RC slab are numerically modeled. Note that the mass is not distributed evenly over the three RC frames as discussed in Section 4.10.1 and shown in Figure 4.23.
- Test structure in **S-3**: The test structure is the same as the one in S-2, with the exception that the column post-tensioning is removed. Frame F1BU or F2BU is used as the physical substructure interchangeably (one of these two frames is used at a time to study the effect of different parameters in the developed HS), while the remaining two bare frames and the connecting RC slab are numerically modeled.
- Test structure in **P-1** and **P-2**: The test structure is the same as the one in S-2, except that F1B is used instead of F2B.

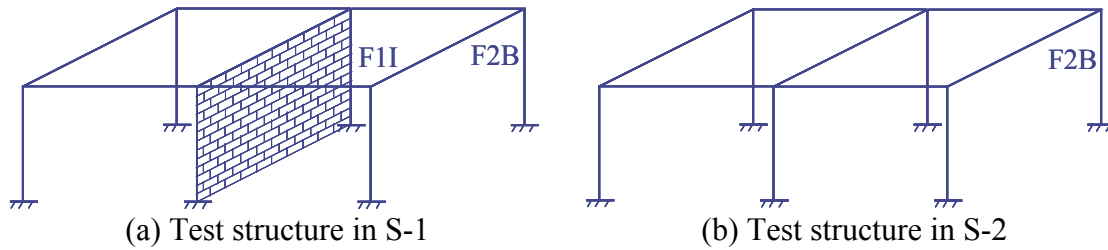


**Fig. 4.5 Test structures in HS.**

#### 4.4 RC FRAME DESIGN

To compare the HS results to its parallel counterpart on the ST, the design of the RC frames tested on the ST (Hashemi and Mosalam 2006, 2007) is adopted in this study (see Fig. 4.6). The center-to-center span of each frame is 13'-6" (4.11 m) with a total height of 10'-9" (3.28 m). Column sections are 12"×12" (305 mm×305 mm) with 8 #6 (19 mm diameter) longitudinal reinforcing bars and an unbonded 1¼" diameter (32 mm) post-tensioning central rod to represent column axial loads from the not modeled upper stories of the prototype building. The transverse reinforcing bars of the columns consist of #3@3¾" (10 mm diameter@95 mm) over 24" (610 mm) from the face of the column-to-footing and beam-to-column joints and #3@6" (10 mm diameter@152 mm) elsewhere. Long-direction single-span beam sections are 10½"×13½" (267 mm×343 mm) with 3#6 (19 mm diameter) top and bottom longitudinal reinforcing bars. Beam transverse reinforcing bars are #3@2¾" (10 mm diameter@70 mm) over 28" (711 mm) from the face of the beam-to-column joint and #3@8" (10 mm diameter@203 mm) elsewhere. Design details are illustrated in Figure 4.7, and more information on the prototype structure is documented in Hashemi and Mosalam (2006). While the ST test structure consists of RC frames connected using a 3¾" (95 mm) thick RC slab with #3 (10 mm diameter) reinforcing bars top and bottom at 12" (305 mm) on center each way, the HS test structure consists of two separately constructed frames and the RC slab is numerically simulated, as discussed in the following chapters. However, in addition to the role of the RC slab in connecting the frames, it contributes to the beam structural strength and stiffness with an effective slab width. This effective width is estimated to be 20.25" (514 mm) from the center of the beam to each side according to ACI318-02 Section 8.10.2 (total effective width ≈ 40.5" (1029 mm)). However, in the ST experiment (Hashemi and Mosalam 2007), this width was estimated to be on the order of 10" (254 mm) on

each side of the beam center line (total effective width  $\approx 20''$  (508 mm)). A total effective RC slab width of 28.5'' (724 mm) is adopted in the HS test structure, which falls between the American Concrete Institute (ACI) and the experimental estimates, and the slab is constructed integrally with the RC beam. The URM infill wall is made of clay bricks with modular size of 4'' $\times$ 8'' $\times$ 2 $\frac{2}{3}$ '' (102 mm $\times$ 203 mm $\times$ 68 mm) and ASTM C270 (2003) Type N mortar. The infill wall is constructed over a RC grade beam as shown in Figure 4.6. Design details including beam, column, and foundation cross sections, and concentric post-tensioning rods of the column, are shown in Figure 4.7.

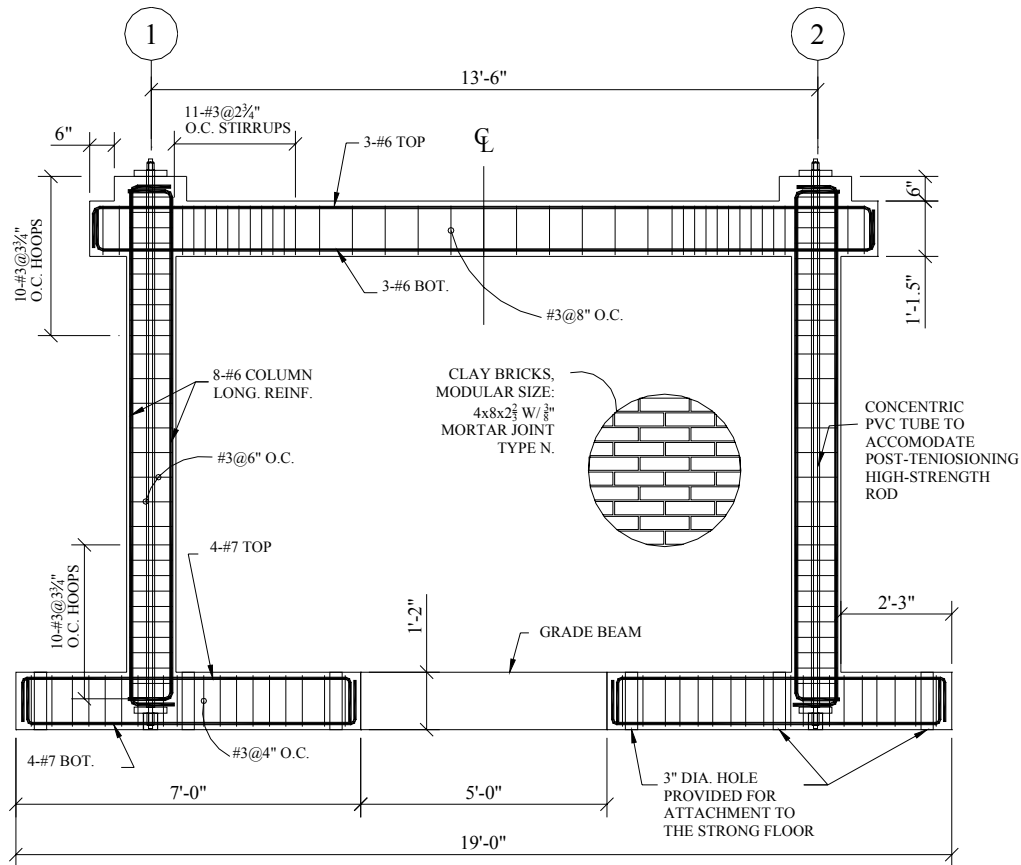


**Fig. 4.6 Infilled frame reinforcement (bare frame is similar without URM infill wall and grade beam) (1'=304.8 mm, 1''=25.4 mm).**

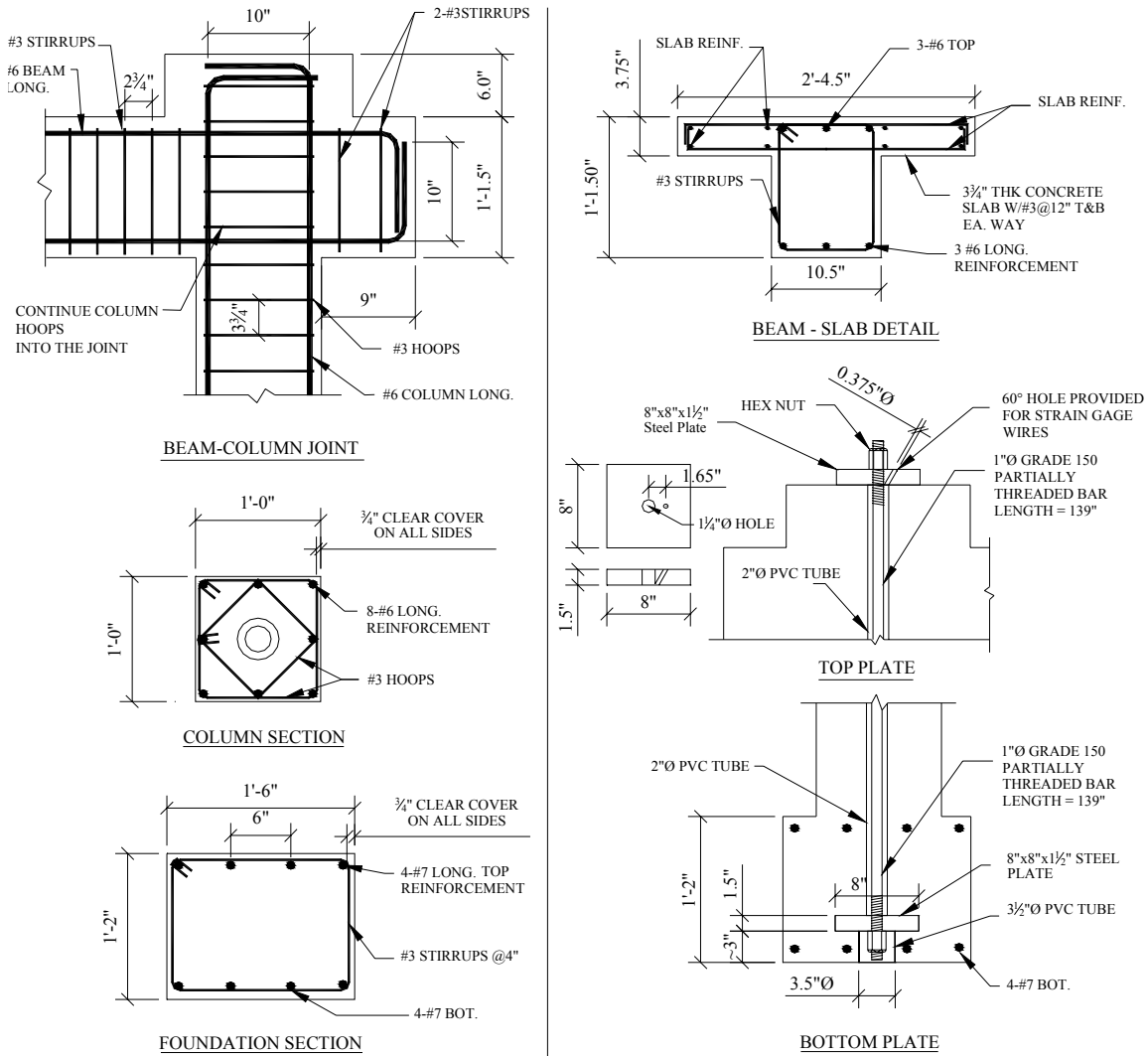
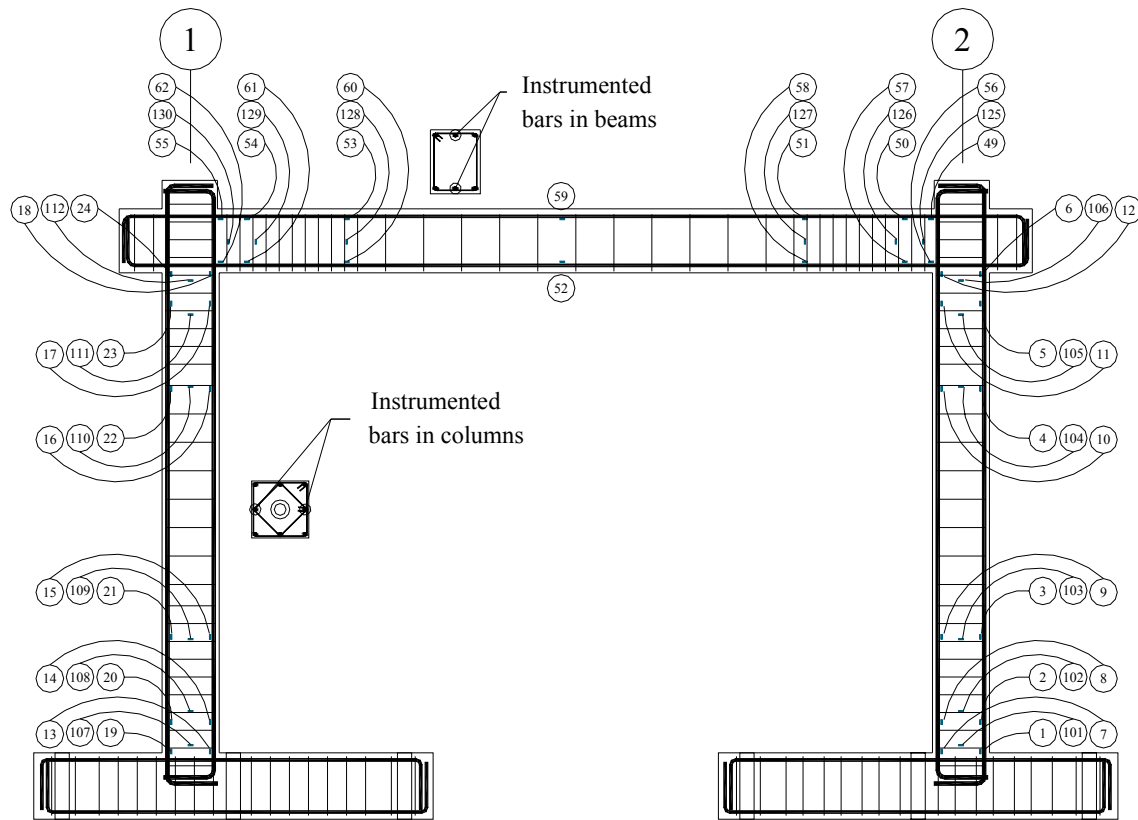


Fig. 4.7 Design details of RC frames (1'=304.8 mm, 1''=25.4 mm).

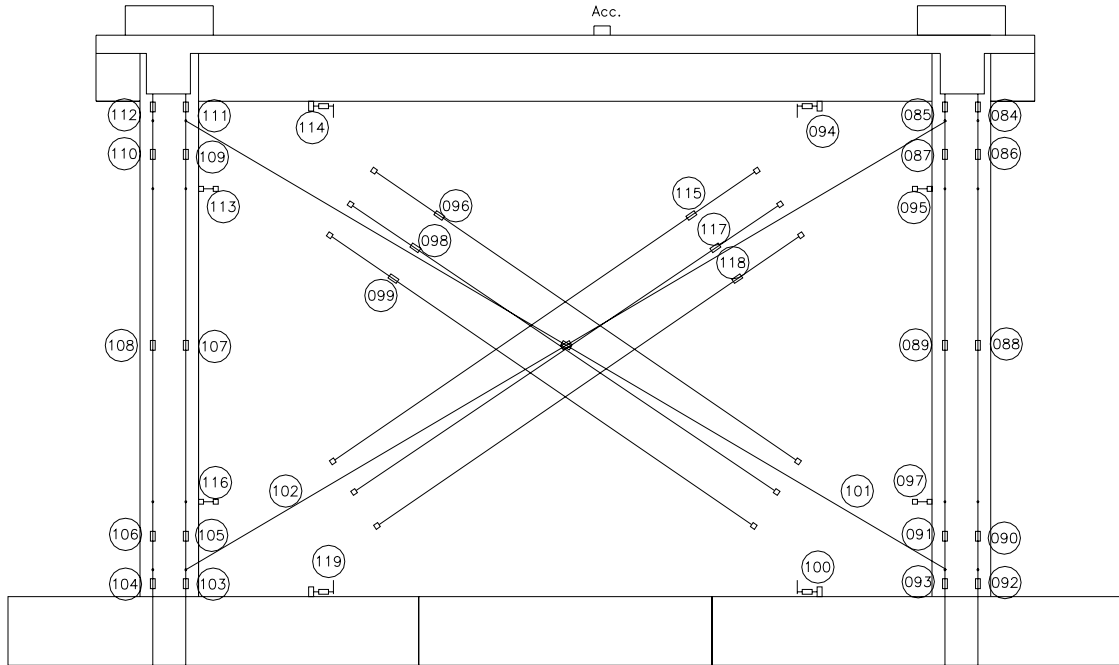
#### 4.5 INSTRUMENTATION

The two RC frames of the test structures are identically instrumented. Strain gages are installed on the reinforcing steel bars in the beams and columns. Starting from the beam-to-column and the column-to-footing joints, the strain gages are positioned at six cross sections in the beam and six cross sections in the columns at increasing distances from these joints (Fig. 4.8). Each cross section contains three strain gages, two on the middle bars of the longitudinal steel, and the third on a transverse reinforcing bar. A total of 54 strain gages are employed per frame (Fig. 4.8).



**Fig. 4.8 Strain gages numbering on reinforcing steel bars in RC frames.**

External instrumentation consists of displacement transducers in the columns along the height of each column (Fig. 4.9). Additional 14 transducers are used for the URM infill wall to measure diagonal deformations as well as relative movement (opening and sliding) between the infill wall and the bounding frame. In addition, one accelerometer is installed on top of each frame to measure in-plane accelerations in the case of fast rate loading. As an example, the ground motion LPB-9 (Tables 4.1–4.2) is conducted 20 times slower than real time. The ratio of the measured acceleration, on the physical substructure F1B, is theoretically  $10^2 = 100$  times less than the numerically simulated one as is confirmed by the plotted acceleration time histories in Figure 4.10.

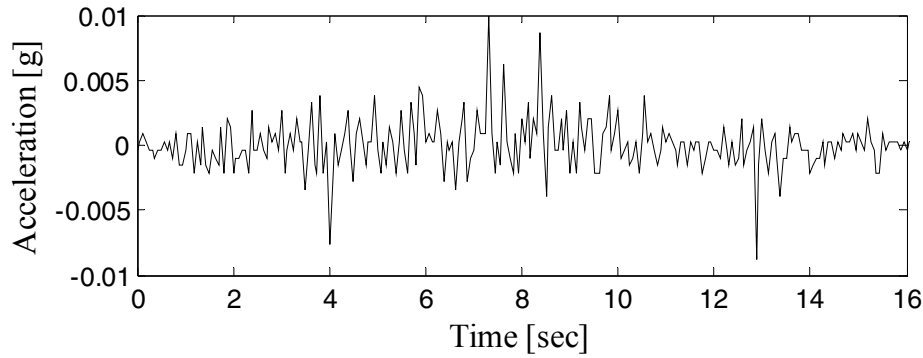


(a) Layout and numbering of displacement transducers

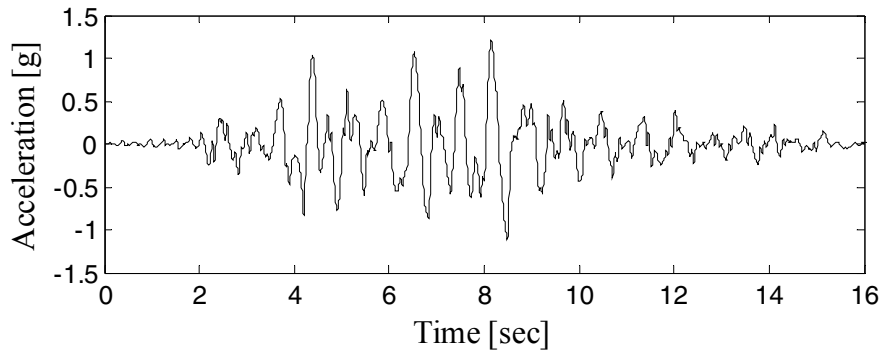


(b) Photograph of instrumented URM infilled frame

**Fig. 4.9 Numbered displacement transducers on URM infilled RC frame.**



(a) Measured acceleration on physical substructure F1B



(b) Numerically simulated acceleration

**Fig. 4.10 Accelerations at faster rate execution, LPB-9 at 20 times slower than real time.**

Two wire potentiometers per frame, labeled 1 to 4 in Figure 4.16(a), measure the out-of-plane displacements at the centerline of each column. The maximum out-of-plane drift, defined with respect to the frame height, i.e., 110 in. (2794 mm), in the case where the structure in phase S-1 (see Fig. 1.2) is subjected to the strong motion TAR-6 (Tables 4.1–4.2) and is evaluated to be 0.3% for F2B (Fig. 4.11). These recorded out-of-plane drifts are considered not large enough to require any out-of-plane restraint for the test structure such that the pure in-plane loading nature of the test is practically preserved.

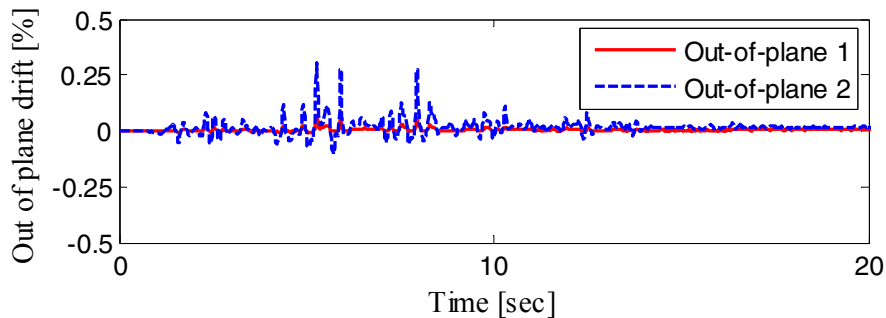


**Fig. 4.11 Out-of-plane drift measurements in TAR-6 frame F2B, phase S-1.**

## 4.6 CONSTRUCTION AND MATERIAL PROPERTIES

The RC frames are constructed using professional contractors. The strain gages are installed on the reinforcing steel bars and covered with adequate protection layers to ensure their continuous functionality after the concrete is cast (Fig. 4.12(a)). The concrete is placed on three lifts (foundations, columns, and beams) to simulate the typical construction joints in real conditions (Fig. 4.12). Concrete cylinders are cast from the same concrete mix and tested at progressing ages. Table 4.4 and Figure 4.13 show the values of the estimated compressive strength from the average of three 6"×12" standard cylinders (ASTM C837-99) at different ages and locations. After the RC frames are placed in their setup positions on the strong floor, the URM infill wall is constructed in place by professional masons. Masonry prisms (4"×8"×12") are constructed for the purpose of determining the uniaxial compressive strength of masonry. The average compressive strength of three prisms tested at 28 days is 2087 psi (14.4 N/mm<sup>2</sup>), with failure characterized by double face shell crushing mode (ASTM C1314-02a).

## 4.7 EXPERIMENTAL SETUP DESIGN

The RRW of the structural laboratory as part of *nees@berkeley* offers flexibility in the layout of the test setup. This section describes the steps in the design of the experimental setup for the purpose of the present study.

### 4.7.1 Reaction Wall Design and Actuator Selection

For each experimental substructure, one reaction wall and one actuator are utilized. Table 4.5 summarizes the main properties of the two substructures, based on which the proper actuators are selected and the reaction wall heights and locations on the strong floor are determined. The expected maximum applied loads in Table 4.5 are based on the performance of the ST test structure (Hashemi and Mosalam 2007). The displacement limits are related to the expected largest lateral drift. Note that the ±8 in. (±203 mm) limit corresponds to ±7.3% lateral drift of the one-story RC frames of test structure A.



(a) Strain gage on reinforcing steel bar



(b) Overview of forms and column cages



(c) Placement of concrete in foundation



(d) Top view of concentric post-tensioning rod



(e) Steel reinforcement in beam and slab



(f) Construction of URM infill wall

**Fig. 4.12 Construction of RC frames.**

**Table 4.4 Concrete compressive strength of tested cylinders.**

Structural element	Average compressive strength @ 7 days [psi (N/mm <sup>2</sup> )]	Average compressive strength @ 28 days [psi (N/mm <sup>2</sup> )]
Foundation	2988 (20.6)	4548 (31.4)
Columns	3174 (21.9)	4562 (31.5)
Beams and Slab	2940 (20.3)	4547 (31.4)

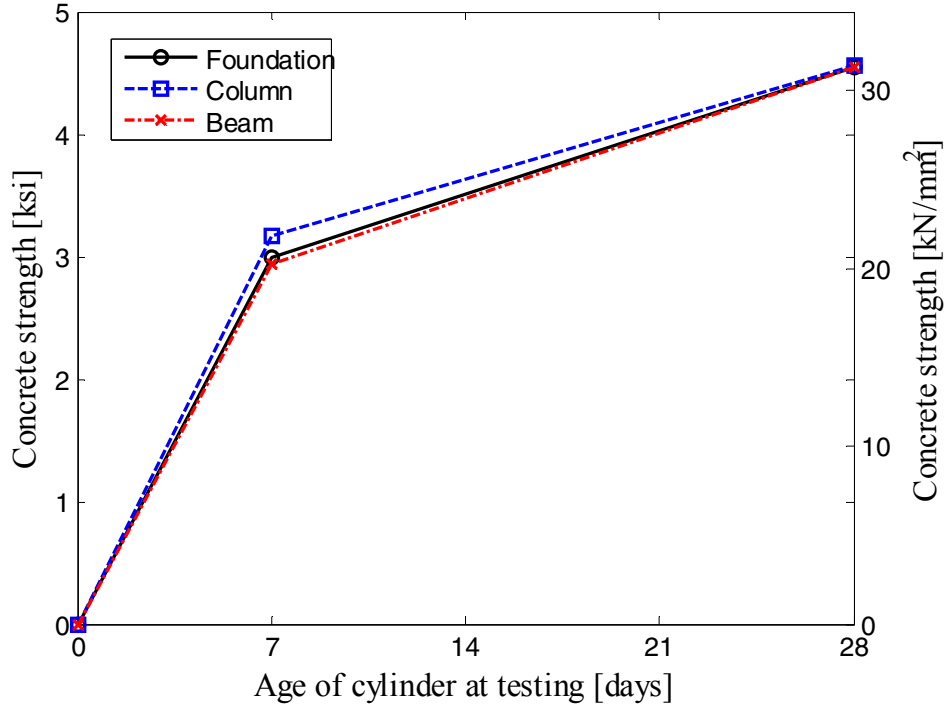


**Fig. 4.13 Strength gain with time for concrete compressive strength of tested cylinders.**

**Table 4.5 Expected load and displacement requirements of substructures in test structure A.**

Substructure	Infilled frame F1I	Bare frame F2B
Height at load application point [in. (mm)]	124 (3150)	124 (3150)
Expected maximum load [kips (kN)]	±150 (±667)	±60 (±267)
Expected maximum displacement [in. (mm)]	±8 (±203.2)	±8 (±203)

Two 220 kip (979 kN) dynamic actuators (see Table 3.1) are chosen to implement the planned test runs. The actuators satisfy the load requirement with a maximum dynamic stroke of ±10 in. (±254 mm) satisfying the displacement requirement as well. The required number of wall

units is determined as the height at the load application divided by the height of one unit,  $n = 124/30 = 4.1$  units. Therefore, five units are needed to construct each reaction wall. It is decided to use seven units for each wall to provide sufficient height for a diagonal chain to carry the self-weight of the actuator (Fig. 4.14).

The structural properties of the selected configuration of each RRW are evaluated using the design spreadsheet, Appendix A. As illustrated by the results of the spreadsheet in Figure 4.15, each reaction wall is checked for tension, shear, lateral displacement, and sliding limits. The tension limit, which is selected such that no tension is allowed in the wall cross section, governs at the actuator height of 124" (3150 mm) with an allowable load of 220 kips (979 kN). This load is equivalent to the capacity of the actuator, thus the RRW design is adequate. Moreover, an evaluation of the RRW natural vibration properties estimates the main frequency to be 62.5 Hz, Appendix A. This frequency is judged to be large enough not to cause any coupling effects of the reaction wall dynamics with the dynamic response of the test structure.



**Fig. 4.14 A 220-kip (979 kN) actuator mounted on RRW.**

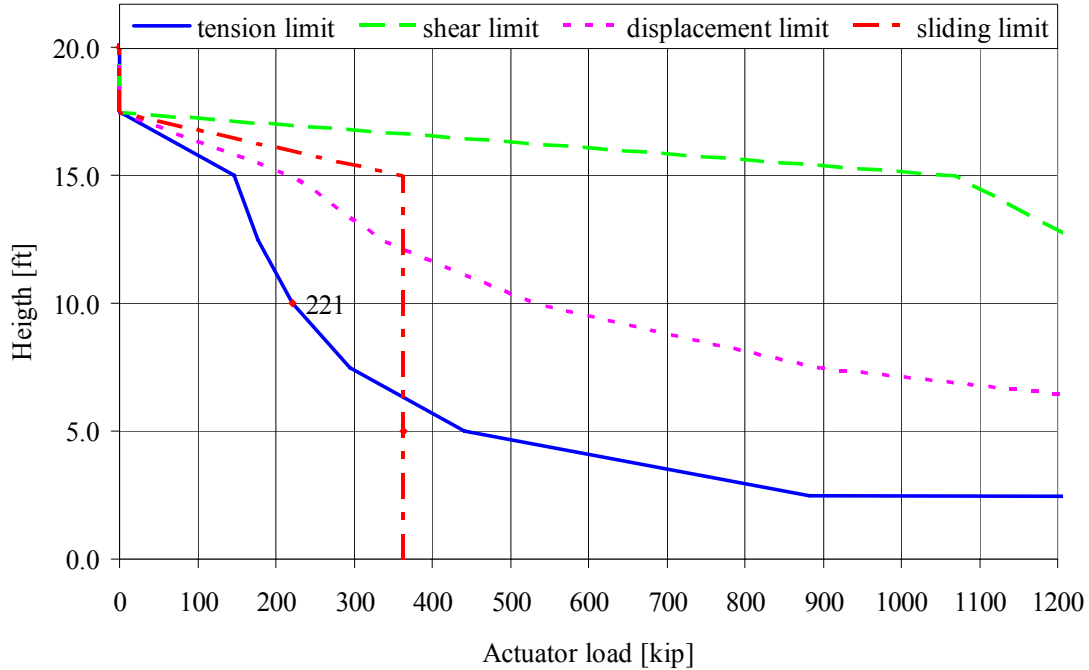


**Fig. 4.15 Design spreadsheet output for used RRW (1 ft = 304.8 mm, 1 kip = 4.448 kN).**

#### 4.7.2 Setup on Strong Floor

Figure 4.16 shows the experimental setup including the RRW and the test substructures on the strong floor. The positions of the RRW and the attached actuators and test substructures are selected according to the limitations of the space and geometry of the floor, as well as to provide different opportunities for future test setups. In addition, this configuration allows the possibility of using out-of-plane restraints if needed for the RC frames. During the test, the out-of-plane displacements are monitored and it is determined that they are of insignificant amplitude in the conducted experiments (see Section 4.5 and Fig. 4.11).

### 4.8 EXPERIMENTAL SETUP IMPLEMENTATION

The assembly of the test setup consists of the construction of the RRW, the attachment of the test substructures to the strong floor, and the installation of the loading apparatus to connect the actuators to the test substructures. This section summarizes these steps for constructing the test setup.

### **4.8.1 Construction of RRW**

The construction of the RRW consists of placing the wall units in their setup positions with a layer of special grout between the strong floor and the lower unit, and between every two subsequent units. High-strength steel rods are then placed in the allocated vertical tubes, aligned through the wall height and the strong floor thickness (Fig. 4.16), and post-tensioned to the desired load of 100 kips (450 kN) per rod. The main steps are illustrated in the photographs of Figure 4.17.

### **4.8.2 Attachment of Actuator to RRW**

A steel base plate serves as the interface between the actuator and the RRW. It is first installed on the face of the RRW at the actuator intended height, then grouted and post-tensioned to ensure perfect contact. The base plate includes threaded holes which allow its connection with the actuator end plate. The actuator is then bolted to its end plate and connected to the hydraulic system. Figure 4.18(a) shows the end plate installation on the RRW, and Figure 4.18(b) shows the actuator placed in position.

### **4.8.3 Attachment of Test Substructures to Strong Floor**

The RC frames are first placed in their specified location on the strong floor. The footing of each RC column contains several built-in PVC tubes extending through the thickness of the footing (Fig. 4.6). High-strength rods with an end plate from each side are passed in these tubes and through the thickness of the strong floor. These rods are post-tensioned with a load of 100 kips (450 kN) (Fig. 4.19). This level of post-tensioning ensures the complete fixity (with no tension developing at the footing–strong floor interface) at any stage of lateral loading.

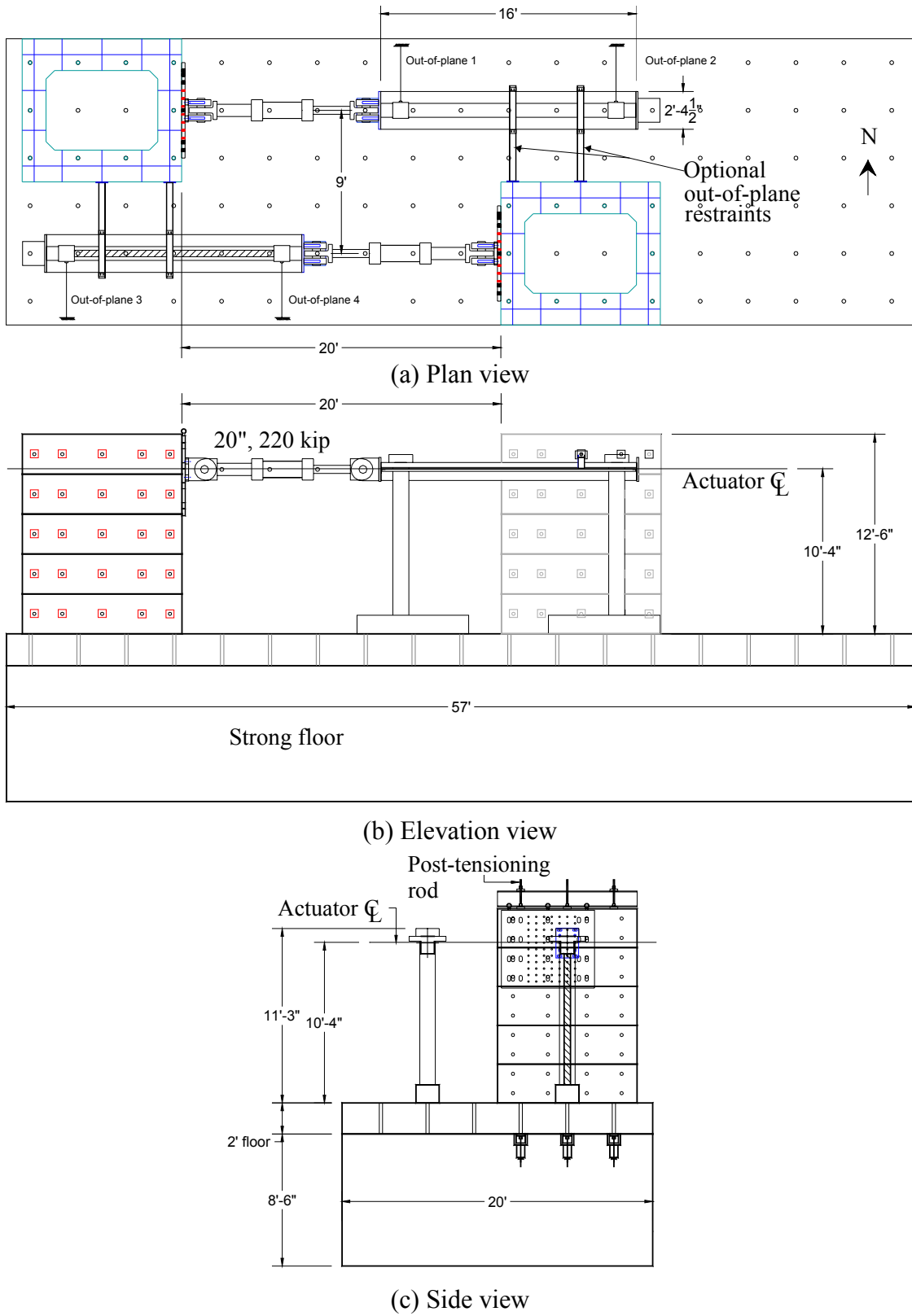


**Fig. 4.16** Test setup on strong floor for test structure A (1'=304.8 mm, 1"=25.4 mm, 1 kip = 4.448 kN).



(a) Grout placement on strong floor



(b) Transportation of an upper wall unit



(c) Grout placement between two upper units



(d) High-strength post-tensioning rod

**Fig. 4.17 Construction of RRW.**



(a) Installation of base plate onto face of RRW



(b) Actuator installation and connection to base plate

**Fig. 4.18 Installation of actuator at desired height.**

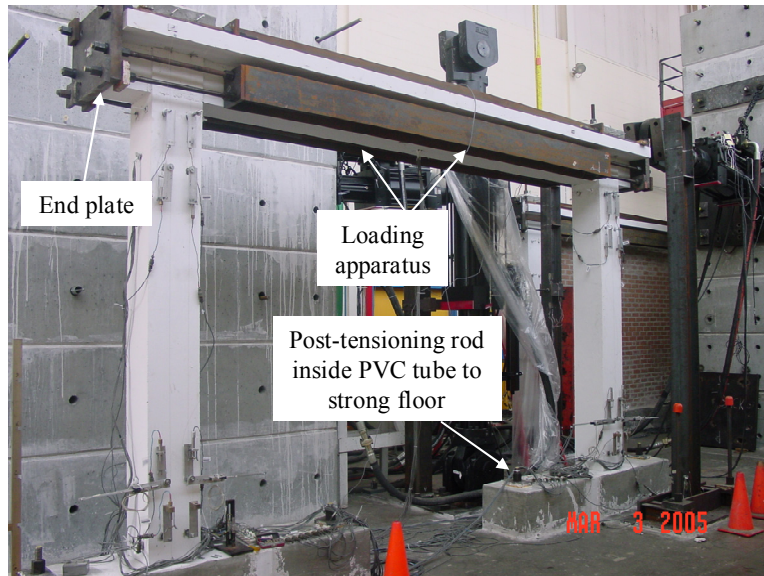


**Fig. 4.19 Loading apparatus mounted on RC bare frame.**

#### **4.8.4 Installation of Loading Apparatus**

The attachment of the actuator clevises to the test substructures needs to accommodate the application of tension and compression forces. Steel plates are positioned at each end of the RC frame at the beam level. The plate on the actuator end of the frame provides the interface between the actuator and the test substructure. Two steel W-beams and two angles are positioned along the length of the RC beam of each frame (Figs. 4.19–4.20). These steel elements are connected to the end plates using high-strength rods. The loading apparatus provides the grip necessary to attach the actuator to the frame. In addition, the steel beams are tensioned prior to the test, thus subjecting the RC beams to axial compression forces.

The post-tensioning forces are intended to counteract the tension forces in the steel beams during the application of pulling loads by the actuators. Accordingly, permanent contact between the end plates and the beam ends of the RC frame is maintained throughout the test. However, the post-tensioning increases the cracking load of the beams and joints and may lead to a delay in the initiation and propagation of cracking and reduced deterioration of the joints. Moreover, the applied displacement in HS, which is constant along the length of the RC beam, does not exactly simulate the deformation corresponding to the inertial forces in the ST test. In this latter test, the inertial force is distributed uniformly within the area of the RC slab and results in a uniformly

distributed lateral load along the length of the RC beams. Therefore, two sources of discrepancy between the ST test and the pseudo-dynamic test are attributed to the way the test substructures are loaded, namely (1) the application of a constant displacement versus a uniformly distributed lateral load and (2) the post-tensioning of the RC beams causing an increase in the cracking load along the RC beam and at beam-to-column joints. The effects of these two sources are discussed in the comparison between the ST and HS tests at the different phases of the experiment in Chapter 8.

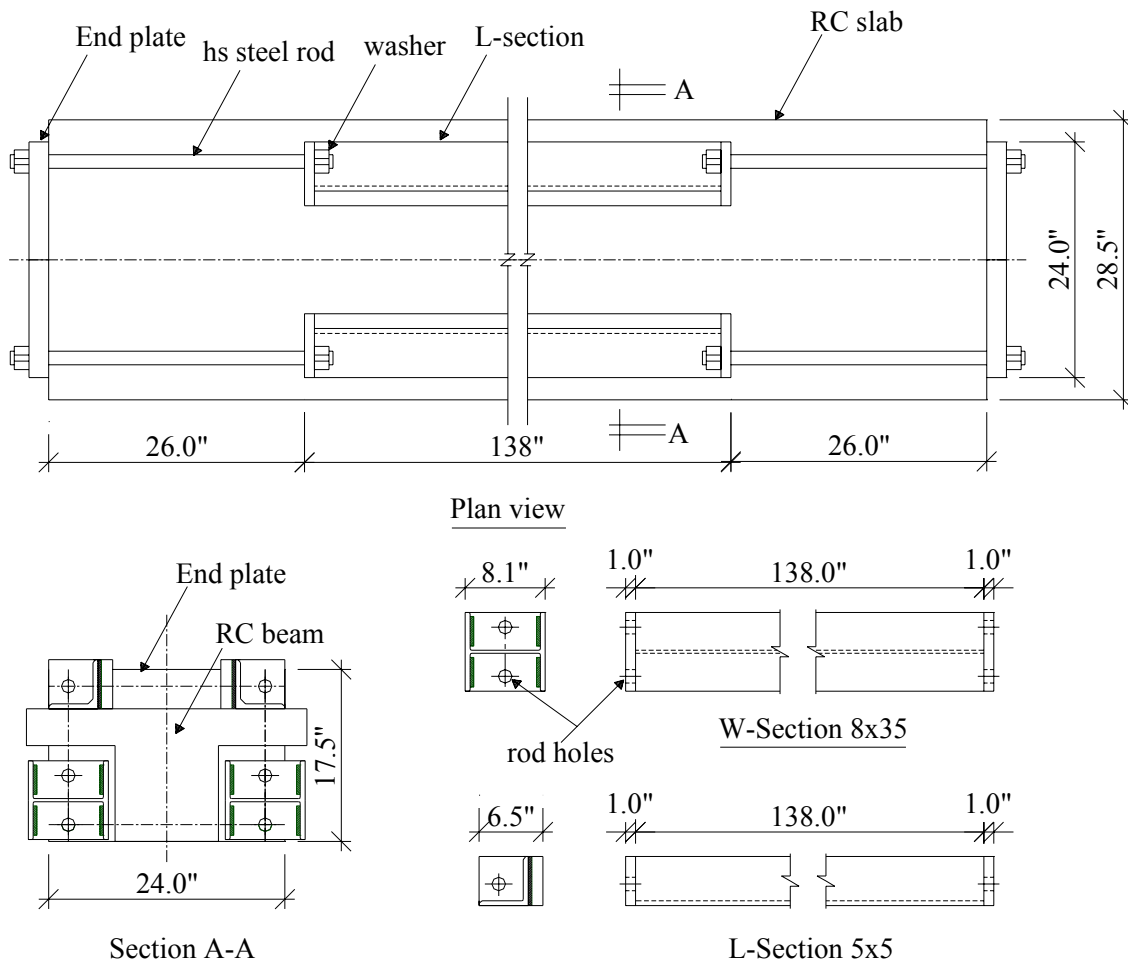


**Fig. 4.20 Details of loading apparatus for test structure A (1"=25.4 mm).**

A torque moment corresponding to a load of 20 kips (88.9 kN) is applied on each of the six high-strength steel rods used in the loading apparatus (Section A-A of Fig. 4.20). Accordingly, a total of 120 kips (533.8 kN) per RC frame is applied as post-tensioning force in the RC beam. This load is larger than the expected maximum load to be applied on the RC frame (Table 4.5) and translates into an axial compressive stress of less than 600 psi (4.14 N/mm<sup>2</sup>)

(< 13%  $f'_c$ ) on the beam. This compressive stress, although not large, is not insignificant and is expected to influence the behavior of the beam-to-column joints and RC beams as mentioned above and discussed further in Chapter 8. The alignment of the end plates, which transfer the load to the RC beam, within the beam cross section is such that the post-tensioning load resultant is applied in the center of gravity of the combined cross section of the RC beam and slab (T-beam), i.e., the eccentricity of the post-tensioning force is zero.

#### **4.9 HS IDEALIZATION OF TEST STRUCTURE**

An essential limitation of the HS is entailed by the method used to load the experimental substructures. The actuators are attached to specific points on the physical substructures and it is not practically possible to distribute the load along the inertial mass of the substructure as in the actual case of ground shaking. Therefore, the test structure needs to be carefully idealized into a distinct number of DOF. Subsequently, the dynamic properties are defined in terms of these selected DOF only.

In this study, the test structure is loaded in-plane in a direction parallel to the frames. Each frame may be represented by a large number of DOF along the length of the beam and the height of the columns (Fig. 4.21(a)). A lumped mass is assigned to each degree of freedom, such that the total inertial mass is represented by the selected degree of freedom. Note that the inertial mass in this case reflects the weights of the RC columns, the RC beam and the part of the adjacent RC slab tributary to the frame in question. Moreover, any additional weights due to gravity loads should be also included. The higher the number of DOF, the more accurate this idealization would be and the closer it is to the distributed nature of the inertial mass of the frame. Although this representation may be accurate in describing the dynamic response of the test structure, the application of the load to this large number of DOF is not practically feasible.

For simplicity and practicality, the idealization is simplified to the representation of each frame as a single degree of freedom (SDOF) (Fig. 4.21(b)). The validity of this further simplification is based on the assumption that the beam in each frame is rigid in the loading direction and thus is subjected to the same displacement along its length. This allows the seismic demand to be applied to the test structure using one actuator attached to the RC beam for each frame.

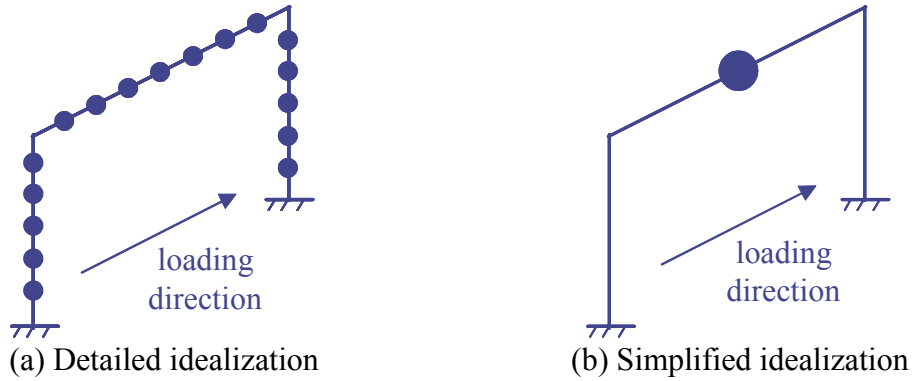


**Fig. 4.21 Idealizations of test frame into DOF.**

Extending the simplified idealization above of one RC frame to the whole test structure, three DOF are identified for the case of test structures in phases S-1, S-2, S-3, P-1, and P-2 in Figure 1.2. Moreover, a linear spring connecting the RC frames is assumed to represent the RC slab. The idealization of the RC slab is based on the assumption that a uniform displacement is experienced by the slab parallel to the frame due to its high stiffness in its plane. Figure 4.22 illustrates this idealization for the test structure in phase S-1. Similar idealization applies for the test structures in phases S-2, S-3, P-1, and P-2.

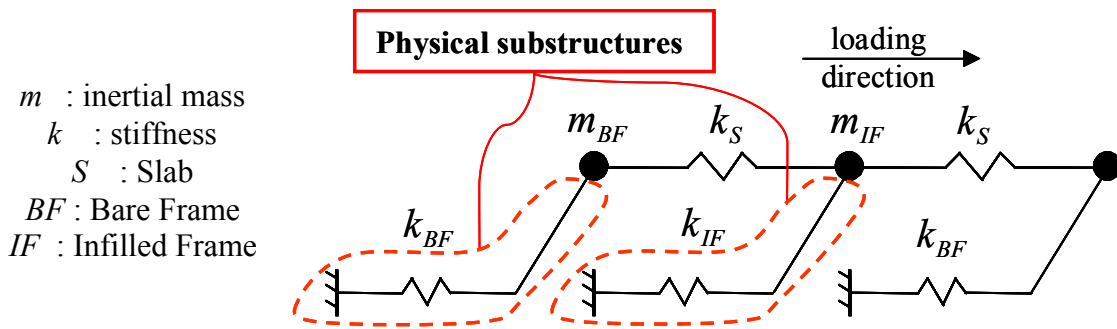


**Fig. 4.22 Idealized test structure in phase S-1 (see Fig. 1.2).**

#### 4.10 GOVERNING EQUATIONS OF MOTION AND PARAMETERS

After the idealization of the test structure into a distinct number of DOF, the governing equations of motion for these DOF are written in the following form:

$$\mathbf{M}\ddot{\mathbf{u}} + \mathbf{C}\dot{\mathbf{u}} + \mathbf{K}\mathbf{u} = -\mathbf{M}\mathbf{1}a_g \quad (4.1)$$

where  $\mathbf{M}$  is the mass matrix,  $\mathbf{C}$  is the damping matrix,  $\mathbf{K}$  is the stiffness matrix,  $\mathbf{1}$  is the influence vector which is a vector of ones in this case, since all the masses are assumed to be excited by the ground motion,  $a_g$  is the ground acceleration to which the test structure is assumed to be subjected to and  $\ddot{\mathbf{u}}$ ,  $\dot{\mathbf{u}}$ , and  $\mathbf{u}$  are the acceleration, velocity, and displacement vectors, respectively, of the idealized test structure. In the following sections, the estimation of  $\mathbf{M}$ ,  $\mathbf{C}$ , and  $\mathbf{K}$  are derived from the parallel ST test conducted on a test structure similar to that of phase S-1.

#### 4.10.1 Mass Matrix

The mass matrix represents the inertial mass present on the ST test structure. The sum of the mass of the ST test structure and the additional mass attachments on top of the RC slab (Hashemi and Mosalam 2006) are estimated based on the tributary areas of the floor for each frame into the three DOF representing the test structure (Fig. 4.23). Accordingly, two similar masses are allocated for the exterior bare frames,  $m_{BF}$ , and one larger mass allocated for the interior infilled frame,  $m_{IF}$ . The resulting diagonal mass matrix becomes:

$$\mathbf{M} = \begin{pmatrix} m_{BF} & 0 & 0 \\ 0 & m_{IF} & 0 \\ 0 & 0 & m_{BF} \end{pmatrix} \quad (4.2)$$

The same procedure is applied to the test structures in phases S-2, S-3, P-1, and P-2.

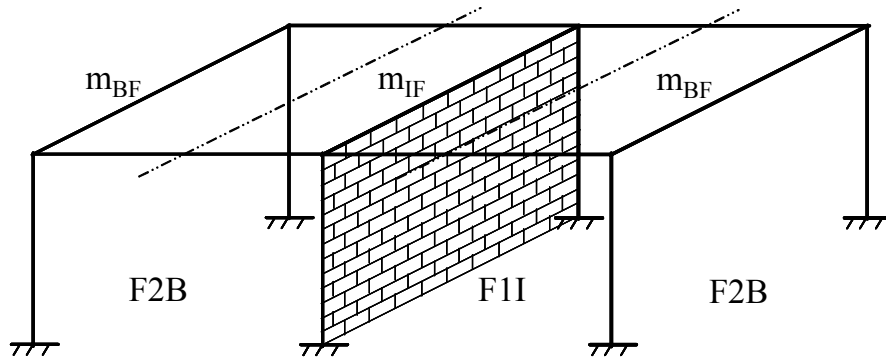


Fig. 4.23 Mass allocation by tributary areas.

### 4.10.2 Damping Matrix

The damping ratio suitable for the test structure in phase S-1 is evaluated based on a pull-back test before the ST experiments. In this pull-back test, the ST test structure is pulled from the top RC slab causing a small deformation and then suddenly released to freely vibrate (Hashemi and Mosalam 2007). The resulting damping ratio  $\zeta$  and natural frequency  $\omega_n$  are subsequently estimated. For simplicity in HS, damping is assumed to be first-mode mass proportional (Chopra 2001), as follows:

$$\mathbf{C} = 2\zeta \mathbf{M} \omega_n \quad (4.3)$$

### 4.10.3 Stiffness Matrix

The stiffness matrix is derived from the idealized form of the test structure (Fig. 4.22). This yields the stiffness matrix below:

$$\mathbf{K} = \begin{pmatrix} k_{BF} + k_S & -k_S & 0 \\ -k_S & k_{IF} + 2k_S & -k_S \\ 0 & -k_S & k_{BF} + k_S \end{pmatrix} \quad (4.4)$$

where  $k_{BF}$ ,  $k_{IF}$ , and  $k_S$  are the stiffness of the bare frame, infilled frame and slab, respectively.

This stiffness matrix can be expressed as the sum of two matrices  $\mathbf{K}_F$  and  $\mathbf{K}_S$ , where:

$$\mathbf{K} = \mathbf{K}_F + \mathbf{K}_S$$

$$\mathbf{K}_F = \begin{pmatrix} k_{BF} & 0 & 0 \\ 0 & k_{IF} & 0 \\ 0 & 0 & k_{BF} \end{pmatrix} \text{ and } \mathbf{K}_S = k_S \begin{pmatrix} 1 & -1 & 0 \\ -1 & 2 & -1 \\ 0 & -1 & 1 \end{pmatrix} \quad (4.5)$$

Noting that the product  $\mathbf{R}_F = \mathbf{K}_F \mathbf{u}$  is a  $3 \times 1$  vector representing the restoring forces to be measured from the test substructures, only one exterior bare frame is tested together with the interior infilled frame for phase S-1. From symmetry, the restoring force in the other (numerically simulated) bare frame is estimated as having the same value as the one that is physically tested. Accordingly, the equations of motion are written in the form:

$$\mathbf{M} \ddot{\mathbf{u}} + \mathbf{C} \dot{\mathbf{u}} + \mathbf{R}_F + \mathbf{K}_S \mathbf{u} = -\mathbf{M} \mathbf{1} a_g \quad (4.6)$$

For phases S-2, S-3, P-1, and P-2, the physical substructure consists of one RC bare frame. The RC slab, due to its high lateral stiffness (see Section 4.12) forces the three RC bare frames of the test structure to be subjected to almost the same displacement demand. The restoring forces in each of the other two numerically simulated frames are thus taken the same as the measured restoring force from the physically tested substructure. Note that the inertial forces are different for the URM infilled frame and bare frames because of differences in the associated masses.

#### **4.11 INITIAL STIFFNESS ESTIMATION FOR PHYSICAL SUBSTRUCTURES**

A set of pull-back tests is performed on each of the two RC frames in the direction of their plane. While pull-back tests are useful in evaluating the damping properties of the structure as well as its initial stiffness, the damping properties in this HS test are specified in the numerical-integration algorithm, based on the measured values from the structure tested with the proper mass on the ST. Therefore, the only results sought from these pull-back tests are the initial stiffness of the RC frames. The estimated values serve as guidelines before starting the HS test to estimate the modal frequencies (see Section 4.13) and the stiffness matrix in its undamaged state, which is needed to initiate the simulation using the numerical-integration algorithm, discussed in Section 6.1.

A load cell is connected in series with a lever chain hoist and a short piece of 1/4" (6.4 mm) steel rod between the reaction wall and the RC frame (Fig. 4.24). The chain is used to load the attachment to the desired load and the steel rod is cut abruptly to release the frame, which is left to vibrate freely. The measured force and displacement while loading are used to evaluate the stiffness. The test is performed on the URM infilled RC frame (F1I) with post-tensioned columns using a load of 5 kips (22.2 kN) and on the RC bare frame before post-tensioning (F2BU) and after post-tensioning the columns (F2B) with a load of 3 kips (13.3 kN) in both cases. The test is performed twice for each case and the stiffness is evaluated as the average of the two results; refer to the summary of results in Table 4.6. Note that the ratio between the stiffness of the URM infilled and bare RC frames is rather high (21.8) compared to what is typically found in the literature (Mosalam et al. 1997b, c, and d). This may be attributed to the fact that the interface between the URM infill wall and the surrounding RC frame remained intact at these low levels of lateral forces. Once hairline separation cracks form along the frame/wall interface when the

RC frame is loaded to a magnitude of deformation capable of overcoming the bond at the interface, the stiffness is expected to reduce significantly.

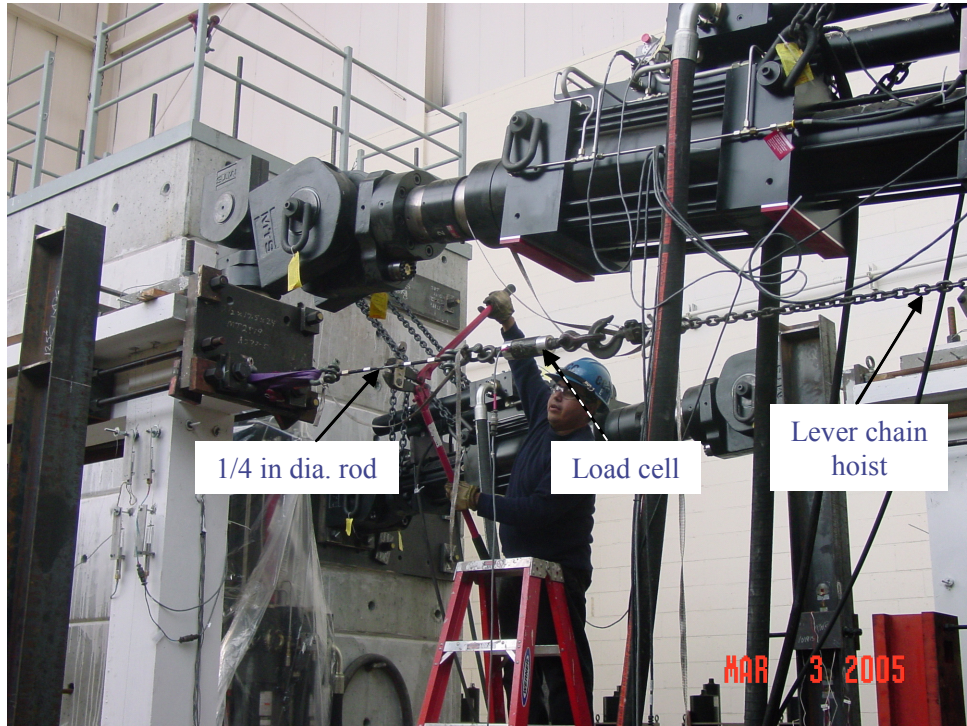


**Fig. 4.24 Pull-back test setup.**

**Table 4.6 Pull-back test results for substructures of test structure A.**

Frame	F1I	F2B	F2BU
Stiffness from test 1 [kips/in. (kN/mm)]	840 (147.1)	40.4 (7.08)	37.9 (6.64)
Stiffness from test 2 [kips/in. (kN/mm)]	950 (166.4)	41.6 (7.29)	37.7 (6.60)
Average stiffness [kips/in. (kN/mm)]	895 (156.7)	41.0 (7.18)	37.8 (6.62)

The initial stiffness is re-estimated during a set of preliminary runs applied before the start of phase S-1 (see Fig. 1.2) to have a more realistic estimation of the initial stiffness. These low-level preliminary runs are aimed at estimating the integration time step  $\Delta t$  to be used in the HS experiments (see Section 4.14) and for obtaining a more representative estimate of the initial stiffness. Figure 4.25 shows the restoring force of the URM infilled RC frame versus its lateral displacement for the fourth and last of these preliminary runs. The initial stiffness is estimated by computing an average tangent stiffness over the time history, using the least-squares method to

obtain a best linear fit for the initial stiffness but excluding the major loading cycles beyond 0.04" (1 mm). The value of  $K \approx 700$  kips/in. (122.6 kN/mm), i.e., 78% of the average stiffness obtained from the pull-back test, is determined from all four runs and is therefore adopted as the initial stiffness in the numerical-integration algorithm.

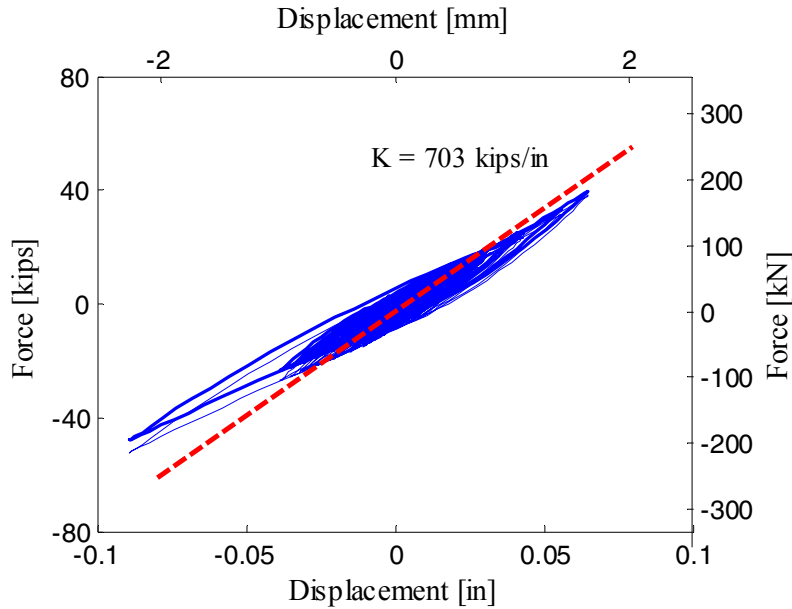


**Fig. 4.25 Restoring force versus lateral displacement of URM infilled RC frame from preliminary run (1 kip/in. = 0.175 kN/mm).**

## 4.12 RC SLAB STIFFNESS ESTIMATION

The RC slab is assumed to have in-plane linear behavior within the range of deformation introduced by the applied earthquake motions. To determine the value of the in-plane stiffness, a theoretical value is calculated and verified against the experimental results from the ST tests as described below.

### 4.12.1 Theoretical In-Plane Stiffness of RC Slab

To estimate a theoretical value of the RC slab in-plane stiffness, the slab is assumed to act as a shear element between the two adjacent frames (Fig. 4.26). Accordingly, the theoretical stiffness  $k_s$  is estimated as follows:

$$k_s = \frac{F}{\Delta} = \frac{F/A}{\Delta/L} \times \frac{A}{L} = G \frac{bt}{L} \quad (4.7)$$

$$G = \frac{\tau}{\gamma} = \frac{F/A}{\Delta/L} = \frac{E_c}{2(1+\nu_c)} \quad (4.8)$$

where  $E_c$  and  $\nu_c$  are the concrete elastic Young's modulus and Poisson's ratio, respectively. Other parameters in the above equations are shown in Figure 4.26. These parameters are substituted by their estimated values listed in Table 4.7, and the resulting stiffness is evaluated as  $k_s = 16500$  kips/in. (2889.6 kN/mm).

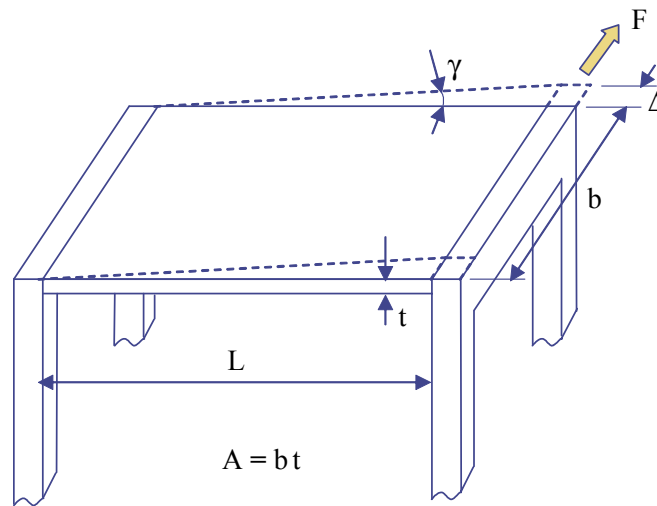


**Fig. 4.26 RC slab stiffness estimation (not to scale).**

**Table 4.7 Values of parameters used in RC slab in-plane stiffness estimation.**

Parameter	$E_c$ [ksi (kN/mm <sup>2</sup> )]	$\nu_c$	$t$ [in. (mm)]	$b$ [in. (mm)]	$L$ [in. (mm)]
Value	4000 (700.5)	0.2	3.75 (95)	192 (4877)	72 (1829)

#### 4.12.2 Experimental In-Plane Stiffness for RC Slab

Several runs are executed in the HS setup on the test structure of phase S-1 subjected to the low-level seismic motion, TAR level 2 (TAR-2) in Table 4.2. The test is repeated four times using different values for the stiffness of the RC slab corresponding to 1%, 3%, 10%, and 100% of the theoretical value  $k_s = 16500$  kips/in. (2889.6 kN/mm). The results are plotted in Figure 4.27 on

a log-log scale and a linear relationship is observed between the calculated maximum differential drift between the two frames F1I and F2B at the beam level and the stiffness of the RC slab.

The ST test results, performed on an identical test structure to that of phase S-1 of the HS, are used as a reference to estimate an experimental value of the in-plane stiffness of the RC slab. Figure 4.28 shows the maximum differential drift between the parallel frames, estimated as the differential drift between the middle infilled frame and the average of the two exterior bare frames. This differential drift is plotted against the maximum applied lateral displacement for different test levels. The results are plotted at six different levels of the applied table motions, each represented by a point on the curve, the lowest level corresponding to TAR-2 and the highest to DUZ-8.

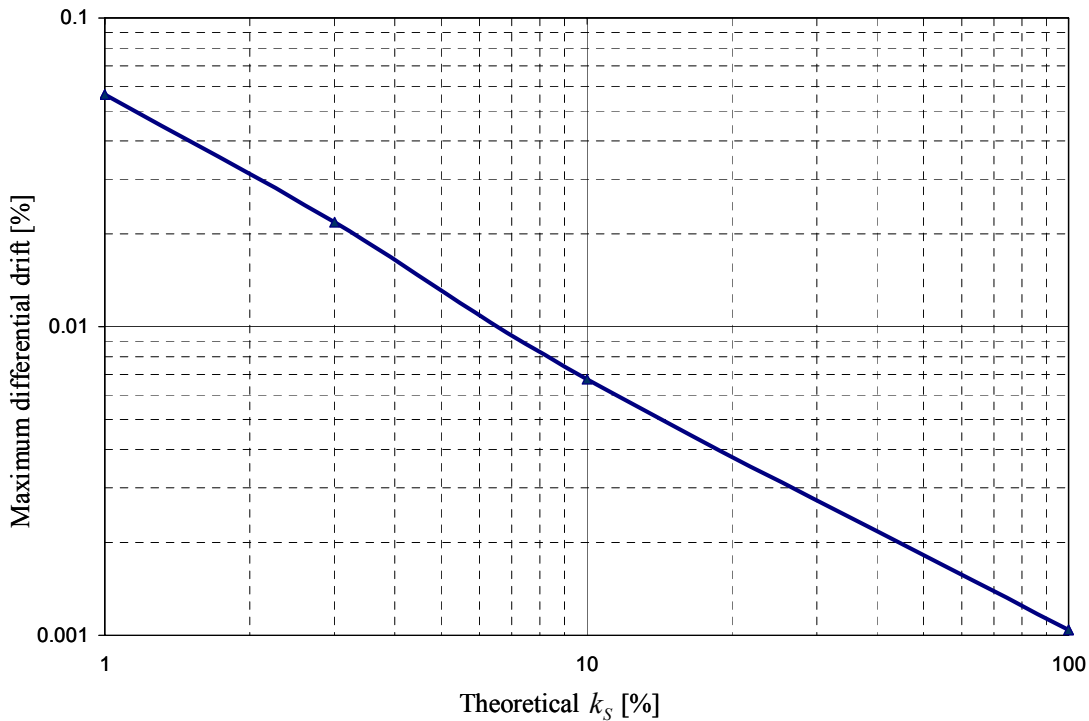


**Fig. 4.27 Differential drift in pseudo-dynamic test between F1I and F2B as function of theoretical in-plane stiffness of RC slab.**

At the three lower levels of Table 4.7, the differential drift is almost constant at a value of 0.001% and increases almost linearly for the three higher levels to reach a value of 0.015% at the sixth level. This shift in behavior is partly due to the fact that the rods attaching the added lead weights in the ST test structure to the top of the RC slab are retightened after TAR-4, thus causing some minor cracking and a reduction in the RC slab stiffness. Based on these results and the deduced relationship in Figure 4.27, the RC slab in-plane stiffness is estimated as 100% of

the theoretical value of  $k_s$  up to TAR-4, corresponding to 0.001% differential drift and for simplicity 10% of  $k_s$  thereafter, corresponding to approximately 0.007% differential drift. It is important to note the ratio between differential drift and global drift at the beam level. For the strongest motion DUZ-8, this ratio is calculated as 1/169, implying that the RC slab in the ST experiment acted as a rigid diaphragm between the RC frames and forced them to be subjected to almost the same amount of lateral deformation. In other words, the first natural mode of vibration dominates the response of the test structure. The natural vibration modes are discussed in more details in the next section.

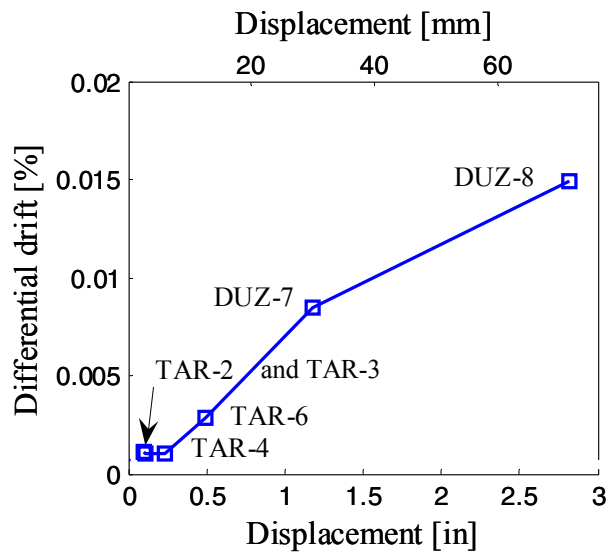


**Fig. 4.28 Differential drift in dynamic (ST) tests against applied maximum lateral displacement.**

#### 4.13 PARAMETERS OF EQUATIONS OF MOTION

At this point, all of the properties of the test structure are determined for the structure in phase S-1 (see Fig. 1.2). These properties are summarized in Table 4.8 with the parameters defined in previous sections. The natural modes of vibration are determined by solving the following eigenvalue problem (Chopra 2001):

$$\mathbf{K}\phi_n = \lambda_n \mathbf{M}\phi_n \quad (4.9)$$

where  $\mathbf{K}$  and  $\mathbf{M}$  are the stiffness and mass matrices of the test structure,  $\phi_n$  is the modal shape vector, and  $\lambda_n = \omega_n^2$  are the eigenvalues with  $\omega_n$  as the natural frequencies. For the three DOF system studied, the dynamic response is governed by three natural modes of vibration with different participation factors (Chopra 2001), i.e.,  $1 \leq n \leq 3$ . The natural period is defined as  $T_n = 2\pi/\omega_n$ . The results of the modal properties are summarized in Table 4.9 in the case of test structure A in phase S-1 (see Fig. 1.2), and Figure 4.29 describes the corresponding mode shapes.

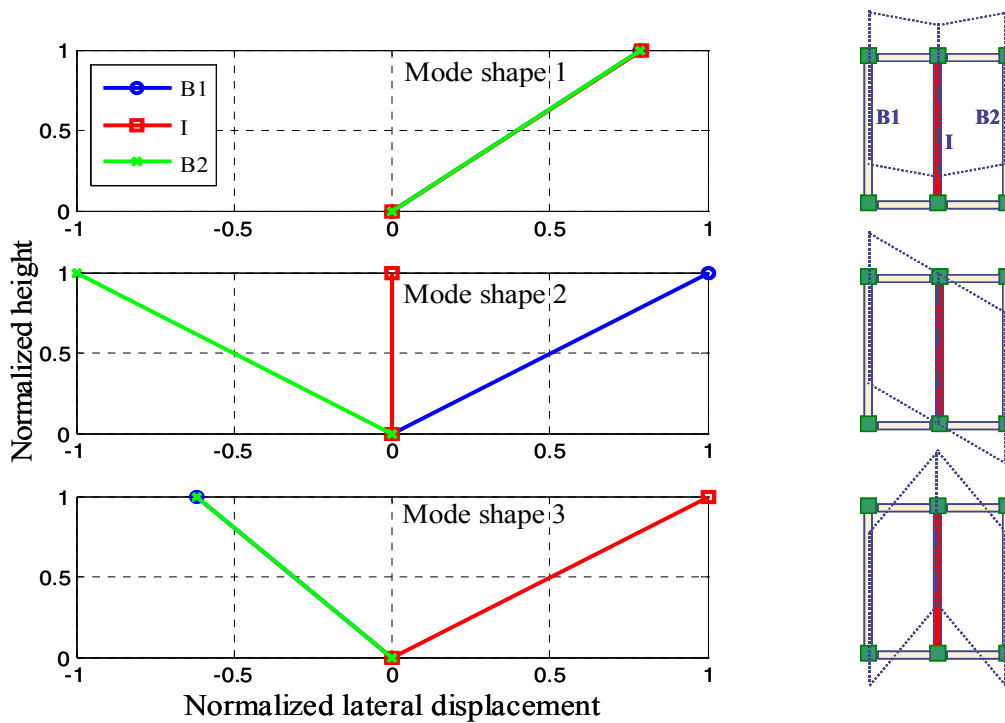


**Fig. 4.29 Mode shapes for test structure A in phase S-1.**

**Table 4.8 Estimated parameters for test structure A in phase S-1.**

Parameter	$m_{BF}$ [kips-sec <sup>2</sup> /in. (kN-sec <sup>2</sup> /mm)]	$m_{IF}$ [kips-sec <sup>2</sup> /in. (kN-sec <sup>2</sup> /mm)]	$\zeta$ [%]	$k_{BF}$ [kips/in. (kN/mm)]	$k_{IF}$ [kips/in. (kN/mm)]	$k_S^*$ [kips/in. (kN/mm)]
Value	0.106 (0.019)	0.070 (0.012)	6.2	41 (7.2)	700 (122.6)	16500 (2889.6)

\* For levels TAR-4 or lower and reduced to 10% of this value for higher levels

**Table 4.9 Natural frequencies and periods for test structure A in phase S-1.**

Mode	1	2	3
$\omega_n$ (rad/sec)	61.3	486.3	742.6
$f_n$ (Hz)	9.80	76.92	117.65
$T_n$ (sec)	0.1020	0.0130	0.0085

#### 4.14 INTEGRATION TIME-STEP ESTIMATION

Ideally, the integration time step is chosen as small as possible to yield the most accurate numerical integration. However, typically, it is required to capture the response of the test structure in its major influential modes, which does not necessarily require that extreme level of accuracy for the choice of the integration time step. Another controlling factor in the choice of the numerical-integration time step may be a condition of stability (see Section 2.3). Since the selected algorithm is unconditionally stable for test structures with a softening stiffness (Nakashima et al. 1990), this stability condition is no longer a limitation. To accurately capture the response, the numerical-integration time step  $\Delta t$  is selected to be less than  $T/10$ , where  $T$  is the smallest natural period of the test structure corresponding in this case to the third mode,  $T_3 = 0.0085$  sec, thus  $\Delta t = 0.0008$  sec is considered.

To examine the choice of the numerical-integration time step, the low-level strong motion, TAR-2, is applied on the test structure in phase S-1 four times using different integration time steps, namely  $\Delta t = 0.0008$ , 0.002, 0.0025, and 0.005 sec. Figure 4.30 illustrates the corresponding responses, which show minimal differences when comparing the displacement time histories. The fast Fourier transform plots are especially revealing, since the second and third modes do not show any noticeable influence in the response, and the peaks recorded are in the first mode (9.8 Hz), at about  $T_1 = 0.1$  sec (10 Hz) or higher ( $< 10$  Hz frequency). This finding is in agreement with the role of the stiff RC slab in minimizing the response in the second and third modes of vibration. This in turn allows increasing the integration time step to  $\Delta t = 0.0025$  sec when applying HS to test structure A in phase S-1. For other phases, where the URM infill wall is removed and the test structure is much less stiff,  $\Delta t = 0.005$  sec is adopted with high accuracy.

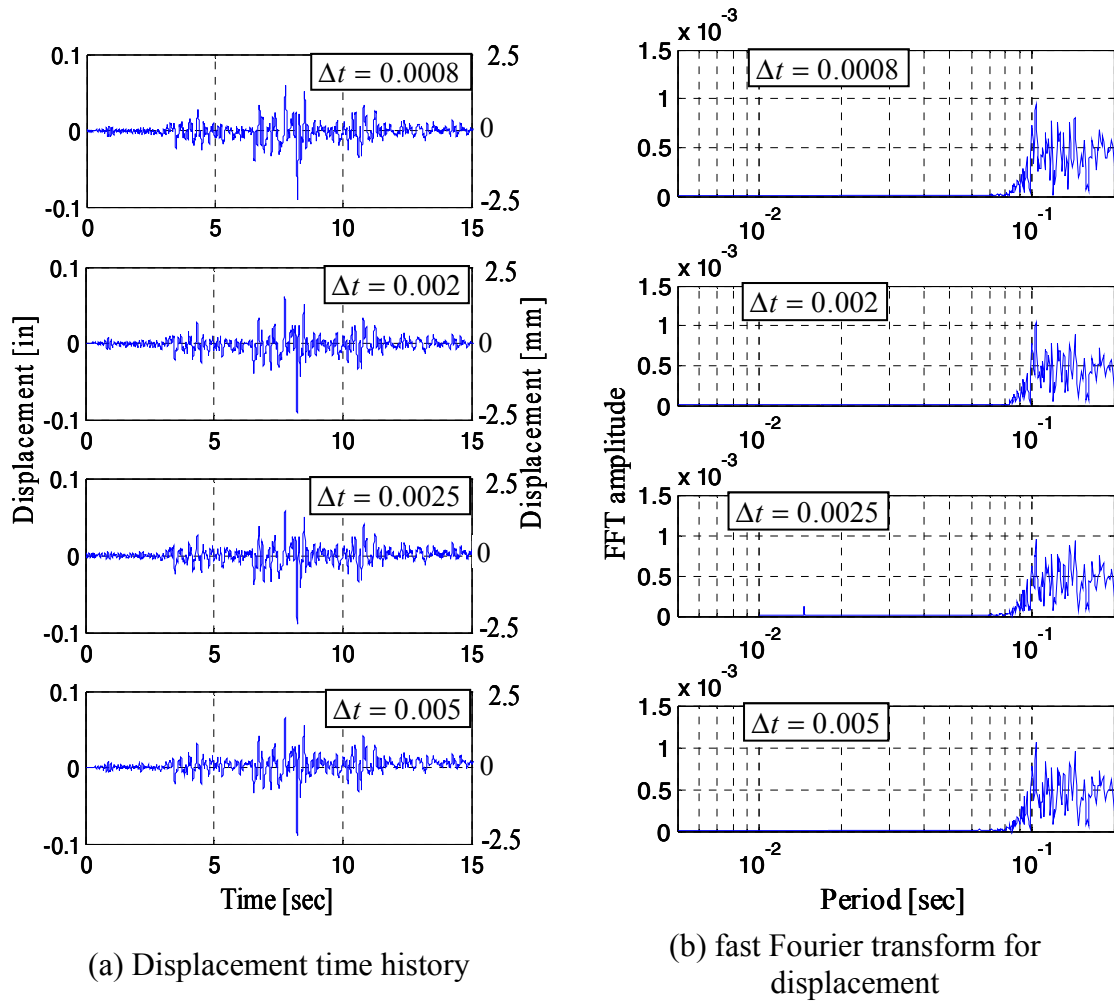


**Fig. 4.30 Comparison of response for TAR-2 using different integration time steps  $\Delta t$  in HS.**

#### 4.15 SUMMARY

The shaking table experiments, which preceded the hybrid simulation on an identical test structure, serve as benchmarks for the hybrid simulation experiments. Therefore, in all the steps concerning the construction of the hybrid simulation experiments, measures are taken to eliminate any avoidable deviations between the two tested structures. The hybrid simulation system test structure in question is divided into physically tested substructures and numerically modeled substructures. For each phase of the experimental program (see Fig. 1.2), these substructures are identified and the basis for modeling the computational part is presented. The physical substructures used in all tests are two  $\frac{3}{4}$ -scale RC frames, one a bare frame, the other

infilled using an URM wall. The structural design of the RC frames is detailed, as well as their construction, material properties, and instrumentation. The experimental setup design in the structural laboratory is discussed, including the design of the reconfigurable reaction walls, their positions on the laboratory strong floor and the selection of the actuators. A loading apparatus is designed to attach the actuators to the RC frames while avoiding the creation of any gaps between the test substructures and the used actuators during the push/pull loading actions of the actuators. A set of low-amplitude hybrid simulation runs on test structure A in phase S-1 are performed to evaluate key parameters in the equations of motion, namely the initial stiffness of the test structure, the RC slab in-plane stiffness  $k_s$ , and the integration time step  $\Delta t$ .

## **5 Test Structure B**

The second test structure presented in this chapter consists of two large substructures of a ST experiment conducted at UCB. The ST test structure is briefly presented along with the selection of the strong motions applied during different phases of the ST experiment. This chapter describes the physical substructures of the HS test structure including design, construction, and instrumentation. Moreover, the test setup on the strong floor is discussed in terms of its design and assembly. Similar to test structure A, discussed in the previous chapter, the development of the computational part of the HS for test structure B is discussed. This includes the idealization of test structure B, the formulation of the governing equation of motion, and the estimation of some key parameters in this equation of motion.

### **5.1 ST TEST STRUCTURE**

The seismic vulnerability of timber structures was demonstrated during recent earthquakes in California. In particular, a wood-frame building with an open front due to tuck-under parking is characterized by a soft first story (Mosalam et al. 2002; Mosalam and Mahin 2007). The building used in the ST experiment is a hypothetical two-story single-family “house-over-garage” representing the plethora of houses in San Francisco, California, constructed in the 1930s. The ST experiment is carried out on the full-scale two-story structure on the seismic simulator test facility of UCB (Fig. 5.1).



**Fig. 5.1 Two-story wood house over garage on ST.**

## 5.2 TEST STRUCTURE DESIGN

The design of the shear walls in the ST test structure is presented in this section and is adopted for the HS physical substructure, discussed in Section 5.4. The plan dimensions are 19' 6"×13' 6" (5944 mm×4115 mm) (Fig. 5.2). The height is 18' 6" (5639 mm) from the bottom to the highest point of the roof, which is partially covered by a parapet of 2' 10" (864 mm) height (Fig. 5.3(a)). The shear walls are constructed using 1×12 shiplap siding (3-8d common nails per stud crossing) reinforced by V-shaped 2×4 diagonal blocking between studs (2-16d toe common nails) (Figs. 5.3(b) and 5.5). The two longitudinal (north and south) shear walls are 19' 6"×9' (5944 mm×2743 mm) with 2×4 studs at 16" (406 mm) spacing. The studs are end nailed (2-16d common) to double 2×4 top plates and toe nailed (3-16d common) to 3×6 sill plate with 1/2"×12" (13 mm×305 mm) anchor bolts at 4' (1219 mm) spacing with 1½" (38 mm) cut washers and square nuts to connect the sill plates to RC wall footings (Fig. 5.4). All lumber is Douglas Fir-Larch.

### 5.3 STRONG MOTION SELECTION

In the ST experiment, Loma Prieta, Los Gatos station, 1989 (LPG) was chosen to match the design basis earthquake (DBE) (10% probability of exceedance in 50 years) and upper-bound earthquake (UBE) (10% probability of exceedance in 100 years) levels of shaking. This ground motion is scaled to match design spectra of a stiff site in the Richmond district of San Francisco. Both fault-normal (FN) and fault-parallel (FP) components of this chosen ground motion are presented in Table 5.1. While on the ST, the test structure was subjected to a bidirectional motion, the HS test structure is tested in one direction parallel to the shear walls (E-W direction on the ST). The ground motion is scaled to generate different levels of intensity as listed in Table 5.2. As for test structure A in Chapter 4, the accelerations are measured on the ST during each run and applied in the HS, rather than the original scaled input motions. Prior to use in the HS experiments, these measured table accelerations are subjected to a low-pass filter at 25 Hz cut-off frequency.

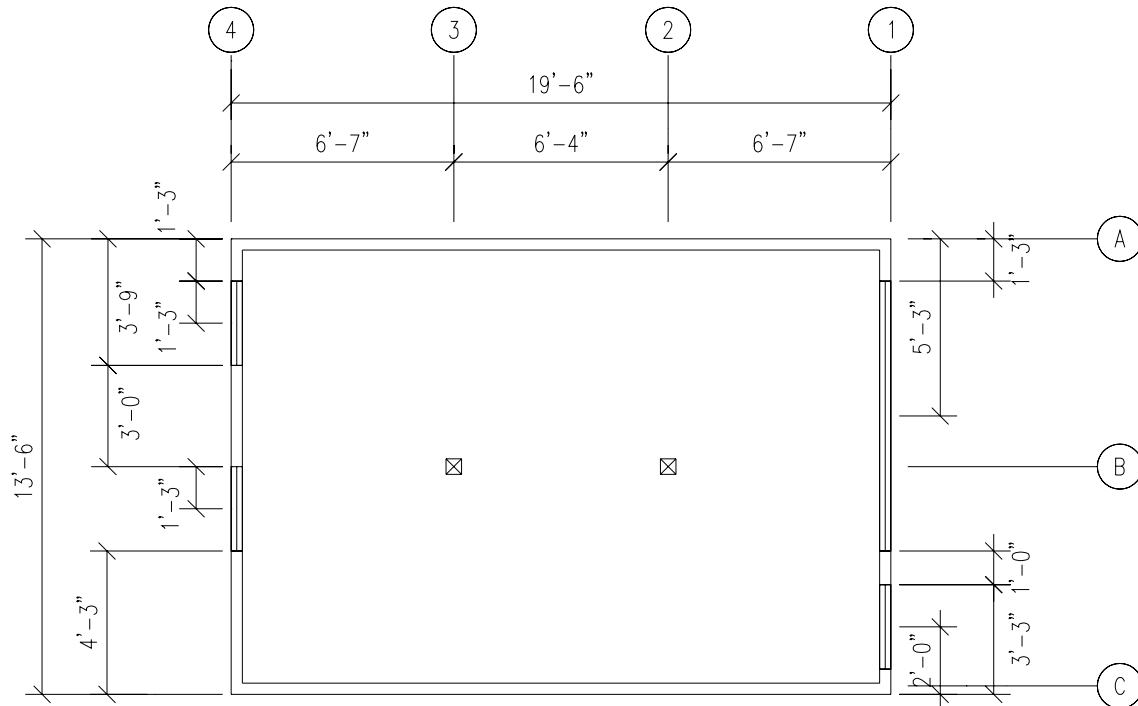
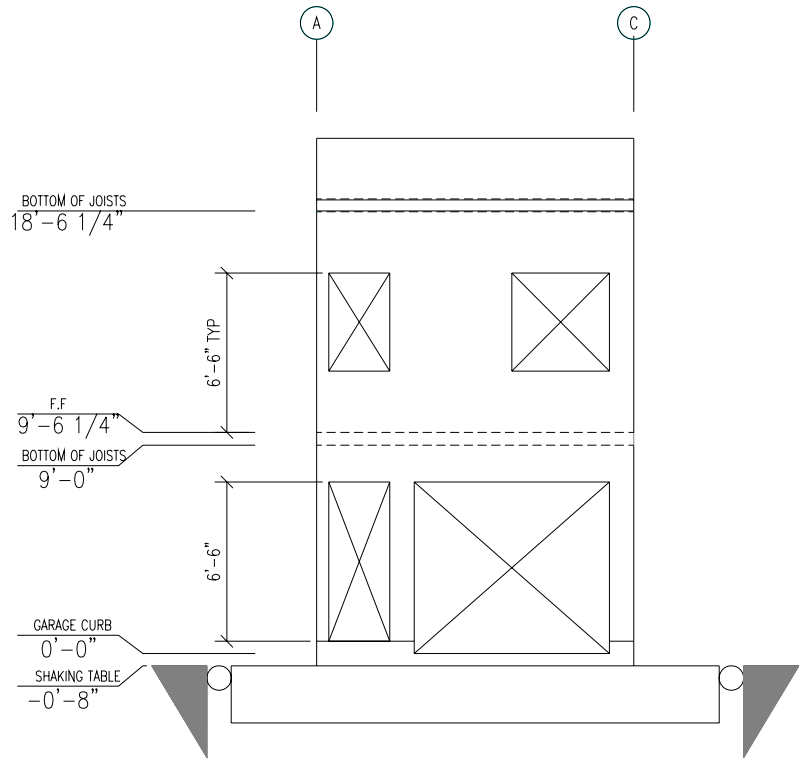
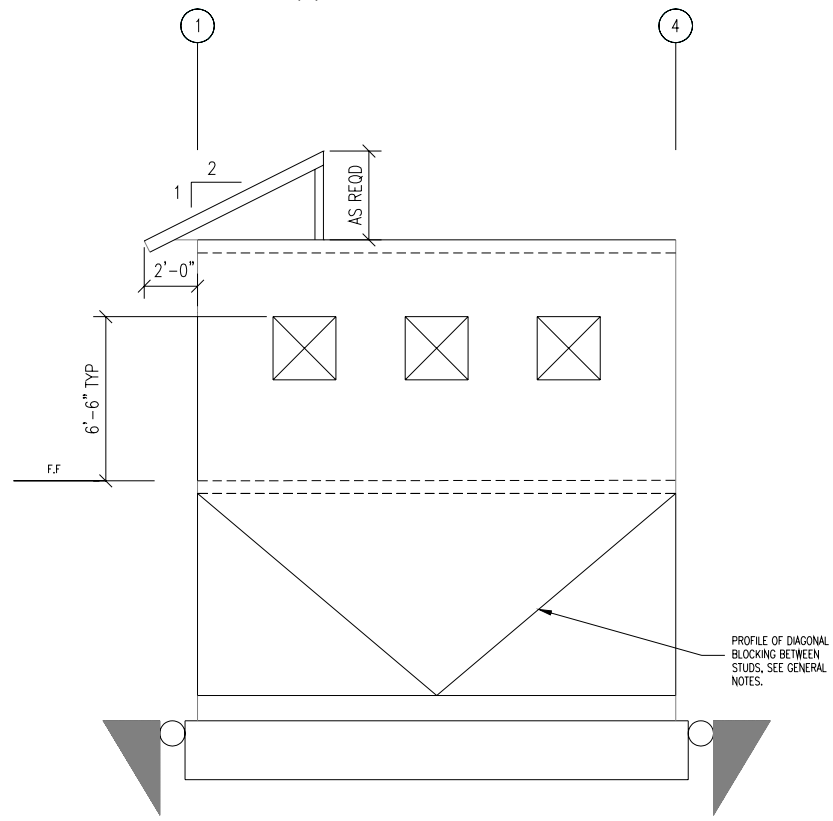


**Fig. 5.2 Wood house first-floor plan.**



(a) East wall elevation



(b) North wall elevation

**Fig. 5.3 Wood house elevation views.**

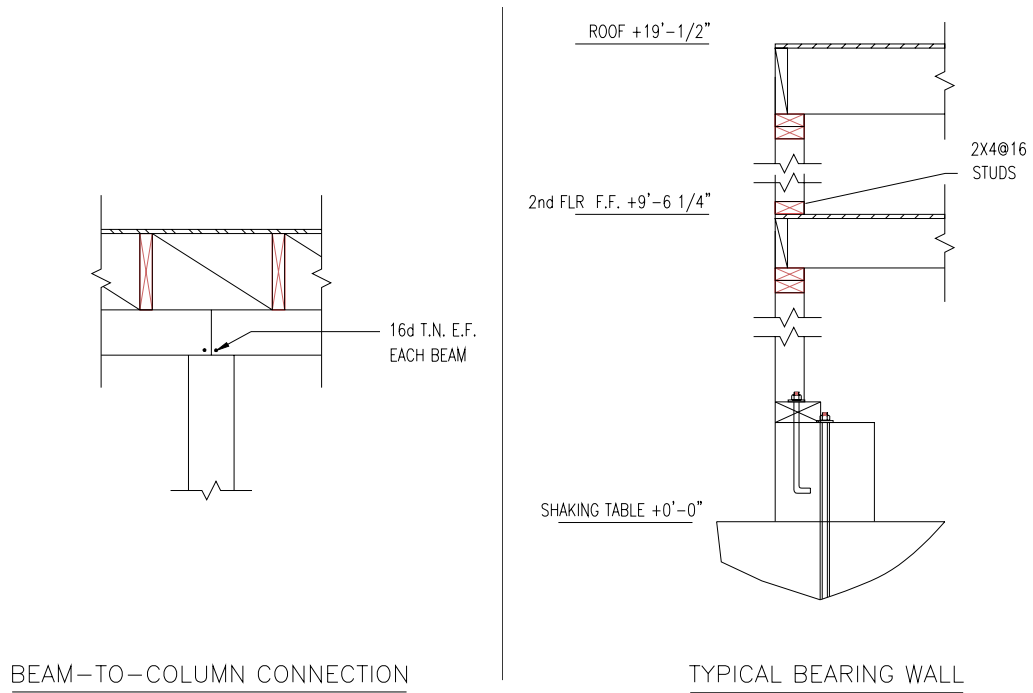


**Fig. 5.4 Design details of wood house.**



**Fig. 5.5 Blocking used to brace shear-wall framing of test structure B.**

**Table 5.1 Loma Prieta 1989, Los Gatos Station strong motion (LPG).**

Direction	Design Basis Earthquake (DBE)			Upper-bound Earthquake (UBE)		
	PGA (g)	PGV [in./sec (mm/sec)]	PGD [in. (mm)]	PGA (g)	PGV [in./sec (mm/sec)]	PGD [in. (mm)]
Fault Normal	0.42	21.09 (535.7)	3.77 (95.8)	0.46	25.43 (645.9)	5.06 (128.5)
Fault Parallel	0.38	16.21 (411.7)	2.37 (60.2)	0.57	20.64 (524.3)	3.10 (78.7)

**Table 5.2 Scale factors for different levels of input ground motion (fault normal) except as noted.**

Level	1	2	3	4	5	6*
Motion Scale	0.10×UBE	0.25×UBE	0.50×UBE	1.00×DBE	1.00×UBE	1.00×UBE

\* Fault normal followed by fault parallel

## 5.4 TEST STRUCTURE IN HS

The HS test structure B is presented in this section. The idealization leading to the development of the numerical model and the selection of the physical substructure, as well as the design of the experimental setup and the instrumentation of the test structure are discussed.

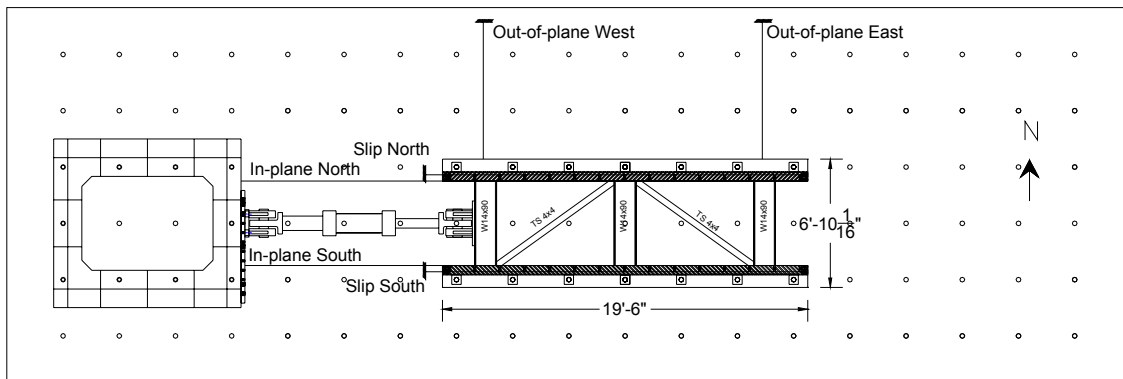
### 5.4.1 Idealization

Since in the ST experiment, the second story behaved very closely to a rigid mass atop the first-story shear walls, the two longitudinal (north and south) shear walls are constructed at full scale and treated in HS as the physical substructure (Figs. 5.6 and 5.7(a)). The test structure for the HS is idealized as a SDOF structure excited by a unidirectional motion parallel to the E-W direction where the north (N) direction is identified in Figures 5.2 and 5.6(a).

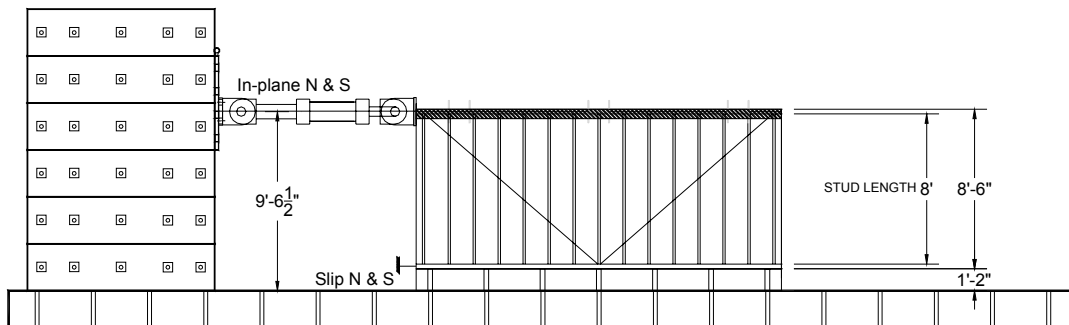
### 5.4.2 Experimental Setup

A rigid steel horizontal frame (Fig. 5.8) connects the two shear walls to a single dynamic actuator as identified in Figures 5.6 and 5.7(c)). Furthermore, three high-strength steel rods,

shown in Figure 5.7(b), each linked to a load cell in series, are connected to the strong floor at one end and the loading steel frame at the other end and are post-tensioned to simulate the gravity load present in the case of the ST test structure. It should be noted that these post-tensioned steel rods provided some resistance to overturning, leading to a change of the applied gravity loads by these rods. From the load cell measurements during the application of the strong motion LPG level 6 (LPG-6) (see Section 5.3), the total variation in the force applied by these rods was between 7.3 kips (32.5 kN) and 15.0 kips (66.7 kN), while the total initial value of the gravity load applied by these rods is 10.5 kips (46.7 kN) (Fig. 5.9). The height of the test structure, including the RC foundation, requires the construction of a five-unit high RRW with total height of 12' 6" (3810 mm). The maximum load of the combined two shear walls is not expected to exceed 30 kips (5.3 kN), and therefore the RRW limits are certainly not exceeded (see Section 4.7.1). The same 220 kips (979 kN) dynamic actuator used in the case of the RC frame structure for test structure A, Chapter 4, is selected for use with test structure B (see Table 3.1).



(a) Plan view and instrumentation



(b) Elevation view and instrumentation

**Fig. 5.6 Test setup and instrumentation on strong floor for test structure B (1' = 304.8 mm, 1" = 25.4 mm)**



(a) Overview of HS physical substructure



(b) Post-tensioned high-strength steel rod monitored using load cell



(c) Horizontal loading steel frame



(d) Detail of shear wall with shiplap siding

**Fig. 5.7 HS physical substructure for test structure B.**

### 5.4.3 Instrumentation

In addition to the internal displacement transducer in the actuator, the in-plane deformations of the two tested shear walls (north and south) are measured using two wire potentiometers fixed to the RRW on one end and the two shear walls on the other end (Fig. 5.6). The measurements serve as a check of the amount of torsion, if any, in the tested shear walls, which would be

manifested in the form of a differential deformation between the two rigidly connected shear walls. Four additional displacement transducers monitor the motion at the bases of the shear walls (north and south) to check if any sliding occurs and out-of-plane movements of the east and west ends (Fig. 5.6(a)). These measurements along with the load cells connected in series with the steel three vertical high-strength rods and the horizontal actuator are recorded using the data-acquisition system described in Section 3.6.

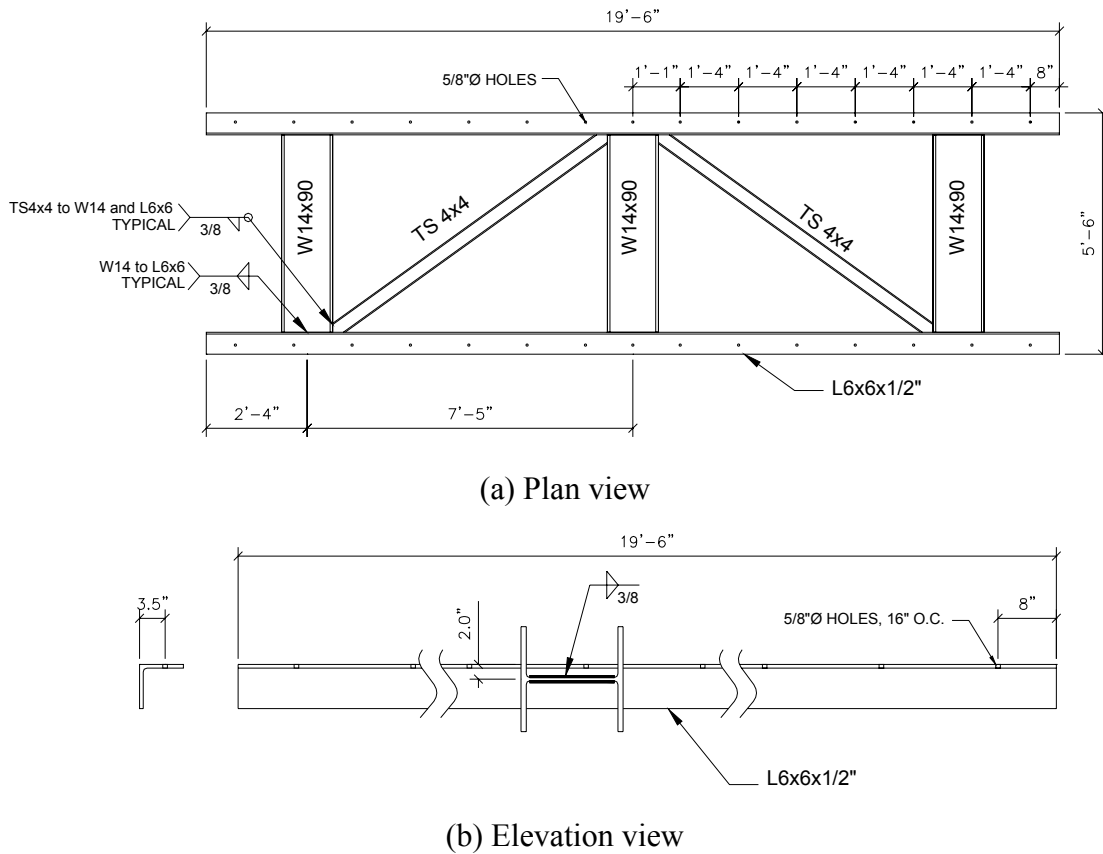


**Fig. 5.8 Loading frame for test structure B (1'=304.8 mm, 1''=25.4 mm).**

A cyclic preliminary test was conducted before the application of the strong motion sequence described later on identical shear walls to the ones being tested using HS with the purpose of assessing the test setup. Figure 5.10 shows the displacement signal applied on the shear walls with a maximum displacement of 10 in. (254 mm) in this cyclic preliminary test. In this figure, the deformation of the two shear walls are plotted and show almost no difference, implying that the test structure was not subjected to any torsional effects. The sliding time histories at the bases of the two shear walls are plotted in Figure 5.11, confirming practically

motionless bases. The out-of-plane measurements in Figure 5.12 record maximum out-of-plane drifts of 0.55% and 1.1% from potentiometers 1 and 2, respectively, Figure 5.6, compared to the 10% imposed in-plane drift. These drifts are estimated as the out-of-plane deformations normalized by the story height, i.e., 8' 6" (2590 mm) and are viewed as small deformations considering the long length of the shear wall of 19' 6" (5944 mm).

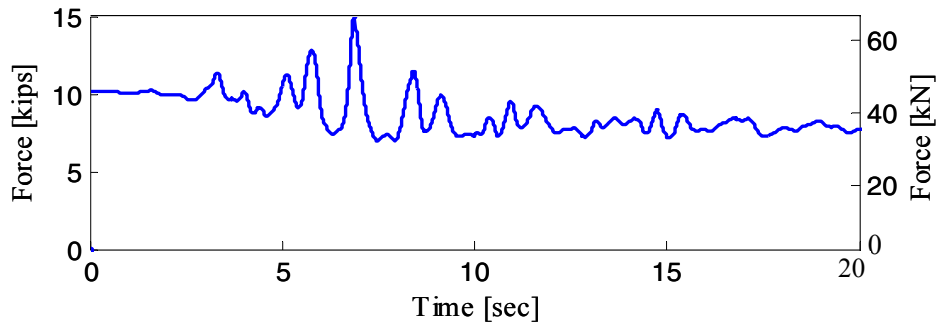


**Fig. 5.9 Vertical force variation in post-tensioned steel rods in LPG-6.**

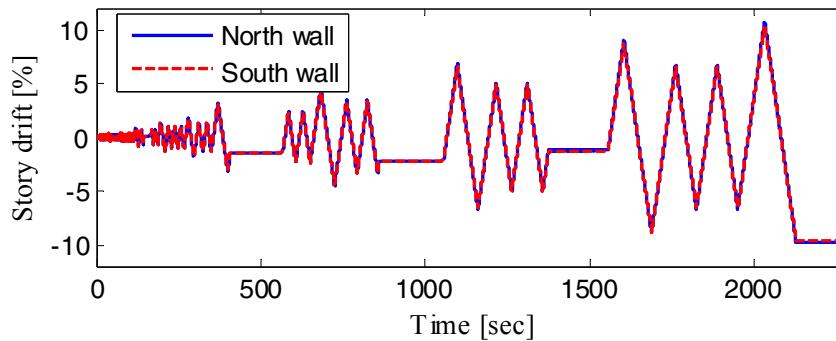


**Fig. 5.10 Displacement time history for preliminary test.**

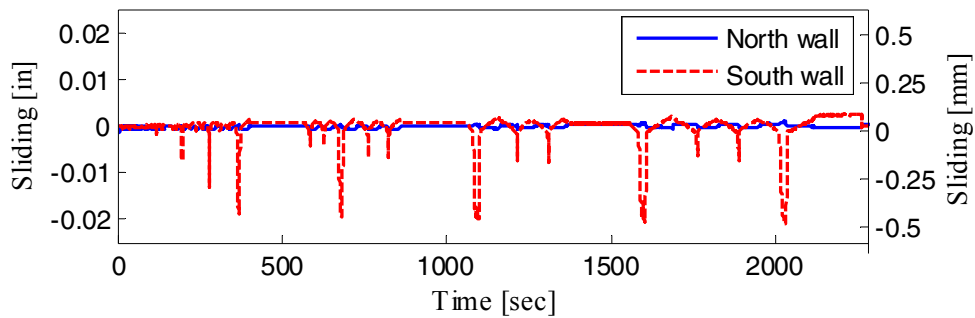


**Fig. 5.11 Sliding at bases of shear walls in preliminary test.**

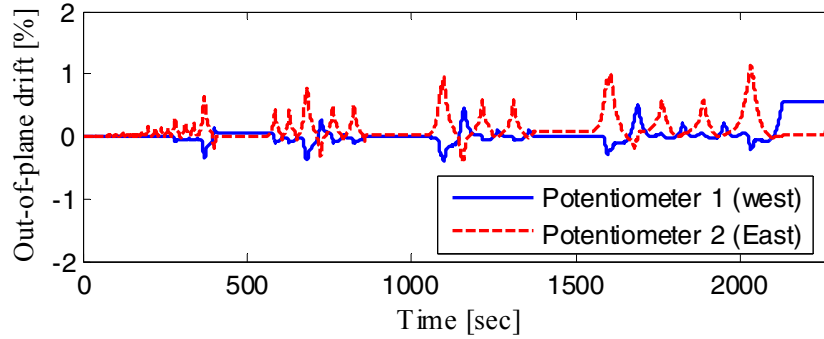


**Fig. 5.12 Out-of-plane drift of north shear wall in preliminary test.**

## 5.5 GOVERNING EQUATION OF MOTION AND PARAMETERS

As discussed in the previous section, the HS test structure is idealized as a SDOF system with the two north and south shear walls being the physical substructure. The equivalent inertial mass,  $m$ , is therefore taken as that of the entire building tested on the ST. Mass proportional damping is selected with damping ratio  $\zeta = 5\%$  to match the pull-back test results from the ST test structure. The initial stiffness  $k$  for the undamaged test structure and is estimated from preliminary low-level ST tests (Table 5.3). The equation of motion governing the dynamics of the test structure becomes,

$$m\ddot{u} + 2\zeta m\omega\dot{u} + ku = -m\ddot{u}_g \quad (5.1)$$

where  $u$ ,  $\dot{u}$ , and  $\ddot{u}$  are the displacement, velocity, and acceleration of the test structure, respectively, and  $\ddot{u}_g$  is the imposed ground acceleration. Based on the estimated parameters of the governing equation of motion, the natural frequency of the undamaged test structure is estimated as  $\omega = \sqrt{k/m}$  and the natural period is  $T = 2\pi/\omega$ . The integration time step adopted is  $\Delta t = 0.005$  sec, corresponding to the sampling frequency in the ST experiment where the motion was recorded. This selected  $\Delta t$  comfortably satisfies the stability and accuracy requirements for capturing the fundamental dynamic response.

**Table 5.3 Estimated parameters for HS of test structure B.**

Parameter	$m$ [kips-sec <sup>2</sup> /in. (kN-sec <sup>2</sup> /mm)]	$\zeta$ (%)	$k$ [kips/in. (kN/mm)]	$\omega$ (rad/sec)	$f$ (Hz)	$T$ (sec)	$\Delta t$ (sec)
Value	0.065 (0.011)	5.0	15 (2.6)	15.2	2.5	0.4	0.005

## 5.6 SUMMARY

A shaking table experiment is conducted on a full-scale two-story wood house over a garage typically characterized as a “soft” first story. The corresponding hybrid simulation test structure is idealized as a single-degree-of-freedom model where the two longitudinal first-story shear walls constitute the physical substructures and are tested with in-plane loading. The structural design of the shear walls is detailed, as well as their instrumentation. Key parameters in the governing equation of motion and the numerical-integration algorithm time step are also estimated.

## 6 New Advances in Hybrid Simulation

This chapter starts by presenting the numerical-integration algorithm in DC to provide the necessary background for discussing the newly developed advances in HS in this report. Two procedures are developed, namely (1) feed-forward error compensation in DC and (2) mixed-variables control (force/displacement) which requires the development of a new FC algorithm. A study of the developed algorithm and practical implementation strategies are also discussed.

### 6.1 INTEGRATION ALGORITHM IN DC

The integration algorithm solves the governing equations of motion in a step-by-step manner. In the present study, a variation of the implicit Newmark's method by Hilber et al. (1977), namely the  $\alpha$ -method, as presented by Shing et al. (1991), is used to solve the governing equations of motion. In addition, an operator-splitting scheme (Nakashima et al. 1990) is used, where the stiffness matrix is divided into numerical and experimental parts. While the numerical part may be solved implicitly, the experimental part is solved using an explicit predictor-corrector method, thus eliminating the need for an iterative procedure, which is not suitable for the experimental part. At any time step  $i + 1$ , the equations of motion are discretized into the form,

$$\mathbf{M}\ddot{\mathbf{u}}_{i+1} + (1 + \alpha)\mathbf{C}\dot{\mathbf{u}}_{i+1} - \alpha\mathbf{C}\dot{\mathbf{u}}_i + (1 + \alpha)\mathbf{R}_{i+1} - \alpha\mathbf{R}_i = (1 + \alpha)\mathbf{P}_{i+1} - \alpha\mathbf{P}_i \quad (6.1)$$

where  $\mathbf{P}_{i+1}$  is the excitation force acting on the numerical model of the structure,  $\mathbf{R}_{i+1}$  is the total restoring force of the structure, and  $\alpha$  is an integration parameter. Note that in the case of seismic excitation,

$$\mathbf{P} = -\mathbf{M}\mathbf{1}a_g \quad (6.2)$$

Variables in the above two equations have been defined in previous chapters when discussing the governing equations of motion of test structures A and B. Let us define  $\tilde{\mathbf{u}}$  and  $\mathbf{u}$  as the predictor and corrector displacements, respectively, such that:

$$\tilde{\mathbf{u}}_{i+1} = \mathbf{u}_i + \Delta t \dot{\mathbf{u}}_i + \Delta t^2(1/2 - \beta)\ddot{\mathbf{u}}_i \quad (6.3)$$

$$\tilde{\dot{\mathbf{u}}}_{i+1} = \dot{\mathbf{u}}_i + \Delta t(1 - \gamma)\ddot{\mathbf{u}}_i \quad (6.4)$$

where a dot above the variable indicates the time derivative of the variable and  $\beta$  and  $\gamma$  are specified parameters defined as follows:

$$\beta = (1 - \alpha)^2 / 4 \quad \text{and} \quad \gamma = 1/2 - \alpha \quad (6.5)$$

The relationships between the predictor and corrector displacements and velocities are defined as follows:

$$\mathbf{u}_{i+1} = \tilde{\mathbf{u}}_{i+1} + \Delta t^2 \beta \ddot{\mathbf{u}}_{i+1} \quad (6.6)$$

$$\dot{\mathbf{u}}_{i+1} = \tilde{\dot{\mathbf{u}}}_{i+1} + \Delta t \gamma \ddot{\mathbf{u}}_{i+1} \quad (6.7)$$

Using the operator-splitting scheme,

$$\mathbf{R}_{i+1} = \mathbf{R}_{i+1}^E + \mathbf{R}_{i+1}^N \quad (6.8)$$

$$\mathbf{R}_{i+1}^E = \tilde{\mathbf{R}}_{i+1}^E + \mathbf{K}^{EI} (\mathbf{u}_{i+1} - \tilde{\mathbf{u}}_{i+1}) \quad (6.9)$$

where  $\mathbf{R}_{i+1}^E$  and  $\mathbf{R}_{i+1}^N$  are the vectors of measured and numerically simulated restoring forces, respectively,  $\tilde{\mathbf{R}}_{i+1}^E$  is the vector of measured restoring forces from the test substructures subjected to the predicted displacements  $\tilde{\mathbf{u}}_{i+1}$ , and  $\mathbf{K}^{EI}$  is the initial stiffness of the experimental substructure. It follows that

$$\mathbf{R}_{i+1} = \tilde{\mathbf{R}}_{i+1}^E + \mathbf{K}^{EI} (\mathbf{u}_{i+1} - \tilde{\mathbf{u}}_{i+1}) + \mathbf{R}_{i+1}^N \quad (6.10)$$

Finally, the equations of motion can be formulated as the following equivalent problem:

$$\hat{\mathbf{M}} \ddot{\mathbf{u}}_{i+1} = \hat{\mathbf{P}}_{i+1} \quad (6.11)$$

$$\hat{\mathbf{M}} = \mathbf{M} + \Delta t(1 + \alpha)\gamma \mathbf{C} + \Delta t^2(1 + \alpha)\beta \mathbf{K}^{EI} \quad (6.12)$$

$$\begin{aligned} \hat{\mathbf{P}}_{i+1} = & (1 + \alpha)\mathbf{P}_{i+1} - \alpha\mathbf{P}_i - (1 + \alpha)\mathbf{C}\tilde{\dot{\mathbf{u}}}_{i+1} + \alpha\mathbf{C}\dot{\mathbf{u}}_i \\ & - (1 + \alpha)\tilde{\mathbf{R}}_{i+1} + \alpha\tilde{\mathbf{R}}_i + \alpha(\Delta t\gamma\mathbf{C} + \Delta t^2\beta\mathbf{K}^{EI})\ddot{\mathbf{u}}_i \end{aligned} \quad (6.13)$$

where  $\tilde{\mathbf{R}}_{i+1} = \tilde{\mathbf{R}}_{i+1}^E + \tilde{\mathbf{R}}_{i+1}^N$  and  $\tilde{\mathbf{R}}_{i+1}^N$  is the vector of numerically simulated restoring forces corresponding to the predicted displacements  $\tilde{\mathbf{u}}_{i+1}$ . In the case of  $\alpha = 0$ , no numerical damping is introduced and the method reduces to the average acceleration method, where  $\beta = 1/4$  and  $\gamma = 1/2$ , which is the adopted case in the experimental investigation in the present study. The implementation of the integration algorithm is shown in Figure 6.1. The equilibrium in this case is satisfied at the end of each integration time step by calculating the acceleration vector  $\ddot{\mathbf{u}}_{i+1}$  from Equation (6.11), after measuring  $\tilde{\mathbf{R}}_{i+1}$  and substituting in Equation (6.13). The corrected displacements  $\mathbf{u}_{i+1}$  from Equation (6.6) are used to calculate a corresponding  $\mathbf{R}_{i+1}^E$  using the assumed initial stiffness  $\mathbf{K}^{EI}$  for the experimental part from Equation (6.9) (without applying the load on the physical substructure) as well as a corrected  $\mathbf{R}_{i+1}^N$  using the model of the numerical substructures. Note that the predicted displacement  $\tilde{\mathbf{u}}_{i+2}$  applied in the following time step is calculated from Equation (6.3) using the corrected displacement  $\mathbf{u}_{i+1}$  from the preceding time step. Therefore, in the process of applying  $\tilde{\mathbf{u}}_{i+2}$  on the physical substructure, the substructure is subjected to the calculated corrected displacement  $\mathbf{u}_{i+1}$  before continuing to  $\tilde{\mathbf{u}}_{i+2}$ .

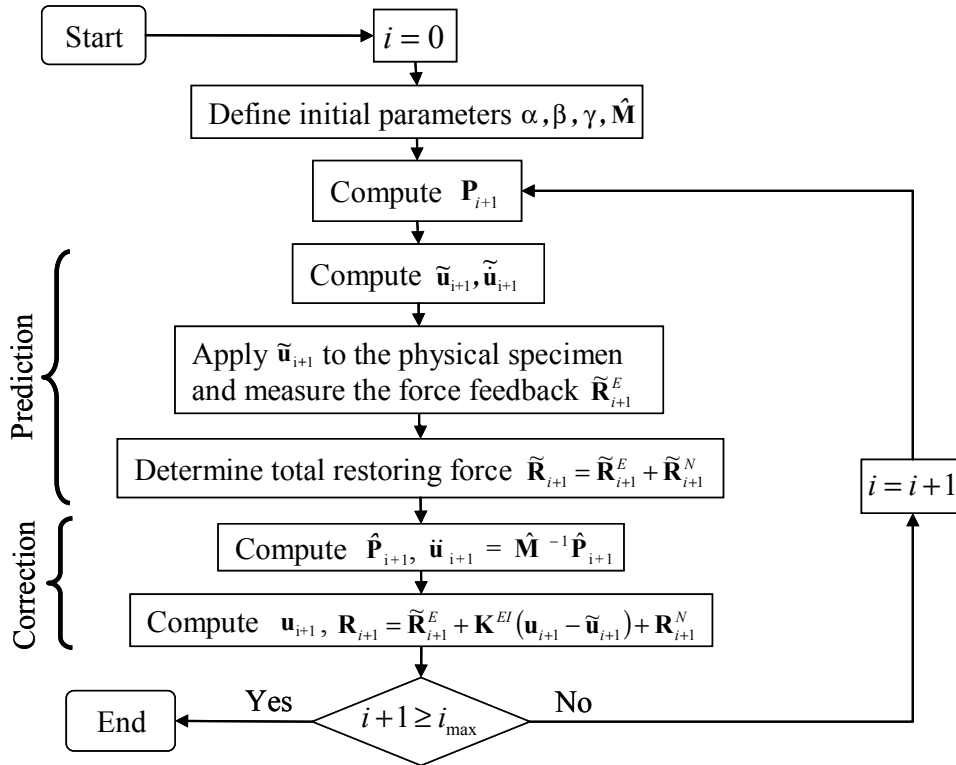


Fig. 6.1 Flowchart of DC algorithm.

The predictor-corrector approach may be implemented with higher accuracy if several iterations, rather than one as depicted in Figure 6.1, are performed. In this case, the corrected displacements  $\mathbf{u}_{i+1}^1$ , where the superscript refers to the iteration number, are applied and their corresponding restoring forces  $\mathbf{R}_{i+1}^1$  are estimated, measured for the physical substructures and computed for the numerical substructures, and used in Equation (6.13) instead of  $\tilde{\mathbf{R}}_{i+1}$  to calculate a more accurate corrected displacement vector  $\mathbf{u}_{i+1}^2$  from Equation (6.6). The process is then repeated until the difference between  $\mathbf{u}_{i+1}^j$  and  $\mathbf{u}_{i+1}^{j-1}$  satisfies a specified tolerance, i.e., adopting an implicit approach. However, the implementation of one iteration cycle for the physical substructure is reported to be accurate enough (Mosalam 1998; Nakashima 1990) for the purpose of HS with the added advantage of avoiding unrealistic loading and unloading iterative cycles on the physical substructures in an implicit approach.

## 6.2 FEED-FORWARD ERROR COMPENSATION IN DC

A feed-forward error prediction-correction scheme is applied to the actuators displacement command signals, with the aim of minimizing the experimental execution error. The employed error prediction method is closely linked to the rate of loading of the test structure.

### 6.2.1 Test Rate

The seismic motions, LPB level 6 (see Tables 4.1–4.2) and LPG level 5 (see Tables 5.1–5.2) are used to test structures A and B, respectively. These motions are applied to the respective test structures at different rates. The test rate  $TR$  is defined as the ratio of the execution time of one integration time step  $t_d$  to  $\Delta t$ ; e.g.,  $TR = 10$  indicates that the test is run ten times slower than real time. Note that in the case of both test structure A in phase P-1 and test structure B (see Fig. 1.2), the numerical-integration time step is chosen to be  $\Delta t = 0.005$  sec. The operator-splitting scheme (Nakashima et al. 1990) (see Section 6.1) is chosen as the numerical-integration algorithm for this part of the study. Several test rates ranging from 50 to 6.25 times slower than real time are applied on test structures A and B. Faster rates could not be executed without considerable hold periods. The monitored execution periods of the different operations within

one integration time step show that the total time needed for numerical integration, operations within Simulink, and signal transfer between Simulink and MATLAB are insignificant. However, the data transfer time through the Ethernet connection (see Fig. 3.2) between the host Simulink PC and xPC target ( $D_{i-1}$  to  $A_i$  and  $B_i$  to  $C_i$  in Fig. 3.11) is the limiting operation in the HS process. A minimum time of  $t_d \approx 0.02$  sec is therefore needed to execute one integration time step, which translates into a limiting  $TR \approx 4$  in the case of  $\Delta t = 0.005$  sec. A by-pass to the Ethernet connection between the host Simulink PC and xPC target is possible if the tasks executed in the MATLAB environment are instead implemented in the Simulink model. This approach would eliminate the time limitation by increasing the communication speed and allowing the used HSS within *nees@berkeley* to achieve faster test rates (Schellenberg et al. 2007). In this study, since developing real-time HS is not set as one of the sought objectives and to allow efficient and detailed monitoring of the HS during the development of the algorithms for the two procedures discussed in this chapter, the HSS is used with the architecture illustrated in Figure 3.2 and as previously described.

### 6.2.2 Error Prediction

The execution error of the displacement command is measured in all runs and is defined for time step  $i$  as follows:

$$Er_i^{cc} = \frac{d_i^c - d_i^m}{d^{\max}} \quad (6.14)$$

where  $d_i^c$  is the command displacement,  $d_i^m$  is the measured feedback displacement, and  $Er_i^{cc}$  is the calculated error in  $d_i^c$  when  $d_i^c$  is applied. This error is arbitrarily normalized for simplicity by the maximum actuator stroke  $d^{\max} = 10$  in. (254 mm). The actuator velocity  $v_i^{Act}$  is calculated, throughout the entire test, for an assumed constant value of  $t_d$  as follows:

$$v_i^{Act} = \frac{d_i^c - d_{i-1}^c}{t_d} \quad (6.15)$$

The assumption of a constant  $t_d$  is valid if the prescribed rate is within reach of the HSS, i.e., 4 times slower than real time or larger in the present study. As an example, Figure 6.2 shows the relationship between  $Er^{cc}$  in percentage and  $v^{Act}$  for test structure B.

At high actuator velocities, linear correlations between the error and the actuator velocity as defined above are obtained for both test structures A and B using the least-squares method. For both test structures, this least-squares method resulted in the so-called “hockey-stick” model. A generic relationship, that is valid for all considered test rates, can be represented by,

$$\begin{aligned} Er_i^{cc} &= 0 & |v_i^{Act}| &\leq a \\ Er_i^{cc} &= \text{sign}(v_i^{Act}) \times b (|v_i^{Act}| - a) & |v_i^{Act}| &> a \end{aligned} \quad (6.16)$$

where  $a$  and  $b$  are two positive calibration parameters. It is to be noted that the error carries the same sign as the actuator velocity, implying that the measured displacement feedback is lagging behind the displacement command. Moreover, the value of the parameter  $a$  is the threshold of the actuator velocity after which the systematic error, defined above, occurs. The error remainder, i.e., the difference between the recorded and predicted values in Figure 6.2 is plotted versus the actuator velocity in Figure 6.3. The randomness of the error remainder confirms the goodness of fit of the model in Equation (6.16) and the relatively small values of this error remainder confirm the effectiveness of the model in capturing a large portion of the recorded error.

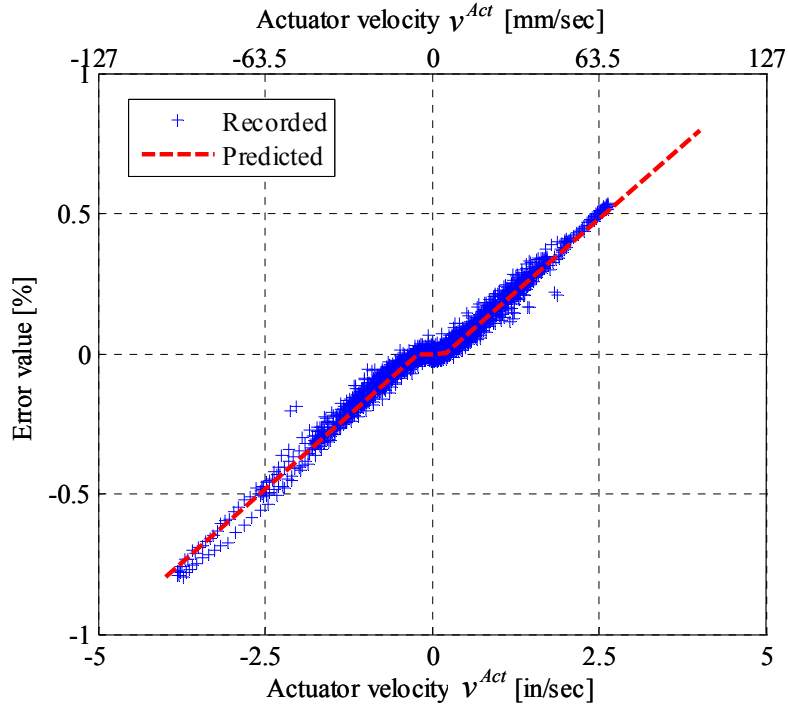


**Fig. 6.2 Correlation relationship between error  $Er_i^{cc}$  and actuator velocity for test structure B.**

### 6.2.3 Feed-Forward Error Compensation

Based on the above error relationship with the actuator velocity after calibrating its parameters, and noting that  $v_i^{Act}$  can be calculated before applying  $d_i^c$ , an error compensation scheme is devised to eliminate the predicted error. This error compensation is based on adding the predicted error to the command signal to obtain an adjusted command signal. Subsequently, this adjusted command signal  $d_i^a$  is sent to the actuator in lieu of  $d_i^c$ , where

$$\begin{aligned}
 d_i^a &= d_i^c & |v_i^{Act}| &\leq a \\
 d_i^a &= \frac{d_i^c - b d^{\max} \left[ \left( \frac{d_{i-1}^a}{t_d} \right) + \text{sign}(v_i^{Act}) \times a \right]}{1 - \left( b d^{\max} / t_d \right)} & |v_i^{Act}| &> a
 \end{aligned} \tag{6.17}$$

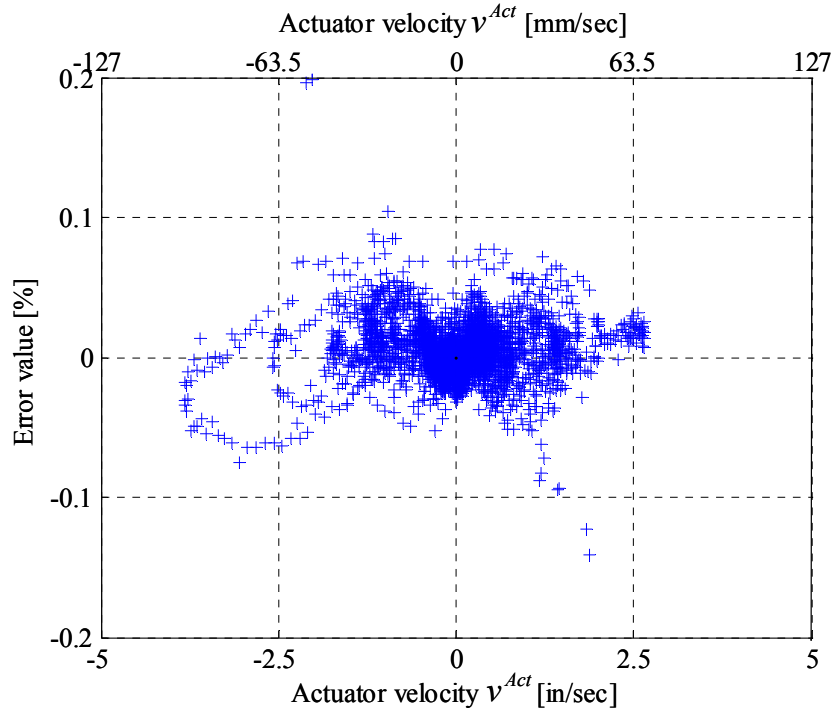


**Fig. 6.3 Error remainder (difference between recorded and predicted error values) for test structure B.**

This modified command signal aims at the execution of the desired command  $d_i^c$  with a much smaller error  $Er_i^{ca}$  than  $Er_i^{aa}$ , where  $Er_i^{ca}$  is the error in  $d_i^c$  when  $d_i^a$  is applied and  $Er_i^{aa}$  is the error in  $d_i^a$  when  $d_i^a$  is applied analogous to  $Er_i^{cc}$  when error compensation is not accounted for. An online estimation procedure of the parameters  $a$  and  $b$  may be developed by continuously updating the estimates of these parameters during the HS run as the test progresses. These estimates may be based on an adequate number, to be defined according to the nature of each HS experiment, of the most recently implemented integration time steps, analogous to the practical approach in estimating the secant stiffness in FC that is discussed later in Section 6.5.1. Such a procedure would allow the error prediction and compensation to be implemented during the same test run thus eliminating the impractical need for a separate run for the purpose of calibration of the error prediction model and would also make the procedure suitable for situations where these calibration parameters may change during testing. This is an important endeavor to be pursued in future enhancements of the develop HSS. The implementation and test results, validating the developed procedure of the feed-forward error compensation within the HSS on test structures A and B, are presented in Chapter 7.

### 6.3 MIXED-VARIABLES CONTROL IN HS

While almost all available numerical-integration algorithms implemented in HS solve the governing equations of motion to yield displacement commands, the idea of solving for force instead of displacement and conducting the test in FC is an attractive one when considering stiff structural systems (Thewalt and Mahin 1987). From a computational point of view, analysis based on a displacement method for structures incorporating flexible and stiff structural elements may suffer from ill-conditioning of the governing equilibrium equations. Physical modeling of multiple components (substructures) in a hybrid structural system with different stiffness properties faces the same difficulties in the conventional pseudo-dynamic testing, with the added effect of the associated experimental errors. If run in DC, the displacement command values applied on such systems with high stiffness states would be very small compared to the resolution of the measuring devices and experimental errors that threaten the accuracy and stability of the involved numerical integration in the HS. On the other hand, for a certain value of displacement increment at a given time step, the corresponding restoring-force increment from such stiff systems is considerably large. Therefore, from the control point of view, these force increments are more accurate to implement and control than their corresponding small displacement increments.

It is plausible to envision a situation that requires the use of both control methods, i.e., the conventional DC and a newly developed FC. For example, in testing systems with bilinear stiffening behavior, DC may be employed in the flexible state (lower stiffness) and FC in the stiff state (higher stiffness). In the case of a hybrid structural system, where some substructures exhibit stiff behavior, while the other substructures exhibit flexible behavior, a mixed-variables formulation is needed. The governing equations of motion are solved for displacement for the DOF representing the flexible substructures and solved for force for the DOF representing the stiff substructures. This leads to a set of mixed variables (forces and displacements) that can be applied on the respective substructures. The use of mixed-variables “diakoptics” (Kron 1963 and Wiberg 1974) may alleviate some of the difficulties encountered in testing such hybrid systems by minimizing the experimental errors and the ill-conditioning of the governing equilibrium equations. The procedure presented in this chapter offers the possibility of conducting the online test in any of the two control modes, force or displacement, and switching back and forth between these modes based on the variation of the state of the DOF in question.

### 6.3.1 FC Integration Algorithm

An integration algorithm with a mixed formulation between force and displacement is formulated departing from the implicit  $\alpha$ -method. First, the implicit FC algorithm is derived. Second, variation is made to obtain the mixed formulation algorithm. Starting from the equations of motion defined by Equations (6.1)–(6.7), the following equivalent problem can be formulated,

$$\mathbf{K}^* \mathbf{u}_{i+1}^j + (1 + \alpha) \mathbf{R}_{i+1}^j = \mathbf{P}_{i+1}^* \quad (6.18)$$

where  $\mathbf{K}^*$  and  $\mathbf{P}_{i+1}^*$  are defined as follows:

$$\mathbf{K}^* = \frac{\mathbf{M}}{\Delta t^2 \beta} + \frac{(1 + \alpha) \gamma \mathbf{C}}{\Delta t \beta} \quad (6.19)$$

$$\mathbf{P}_{i+1}^* = (1 + \alpha) \mathbf{P}_{i+1} - \alpha \mathbf{P}_i - (1 + \alpha) \mathbf{C} \tilde{\mathbf{u}}_{i+1} + \alpha \mathbf{C} \dot{\mathbf{u}}_i + \mathbf{K}^* \tilde{\mathbf{u}}_{i+1} + \alpha \mathbf{R}_i \quad (6.20)$$

Considering an iterative solution based on an implicit numerical-integration algorithm, the displacement at integration time step  $i + 1$  and iteration  $j$  is stated as follows:

$$\mathbf{u}_{i+1}^j = \mathbf{u}_i + \Delta \mathbf{u}_{i+1}^j = \mathbf{u}_i + [\mathbf{K}_{i+1}^j]^{-1} (\mathbf{R}_{i+1}^j - \mathbf{R}_i) \quad (6.21)$$

where  $\mathbf{K}_{i+1}^j$  is the estimated secant stiffness matrix at integration time step  $i + 1$  and iteration  $j$ , with  $\mathbf{K}_{i+1}^1 = \mathbf{K}_i^{last}$  where  $\mathbf{K}_i^{last}$  is the estimate of the secant stiffness in the previous ( $i^{\text{th}}$ ) time step at the last iteration. This estimation is iteratively acquired such that the secant stiffness  $\mathbf{k}_{i+1}^j$  for every degree of freedom is expressed as follows:

$$\mathbf{k}_{i+1}^j = (\mathbf{R}_{i+1}^{j-1} - \mathbf{R}_i) / (\mathbf{u}_{i+1}^{j-1} - \mathbf{u}_i) \quad (6.22)$$

The individual stiffness terms for all DOF are then assembled in the stiffness matrix  $\mathbf{K}_{i+1}^j$ . Note that Equation (6.22) is valid only for physical substructures with a diagonal stiffness matrix, i.e., systems that may be represented as in parts (A) or (C) in Figure 6.4, where the linking springs  $k_{C_i}$ ,  $i = 1, 2, \dots$  in part (C) are numerically simulated, similar to test structure A. For systems as in part (B) of Figure 6.4, the computation of the stiffness matrix is possible, making use of Equation (6.22), but involves solving simultaneous equations. Systems as in part (D), where the linking springs  $k_{P_i}$ ,  $i = 1, 2, \dots$  are modeled physically, are not suited for

estimating the stiffness matrix using the simple approach expressed in the above equation (Eq. 6.22) and are out of the scope of this study.

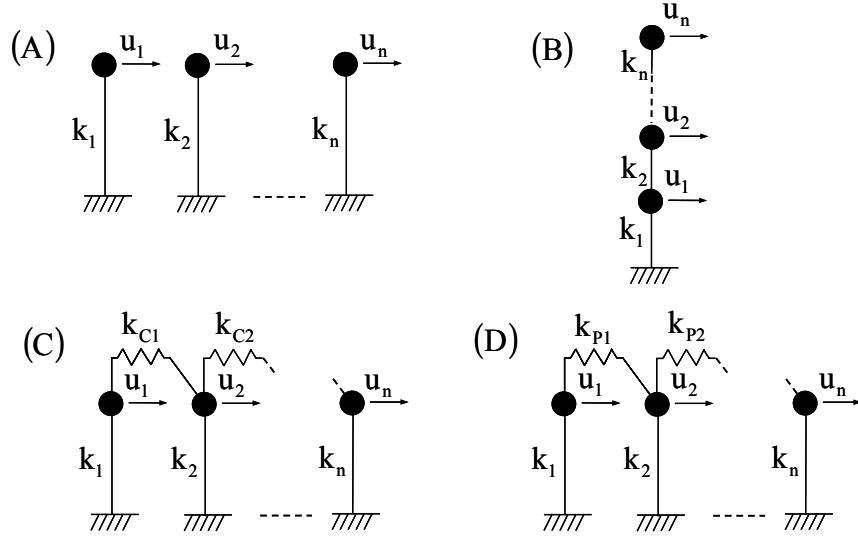


**Fig. 6.4 Different lumped spring–mass systems.**

Rewriting Equation (6.18) using Equation (6.21) one obtains

$$\left\{ \mathbf{K}^* [\mathbf{K}_{i+1}^j]^{-1} + (1 + \alpha) \mathbf{I} \right\} \mathbf{R}_{i+1}^j = \mathbf{P}_{i+1}^* + \mathbf{K}^* [\mathbf{K}_{i+1}^j]^{-1} \mathbf{R}_i - \mathbf{K}^* \mathbf{u}_i \quad (6.23)$$

where  $\mathbf{I}$  is the identity matrix. From Equation (6.23), the restoring-force vector is obtained and applied to the test structure under FC. The above algorithm is illustrated in Figure 6.5 where  $i_{\max}$  and  $j_{\max}$  are the maximum number of time steps and iterations, respectively, and other parameters are previously defined in Section 6.1 and Equations (6.18)–(6.23). The stiffness matrix is updated at the end of each iteration within the integration time step using the last acquired values of restoring forces  $\mathbf{R}$  and displacements  $\mathbf{u}$  and assembled as discussed earlier with reference to Figure 6.4. The estimation of the components of the stiffness matrix corresponding to the physical substructures is discussed in details in Section 6.5.1. The tolerance to be checked for convergence of the iterative solution  $\varepsilon_R$  is expressed in terms of the change of the restoring force, i.e., the condition for convergence is that for each degree of freedom  $|\mathbf{R}_{i+1}^{j+1} - \mathbf{R}_{i+1}^j| \leq \varepsilon_R$ , where  $\varepsilon_R$  is determined based on the resolution of the load cells connected to the actuators. The higher the number of implemented iterations, the better the chance of satisfying the convergence tolerance  $\varepsilon_R$ . However, a maximum allowed number of iterations

$j_{\max}$  is specified for practical reasons and to prevent the HS system from iterating within the same numerical-integration time step indefinitely. Note that a practical iterative procedure is developed in Section 6.5.3 to avoid subjecting the physical substructure to unrealistic loading/unloading cycles that might be dictated by the implicit FC integration algorithm.

### 6.3.2 Extension to Mixed-Variables Control

The same integration algorithm in FC can be extended to mixed variables by allocating flexible DOF to DC and stiff DOF to FC and proceeding as shown in Figure 6.6. Notice that the DC integration algorithm implemented in the flowchart is the implicit  $\alpha$ -method as presented by Shing et al. (1991). The stiffness matrix is updated at the end of each iteration within the integration time step for the whole test structure using the same approach discussed in Section 6.3.1. The implicit approach in both DC and FC ensures that equilibrium is satisfied for the whole test structure, i.e., physical and numerical substructures in DC as well as physical substructures in FC, at the end of each integration time step. Equilibrium in this case is represented by Equation (6.23) and is satisfied within acceptable accuracy once the difference between  $\mathbf{R}_{i+1}^{j+2}$  and  $\mathbf{R}_{i+1}^{j+1}$  is less than the specified tolerance  $\varepsilon_R$ .

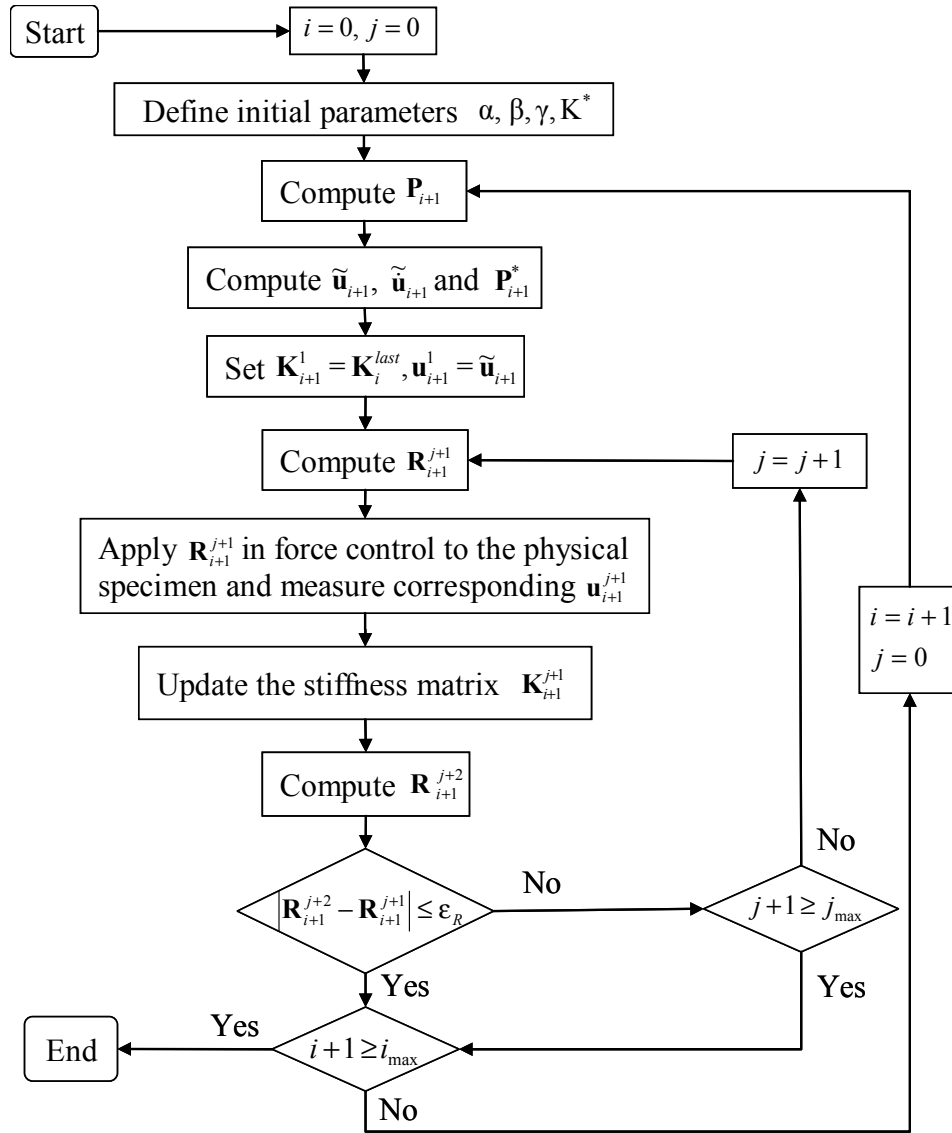


**Fig. 6.5 Flowchart of FC algorithm.**

The target displacements and forces as well as the estimated secant stiffness are computed for all DOF of the test structure (whether selected for DC or FC) along the entire duration of the HS experiment. These computed quantities or their derivatives, e.g., velocities, can be used as a criterion for switching between DC and FC for some DOF. Indeed, switching between DC and FC for the same physical substructure is a useful approach in the case of a substructure exhibiting nonlinear hybrid flexible/stiff behavior.

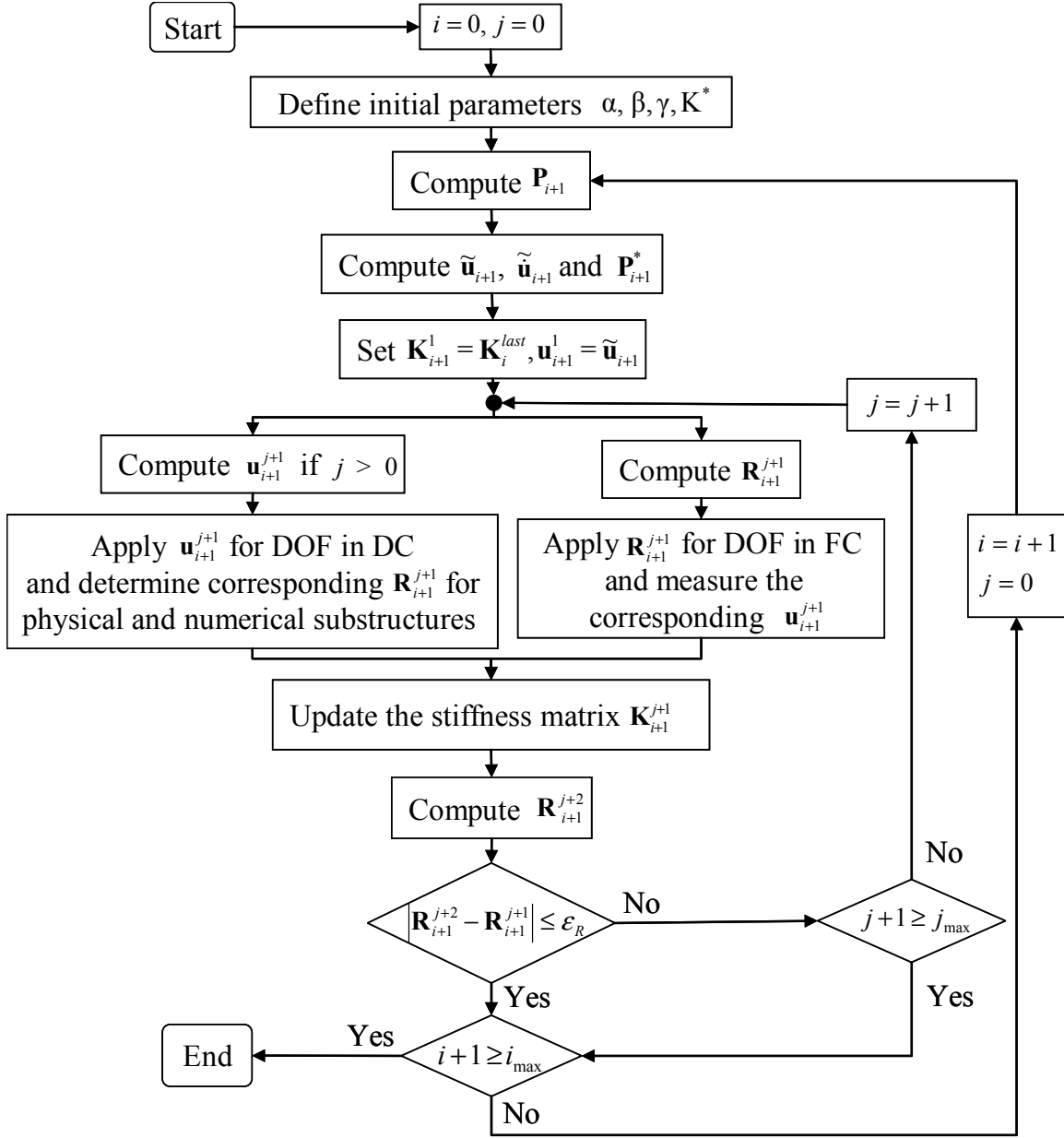


**Fig. 6.6 Flowchart for integration algorithm with mixed-variables control without mode switch (DC for flexible DOF and FC for stiff DOF).**

The flowchart in Figure 6.7 illustrates the implementation of the integration algorithm with mode switch between DC and FC for a SDOF system, where  $l_{\max}$  and  $j_{\max}$  are the maximum number of iterations in DC and FC, respectively. Note that the DC numerical-integration algorithm in Figure 6.7 is chosen as the  $\alpha$ -method with an operator-splitting scheme with multiple iterations within the time step, as described in Section 6.1, where the difference between  $\mathbf{u}_{i+1}^{l+2}$  and  $\mathbf{u}_{i+1}^{l+1}$  needs to satisfy a prescribed tolerance  $\varepsilon_u$ , analogous to  $\varepsilon_R$  in FC.

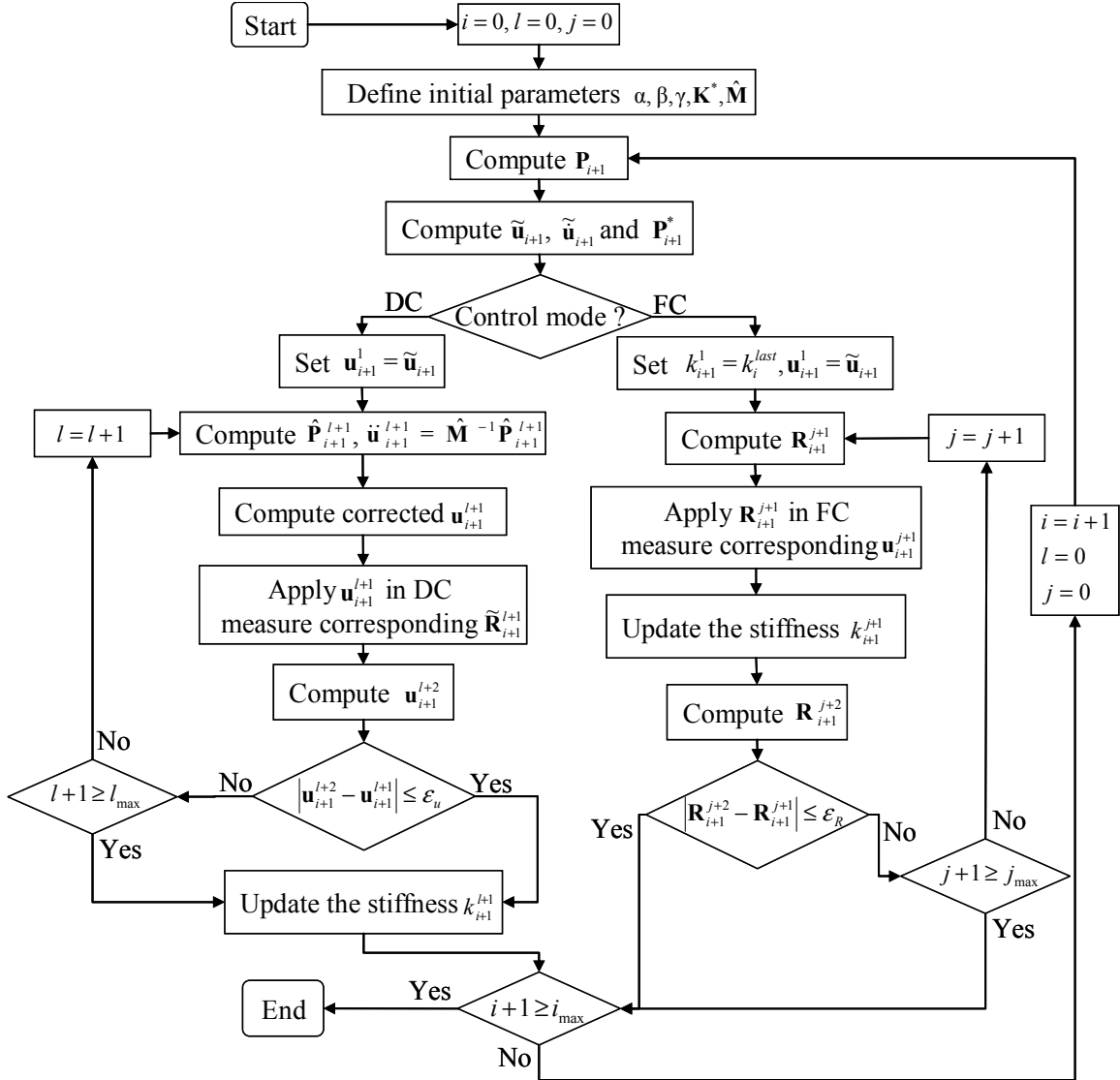


**Fig. 6.7 Flowchart for integration algorithm with mode switch between DC and FC for SDOF system.**

However, other DC numerical-integration algorithms may be used as long as equilibrium is satisfied at the end of each integration time step, as discussed in Section 6.1 for the selected DC integration algorithm. The stiffness matrix is updated at the end of each iteration within the integration time step for the whole test structure using the same approach discussed in Section 6.3.1, and the decision to switch between the two control modes is discussed in details in Section 6.5.2. Note that selecting DOF for pure DC and others for DC with the possibility of switching to FC and back, according to the state of the test structure, is possible by using the algorithm shown in Figure 6.6 and adopting for each degree of freedom, having the possibility of mode switch, the algorithm shown in Figure 6.7.

## 6.4 NUMERICAL EVALUATION OF FC ALGORITHM

To evaluate the performance of the formulated implicit FC algorithm, a numerical parametric study is conducted. For linear systems, the FC algorithm is equivalent to the corresponding DC algorithm ( $\alpha$ -method as presented by Shing et al. (1991)), thus it has the same characteristics such as period distortion and numerical damping effects. This parametric study aims to evaluate the ability of the FC algorithm, in the case of nonlinear systems, to detect the correct stiffness value through the proposed iterative solution and to converge to the “exact” solution. Two  $\alpha$ -values ( $\alpha = 0$  and  $\alpha = -0.3$ ) are adopted in this study, spanning the recommended range of this integration parameter and presenting two different cases of artificial numerical damping. For  $\alpha = 0$ , no numerical damping is introduced and the algorithm reduces to the average acceleration method with  $\beta = 1/4$  and  $\gamma = 1/2$ .

A constant impulse force (Fig. 6.8(a)), is applied to the considered system and the response is evaluated using both the well-known implicit DC  $\alpha$ -method algorithm as presented in Shing et al. (1991) and the developed implicit FC algorithm (see Section 6.3.1). For this purpose, undamped ( $\zeta = 0\%$ ) and damped ( $\zeta = 5\%$ ) SDOF nonlinear elastic systems (Fig. 6.8(b)), with unit mass and unit initial natural period are considered. The considered force-displacement relationship is based on the following nonlinear elastic Menegotto-Pinto model (Menegotto and Pinto 1973):

$$R = \theta u + \frac{(1 - \theta)u}{(1 + |u|^n)^{1/n}} \quad (6.24)$$

where  $\theta$  is the ratio of the secondary stiffness ( $k_s$ ) to initial stiffness ( $k_l$ ) and the parameter  $n$  controls the sharpness of the transition between these two stiffness values. In this study,  $n = 1$  and  $\theta$  is varied through a large range from 0.2 to 5.0 to capture both softening ( $\theta < 1$ ) and stiffening ( $\theta > 1$ ) behaviors. In Figure 6.9, two examples of the response for  $\theta = 0.2$  and  $\theta = 5.0$  are presented to demonstrate the range of the numerical parametric study spanning both softening and stiffening responses.

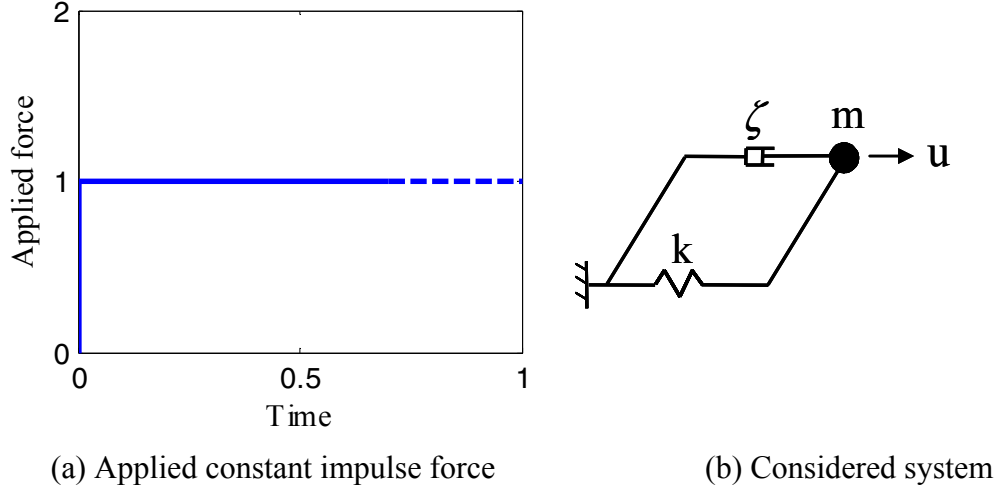


**Fig. 6.8 Applied force and considered system for numerical evaluation of FC algorithm.**

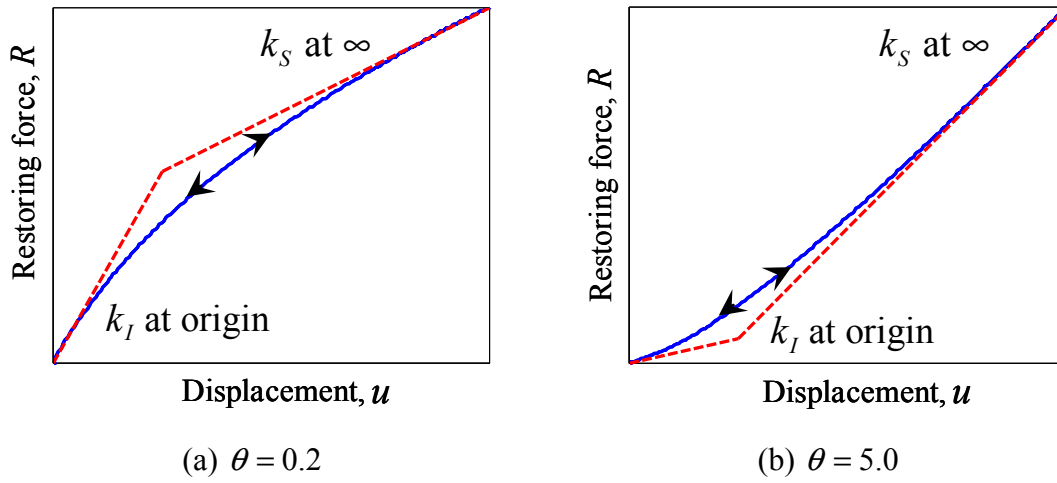


**Fig. 6.9 Nonlinear elastic response using Menegotto-Pinto model ( $\theta = k_s/k_l$ ).**

To evaluate the deviation of the numerical solution from the exact solution, the following error quantity is defined for the considered cases,

$$Er^{Alg} [\%] = \frac{\sum_i |S_i^{Alg} - S_i^{Exact}|}{\sum_i |S_i^{Exact}|} \times 100 \quad (6.25)$$

where  $S_i = S_{i-1} + (R_i + R_{i-1}) \times (u_i + u_{i-1})/2$  is the strain energy at time step  $i$ , and  $R_i$  and  $u_i$  are the restoring force and displacement at time step  $i$ , respectively. The superscripts *Alg* and *Exact* refer to the response of the algorithm in question and the exact response, respectively. This exact

response is the converged solution obtained using the implicit average acceleration method with a very small integration time step, namely  $\Delta t = 2 \times 10^{-5}$  sec. The secant stiffness is calculated numerically as in Equation (6.22), the convergence tolerances for displacement and force are  $\varepsilon_u = \varepsilon_R = 10^{-10}$ , respectively, with a maximum of 10 iterations, where  $\varepsilon_R$  and  $\varepsilon_u$  are defined in Section 6.3.1 and 6.3.2, respectively. Eight cases are studied (Table 6.1) for each of the two integration algorithms resulting from the eight possible different combinations of the three varied parameters,  $\alpha$ ,  $\zeta$ , and  $\Delta t$ . Figure 6.10 shows two identical curves (solid for FC and dashed for DC), for each of the eight studied cases, designating the calculated responses using the implicit FC method and the DC method, thus confirming the ability of the new FC algorithm to produce as accurate a solution as the DC algorithm. Note that the estimated error values increase with the increase of  $\theta$ , plotted on the x-axis in a logarithmic scale, due to the decrease of the natural period of the studied system, while the integration time step  $\Delta t$  is kept constant. For a smaller  $\Delta t$  for the same considered system, the error significantly decreases as expected. The level of variation in the estimated error is much higher in the case of  $\Delta t = 0.02$  sec, implying that the ratio  $T/\Delta t$  reaches levels where the accuracy of the numerical-integration algorithm is affected significantly, when compared to the case of  $\Delta t = 0.005$  sec.

**Table 6.1 Varied parameters for numerical evaluation of FC algorithm.**

Integration parameter	Damping ratio	Integration time step
$\alpha = 0$	$\zeta = 0\%$	$\Delta t = 0.02$ sec
$\alpha = -0.3$	$\zeta = 5\%$	$\Delta t = 0.005$ sec

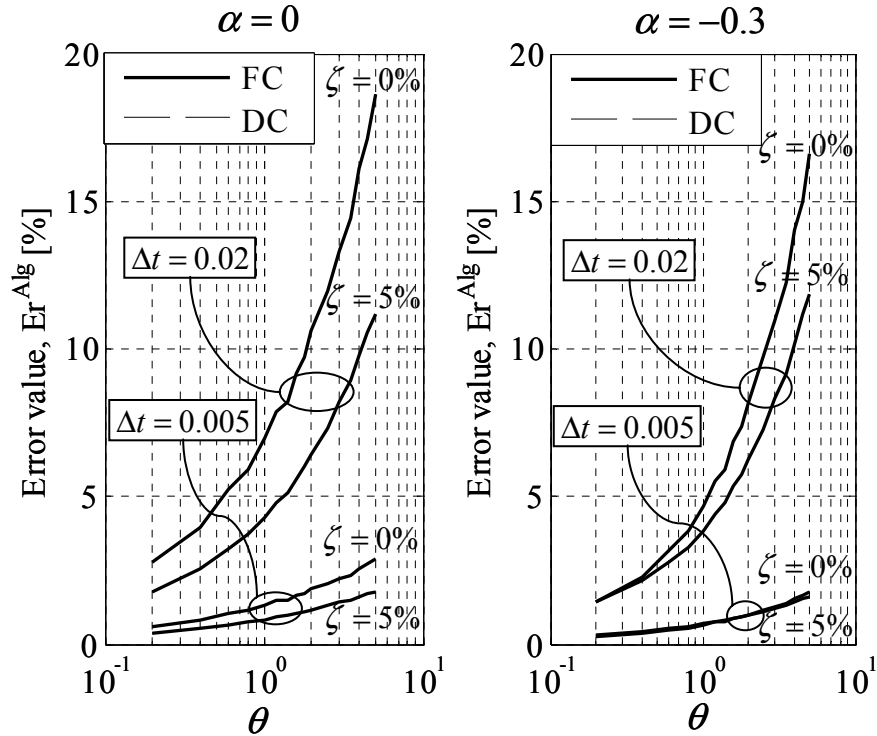


**Fig. 6.10 Parametric study of FC and DC algorithms using nonlinear elastic SDOF systems.**

## 6.5 IMPLEMENTATION STRATEGIES OF MIXED-VARIABLES CONTROL

The different operations and strategies needed for the implementation of the mixed-variables HS procedure are presented in this section. This includes the procedure of stiffness estimation, criteria, and decisions on control mode switching between force and displacement and a practical iterative approach to avoid unrealistic loading and unloading cycles.

### 6.5.1 Secant Stiffness Estimation

The developed FC algorithm relies on the estimation of the secant stiffness during the HS experiment at the end of each iteration within the integration time step. The most direct way of estimating the stiffness is by using the displacement and force feedback signals at the end of each iteration using Equation (6.22). However, the resolutions of the measuring sensors for force and displacement in addition to the random noise associated with the feedback signals can

considerably affect this estimation. A procedure is therefore developed to minimize these effects and to obtain an improved accuracy in estimating the secant stiffness. Noting that the feedback signals are available at a very high frequency in the xPC target (1024 Hz) through ScramNet (see Section 3.3), average values over the last  $N^{Avg}$  feedbacks in one iteration within the time step for each of the quantities in Equation (6.22) are used instead, e.g., in the application example discussed in Chapter 7 with  $t_d = 2\text{sec}$ ,  $TR = 400$ , and  $\Delta t = 0.005\text{ sec}$ ,  $N^{Avg}$  is taken as 100 out of  $1024t_d = 2048$  points, i.e., by averaging the last 5% of the available feedbacks in one iteration within the time step. Subsequently, the averaged signals are passed to the numerical-integration algorithm in the MATLAB environment to calculate an average stiffness  $(k_i^{j+1})^{Avg}$  for each degree of freedom (Fig. 6.11). These average stiffness are subsequently assembled into the stiffness matrix  $(\mathbf{K}_i^{j+1})^{Avg}$  with the limitations discussed in reference to Figure 6.4. Figure 6.12 shows a more reliable  $(\mathbf{K}_{i+1})^{Avg}$  when compared to  $\mathbf{K}_{i+1}$ , using the displacement and force feedback signals at the end of each iteration, for a representative HS of test structure B. Although yielding similar values in most of the shown plot, where the restoring force  $R$  and the displacement increments become smaller at the peaks of a loading cycle, an unrealistic large negative stiffness  $K$  is estimated, while  $K^{Avg}$  does not suffer from this anomalous fluctuation. Note that for faster rates, where the time-step duration decreases and the available number of feedback signals in the xPC target within one iteration decreases, if  $N^{Avg}$  needs to be reduced to the point where the averaging effect would be lost, other techniques may be implemented such as the least-squares method to evaluate a linear secant stiffness over the whole integration time step.

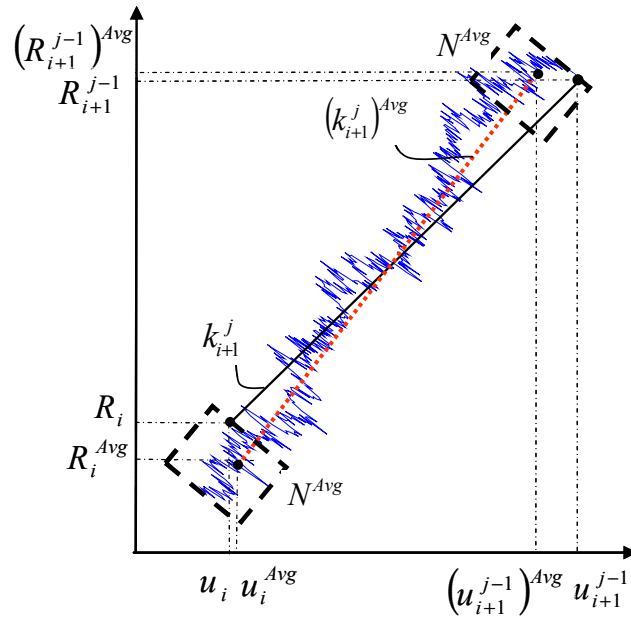


**Fig. 6.11** Schematic representation of secant stiffness estimation at time step  $i+1$  and iteration  $j$ .

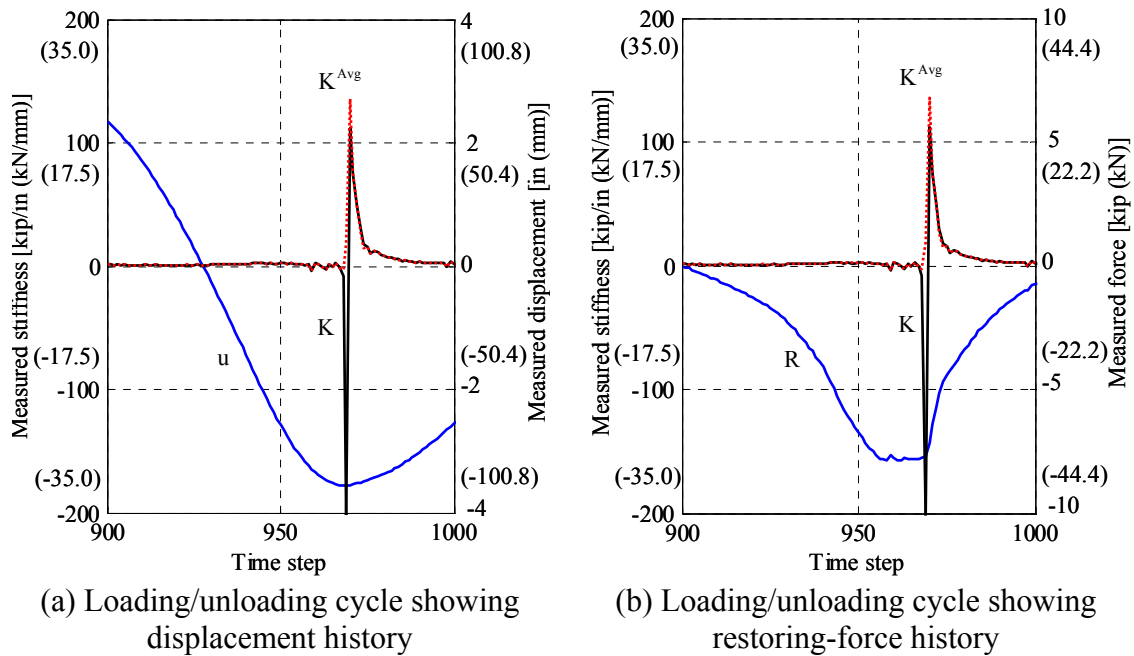


**Fig. 6.12** Example results from test structure B for estimation of secant stiffness.

## 6.5.2 Mode-Switch Decision Implementation

There are constraints on the use of FC, which are different in nature than in DC. For instance, if the substructure approaches its ultimate load-carrying capacity during the HS experiment, the force command may exceed that capacity and the control system may drive the test structure to failure. Therefore, switching criteria are needed to carefully decide on the control mode, in which any integration time step  $i$  will be executed, for the DOF in question. These criteria are adopted based on the knowledge of the behavior of the test structure, such as applying tension or compression load as in Pan (2004) and Pan et al. (2005). Both DC and FC integration algorithms are performed in parallel during the full time history, as described in Section 6.3.2, and at the end of each time step, a decision is made whether to stay in the current control mode (e.g., DC) or to switch to the other control mode (e.g., FC). Figure 6.12 shows the decision-making scheme implemented using as an example two criteria for switching, namely the secant stiffness  $K$  and the restoring force  $R$  with estimated values  $K_i$  and  $R_i$  at the  $i$ -th time step, respectively. Two threshold values are needed for each switching criterion, e.g.,  $K_d$  and  $K_f$  for  $K$ , where  $K_d < K_f$ . This provides a buffer zone to avoid switching back and forth between the two control modes in the case where the measured  $K^{Avg}$  fluctuates slightly in the range of these threshold values. The threshold values are determined based on the expected fluctuations of the estimated quantity they are being compared to, e.g., a minimum difference between  $K_d$  and  $K_f$  would be the resolution at which  $K^{Avg}$  is estimated, plus a certain margin of fluctuation. In the present study, this margin was estimated by monitoring  $K^{Avg}$  in the regions where mode switching is expected to take place from past experiences. An example for the evaluation of these thresholds in the case of test structure B is discussed in Chapter 7.

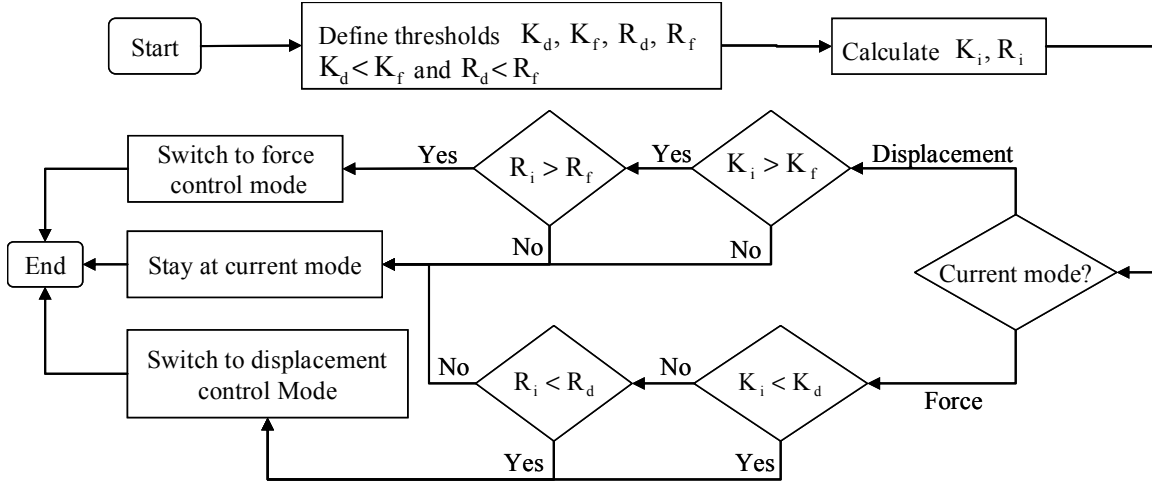


**Fig. 6.13 Mode-switch decision-making scheme.**

Once the decision is made to switch between control modes, the STS controller needs to switch to that mode and to execute the corresponding command signal. In the present study, this is accomplished by having the control mode as an additional Boolean command conveyed by Simulink to STS along with the displacement and force command signals (see Fig. 3.2). This feature was incorporated into the HSS to accommodate the possibility of conducting HS experiments with control mode switch<sup>1</sup>. It is worth mentioning that the extrapolation/interpolation implementation strategy is not suitable for an implicit algorithm where iterations are required as discussed in Section 3.5. This feature is therefore turned off when the implicit mixed-variables algorithm with mode-switching capabilities is invoked and a linear interpolation, from the current state to the new command, is implemented instead.

At the end of the integration time step  $i$ , if mode switch is decided to take place in step  $i+1$ , e.g., from DC to FC, the actuator is locked at the current displacement  $u_i^{last}$ , which is the calculated target displacement command by the DC integration algorithm at the last iteration of time step  $i$ . Next, the control mode switch takes place and the actuator is locked at the current force command  $R_i^{last}$ , which is the last restoring-force feedback in time step  $i$  corresponding to  $u_i^{last}$ , i.e., maintaining and starting from an equilibrium state. The actuator is ready at this point to implement the next target force  $R_{i+1}^1$  calculated iteratively by the FC integration algorithm.

<sup>1</sup> The authors would like to acknowledge the collaboration of MTS in adding the mode switch feature to the hybrid controller at [nees@berkeley](mailto:nees@berkeley)

### 6.5.3 Practical Iterative Solution

The developed mixed-variables algorithm (for DC and FC, see Fig. 6.7) is implicit and thus requires iterations. However, the loading and unloading of a nonlinear inelastic system may cause unrealistic loading/unloading cycles and subsequently a distortion of the calculated secant stiffness. From Equation (6.23), we note that the only implicit term in calculating  $\mathbf{R}_{i+1}^{j+1}$  is  $\mathbf{K}_{i+1}^{j+1}$ . This secant stiffness may be estimated by applying a fraction of the increment  $\mathbf{R}_{i+1}^{j+1} - \mathbf{R}_{i+1}^j$  at each time step until convergence is reached, thus avoiding the unrealistic loading/unloading cycles. Therefore, instead of applying the full increment, as implied by the algorithm in Figures 6.5–6.7, only a fraction  $\lambda(\mathbf{R}_{i+1}^{j+1} - \mathbf{R}_{i+1}^j)$  is applied for each iteration, where  $\lambda < 1$ , and  $\mathbf{K}_{i+1}^{j+1}$  is estimated until the tolerance  $\varepsilon_R$  (Fig. 6.5) is satisfied and finally the remaining of  $\mathbf{R}_{i+1}^{last}$ , which is the calculated force command by the integration algorithm in the last iteration is fully implemented on the test structure.

To evaluate the effect of this iterative implementation strategy including the mode-switch decision-making scheme, a stiffening bilinear elastic SDOF undamped system (Fig. 6.14) with similar properties to that used in the previous parametric study, discussed in Section 6.4, is selected and subjected to the same impulse force (see Fig. 6.8(a)). Displacement control with an operator-splitting scheme and one predictor-corrector cycle, discussed in Section 6.1, is used during the initial (smaller) stiffness,  $k_I$ , while FC is used during the (higher) secondary stiffness,  $k_S$ , for ( $\theta = k_S/k_I > 1$ ). Four cases are studied (Table 6.2) resulting from the four possible different combinations of the two varied parameters,  $\alpha$  and  $\Delta t$ .

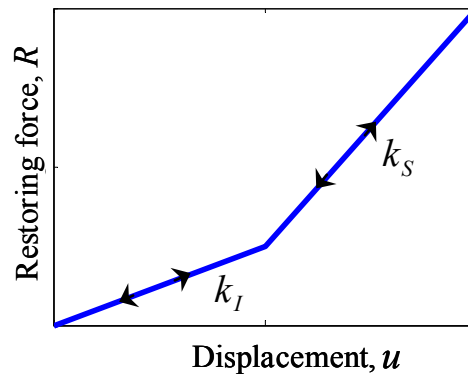


**Fig. 6.14** Considered stiffening bilinear elastic system for numerical evaluation.

The strain energy error in the present parametric study is calculated from Equation (6.25) based on a closed-form solution of the dynamic problem, Appendix B. The shown numerical solutions labeled “MS,” i.e., mode switch, in Figure 6.15 correspond to  $j_{\max} = 2$ , and  $\varepsilon_R = 0$ , i.e., two iterations are always carried out. Moreover,  $\lambda = 0.5$  is selected in the present numerical parametric study. These parameters are selected to simulate the case of a HS experiment with a limited number of iterations applied within each integration time step. In the DC solution (Fig. 6.15), the DC integration algorithm with one predictor-corrector cycle, discussed in Section 6.1, is used for the entire length of the applied motion without mode switch for the purpose of comparison with the mode switch (MS) curves. While in the case of  $\Delta t = 0.02$  sec, the DC solution is more accurate, in the case of  $\Delta t = 0.005$  sec, the two approaches yield almost identical error values indicating the accuracy of this solution if an adequate  $\Delta t$  is used. Note that the same increase of the error values with the increase in  $\theta$  observed in Figure 6.10 is observed in this numerical study as well. The higher error values for the case where  $\alpha = -0.3$  are due to the exact solution, with respect to which the error is calculated. As this solution is in closed form, the numerical dissipation introduced by the non-zero value of  $\alpha$ , leads to an additional source of error.

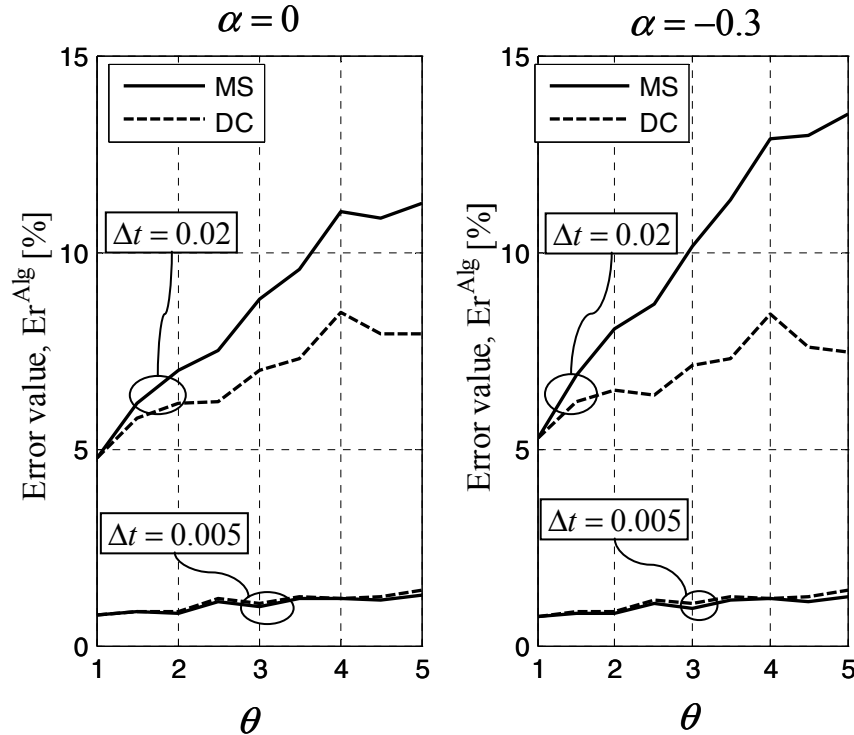


**Fig. 6.15 Parametric study of mode-switch algorithm using bilinear elastic SDOF systems.**

**Table 6.2 Varied parameters for numerical evaluation of mode-switch and iterative approach.**

Integration parameter	Integration time step
$\alpha = 0$ and $-0.3$	$\Delta t = 0.02$ and $0.005$ sec

## 6.6 SUMMARY

The present study uses the  $\alpha$ -method (Hilber et al. 1977) as presented by Shing et al. (1991) along with the operator splitting scheme (Nakashima 1990) to solve the governing equations of motion and to perform the experiments in displacement control. This numerical-integration algorithm is presented in detail. Two procedures are developed and implemented in the hybrid simulation system with the aim of enhancing the accuracy and reliability of the pseudo-dynamic test results. The first procedure aims at correcting the experimental systematic error in executing the displacement command signal. The error is calculated as the difference between command and feedback signals and correlated with the actuator velocity using a “hockey-stick” model. A feed-forward scheme for error compensation is devised leading to a more accurate execution of the hybrid simulation experiment. The second procedure employs mixed-variables with mode switching between displacement and force controls. The newly derived force-control algorithm is evaluated using a parametric study to assess its stability and accuracy by comparing its numerical results to those of the  $\alpha$ -method in displacement control. The implementation of the mixed-variables control procedure is designed to adopt force control for high stiffness states of the structural response and displacement control otherwise, where the resolution of the involved instruments may favor this type of mixed control. A number of practical implementation strategies are developed to support the execution of the new force-control algorithm within the hybrid simulation system of *nees@berkeley*.

# 7 Applications of Developed Hybrid Simulation Procedures

This chapter focuses on presenting results from phases P-1 and P-2 (see Fig. 1.2). The two developed procedures presented in Chapter 6, namely: (1) feed-forward error compensation and (2) mixed-variables control are applied on the two test structures, A and B, presented in Chapters 4 and 5, respectively.

## 7.1 FEED-FORWARD ERROR COMPENSATION

The feed-forward error prediction, presented in Section 6.2.2, is applied on test structures A and B. For each test structure, the calibration parameters in Equation (6.16) are evaluated using the least-squares method and used as described in Section 6.2.3 to compensate for these predicted displacement execution errors.

### 7.1.1 Calibration Parameter Evaluation

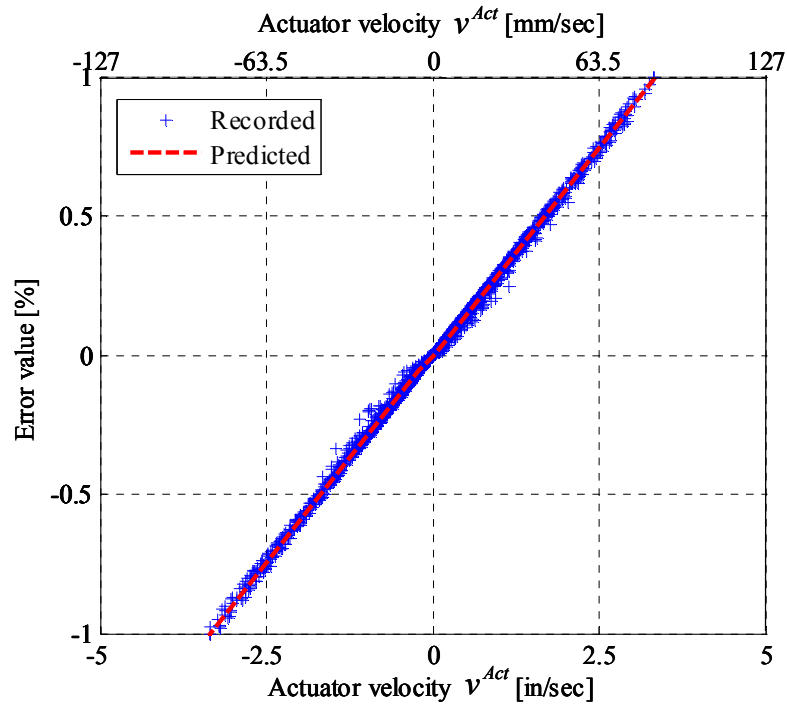
The strong motion LPB level 9 (see Tables 4.1–4.2) is applied on test structure A, while LPG level 5 (see Tables 5.1–5.2) is applied on test structure B, at varying test rates from 50 to 6.25 times slower than real time. Note that at faster test rates, the inertial force experienced by the physical substructures is included in the actuator force feedback signal and may be a source of error in the estimation of the restoring forces. However, the mass of the physical substructures in test structures A and B constituted  $\approx 5\%$  in both cases from the total numerically simulated mass of the HS test structure. In the case of the fastest test rate applied (6.25 times slower than real time), the accelerations imposed on the physical substructure are  $6.25^2 = 39$  times less than the numerically simulated ones, which was confirmed by the measured accelerations at the RC beam level of test structure A (see Section 4.5). Therefore, the total inertial force added to the actuator

force feedback signal amounts to less than 0.13% of the total numerically simulated inertial force and is safely neglected. The actuator velocity and the corresponding predicted error at the end of each integration time step are recorded (see Section 6.2) and plotted in Figure 7.1(a) and (b), for test structures A and B, respectively, along with their least-squares fits based on the calibrated parameters. The values of the calibration parameters are presented in Table 7.1.

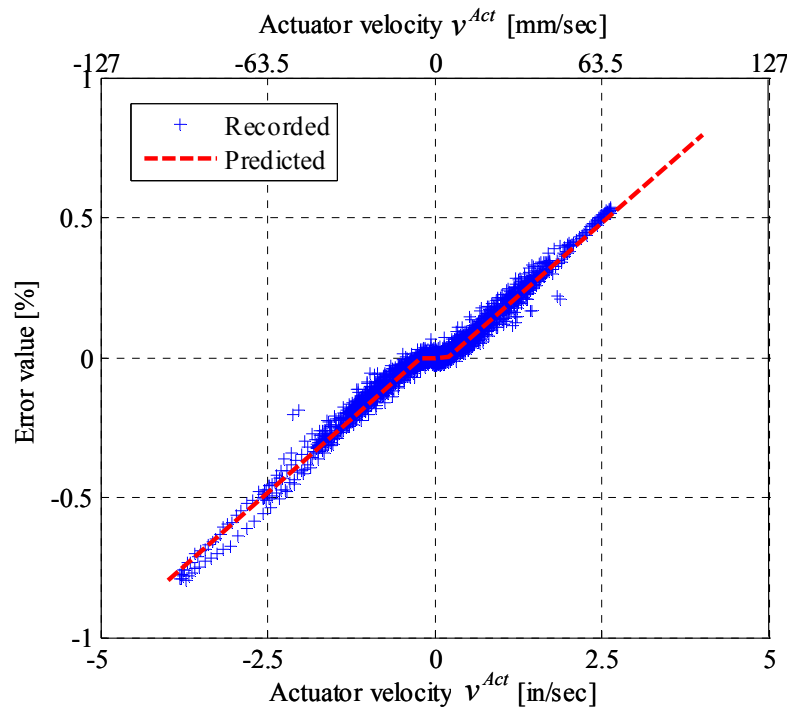
The two application examples are different in terms of the applied strong motion, the test structures, and their corresponding structural behaviors, as well as the PIDF tuning control parameters (see Section 3.4.1). Note that while the same actuators are used in the two experiments, two different sets of tuning parameters were used as the framework was being developed and better tuning was achieved in the case of test structure B than that of test structure A. The parameters  $a$  and  $b$  are therefore different in value (larger  $a$  and smaller  $b$  implying better control for test structure B) but the hockey-stick model described by Equation (6.16) holds implying its generic applicability in the case of the used HSS. The limitation of this error compensation procedure is due to the need of evaluating these calibration parameters before the actual test in a trial run, which may not be possible in all experimental investigations. An online calibration process for these parameters is a possible way to counter that problem and may be the subject of future development of the procedure as previously discussed in Section 6.2.3.

**Table 7.1 Calibration parameters for feed-forward error compensation procedure, Eq. 6.17.**

Calibration parameter	$a$ [in./sec (mm/sec)]	$b$ [sec/in. (sec/mm)]
Test structure A	0.0202 (0.51)	0.0030 ( $1.18 \times 10^{-4}$ )
Test structure B	0.2040 (5.18)	0.0021 ( $7.87 \times 10^{-5}$ )



(a) Test structure A



(b) Test structure B

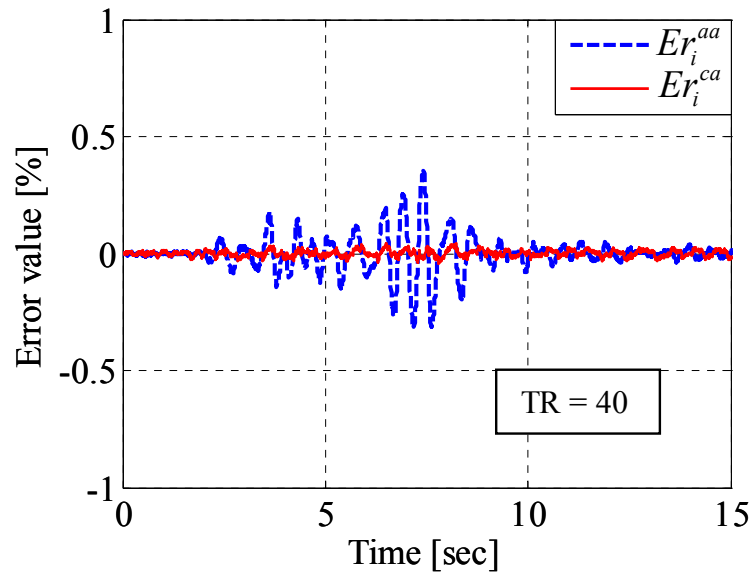
Fig. 7.1 Correlation relationship between error  $Er_i^{cc}$  and actuator velocity.

### 7.1.2 Experimental Results

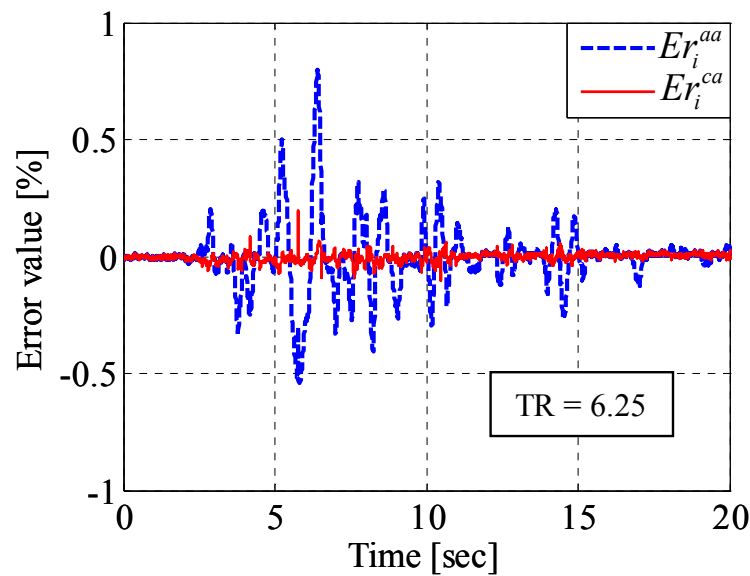
The same strong motions described in the previous section are applied on the respective test structures with the feed-forward error compensation scheme developed in Section 6.2.3. At any time step  $i$ , the adjusted command signal  $d_i^a$  is therefore sent to the actuators instead of the calculated command  $d_i^c$ . This modified command aims at the execution of the desired command  $d_i^c$  with a much smaller  $Er_i^{ca}$  than  $Er_i^{aa}$ , where  $Er_i^{ca}$  is the error in  $d_i^c$  when  $d_i^a$  is applied and  $Er_i^{aa}$  is the error in  $d_i^a$  when  $d_i^a$  is applied. Figures 7.2(a)–(b) show the results of the implementation of the feed-forward error compensation procedure on test structure A at a test rate TR = 40 times slower than real time and on test structure B at TR = 6.25 time slower than real time, respectively. The error signal  $Er_i^{ca}$  is reduced to a maximum of 0.041% from a maximum  $Er_i^{aa}$  of 0.353% in test structure A and 0.104% (excluding one anomalous peak of the recorded  $Er_i^{ca}$  signal treated as an outlier) from 0.797% in the case of test structure B. In both cases the reduced error is much closer than the original error to the displacement feedback resolution level, which is  $\pm 0.001$  in. ( $\pm 0.025$  mm), i.e., 0.01%. The effectiveness of the feed-forward error compensation in executing a more accurate displacement command signal, where the error is reduced to less than 13% of the original error, is therefore confirmed.

## 7.2 MIXED-VARIABLES CONTROL

The mixed-variables (force/displacement) control procedure with mode switch developed in Chapter 6 is implemented on test structures A and B following the algorithm illustrated in Figure 6.7. Force control is adopted for stiff states of the response while DC is adopted otherwise, as discussed in subsequent sections. Note that the developed practical iterative solution strategy (see Section 6.5.3) was not developed at the time of implementing the mixed-variables control on test structure A. In addition, the actuator tuning in FC was not adequate enough to ensure an accurate execution of the force command signal for test structure A which led to a poorly executed test. The following discussion is therefore limited to test structure B where these two limitations were overcome, while a brief discussion of the results of test structure A is included at the end of Section 7.2.3.



(a) Test structure A (TR = 40 times slower than real time)



(b) Test structure B (TR = 6.25 times slower than real time)

**Fig. 7.2 Feed-forward error compensation results.**

### 7.2.1 Structural States

The typical structural behavior exhibited by test structure B is illustrated in Figure 7.3. The wood structure is characterized by a low loading stiffness (< 3 kip/in. (0.53 kN/mm)) and a much higher unloading stiffness (> 30 kip/in. (5.3 kN/mm)) in the circled parts of the response in

Figure 7.3. At these relatively higher stiffness values, the PIDF control can be used to apply the command signal in FC mode with better accuracy than in DC mode. Note that in the stiff state, since the displacement increments are small, the actuator velocity is too small for the feed-forward error compensation procedure to be effective. Therefore, this error compensation is not considered in this section.

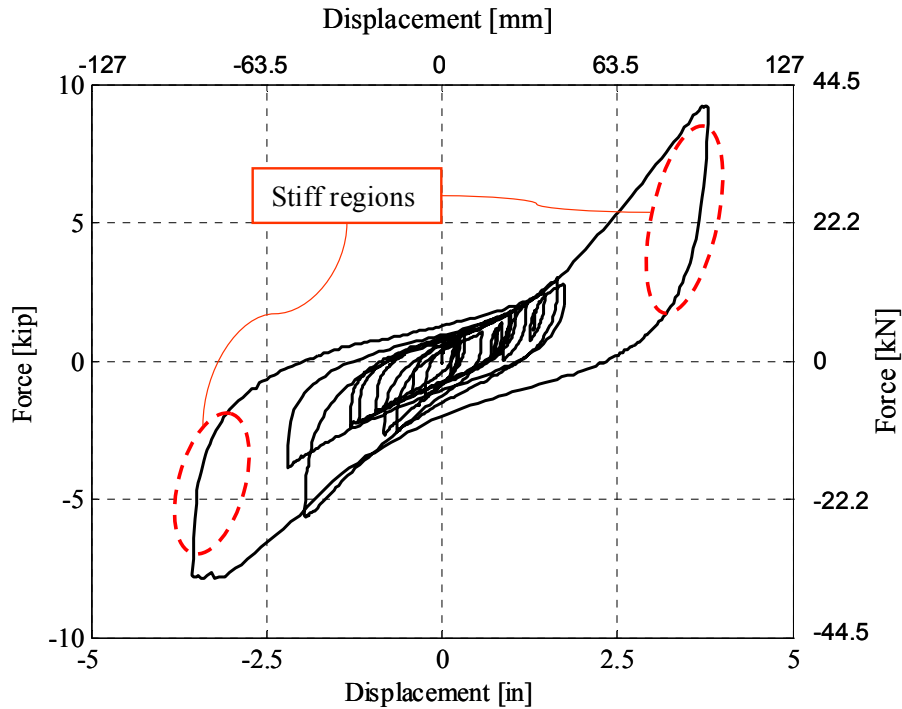


**Fig. 7.3 Typical force-deformation response for test structure B.**

### 7.2.2 Mode-Switch Decision Making

The FC actuator tuning (see Section 3.4.1) is stiffness dependent and requires the presence of a physical specimen to calibrate the PIDF tuning parameters. Accordingly, two shear walls, similar to the physical substructure in test structure B, are used for that purpose, then removed and replaced by the physical substructure of test structure B. The current HS setup does not allow the PIDF tuning parameters to be varied during the test. Therefore, the actuator is tuned in FC for the higher range of stiffness around 40 kips/in. (7.0 kN/mm). Since the stiffness needs to be in the tuning range, i.e., neither much higher nor much lower in order to apply the command in FC accurately, two switching criteria are adopted, both based on the estimated secant stiffness. Each

upper and lower secant stiffness limit is defined by two threshold values  $K_d^{up} = 65$  kips/in. (11.4 kN/mm) and  $K_f^{up} = 60$  kips/in. (10.5 kN/mm) for the upper limit and  $K_f^{low} = 25$  kips/in. (4.4 kN/mm) and  $K_d^{low} = 20$  kips/in. (3.5 kN/mm) for the lower limit. Figure 7.4 illustrates the use of these limits in the mode-switch decision-making procedure (see Section 6.5.2). Notice the two buffer zones between  $K_d^{low}$  and  $K_f^{low}$  on one side and between  $K_d^{up}$  and  $K_f^{up}$  on the other side of the figure. These buffer zones prevent the HSS from switching back and forth between the two control modes in the case where the amplitude of the estimated parameter  $K_i$  fluctuates slightly around the value of one of the thresholds. Based on the above thresholds, the mode-switch decision-making scheme is shown in Figure 7.5. Compared to Figure 6.13, another third criterion for mode switch is added such that FC is used only in the unloading regions, where  $R_i - R_{i-1} = \Delta R_i < 0$ . From Figures 7.4–7.5, FC is used in the unloading parts where the estimated average stiffness lies in the designated range ( $K_{\bullet}^{low} < K^{Avg} < K_{\bullet}^{up}$ ), where subscript  $\bullet$  denotes  $d$  or  $f$  depending on the current control mode, i.e., FC or DC, respectively; otherwise DC is employed.

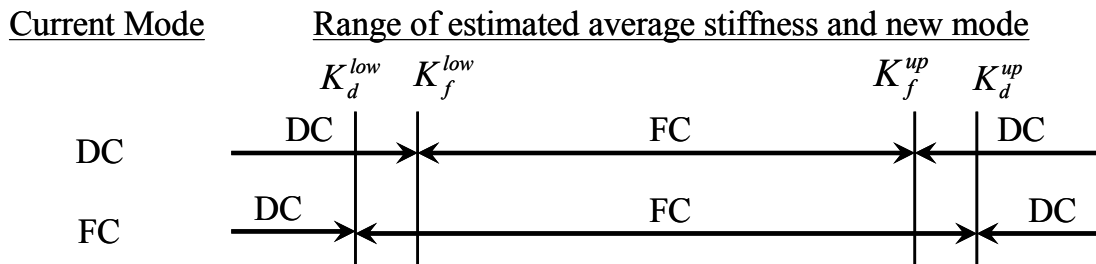


**Fig. 7.4 FC/DC mode-switch criteria for application example (test structure B).**

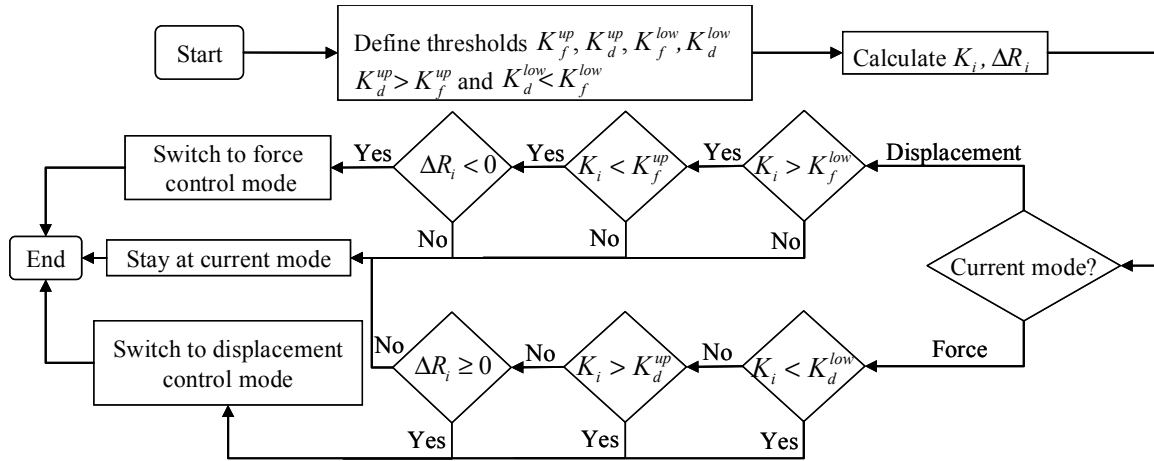


**Fig. 7.5 Mode-switch decision-making scheme for test structure B.**

The time-step duration is selected as  $t_d = 2$  sec with  $\Delta t = 0.005$  sec, i.e.,  $TR = 400$  times slower than real time. The slow execution rate of the procedure is needed to ensure the accuracy of executing the force command signal in FC. While faster rates may be achieved using the same procedure if the fidelity of the actuator control is guaranteed, real-time or close to real-time applications are not suitable for the FC algorithm in its current form. At faster test rates, the actuator load cell feedback readings are affected by the inertial force of the physical substructure, however small, and even if the stability of the control system is ensured, the sporadic “error” in the restoring-force feedback is likely to affect the estimation of the secant stiffness  $K_i$  leading to the lack of accuracy in calculating the force command signal (see Section 6.3.1). For the algorithm used in Figure 6.7, the adopted parameters are  $j_{\max} = 2$ ,  $\varepsilon_R = 0$  and  $\lambda = 0.5$  for the part conducted in FC. The DC integration algorithm is the  $\alpha$ -method with the operator-splitting scheme (Nakashima et al. 1990) as discussed in Section 6.1. Therefore, one iteration (i.e., one cycle of correction) in DC and two iterations in FC are always carried out which is practical for the application on a physical HS substructure. Recall that this case ( $\varepsilon_R = 0$  and  $\lambda = 0.5$  with two iterations for FC) is evaluated numerically in Section 6.5.3, where an adequate accuracy of the mixed-variables control algorithm with mode switch is confirmed.

### 7.2.3 Experimental Results

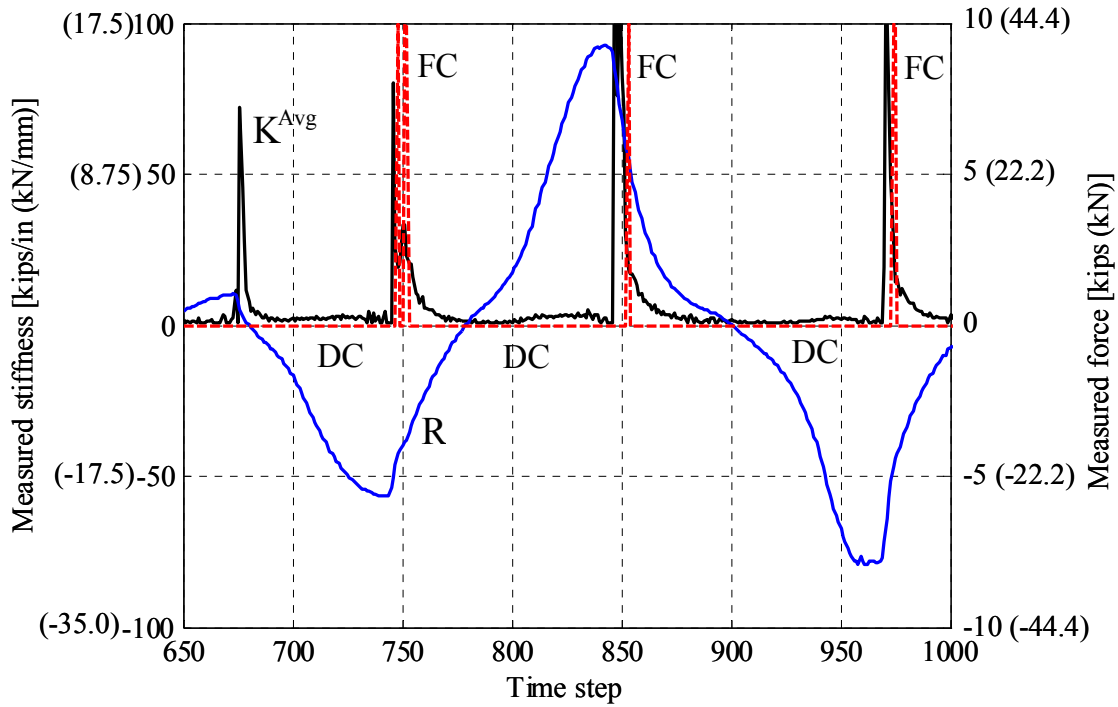
The procedure discussed above is applied on test structure B using the strong motion LPG level 5 (see Tables 5.1–5.2). Figure 7.6(a) shows part of the implemented history where large loading/unloading cycles are reported. The dashed red line indicates whether DC or FC is employed corresponding to zero or non-zero value, respectively. Force control is used in the unloading parts where the measured stiffness lies in the designated range in Figures 7.4–7.5; otherwise DC is employed. This is illustrated more clearly in Figure 7.6(b) where an enlarged part of a cycle is shown. Due to the fast rate of change of stiffness during unloading, two integration time steps (number 974 and 975) are implemented in FC. Nevertheless, mode switch within the HSS occurs smoothly between DC and FC and vice versa, without disturbing the feedback signals of the restoring force or displacement. The estimation of the secant stiffness, as a result, is reliable for its use in the mixed-variables numerical-integration algorithm. The execution of the force command signals is highly accurate as demonstrated by the measured feedback restoring-force signals,  $R_m$  in Figure 7.6(b), which match the corresponding command signals within the resolution of the measuring sensor, i.e.,  $\pm 0.02$  kip ( $\pm 0.09$  kN).

The accurate application of the force command signal through proper tuning of the actuator is crucial to the correct implementation of the mixed-variables control algorithm. This is clearly demonstrated in the application of the algorithm on test structure A. In this test structure, there was no additional specimen, similar to the case of the physical substructure of test structure B, for the purpose of tuning. Therefore, as discussed in Section 4.3, the FC tuning could not offer the required accuracy. Test structure A (see Section 4.3) is subjected to the strong motion LPB-9, (see Tables 4.1–4.2), and FC is employed, as in the case of test structure B, in the unloading region characterized by a high stiffness. Figure 7.7 shows part of the force time history for a loading/unloading cycle. The irregularity is identified in Figure 7.7 by the observed two consecutive peaks in the estimated  $K^{\text{Avg}}$  signal corresponding to the almost non-varying (plateau-like)  $R$  signal. This unrealistic loading history applied on the test structure is caused by the inaccurate implementation of the force command signal. The lag of the actuator in FC, observed in the difference between the applied  $R$  and measured  $R^m$  in the two integration time steps performed in FC, results in smaller displacement feedback increments (in the absolute sense). This causes an artificial reduction in the increments of the numerically simulated velocity

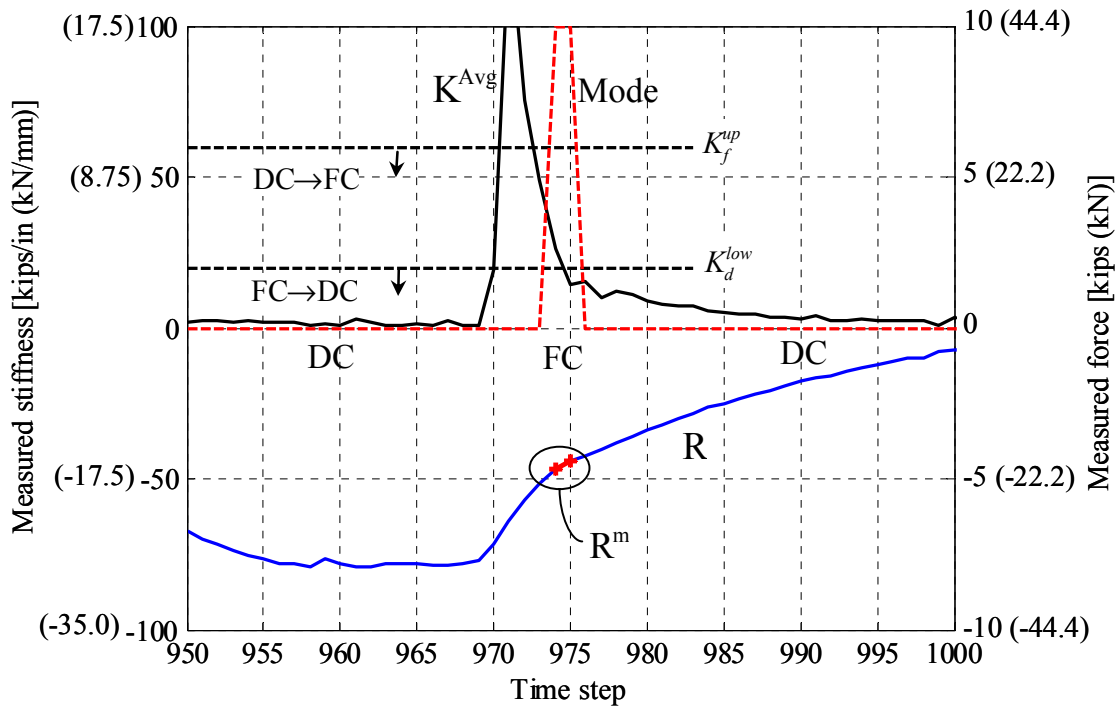
and acceleration of the test structure resulting in an inaccurate estimation of the next force command signal. This error is accumulated at each integration time step in FC, resulting in a disturbance of the loading time history and an additional unrealistic unloading and loading of the physical substructure, illustrated by the second rise and drop of the  $K^{Avg}$  signal and the artificial plateau in the R signal.

### 7.3 PROCEDURE COMBINATION

The two procedures implemented in this study and discussed in Chapter 6 with applications in this chapter aim at improving the accuracy and providing a generalized framework of the HS experimentation. On one hand, feed-forward error compensation is applied for experiments conducted in DC. On the other hand, mixed DC/FC is intended for structures exhibiting mixed flexible/stiff structural behavior. In this mixed-variables formulation, FC is intended for stiff states of the physical substructures. In these states, the resolution of the displacement measurement devices does not offer the desired accuracy to implement the displacement command signals, whereas the resolution of the force measurement devices to implement the force command signals can be more accurate. The two developed procedures may therefore be applied alternately, leading to an improved accuracy in DC for flexible states of the response and better accuracy in stiffer states when conducted under FC. This is demonstrated in Figure 7.8, which shows the actuator velocity  $v^{Act}$  and the secant stiffness  $K^{Avg}$  in a loading/unloading cycle of test structure B. The secant stiffness is rather constant in the loading branch and the actuator velocity increases gradually. At the end of the loading branch and start of the unloading branch, the velocity of the actuator is very small while the estimated stiffness suddenly increases while unloading. The higher actuator velocity is therefore associated with low secant stiffness and vice versa offering the possibility of implementing the suggested novel generalized approach in HS as shown in Figure 7.8.



(a) Loading/unloading cycles with mode switch



(b) Enlarged part (last 50 time steps) of Fig. 7.6(a)

**Fig. 7.6 Results of mixed-variables algorithm with mode switch for HS on test structure B.**

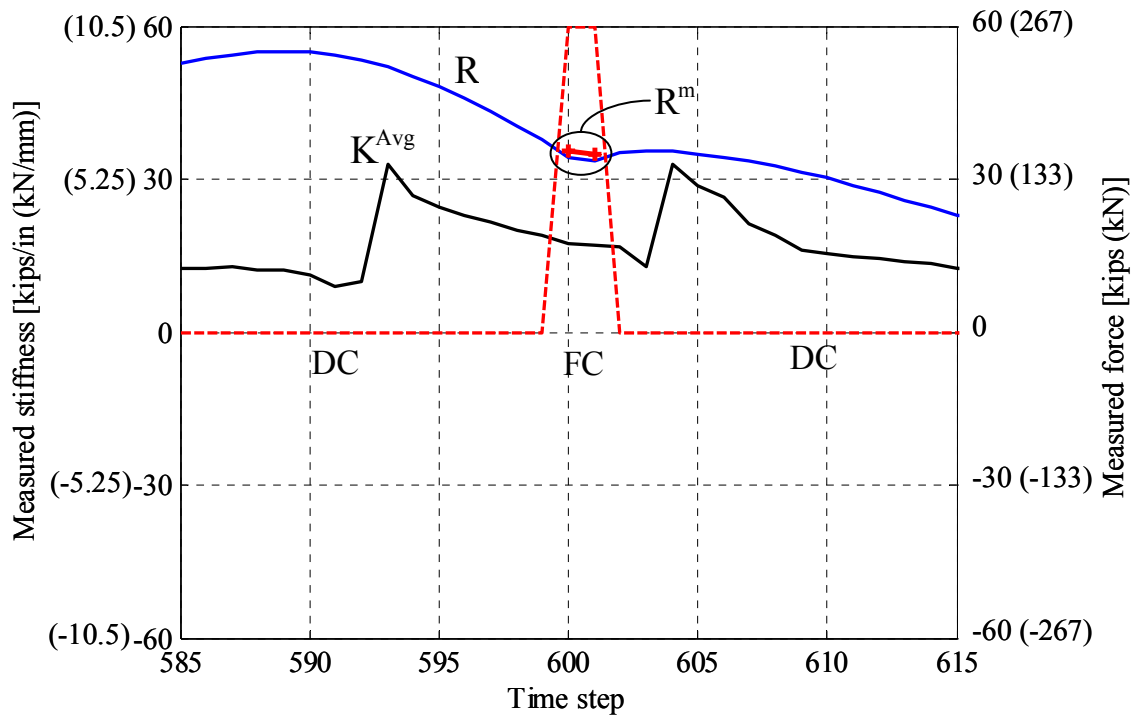


Fig. 7.7 Results of mixed-variables algorithm with mode switch for HS on test structure A.

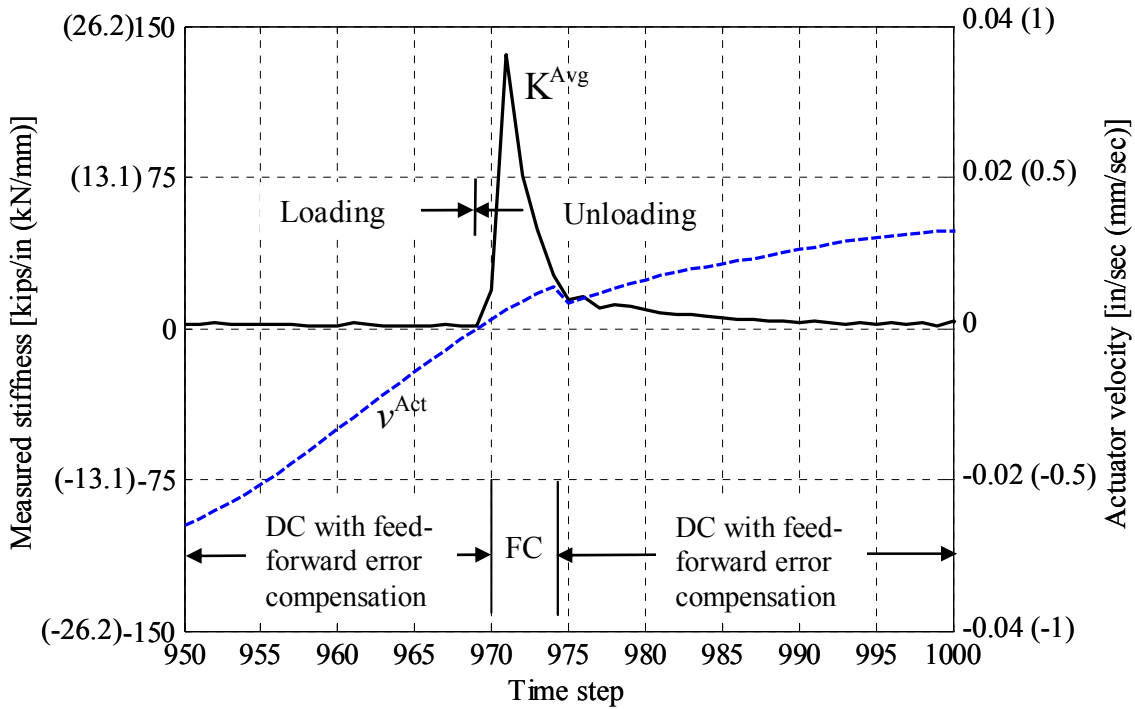


Fig. 7.8 Possible incorporation of two developed procedures in HS.

## 7.4 SUMMARY

The two procedures presented in Chapter 6 are implemented on test structures A and B. Feed-forward error compensation based on the correlation with the actuator velocity is implemented on both test structures and a considerable improvement of the execution of the displacement command signal is achieved as a result. Mixed-variables control is implemented in the hybrid simulation system and is applied on test structure B with mode switch between force and displacement control, and the test is conducted smoothly provided that some restrictions are enforced in the mode-switch decision-making procedure and that the tuning of the actuator in force control is adequate. The displacement control error compensation scheme is found to be complementary in nature with the mixed-variables control and it is proposed to apply the two procedures alternately to achieve a more accurate execution and a generalized framework of the online experiments.

## 8 Structural Evaluation and Comparisons

This chapter addresses phases S-1, S-2, and S-3 for test structure A (see Fig. 1.2), as well as the structural performance of test structure B. The results of test structure A are discussed in terms of its global response, crack pattern, and mode of failure, the structural contribution of the URM infill wall and the local behavior represented by beam-to-column joint rotations. In the case of test structure B, the results are discussed in terms of the global behavior and mode of failure. Comparisons to the corresponding ST experiments for the two test structures A and B are conducted aiming to compare the two testing methods, namely HS and ST.

### 8.1 TEST STRUCTURE A: PHASE S-1

Test Structure A, described in Chapter 4, is subjected to a number of strong motions and categorized into three phases (see Fig. 4.4) based on the state of the test structure, described in Section 4.3. The first phase, namely S-1, represents the test structure with URM infill wall in the middle frame and all columns are post-tensioned.

The execution time for each integration time step is selected as  $t_d = 0.2$  sec. This execution time for the algorithm in DC is sufficient to perform the numerical integration, send the displacement command signal, and receive the restoring-force feedback signal without any delay. Since the time step of the numerical integration  $\Delta t = 0.0025$  sec is selected for all runs in S-1, testing is performed at a rate of  $TR = t_d / \Delta t = 0.2 / 0.0025 = 80$  times slower than real time. Note that in the following discussion, the low-level seismic excitation TAR-1, which is conducted for the purpose of checking the proper functionality of the data-acquisition system, is not discussed.

### 8.1.1 Force-Displacement Behavior

The global response of the test structure is represented by the total base shear versus lateral displacement at the expected level of the total inertial force due to ground shaking of the one-story test structure. The total base shear is estimated as the sum of the lateral restoring forces in the RC frames measured from the actuators force feedbacks and the numerically simulated damping forces. The total base shear is considered in this section, since it is the quantity that can be compared with its equivalent in the ST test results (Hashemi and Mosalam 2007), where the damping force cannot be separated from the total base shear force without a number of uncertain assumptions. The displacements are measured at the height of the load application on the frames. The stiffness values in the following discussion are estimated based on the average tangent slope at distinct stages of the applied strong motion. These stages are defined for each corresponding stiffness value in the following paragraphs, and each of the average tangent slopes is evaluated over all the recorded points of the loading branches of the force-displacement cycles, within that stage, using the least-squares method to obtain a best linear fit of the stiffness value in question.

In TAR-2, TAR-3, and TAR-4, and for the initial range of low-level excitation in each strong motion, where the total base shear forces are lower than  $\pm 15$  kips ( $\pm 66.7$  kN), the response is characterized by a high initial stiffness  $K_s$ ; refer to Table 8.1 and Figure 8.1. This high initial stiffness is attributed to the static friction between the URM infill wall at its interface and the surrounding RC frame. Due to the slow test rate at which the strong motion is applied, this static friction is not overcome at a certain velocity threshold as expected in the ST experiment case. Instead, this static friction is controlled by the static resistance due to the grinding of the particles on the interface between the URM infill wall and the surrounding RC frame members. This high initial stiffness starts at  $K_s = 826$  kips/in. (144.7 kN/mm) in TAR-2 (Table 8.1 and Fig. 8.1(a)), representing 85% of the value obtained from the pull-back test in Section 4.11, where the stiffness for the whole test structure, i.e., F1I and two F2B frames with a connecting RC slab, is evaluated at 977 kips/in. (171.1 kN/mm). This decrease is due to the difference in the amplitude and repetition of the excitation forces in these two tests. While in the pull-back test, the sum of the forces applied on the test structure is only 11 kips (22 kN), described in Section 4.11, the total force applied in TAR-2 in the range of the high stiffness due to static friction is 15 kips

(66.7 kN). More importantly, this higher force in TAR-2 is repeated for a large number of cycles causing the observed decrease in stiffness.

Once the initial resistance of the interface particles is overcome, i.e., once the total base shear exceeds the static friction threshold of  $\pm 15$  kips ( $\pm 66.7$  kN), the stiffness reduces to a preliminary stiffness  $K_P$ . The stiffness value  $K_P$  is evaluated over a number of loading branches, determined by visual inspection, that follow the overcoming of the initial static friction and before any substantial degradation in the stiffness of the test structure is developed as the application of the ground motion progresses. Subsequently, the accumulated damage results in a progressive degradation of the stiffness, reaching a final value  $K_F$  in the last number of force-displacement cycles, determined by visual inspection, of the applied strong motion. The reduction in stiffness is evaluated for each run in Table 8.1. In TAR-6, a considerable deterioration reflected by the reduction of the stiffness is observed and is accompanied by the first visually detectable cracks at the lower corners of the URM infill wall. In this case, the preliminary stiffness reduces by 31% to reach  $K_F = 350$  kip/in. (61.3 kN/mm) at the end of this strong motion.

**Table 8.1 Tangent stiffness evaluation for test structure A, phase S-1.**

Strong Motion	Tangent stiffness [kips/in. (kN/mm)]				$\frac{K_P - K_F}{K_P}$ [%]
	Static friction $K_S$	Preliminary $K_P$	Final $K_F$	Average secondary $K_{F2}$	
TAR-2	826 (144.7)	791 (138.5)	705 (123.5)	--	11
TAR-3	788 (138.0)	715 (125.2)	602 (105.4)	--	16
TAR-4	785 (137.5)	613 (107.4)	502 (87.9)	--	18
TAR-6	736 (128.9)	508 (89.0)	350 (61.3)	--	31
DUZ-7	543 (95.1)	367 (64.3)	84 (14.7)	133 (23.3)	77
DUZ-8	--	80 (14.0)	77 (13.5)	--	4
DUZ-9	--	79 (13.8)	64 (11.2)	82 (14.4)	19
DUZ-9-2	--	51 (8.9)	41 (7.2)	--	20

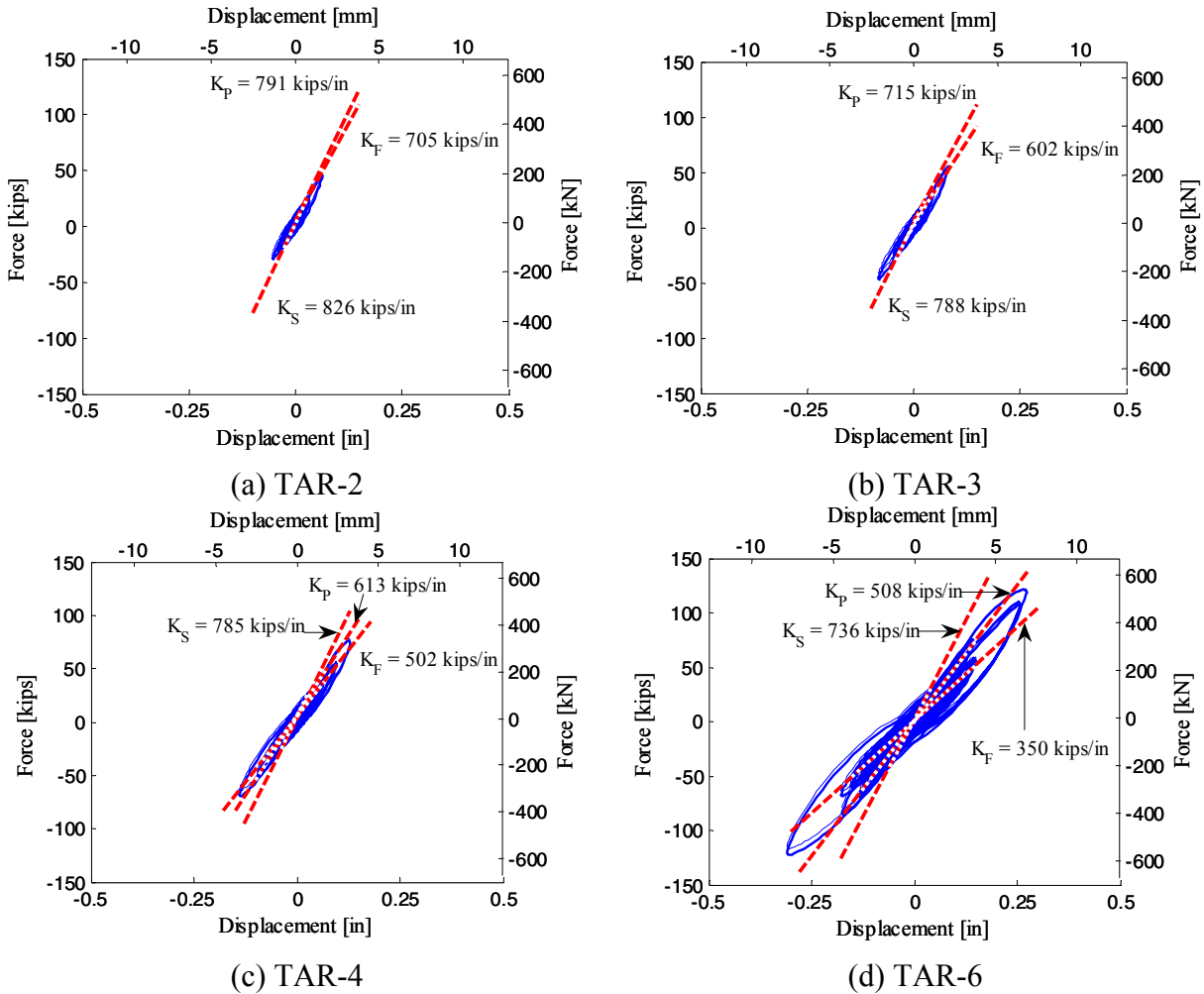


**Fig. 8.1 Total base shear versus lateral displacement for test structure A, phase S-1, TAR-2 to TAR-6 (1 kip/in.= 0.175 kN/mm).**

In DUZ-7, the high initial stiffness due to static friction is much smaller with  $K_S = 543$  kips/in. (95.1 kN/mm) due to the increasingly defined cracking at the smoothed URM infill wall interface with the surrounding RC frame members due to several grinding loading cycles, (Table 8.1 and Fig. 8.2(a)). The preliminary stiffness is 367 kips/in. (64.3 kN/mm) approximately corresponding to the final stiffness of the previous level, i.e., 350 kip/in. (61.3 kN/mm) for TAR-6. The first major crack in the URM infill wall occurs with a sudden drop in stiffness. At this point, a stiffening behavior with pinched loops characterizes the response with a low stiffness  $K_F$  at the origin, where the URM infill wall is not effectively engaged, and higher secondary stiffness  $K_{F2}$ . This secondary stiffness is evaluated over the higher stiffness parts of the loading branches, determined by visual inspection. Note that the transition from  $K_F$  to  $K_{F2}$

coincides with the closing of the gaps between the URM infill wall and the surrounding RC frame members. At the end of DUZ-7, a clear crack pattern in the URM infill wall is observed as shown in Figure 8.3(a).

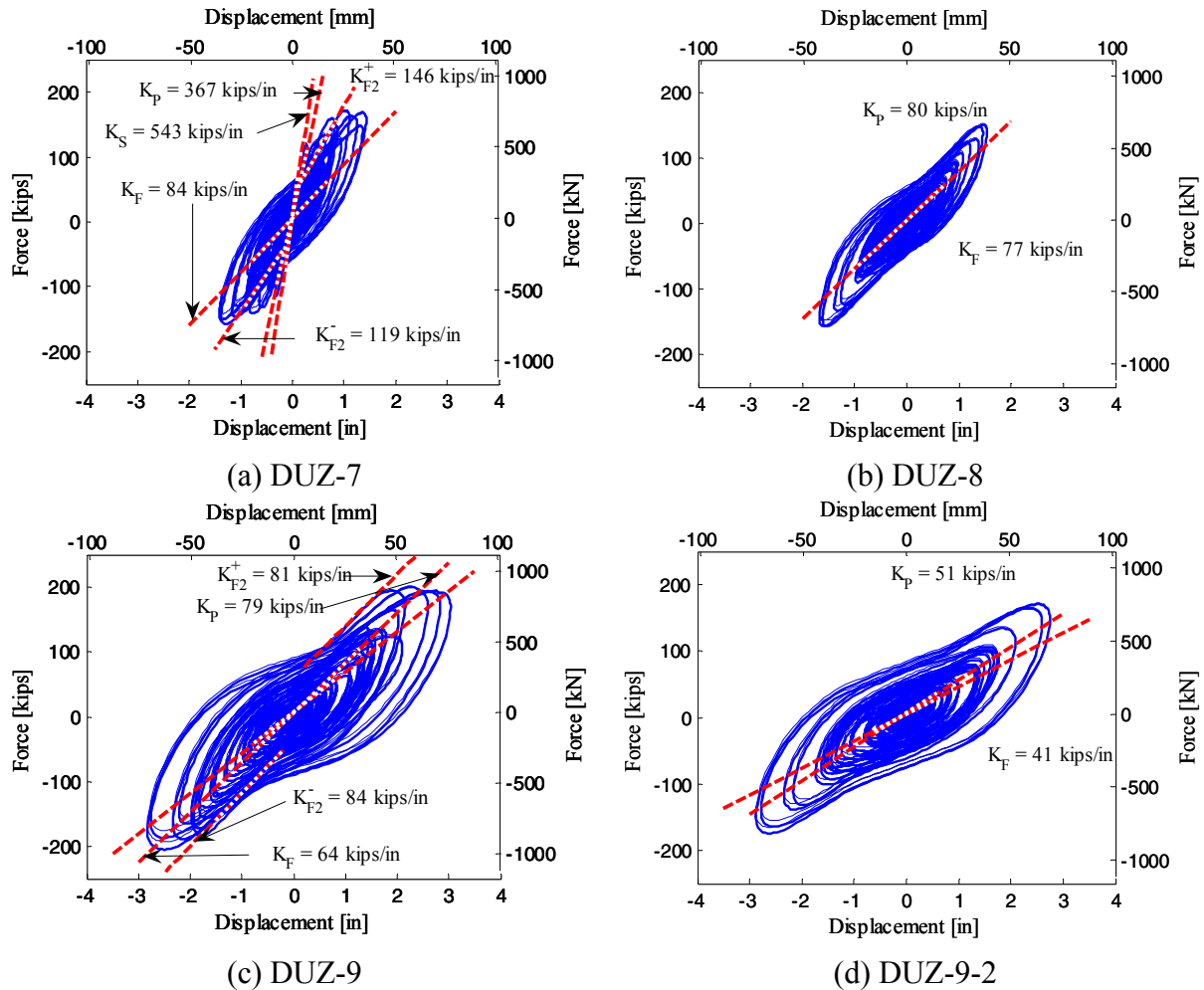


Fig. 8.2 Total base shear versus lateral displacement for test structure A, phase S-1, DUZ-7 to DUZ-9-2 (1 kip/in. = 0.175 kN/mm).

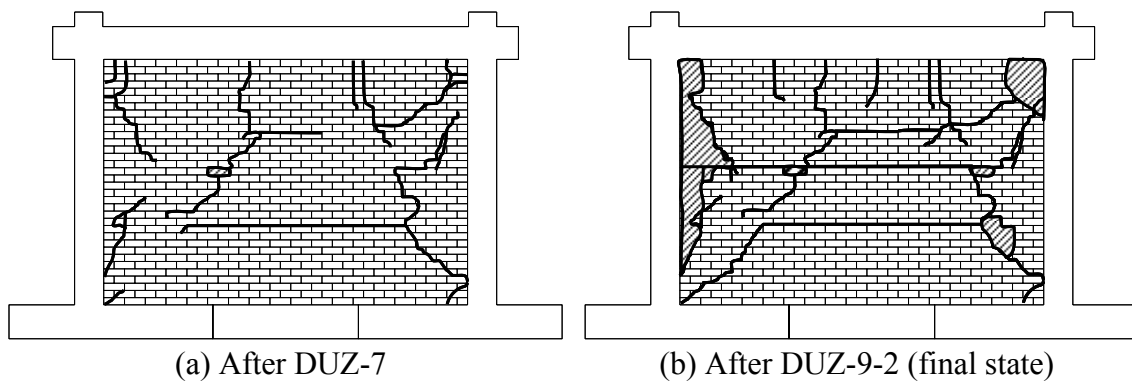
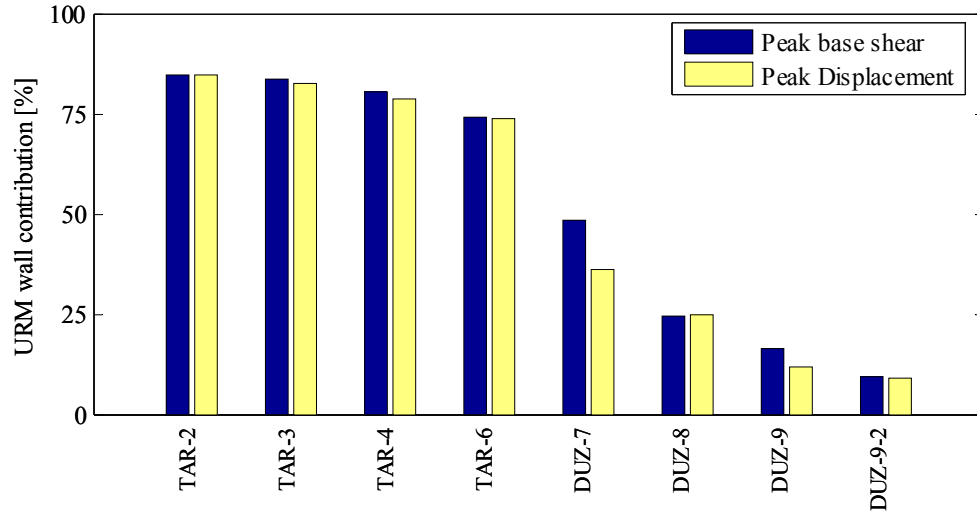
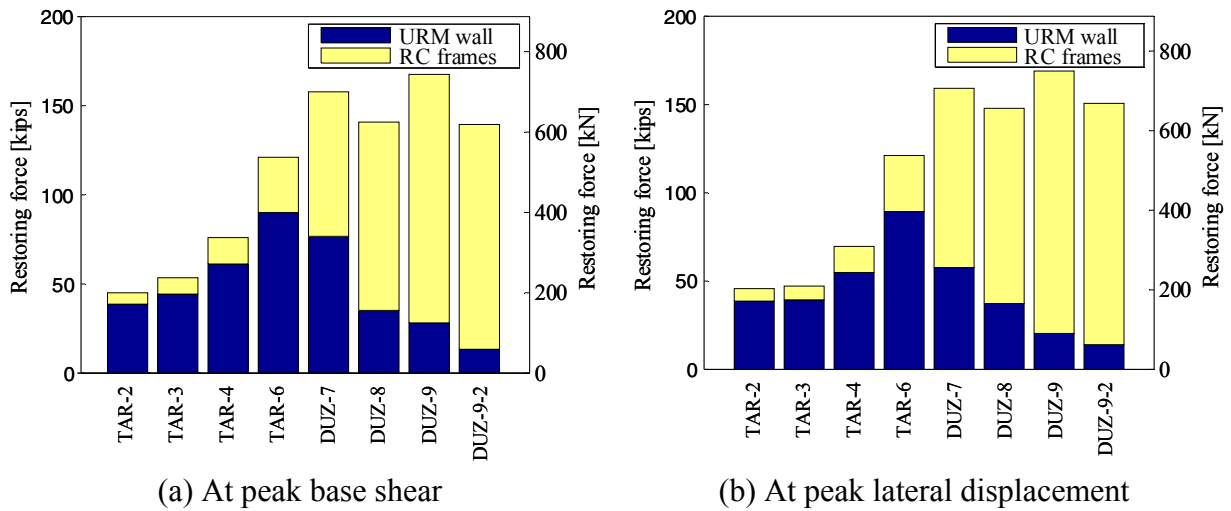


Fig. 8.3 Cracking patterns of URM infill wall in test structure A, phase S-1.

In DUZ-8 (Fig. 8.2(b)), the high initial stiffness due to static friction is absent and the URM infill wall is nearly not engaged in the response. This is confirmed by the absence of the pinching behavior observed in DUZ-7, and the maximum lateral drift is only slightly higher than that in DUZ-7. Furthermore, the crack pattern does not differ significantly from the one at the end of DUZ-7 and the stiffness is only slightly reduced by only 4% as shown in Table 8.1. In DUZ-9, the strong motion excites the test structure beyond the maximum drift reached in DUZ-8 and the pinching behavior reappears, implying the reengagement of the damaged URM infill wall but with less lateral load resistance. At the end of this level, a partial collapse of the URM infill wall occurs. In DUZ-9-2, which is the repeat of DUZ-9, the behavior returns to the one observed in DUZ-8 with little contribution from the disintegrated URM infill wall. The final crack pattern is shown in Figure 8.3(b), where the shaded areas denote the collapsed parts of the URM infill wall. Typical diagonal cracking and crushing at the corners is clearly observed and three major horizontal cracks, along the URM infill wall height, complete the crack pattern and form the failure mechanism, which allows the URM infill wall to deform in its own plane without carrying any substantial part of the applied lateral load. Therefore, in DUZ-9-2, one concludes that the RC frames are effectively the only lateral load-resisting elements.

### 8.1.2 URM Infill Wall Contribution

The URM infill wall contribution to the structural response of test structure A is assessed. The shear force in the URM infill wall  $F_w$  is estimated as the difference between the restoring forces, measured from the load cells directly attached to the actuators, in the infilled RC frame and that in the RC bare frame. The peak values of the restoring force in the URM infill wall and the sum of the restoring forces in the three RC frames comprising the one-story test structure are plotted in Figure 8.4. In this figure, a distinction is made between results recorded at the maximum total base shear (Fig. 8.4(a)), and at the maximum lateral displacement (Fig. 8.4(b)). The corresponding ratio in percentage of the restoring force resisted by the URM infill wall alone with respect to that resisted by the entire URM infilled RC test structure is shown in Figure 8.4(c) and the values are reported in Table 8.2.



**Fig. 8.4 Contribution of URM infill wall and RC frames to restoring forces.**

The contribution of the URM infill wall before cracking (up to TAR-6) represents the major share of the structural components in resisting the total base shear. This contribution starts at about 85% at TAR-2 and gradually decreases to reach 74% at TAR-6. In DUZ-7, where major cracking in the URM infill wall occurs, the decrease of the URM infill wall contribution is substantial and continues, in subsequent test levels, until the RC bare frames control the response, whereas the URM infill wall contribution reaches only 9% in DUZ-9-2. Note that the difference between the two ratios, at peak displacement and at peak base shear, is more apparent in the two events, DUZ-7 and to a lesser extent DUZ-9, where the behavior of the structural system undergoes considerable deterioration of an almost intact URM infill wall and a

significantly damaged URM infill wall, respectively. In this case, peak displacements correspond to greater damage states with smaller corresponding forces than the peak base shear forces.

**Table 8.2 URM infill wall contribution to total restoring force.**

Strong Motion	URM infill wall contribution (%)	
	At peak base shear	At peak displacement
TAR-2	84.8	84.8
TAR-3	83.5	82.4
TAR-4	80.5	78.6
TAR-6	74.1	74.0
DUZ-7	48.5	36.2
DUZ-8	24.6	24.9
DUZ-9	16.5	11.8
DUZ-9-2	9.2	9.0

## 8.2 COMPARISON TO ST EXPERIMENT: PHASE S-1

The sequence of events in phase S-1 (Fig. 4.4) is the same as the one conducted on the ST up to DUZ-8. A complete discussion of the ST experimental study and its results can be found in Hashemi and Mosalam (2006, 2007). It should be reiterated that one of the main contributions of this report is the comparison between the HS and ST approaches for testing hybrid structural systems such as the two cases considered in test structures A and B. The results of test structure A are compared herein for the two experimental methods, namely HS and ST, and conclusions are drawn on the differences and similarities between these two experimental methods.

### 8.2.1 Force-Displacement Behavior

The relationship between the total base shear and the lateral displacement, which is measured at the load application level, is compared for the two experiments in the major events of phase S-1, (Fig. 8.5). Note that the stiffness values in the following discussion are derived using the same procedure, as discussed in Section 8.1.1, for the two test structures. The first noticeable difference is the absence of the high initial stiffness due to static friction in the ST experiment, which is present in the HS experiment up to DUZ-7 before the major cracking of the URM infill

wall, discussed in Section 8.1.1. This is attributed to the high velocity at which the real-time ST experiment is conducted which allows overcoming the static friction much more efficiently than in the HS with slower rate of load application. The second difference is the distinctly higher stiffness values of the HS test structure, e.g., in TAR-6,  $K_p = 508$  kips/in. (89.0 kN/mm) in HS, and  $K_p = 364$  kips/in. (63.7 kN/mm) in the ST, i.e., 1.4 times larger (Table 8.3).

It should be stressed that all feasible efforts were made for the test structure A used in the HS and that used in the ST to be as close, in structural and material properties, as practically possible. Note that the concrete compressive strength is similar, the reinforcing steel is obtained from the same mill, and the masonry units are acquired from the same patch. However, the URM infill wall, which was built by the same professional masons for the HS and ST experiments, is the potential candidate as being the source of difference between the test structures used in these two experiments, particularly from the construction point of view. It is known that the level of tightly *filling* the space defined by the RC frame with URM *infill* wall depends on the masons skills and boundary conditions, e.g., having a roof represented by the connecting RC slab with its lateral and vertical stiffness contributions as in the ST experiment versus not having this physical slab as in the HS experiment where the slab is numerically simulated only in the lateral direction. Therefore, the RC slab and the URM infill wall are potential sources of discrepancy between the two test structures used for the HS and ST experiments. This is discussed in more detail in Section 8.2.2.

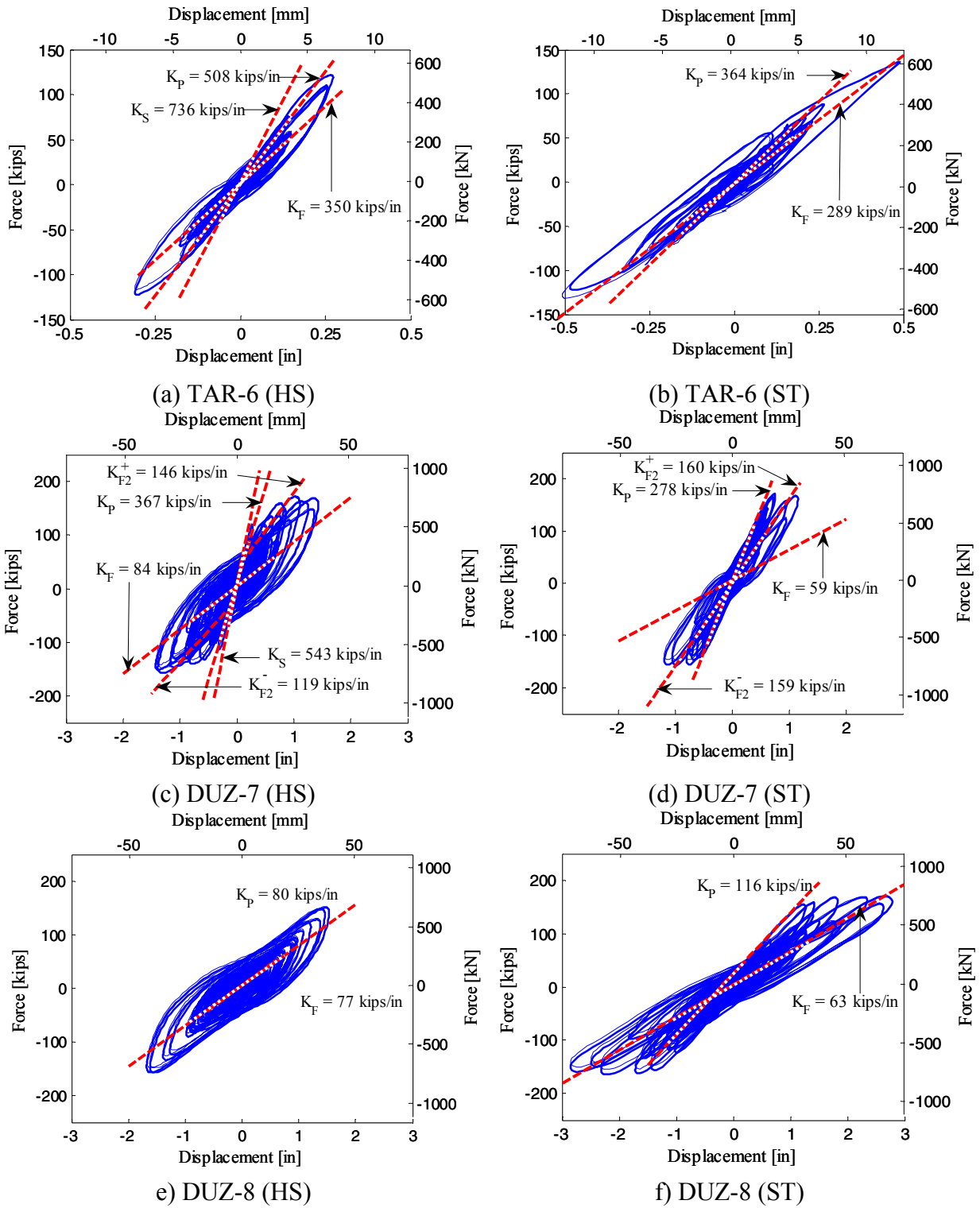


**Fig. 8.5 Total base shear versus lateral displacement comparisons for test structure A, phase S-1 (1 kip/in.=0.175 kN/mm).**

**Table 8.3 Tangent stiffness comparisons for test structure A, phase S-1.**

Strong Motion	Tangent stiffness [kips/in. (kN/mm)]			
	Experiment	Preliminary $K_P$	Final $K_F$	Average secondary $K_{F2}$
TAR-6	HS	508 (89.0)	350 (61.3)	--
	ST	364 (63.7)	289 (50.6)	--
DUZ-7	HS	367 (64.3)	84 (14.7)	133 (23.3)
	ST	278 (48.7)	59 (10.3)	160 (28.0)
DUZ-8	HS	80 (14.0)	77 (13.5)	--
	ST	116 (20.3)	63 (11.0)	--

Aside from the expected discrepancy between the detailed responses from the HS and ST experiments because of the differences in the respective test structures mentioned above, the major events occur almost concurrently in the two experiments. These major events include the close-to-linear response up to TAR-6, the major cracking in DUZ-7, and the observed pinching behavior in the force-displacement response in DUZ-7. However, the hysteretic loops in level DUZ-7 are larger in the HS experiment than those in the ST experiment.

As stated in previous chapters, damping is numerically modeled in HS, based on the snap-back test results for the undamaged experimental ST test structure (see Section 4.10.2) and is kept constant throughout all the HS experiments. However, in reality the damping value changes for different states of testing and degradation of the experimental substructure as discussed in Hashemi and Mosalam (2006, 2007). Therefore, it is worth investigating the total restoring forces versus lateral displacement plot in DUZ-7 for the HS experiment case (i.e., without adding the damping force to the measured restoring force) in Figure 8.6(a). Notice that the restoring-force–displacement hysteretic loops are more comparable in size to their counterparts in the ST experiment (Fig. 8.6(b)), underlining how the assumption of constant mass proportional damping in the HS experiment may not be accurately modeling what is effectively present in the dynamic ST test structure.

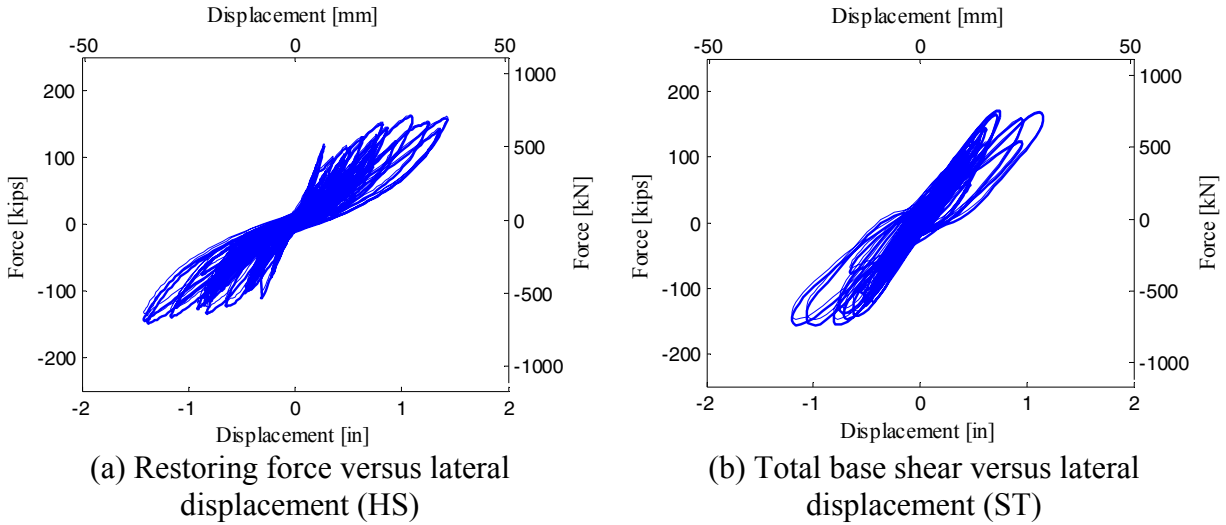


**Fig. 8.6 DUZ-7 comparisons for test structure A, phase S-1.**

In DUZ-8 (Figs. 8.5(e)–(f) and Table 8.3), the results from HS and ST diverge significantly. In HS, where the URM infill wall is close to being structurally insignificant in DUZ-7 (average  $K_{F2} = 133$  kips/in. (23.3 kN/mm) for the positive and negative excursions compared to average  $K_{F2} = 160$  kips/in. (28.0 kN/mm) in the ST), no additional damage or significant degradation occurs in DUZ-8. On the other hand, in ST, a 58% reduction in the preliminary stiffness  $K_p$  is observed from DUZ-7 to DUZ-8 and the cracking pattern of the URM infill wall develops further accompanied by partial collapse of significant parts of the URM infill wall. This is attributed to the slow velocity and the associated low acceleration at which the HS test is conducted compared to the ST, where the in-plane and probably more importantly the out-of-plane inertial forces of the mass of the disintegrated masonry parts do not sufficiently develop to dislocate these parts from the rest of the URM infill wall. Moreover, the interlocking action and the associated friction between these parts is large enough to hold the URM infill wall together under slow loading rates in the HS experiment, which is not the case in the ST experiment.

The cracking patterns of the two URM infill walls for HS and ST at the end of DUZ-7 (Figs. 8.7(a)–(b)) hold the same general features comprising diagonal cracks, crushing at the corners, and horizontal cracking. It is to be noted that one horizontal crack is formed in the ST at approximately one third the height of the URM infill wall, and two horizontal cracks are formed in the HS at approximately one and two thirds the height of the URM infill wall. These horizontal cracks (along the mortar bed joints) link the diagonal ones and form the failure

mechanism of the URM infill wall, matching the shape of the proposed compression-only strut model in Mosalam (1996a). The length of these horizontal (bed joint) cracks depends on the aspect ratio of the URM infill wall panel. However, while dynamically, the URM infill wall disintegrates significantly in DUZ-8 and partial collapse is observed, pseudo-dynamically, two higher level runs (DUZ-9 and DUZ-9-2) are needed to visually reach a comparable partial collapse to that after DUZ-8 in the ST experiment (Figs. 8.7(c)–(d)) due to factors related to the different loading rates at which the two experiments are conducted as discussed above.

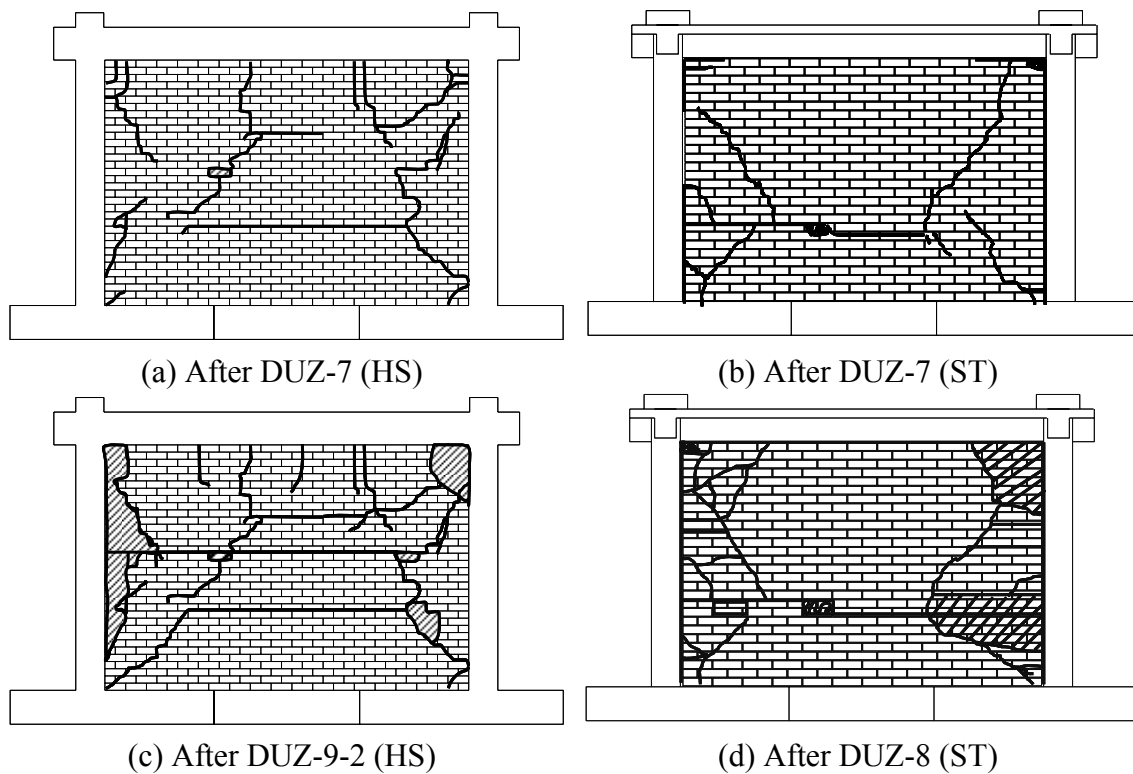


**Fig. 8.7 Cracking patterns developed in URM infill wall in HS and ST experiments (shaded areas indicate dislocated parts of wall).**

Comparing the cracking patterns from the HS to those from the ST in a more detailed level reveals an important difference. In the HS, several vertical cracks took place in the upper edge of the URM infill wall due to the interaction with the RC beam of the bounding frame. These cracks are attributed to the limited flexural stiffness of the RC beam which tends to deflect vertically under the lateral load of the frame, causing contact in the compression corner and loss of contact in the far corner (Fig. 8.8). This deformed shape produces a cantilever action in the URM infill wall and vertical cracks are triggered. This phenomenon was first observed by

Mosalam (1996a) when testing steel frames with URM infill walls. In the ST experiments, this is not observed because of the much higher stiffness of the RC beam due to the effect of the connecting slab.

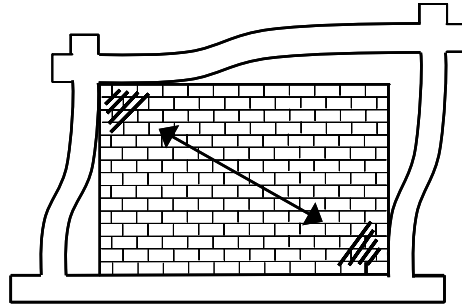
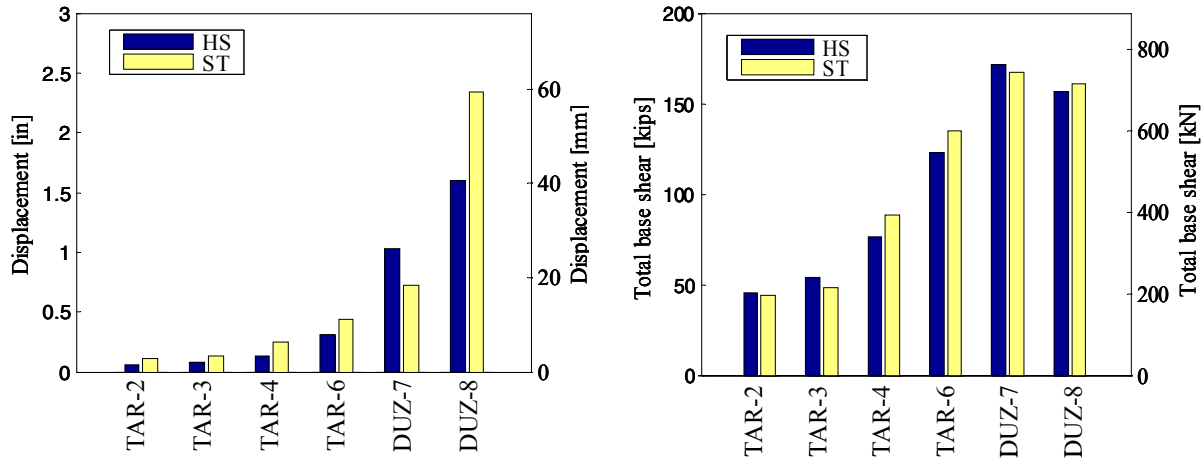


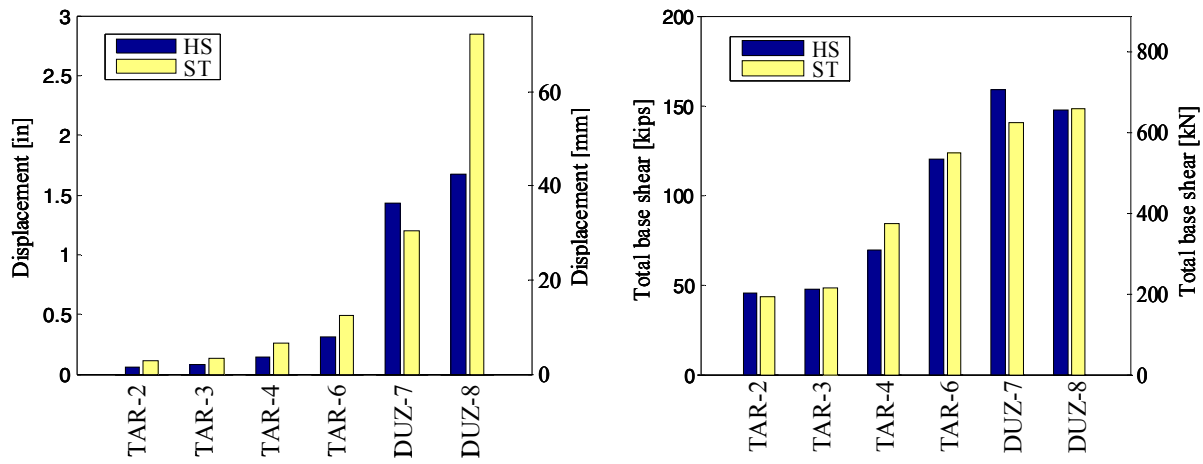
**Fig. 8.8 Deformation of URM infill wall and bounding RC frame.**

The peak global response, represented by the maximum total base shear at different levels of strong motion and its corresponding lateral displacement (Fig. 8.9(a)), as well as the maximum lateral displacement and its corresponding total base shear (Fig. 8.9(b)) are compared for the HS and ST experiments. Note that the plotted peak values for the two experiments do not necessarily occur at the same time during the application of the strong motion.

Up to TAR-6, where the response in the two experiments is close-to-linear with very few visible signs of damage or degradation, the peak lateral displacements in the ST experiment are distinctly larger than in HS (1.6 to 1.8 times larger), while the corresponding base shears are around the same magnitudes. This is in accordance with the higher tangent stiffness in HS, illustrated in Figure 8.5 and Table 8.3. In DUZ-7, the HS test structure is subjected to larger peak lateral displacement and peak base shear than those of the ST test and both URM infill walls in the two tests undergo major cracking. In DUZ-8, as discussed previously, the complete disintegration of the URM infill wall dynamically is accompanied by a larger lateral displacement demand, while pseudo-dynamically, the pseudo-velocity and pseudo-acceleration are not enough to dislocate the disintegrated parts of the URM infill wall. Therefore, much larger peak lateral displacement is recorded during DUZ-8 for the ST test than that for the HS test (Fig. 8.9).



(a) At peak base shear



(b) At peak lateral displacement

**Fig. 8.9 Peak global responses in HS and ST experiments.**

The lateral displacement time-history responses for TAR-6 in the two experiments using HS and ST are presented in Figure 8.10. While the trend of the strong motion is similar experiencing the same peaks, the pseudo-dynamic (HS) test structure lateral displacement is clearly smaller than that for the dynamic (ST) test. However, the total base shear matches more closely (Fig. 8.11), confirming the effect of the higher stiffness of the HS test structure than that for the ST test structure as discussed previously.

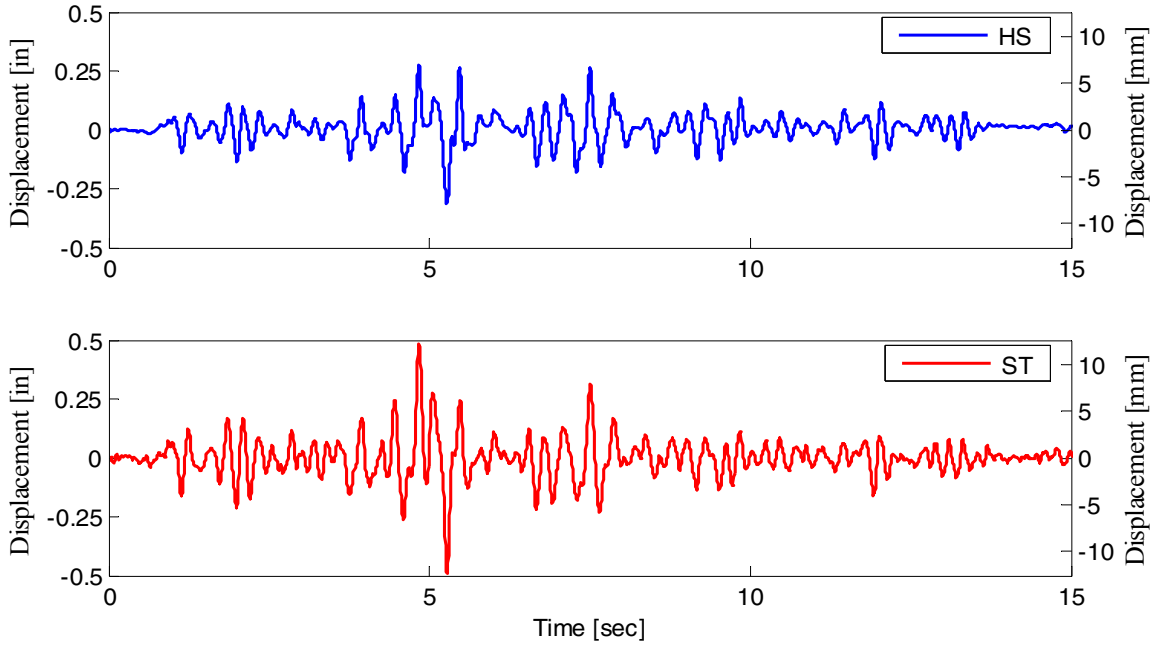


**Fig. 8.10 Displacement time histories for TAR-6.**

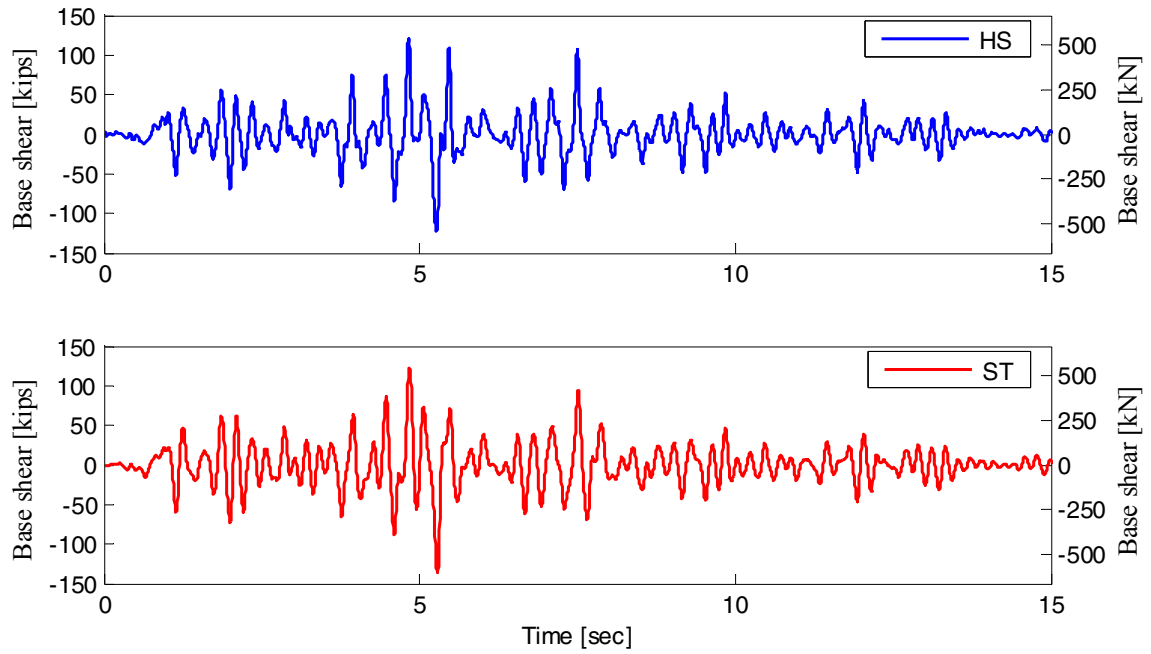


**Fig. 8.11 Total base shear time histories for TAR-6.**

## 8.2.2 URM Infill Wall Contribution

The URM infill wall contribution is estimated in the two experiments and presented in Figures 8.12(a)–(b) at peak base shear and at peak lateral displacement, respectively. While in HS, the restoring force in the wall  $F_w$  is computed as the difference between the restoring forces in the infilled and the bare frames which are readily available through the actuator force feedback measured by the load cells, the estimation of these forces for the ST test structure involves a number of procedures with underlying assumptions using measurements from accelerometers and reinforcing bars strain gages (Hashemi and Mosalam 2006, 2007). The same trend is observed in both experiments where the contribution of the URM infill wall is highest at the start of the experiment and decreases gradually as the URM infill wall deteriorates. The larger decrease is observed between TAR-6 and DUZ-7 as well as between DUZ-7 and DUZ-8 where the URM infill wall undergoes major damage and its structural contribution to the test structure decreases significantly. This is more apparent in Figure 8.12(b) where the peak lateral displacements correspond to later stages within the same run.

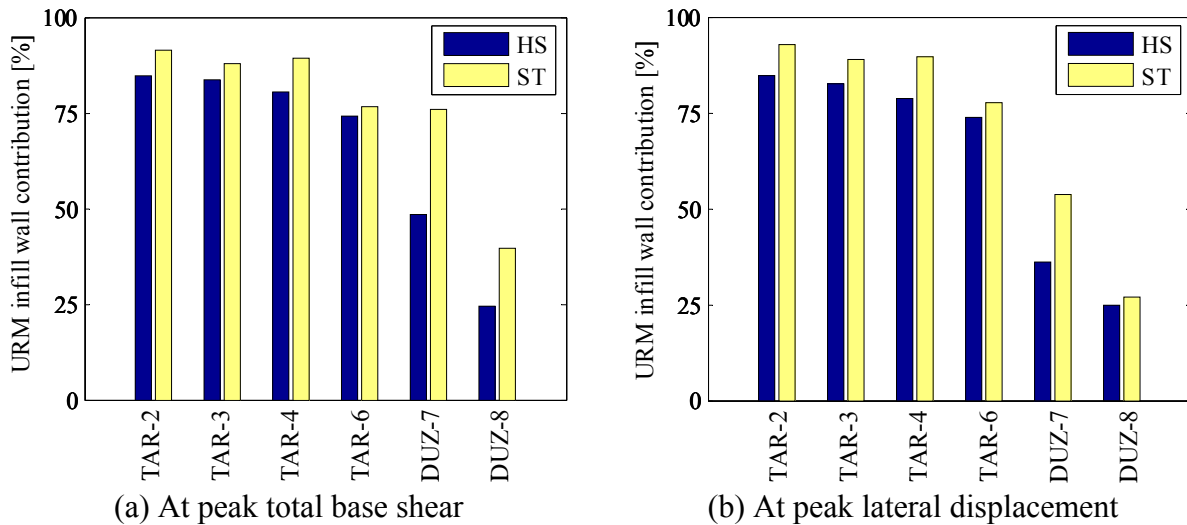


**Fig. 8.12 URM infill wall contributions to restoring forces in HS and ST experiments.**

The shear force  $F_w$  versus the shear strain  $\gamma$  of the URM infill wall panel is shown in Figure 8.13. In this figure,  $\gamma$  is calculated as shown in Figure 8.14, where  $\Delta_1$  and  $\Delta_2$  are determined using the diagonal displacement measurements in the plane of the URM infill wall. In TAR-6 (Figs. 8.13(a)–(b)), the two URM infill walls in the HS and ST experiments behave

very similarly (almost linearly) in terms of both magnitudes of shear strain and restoring force in the URM infill wall. Considering the much larger lateral displacement observed in the ST experiment (Fig. 8.10), which is also the case in the previous strong motion TAR-4, it is deduced that the URM infill walls are of similar stiffness and their behaviors match closely. Therefore, the difference in lateral displacement between the two test structures used in HS and ST experiments is mainly due to larger lateral displacement (in the range of 0.0 to 0.2 in. (5.1 mm)) in the ST experiment corresponding to the total base shear required to engage the URM infill wall to significantly contribute as a load-carrying element to the total restoring force. It is interesting to note that the positive and negative peaks near the time of 5 sec in Figure 8.10 are larger in the ST than the HS by about 0.2 in. (5.1 mm).

The larger lateral displacement in the ST experiment than in the HS may be attributed to a number of factors: (1) the inherent variability taking place during construction because of workmanship leading to a different level of tightness (filling) between the URM infill wall and the surrounding frame with higher filling in the HS test structure; (2) the level of damage at the corners of the URM infill wall where the impact between the wall and the surrounding frame occurs in the ST test structure at a higher velocity causing more damage and therefore creating a larger gap at the frame/wall interfaces; and (3) the different nature of the sliding mechanism and the associated static versus dynamic friction, for the respective HS versus ST tests, at the interface between the URM infill wall and the surrounding frame in the two experiments, whether at the corners or at the top and bottom edges. While in the HS experiment, the slow test rate causes the relative motion along the interface between the URM infill wall and the RC frame members to be controlled by the grinding of the particles of the two surfaces against each other to overcome the static friction, the sliding in the ST experiment is mainly controlled by the velocity at which the static friction is overcome resulting in a more staggered sliding pattern, (Fig. 8.15(b)). The outcome of the above three factors is that the surrounding RC frames in the ST test structure deform more than those in the HS test structure. Therefore, it is concluded that the reason for the higher stiffness in the HS than in ST experiment, discussed in Section 8.2.1 (see Fig. 8.5), is due to the above-mentioned factors rather than to a mere difference in material properties.

Another potential source of discrepancies in the response of the two test structures for the HS and ST experiments is related to the way viscous damping is modeled in the HS experiment. As stated earlier, the numerical model for viscous damping in the HS case is assumed constant

(6.2% of the critical damping in the first mode of vibration) over the entire duration of the experiment and is evaluated based on snap-back test results conducted on the undamaged ST test structure. The estimation of viscous damping in the case of the ST test structure (Hashemi and Mosalam 2006, 2007) shows a changing damping ratio (3% to 13%) as the test progresses and the state of the test structure deteriorates.

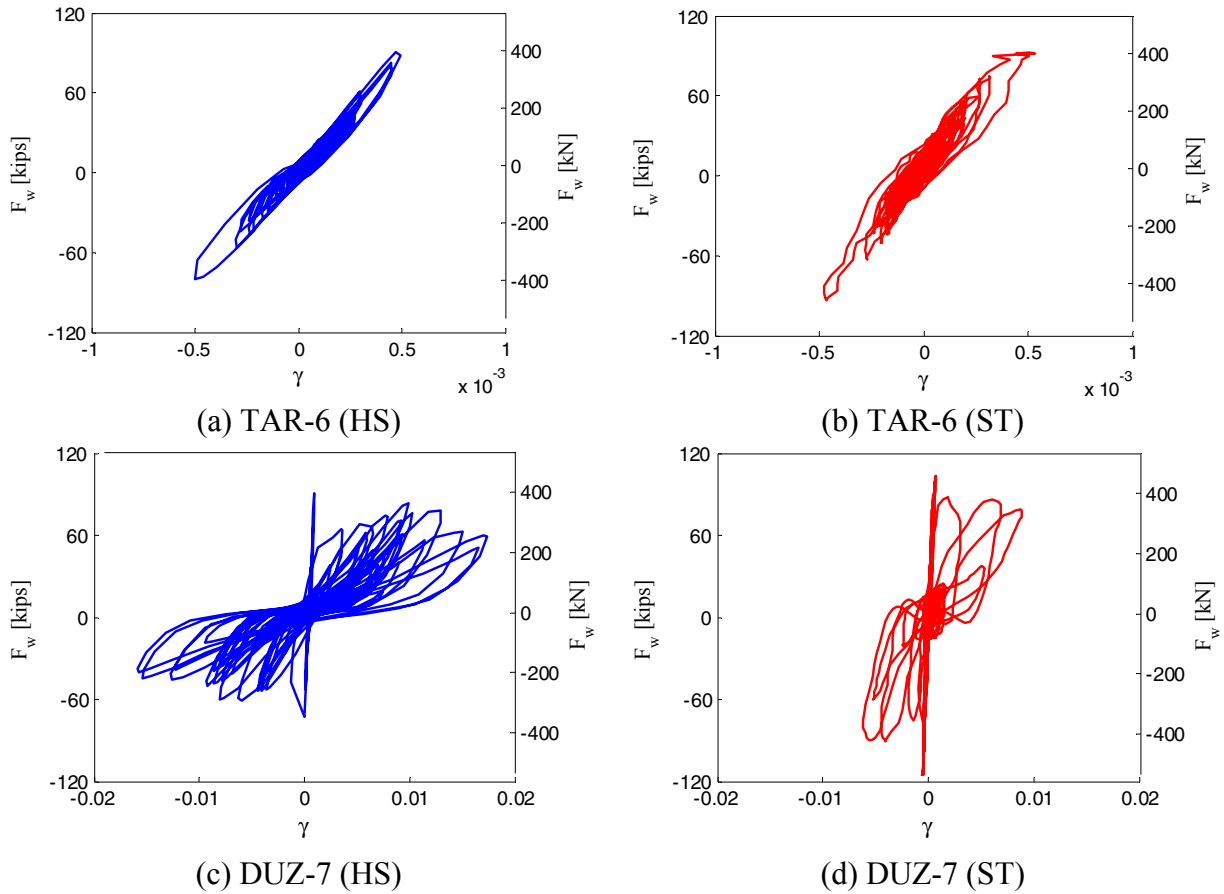


**Fig. 8.13** Shear force versus shear strain of URM infill wall.

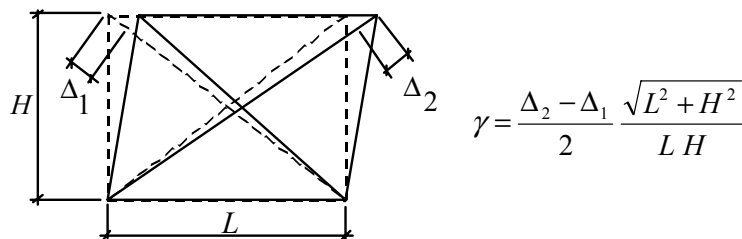


**Fig. 8.14** Estimation of shear strain from diagonal measurements ( $\Delta_1$  and  $\Delta_2$ ).

In DUZ-7 (Figs. 8.13(c)–(d)), although the shear forces in the URM infill wall are quite similar, the shear strain of the HS test structure is almost double the one recorded in the ST test structure. This is attributed to the different cracking pattern in both experiments observed after DUZ-7 (Figs. 8.7(a)–(b)). While diagonal cracking is quite similar, one major horizontal crack is observed in the dynamic test, while an additional horizontal crack is observed in the pseudo-dynamic test. This leads to additional planes of lateral motion for the URM infill wall in the HS test than that in the ST test and accordingly results in a more flexible URM infill wall mechanism leading to larger shear strains. The larger shear strains developed in HS than in ST explain the two exceptions in Table 8.3 where  $K_{F2}$  in DUZ-7 and  $K_P$  in DUZ-8 are larger for the ST test structure, opposite to what is observed in all the other cases as discussed previously.

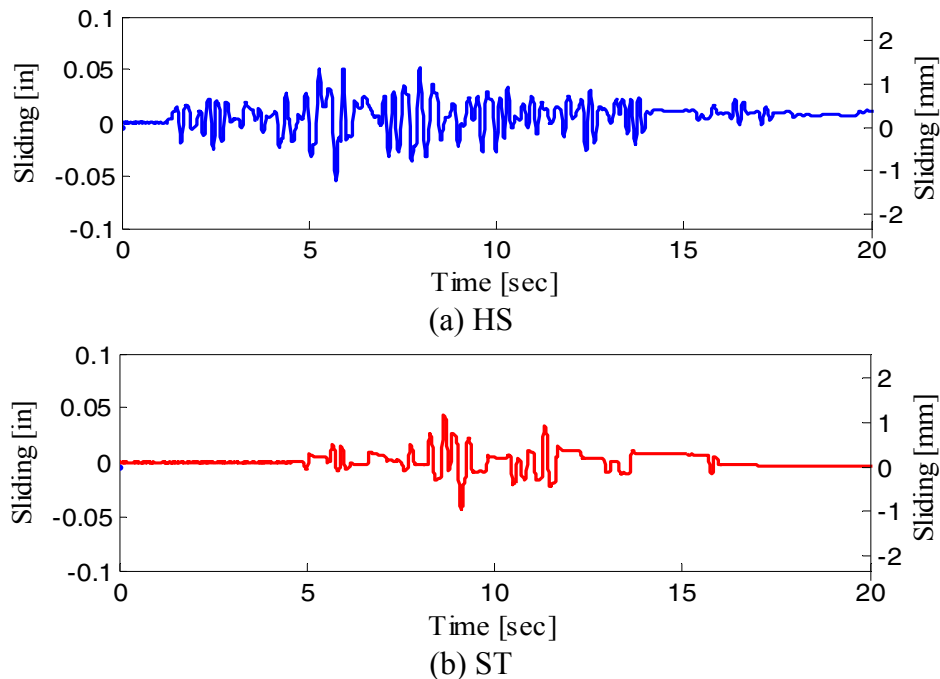


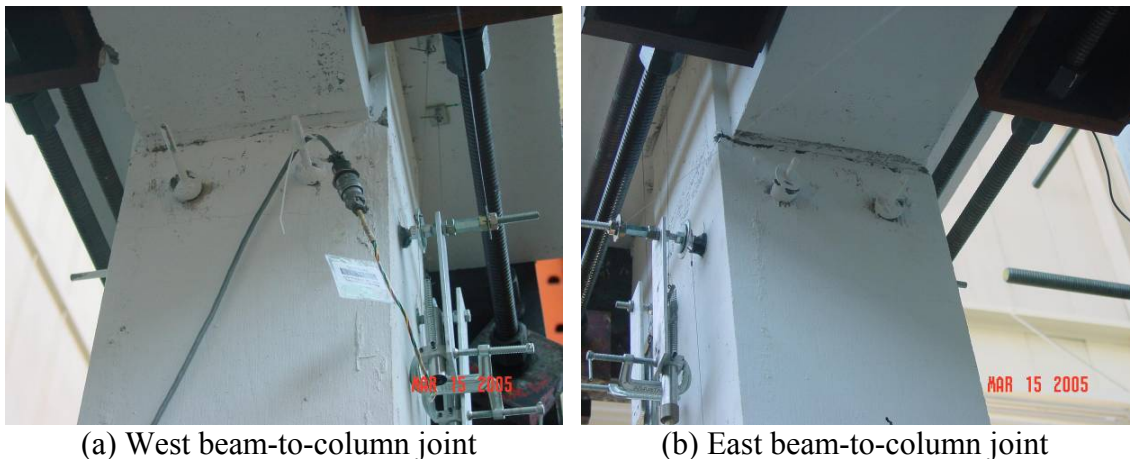
**Fig. 8.15 URM infill wall sliding on bottom interface with respect to surrounding RC frame, TAR-6.**

In addition to the increase in the observed shear strain, the additional horizontal (bed joint) crack causes the URM infill wall to swell (dilate) vertically more than in the case of the ST test structure. This increased dilation causes the URM infill wall to push against the top and bottom RC frame members. The consequence of that phenomenon is two fold: (1) the friction at the bottom and lower interfaces of the URM infill wall and the bounding frame is enhanced

further, supporting the earlier comments in that regard, and (2) the contact between the URM infill wall and the top beam becomes stronger in the middle, where the horizontal cracks occur, than at the corners, supporting the previously discussed cantilevering action which causes the vertical splitting cracks in the URM infill wall near its upper edge.

### 8.3 TEST STRUCTURE A: PHASES S-2 AND S-3

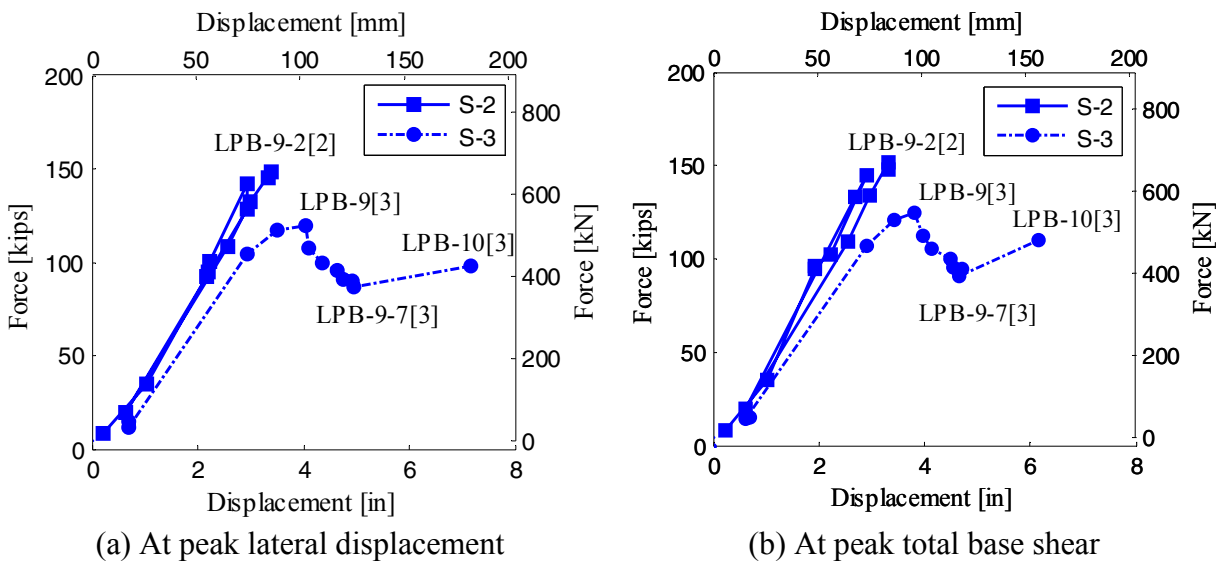
Phases S-2 and S-3 (see Fig. 1.2) are applied to test structure A after the collapse of the URM infill wall and its complete removal. At the end of phase S-1, the RC test structure, frame F2B (refer to Section 4.3) shows minor signs of visible damage at the west and east beam-to-column joints (Fig. 8.16), where the north direction is identified in Figure 4.16(a). As stated earlier, the test structure is excited by a set of strong motions in phase S-2 (see Fig. 4.4), where the columns post-tensioning axial force is maintained. On the other hand, at the start of phase S-3, the post-tensioning force is removed and a new set of strong motions is applied, (see Fig. 4.4).



**Fig. 8.16 Observed damage in RC frame at beginning of phase S-2.**

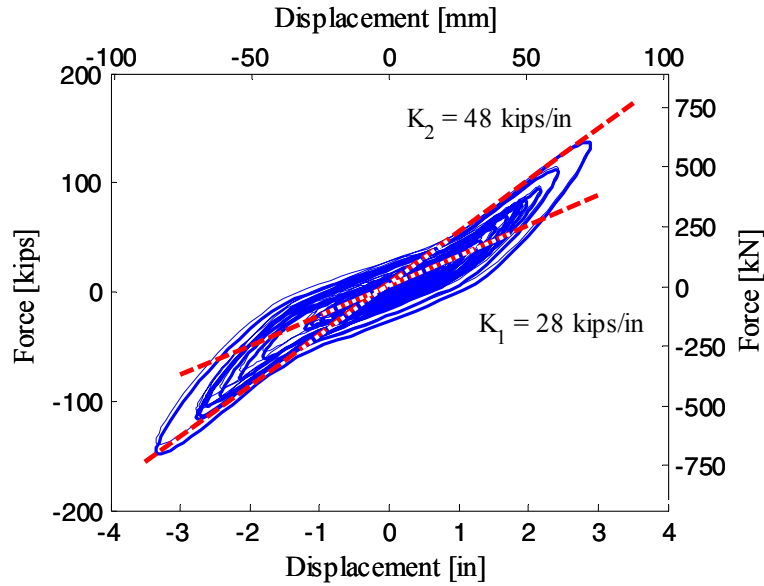
Figure 8.17(a) shows a plot of the peak lateral displacement and its corresponding total base shear, while Figure 8.17(b) is a plot of the peak total base shear and its corresponding lateral displacement, throughout phases S-2 and S-3. The maximum lateral displacement recorded in phase S-2 during LPB-9-2[2] is 3.35 in. (85.1 mm) corresponding to 3.0% story drift and the maximum recorded base shear is 151.6 kips (674.4 kN) during LPB-9[2]. After the removal of the post-tensioning force in the columns, and at the end of phase S-3, the maximum

lateral displacement increases significantly, reaching 4.94 in. (125.5 mm) during LPB-9-7[3] corresponding to 4.5% story drift and 7.17 in. (182.1 mm) during LPB-10[3] corresponding to 6.5% story drift, and the maximum base shear is reduced to 90.9 kips (404.3 kN) during LPB-9-7[3] implying a significant degradation in strength and stiffness of the RC frame.



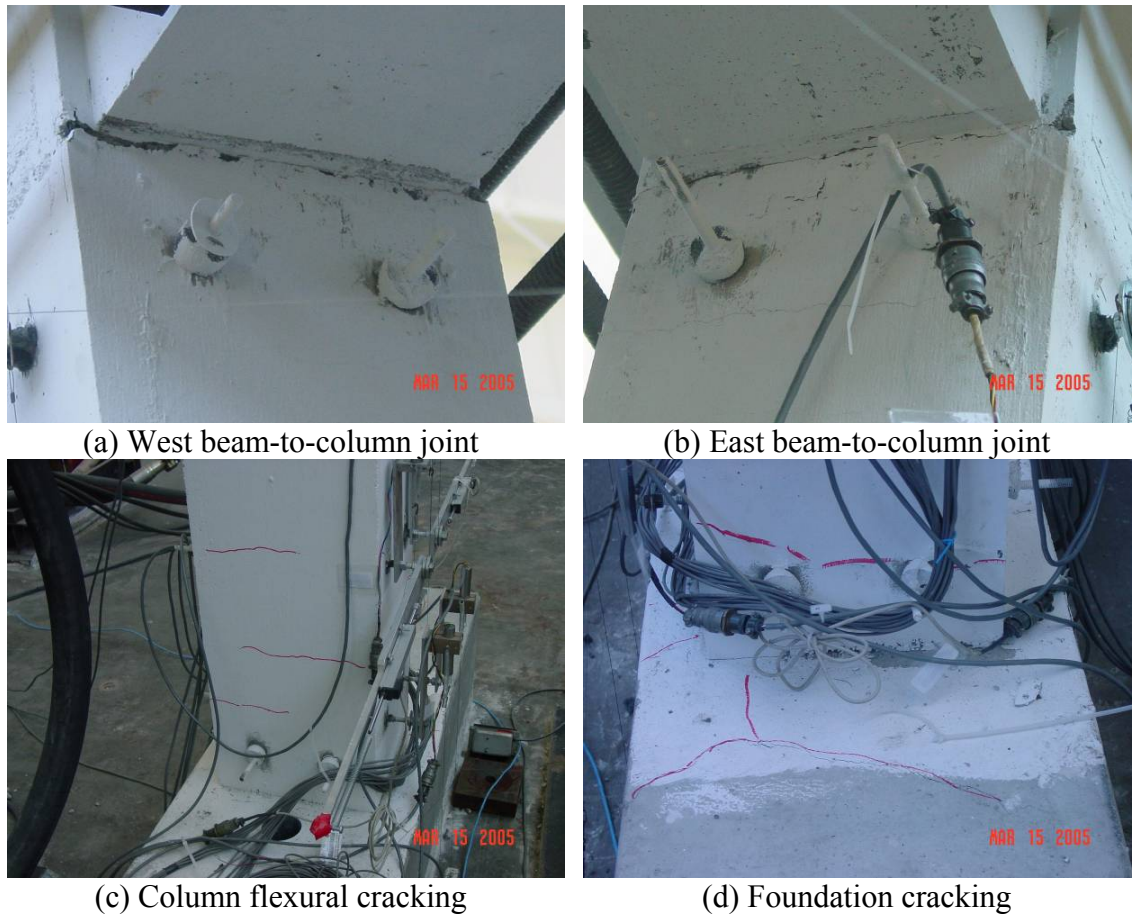
**Fig. 8.17 Peak lateral displacement and peak total base shear for phases S-2 and S-3.**

Figure 8.18 shows the total base shear versus lateral displacement relationship for level LPB-9-2[2]. The bilinear behavior characterizing the response is attributed to the damage developed in the foundations of the RC test structure, thus developing plastic hinges at these column-to-footing joints. The low tangent stiffness  $K_1 = 28$  kips/in. (4.9 kN/mm) is observed to dominate up to  $\pm 1$  in. ( $\pm 25.4$  mm), i.e., in the range of lateral displacement where the plastic hinges are developing in the foundations. This range is determined by the extent of the reinforcing bars, yield penetration on the tension side, and the cracks closing on the compression side. A higher stiffness  $K_2 = 48$  kips/in. (8.4 kN/mm) is estimated beyond that range, with an increase of 71% of  $K_2$  relative to  $K_1$ . Note that these stiffness values are estimated using the same procedure described in Section 8.1.1. Although the beam-to-column joints do not show any major signs of visible damage up to the completion of phase S-2 (Figs. 8.19(a)–(b)), visible flexural cracks are observed at this point in the RC columns, as well as in the foundation (Figs. 8.19(c) and (d), respectively).



**Fig. 8.18 Total base shear versus lateral displacement for test structure A, phase S-2 for level LPB-9-2[2] (1 kip/in.=0.175 kN/mm).**

In phase S-3 for level LPB-9-5[3],(Fig. 8.20), a reduction in stiffness is observed for both  $K_1 = 12$  kips/in. (2.1 kN/mm) up to approximately  $\pm 1.5$  in. ( $\pm 38.1$  mm) of lateral displacement, implying the extension of the yield penetration of the reinforcing bars, when compared to LPB-9-2[2] in phase S-2 (Fig. 8.18), and  $K_2 = 21$  kips/in. (3.7 kN/mm) beyond that lateral displacement. An increase of 75% of  $K_2$  relative to  $K_1$  is recorded in LPB-9-5[3], phase S-3, compared to 71% in LPB-9-2[2], phase S-2. At this point spalling of concrete cover to the reinforcing steel in the RC footing is extensive and the concrete of the footing disintegrates at the column-to-footing joint (Figs. 8.21(c)–(d)).



**Fig. 8.19 Observed damage at end of phase S-2.**

Note that although the RC test structure is subjected to significant lateral story drift reaching 6.5% and the stiffness  $K_2 = 21$  kips/in. (3.7 kN/mm) of the test structure is reduced to only about 17% of the undamaged bare test structure (three frames with 41 kips/in. (7.2 kN/mm) per frame, i.e., 123 kips/in. (21.5 kN/mm)), the extent of damage at the column-to-beam joints is very moderate at the end of phase S-3 (Figs. 8.21(a)–(b)). This is attributed to the post-tensioning force used to attach the RC beam to the actuator (see Section 4.8.4), which forces the columns to behave as almost fixed from top and hinged (because of the formation of plastic hinges in the footings) at the bottom, thus reducing the amount of rotation and damage at the top, i.e., beam-to-column joints. While these boundary conditions lead to higher bending moments in the beam-to-column joints, the post-tensioning force and the seismic reinforcement detailing of the beam-to-column joints (see Fig. 4.7) limit the extent of damage.

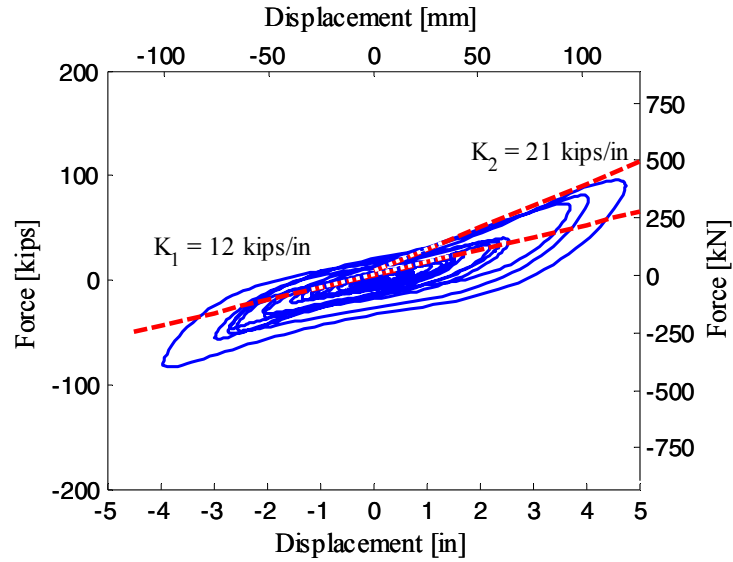


**Fig. 8.20 Total base shear versus lateral displacement for test structure A, phase S-3 for level LPB-9-5[3] (1 kip/in.=0.175 kN/mm).**

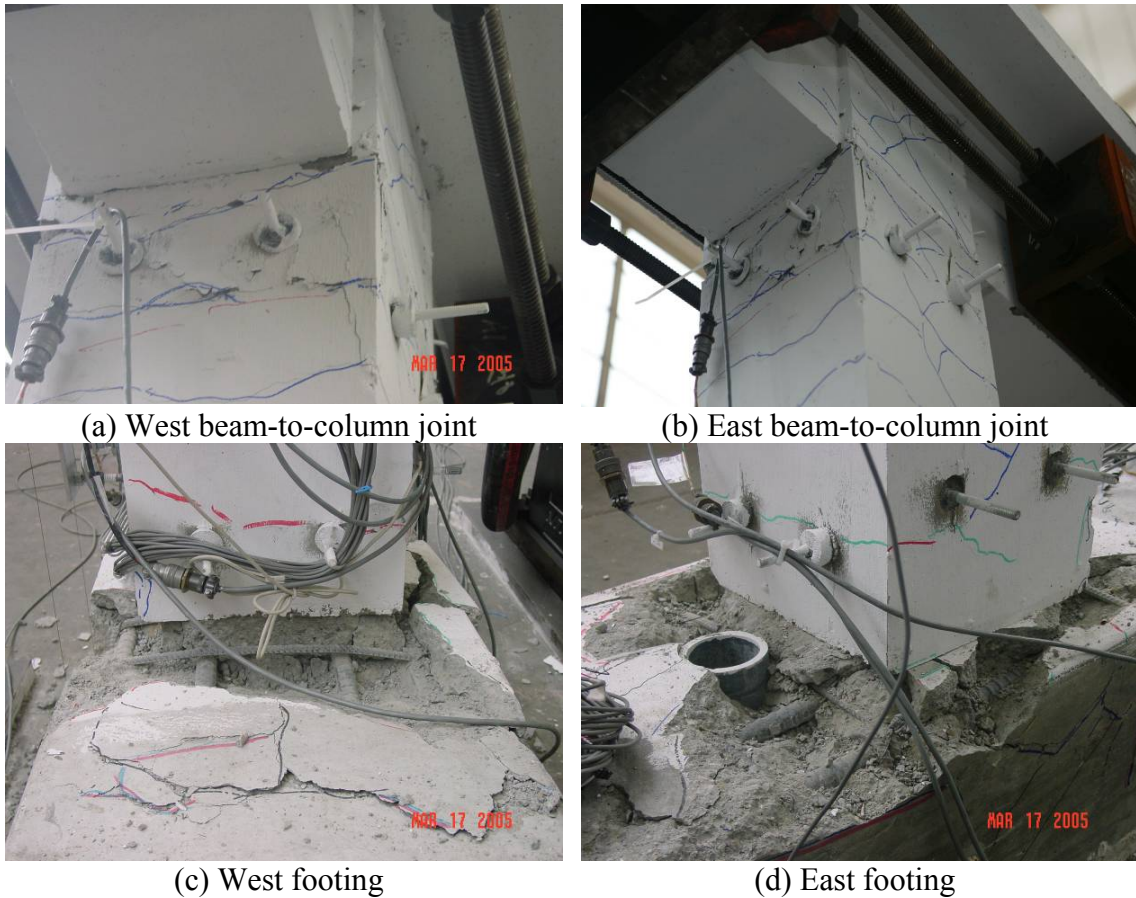


**Fig. 8.21 Observed damage at end of phase S-3.**

The rotations between the beam and columns at the top joints and those between the columns and the footings at the bottom joints are evaluated using the data from the displacement transducers located at the top and bottom of each column (see Section 4.5). The joint rotation (Fig. 8.22) is calculated as  $\theta = (u_1 - u_2)/d_2$ , where  $u_1$  and  $u_2$  are the vertical displacements measured by the two displacement transducers at the same elevation defined by the distance  $d_1$ , and  $d_2$  is the horizontal distance between them. The rotation time histories at the top and bottom east column joints of the physically tested RC frame are shown for LPB-9-2[2] in phase S-2 (Fig. 8.23(a)) and LPB-9-5[3] in phase S-3 (Fig. 8.23(b)). From Figure 8.23, the ratio between top and bottom rotations is significantly higher in phase S-3 than in phase S-2, thus confirming the above reasoning related to the column boundary conditions. These fixed-hinged boundary conditions of the RC columns can be observed in Figure 8.24 where the shown photograph of the RC frame is taken while it is highly deformed at the peak lateral displacement for level LPB-10[3] at the end of phase S-3.

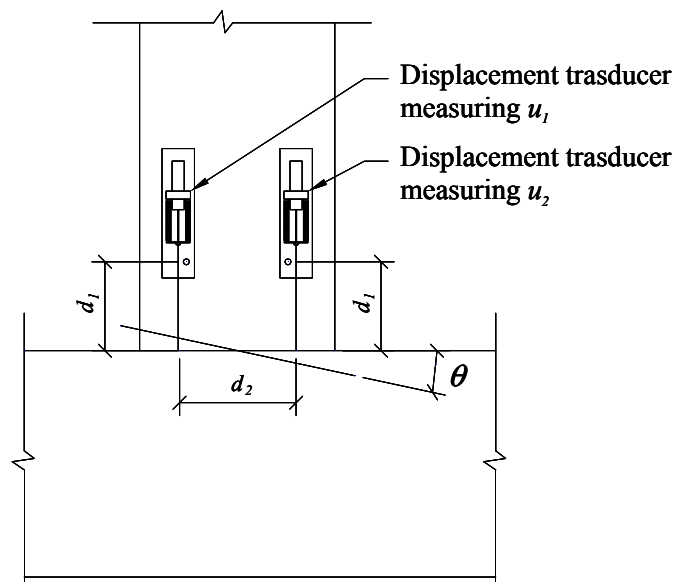
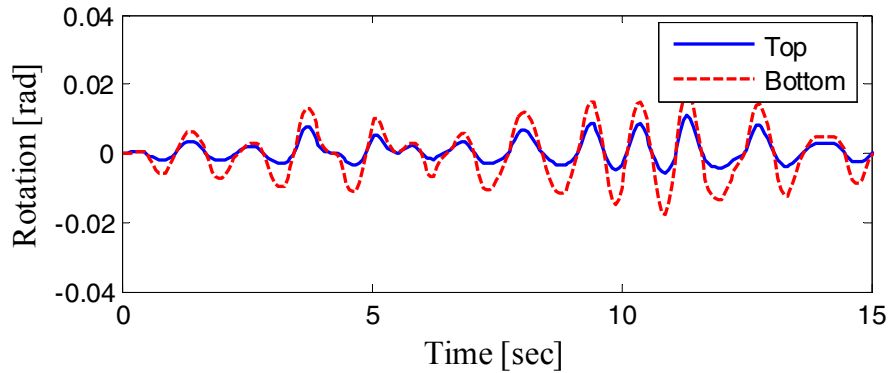


**Fig. 8.22 Rotation measurement in RC column-to-footing joint.**

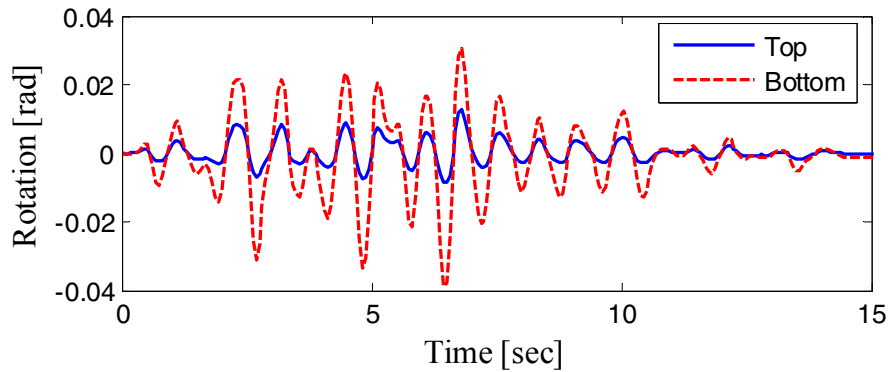
#### **8.4 COMPARISONS TO ST EXPERIMENTS: PHASES S-2 AND S-3**

The peak lateral displacements and the corresponding total base shears as well as the peak recorded base shears and the corresponding lateral displacements are compared for the two experiments, namely HS and ST, in phase S-2 (Fig. 8.25) and in phase S-3 (Fig. 8.26). Note that

the sequence of strong motions applied in the two experiments in phase S-2 is not similar, with seven repetitions of LPB-9[2] in the ST experiment and only two in the HS experiment. Therefore, the accumulation of damage in the ST test structure is more accentuated than for the HS test structure.



(a) Phase S-2 for LPB-9-2[2]



(b) Phase S-3 for LPB-9-5[3]

**Fig. 8.23 Top (beam-to-column) and bottom (column-to-footing) joint rotations for east column.**

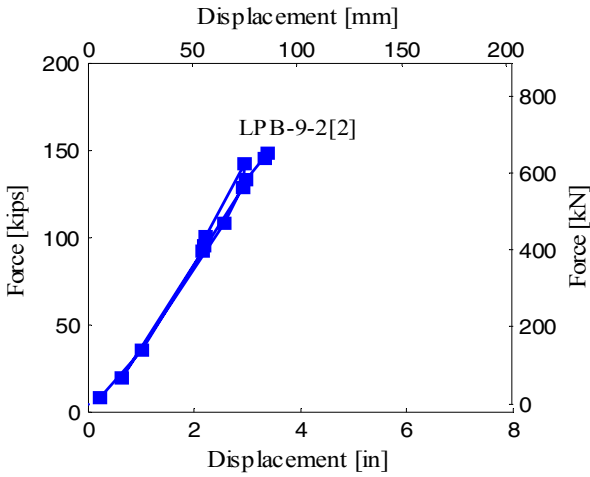
However, comparing the peak lateral displacements for the two test structures in the first repetition of LPB-9[2], the lateral displacement of the HS test structure (3.38 in. (83.3 mm)) is 38% smaller than the one recorded in the ST test structure (5.28 in. (134.1 mm)) while the total base shear is comparable. This is attributed to (1) the post-tensioning of the RC beam of the HS test structure, which limits the rotation at the beam-to-column joints and thus reduces the overall lateral displacement of the HS test structure and (2) at this high level of story drift ratio, e.g., 4.8% in LPB-9[2] and 6.9% in LPB-9[3] in the ST experiment, whether in phases S-2 or S-3, the P- $\Delta$  effect in the ST experiment, where an additional mass is attached at the RC slab level of the

test structure to simulate the weight of the upper stories in the prototype structure (Mosalam and Hashemi 2006, 2007), may be a contributing factor to the increased lateral displacement, while in the HS experiment, where the mass is only numerically simulated, this P- $\Delta$  effect is absent.

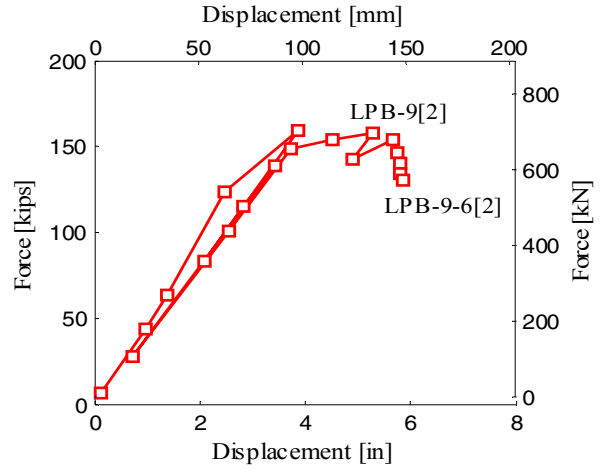


**Fig. 8.24 East column deformed shape at end of phase S-3, LPB-10[3].**

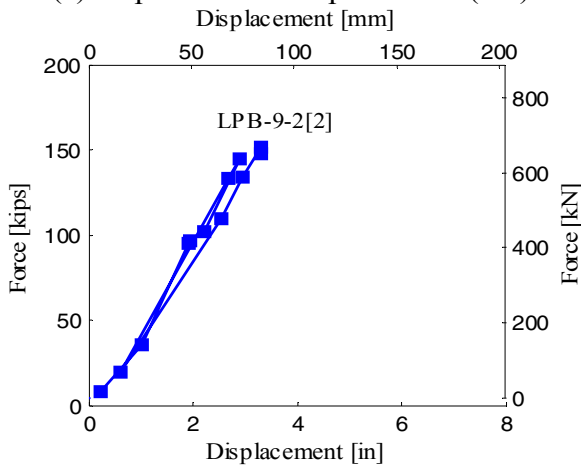
The extent of damage observed in the beam-to-column joints is greater in the case of the ST experiment than that of the HS experiment, as shown in Figures 8.27(a)–(b)), while the damage in the footings is more comparable (Figs. 8.27(c)–(d)). Note that the strong motion LPB-10[3], phase S-3, is applied in the HS experiment, while in the ST experiment the limits of the table in terms of imposed ground displacements at the ST level did not allow this level of strong motion to be applied. The photograph of Figure 8.27(c) corresponds to this higher-level strong motion. Therefore, more concrete spalling is shown in Figure 8.27(c) than that in Figure 8.27(d) for the ST after LPB-9-4[3].



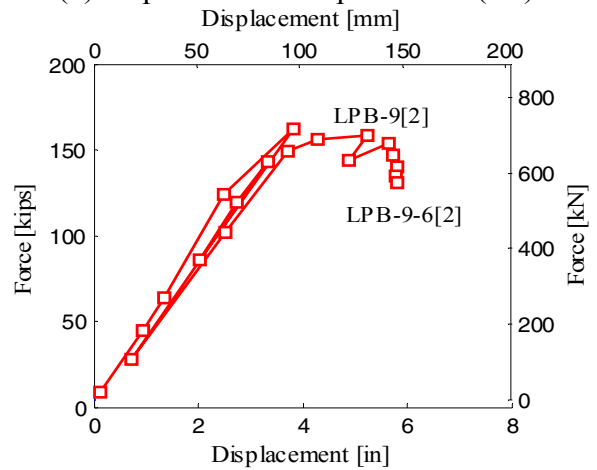
(a) At peak lateral displacement (HS)



(b) At peak lateral displacement (ST)

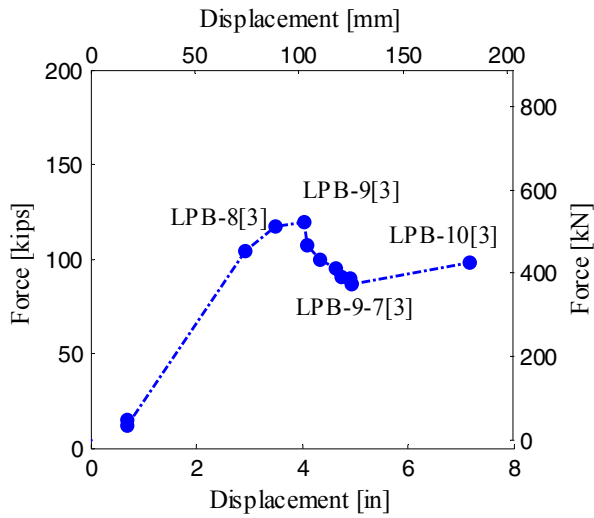


(c) At peak total base shear (HS)

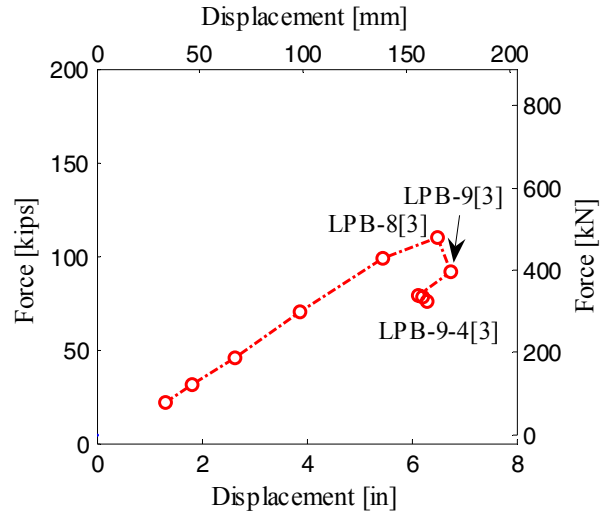


(d) At peak total base shear (ST)

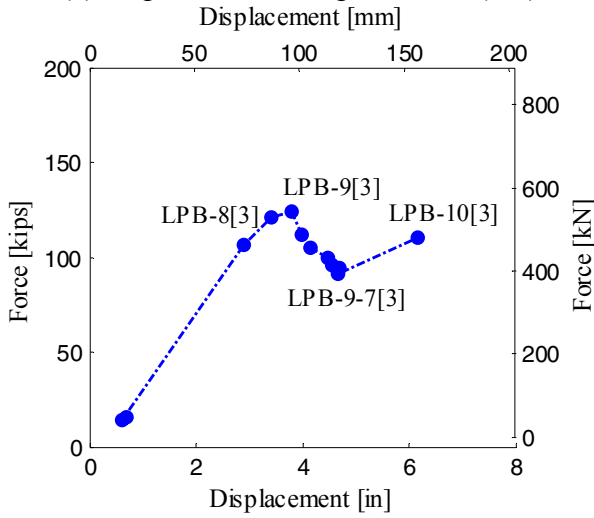
**Fig. 8.25 Peak lateral displacement and peak total base shear relationships for test structure A, phase S-2.**



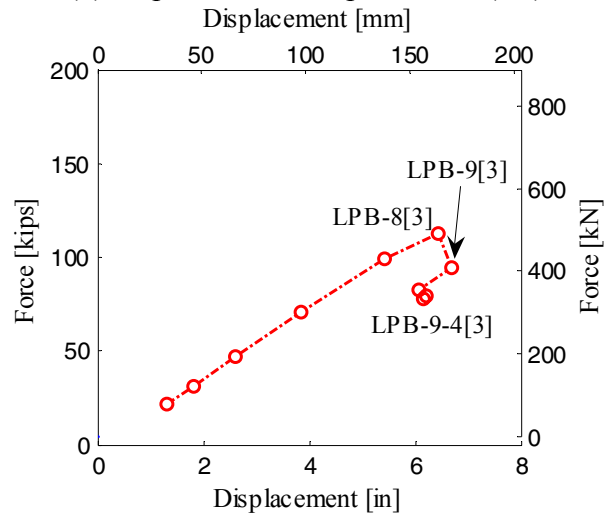
(a) At peak lateral displacement (HS)



(b) At peak lateral displacement (ST)



(c) At peak total base shear (HS)



(d) At peak total base shear (ST)

**Fig. 8.26 Peak lateral displacement and total base shear relationships for test structure A, phase S-3.**



(a) Beam-to-column joint (HS), LPB-10[3]



(b) Beam-to-column joint (ST), LPB-9-4[3]



(c) Column-to-footing joint (HS), LPB-10[3]



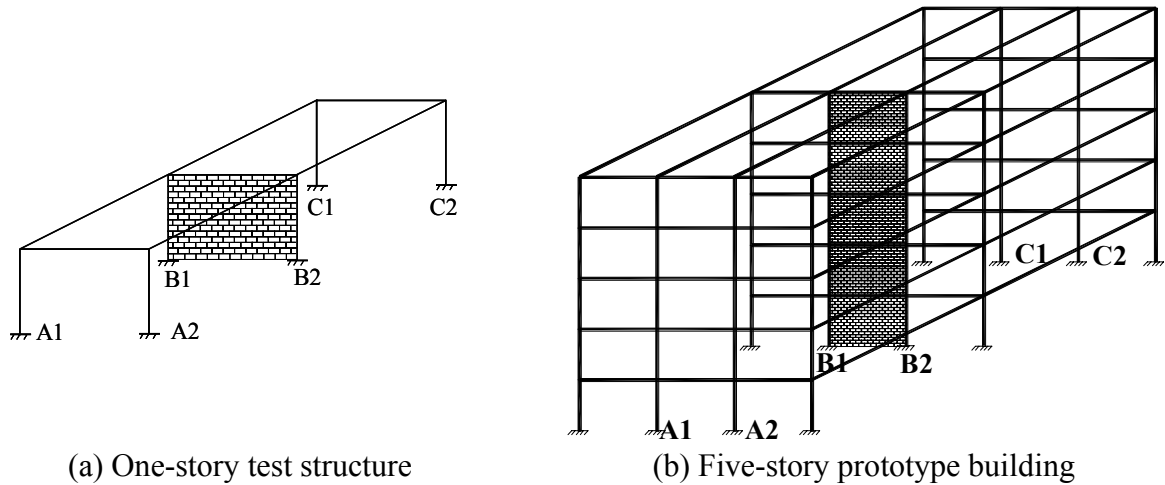
(d) Column-to-footing joint (ST), LPB-9-4[3]

**Fig. 8.27 Comparison of observed damage between HS and ST table test structures at end of phase S-3.**

## 8.5 CONTRIBUTION OF UPPER STORIES

Linear and nonlinear numerical modeling combined with the substructuring technique, within the generalized framework of HS, are employed in this section to conduct an auxiliary study that is otherwise not practically feasible in other testing methods such as the ST. Recalling that test structure A (Fig. 8.28(a)) is a substructure of a hypothetical five-story building (see Fig. 1.1), the contribution of the upper stories to the dynamic structural response is investigated herein. In phase S-1, it was observed that the URM infill wall controls the seismic response of test structure A, discussed in Section 8.1.2, to a greater extent. In the following, the response of the URM infilled frame is numerically modeled using a macro-element following the Bouc-Wen model

(Wen 1976; Baber and Wen 1981; Baber and Noori 1986) (see Appendix C). This numerical model is chosen for its versatility and flexibility in simulating the structural response of the nonlinear hysteretic behavior of the type exerted by the infilled frame.



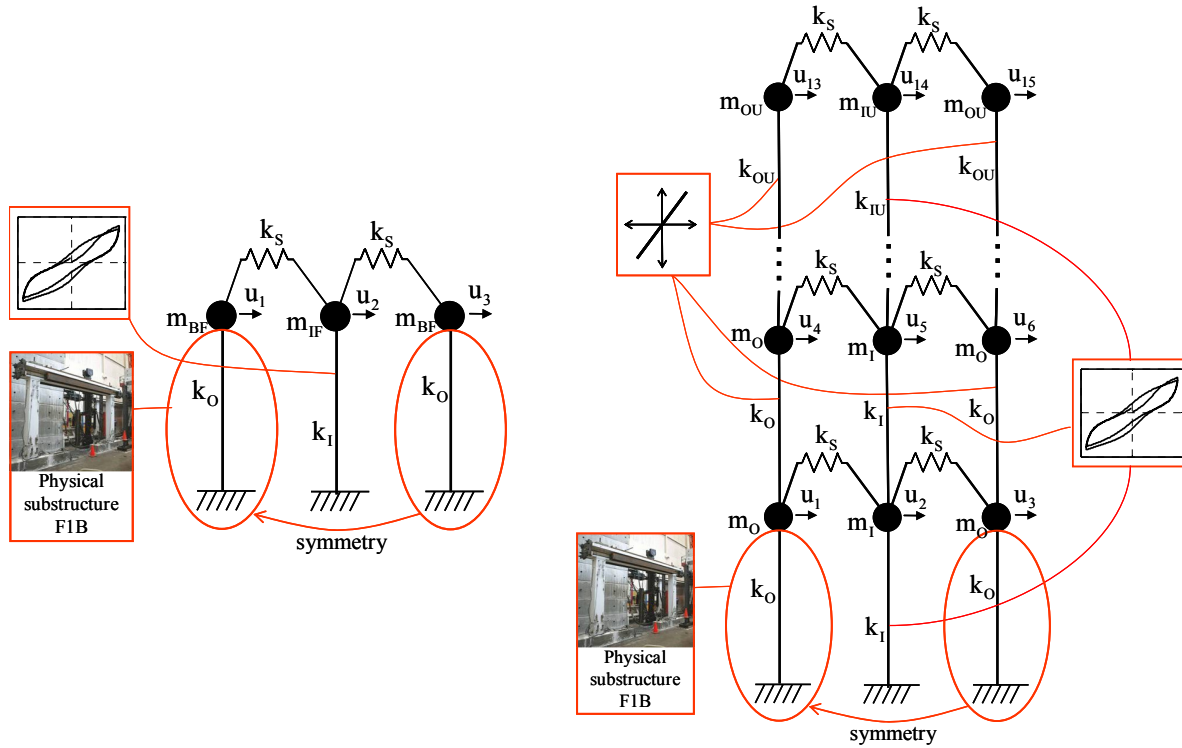
**Fig. 8.28 Schematic representation of test structures for quantifying contribution of upper stories**

Figure 8.28 illustrates test structure A and the corresponding hypothetical five-story building examined in this section, which are modeled as 3 DOF and 15 DOF systems (three for each floor), respectively, with the direction of motion parallel to the plane of the URM walls. Note that the simulated 15 DOF structure in this study is different from the prototype structure (see Fig. 1.1), where the middle bay frames are all infilled with URM walls. This simplified prototype is modeled using a calibrated Bouc-Wen model for the infilled frame, based on the HS experimental results in phase S-1 (see Section 8.1), as discussed later. Since this calibrated model for the middle bay infilled frame cannot be directly extended to model the adjacent infilled bays in the case of the original prototype model, this simplified prototype is considered in this section. The five-story building, depicted in Figure 8.28(b), is therefore adopted to serve the objective of the present study which is to assess the effect of the upper stories on the seismic response of the one-story test structure.

Figure 8.29 shows the idealized models of test structure A and the corresponding five-story structure. For the five-story structure, every group of three adjacent RC frames on one axis A, B, or C in the three adjacent bays, in Figure 8.28(b), are represented by one degree of freedom. This model assumes that the three frames are subjected to the same lateral

displacement, i.e., the RC beams are axially rigid. In this figure,  $m_o$  and  $m_I$  are the masses of the outer and inner frames (comprising the URM infilled frame), respectively, while  $k_o$ ,  $k_I$ , and  $k_s$  are the stiffness of the outer and inner frames and the connecting RC slab, respectively, and the added subscript  $U$  refers to these parameters at the upper (fifth) story where the adopted values are different due to assumed lower gravity loads on the roof and the corresponding lower stiffness of the RC columns. The adopted values of the different parameters, identified in Figure 8.29, are listed in Table 8.4, where damping is mass proportional with damping ratio  $\zeta$  for the first mode. In the case of the studied five-story structure, the adopted mass values are 45% of the ones for the original five-story prototype structure in Hashemi and Mosalam (2007). The stiffness values are 60% of the ones estimated for the original five-story prototype structure except for the stiffness of the middle bays  $k_I$  and  $k_{IU}$ , on axis B, where the stiffness of the outer URM infilled RC frames in the five-story prototype structure (Hashemi and Mosalam 2007) are replaced by the stiffness of the outer bare frames in the studied five-story structure. Note that the upper (fifth) story has smaller masses  $m_{oU}$  and  $m_{IU}$  than  $m_o$  and  $m_I$ , respectively, due to the smaller assumed dead and live loads on the roof than on the other floors. The stiffness  $k_{oU}$  and  $k_{IU}$  as well are smaller than  $k_o$  and  $k_I$ , respectively, due to smaller assumed inertial masses requiring smaller cross sections to resist the induced lateral load.

One bare frame at the middle bay of the first story, A1-A2 in Figure 8.28, is simulated by the physical substructure, F1B, and the other bare frame in the middle bay on the first story, C1-C2, is simulated by symmetry. The outer bare frames in the first story and all the bare frames in the upper four stories are numerically simulated by linear springs while the URM infilled frames in all five stories are numerically simulated using the calibrated nonlinear Bouc-Wen model, Appendix C.



(a) One-story structure (3 DOF system)

(b) Five-story structure (15 DOF system)

**Fig. 8.29 Idealized computational models of test structures for quantifying contribution of upper stories.**

Two levels of strong motions are applied on the test structure representing two distinct states of degradation of the test structure, namely TAR-2 at the preliminary undamaged state and DUZ-8 after the development of a clear crack pattern in the URM infill wall (see Section 8.1.1). In each case, the strong motion is re-applied on a three-DOF one-story test structure (Figs. 8.28(a) and 8.29(a)), consisting of the middle bay of the first story in the five-story building for comparison purposes. In this one-story test structure, one bare frame, F1B, represents the physical substructure, while the other bare frame is simulated by symmetry and the URM infilled frame is numerically simulated using the aforementioned nonlinear Bouc-Wen model (see Appendix C). The masses of the bare frame  $m_{BF}$  and the infilled frame  $m_{IF}$ , as well as the respective stiffness values  $k_{BF}$  and  $k_{IF}$ , are listed in Table 8.4. Given the assigned parameters, the natural periods for the two test structures are identified in Table 8.5 by solving the eigenvalue problems of the two systems (see Section 4.13).

**Table 8.4 Parameters for quantifying of contribution of upper stories.**

Parameter	Value
$k_o$ [kip/in. (kN/mm)]	224 (39.2)
$k_I$ [kip/in. (kN/mm)]	827 (144.8)
$k_{OU}$ [kip/in. (kN/mm)]	131 (22.9)
$k_{IU}$ [kip/in. (kN/mm)]	750 (131.3)
$k_S$ [kip/in. (kN/mm)]	1650 (289.0)
$k_{BF}$ [kip/in. (kN/mm)]	37 (6.5)
$k_{IF}$ [kip/in. (kN/mm)]	640 (112.1)
$\zeta$ (%)	6.2
$m_o$ [kip-sec <sup>2</sup> /in. (kN-sec <sup>2</sup> /mm)]	0.072 (0.013)
$m_I$ [kip-sec <sup>2</sup> /in. (kN-sec <sup>2</sup> /mm)]	0.094 (0.016)
$m_{OU}$ [kip-sec <sup>2</sup> /in. (kN-sec <sup>2</sup> /mm)]	0.034 (0.006)
$m_{IU}$ [kip-sec <sup>2</sup> /in. (kN-sec <sup>2</sup> /mm)]	0.068 (0.012)
$m_{BF}$ [kip-sec <sup>2</sup> /in. (kN-sec <sup>2</sup> /mm)]	0.070 (0.012)
$m_{IF}$ [kip-sec <sup>2</sup> /in. (kN-sec <sup>2</sup> /mm)]	0.106 (0.019)

**Table 8.5 Estimated natural periods (sec) for 3 DOF and 15 DOF systems.**

Mode	1	2	3	4	5
3 DOF system	0.119	0.040	0.026	N/A	N/A
15 DOF system	0.256	0.090	0.059	0.046	0.040

Figure 8.30 shows comparisons between the structural response of the 3 DOF and the 15 DOF systems represented by the restoring force versus lateral displacement of the numerically simulated first-story URM infilled frame. The differences are obvious in terms of the lateral displacement demand and the corresponding restoring force in the results shown from the applied two strong motions, TAR-2 and DUZ-8. However, while in TAR-2 the 15 DOF system deforms much more than does the 3 DOF system (88% more in peak lateral displacement demand), the opposite is true in the case of DUZ-8, with the 15 DOF system having 21% less in peak lateral displacement demand than that of the 3 DOF system, as reported in the last column of Table 8.6. This is attributed to the difference in the natural periods of the two structural systems and their corresponding spectral accelerations with respect to each of the two applied strong motions, as well as to the higher mode in the case of the 15 DOF system.

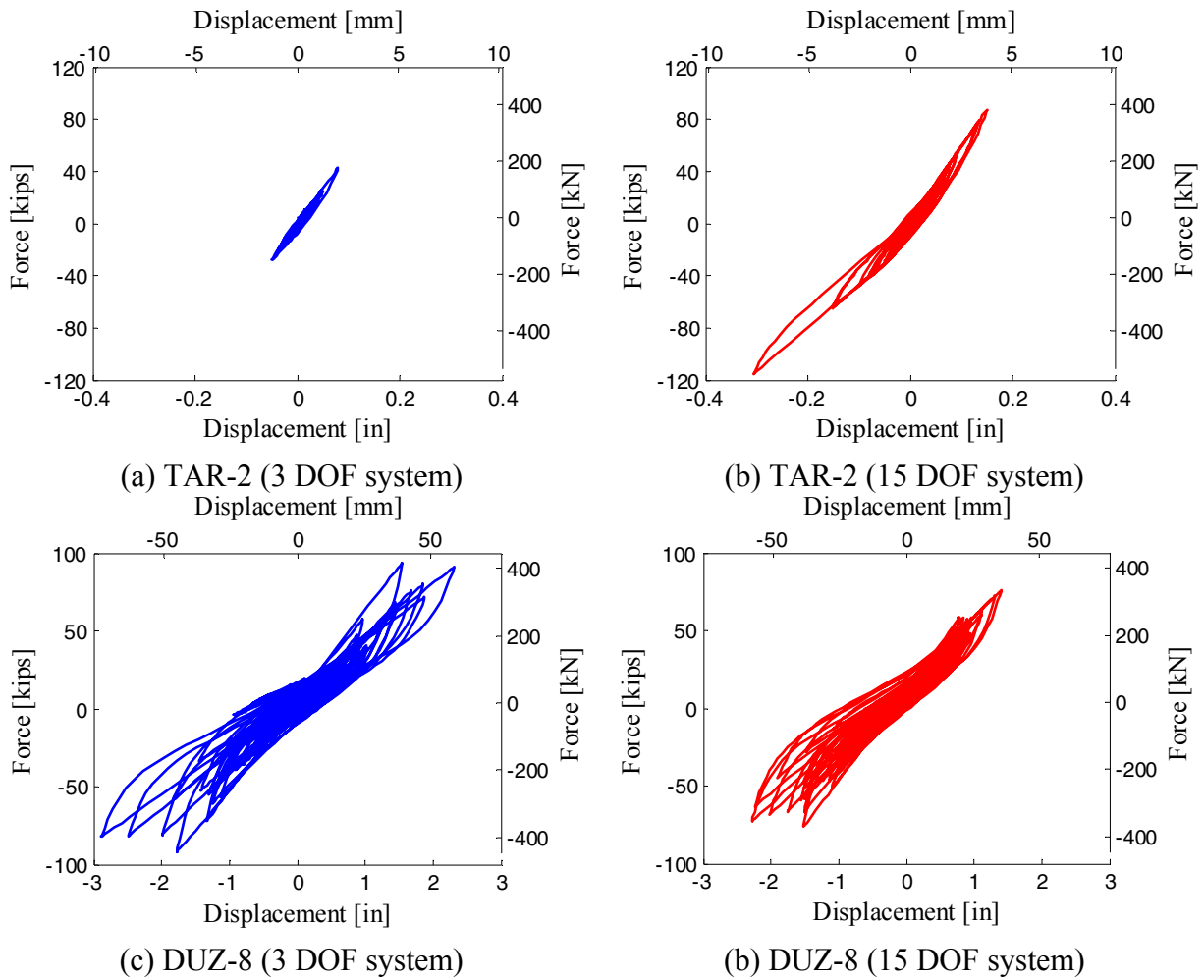


**Fig. 8.30 Restoring force versus lateral displacement of first-story URM infilled frame.**

The fundamental frequencies of each of the two test structures (Figs. 8.28–8.29) are deduced from the peaks recorded in the fast Fourier transform of the lateral displacement response normalized by the fast Fourier transform of the input strong motion, shown in Figure 8.31 for TAR-2, Figure 8.32 for DUZ-8, and Table 8.6. Each peak identified in Figures 8.31–8.32 is surrounded by a number of smaller valued peaks indicating the progressive degradation of the test structure along the time history of the applied ground motion, translated into a progressive change of the fundamental frequencies. Note the existence of more than one dominant fundamental frequency with high normalized fast Fourier transform ratio in the case of the 15 DOF system, while the 3 DOF system is dominated by the first mode response.

These fundamental frequencies of vibration are identified on the plots of the acceleration spectra by their corresponding fundamental natural periods for the two strong motions used, shown in Figure 8.33; the corresponding spectral accelerations are identified in Table 8.6. These

spectral values are rather consistent with the observed response discussed above. This is particularly true when taking into consideration another contributing factor to the observed difference in response between the 3 DOF and 15 DOF systems which are the higher-mode effects in the 15 DOF system. While the 3 DOF system is dominated by the first mode response, shown in Figures 8.31(a) and 8.32(a), the higher modes in the 15 DOF system contribute significantly to the response as demonstrated by the peaks observed in Figures 8.31(b) and Figure 8.32(b).

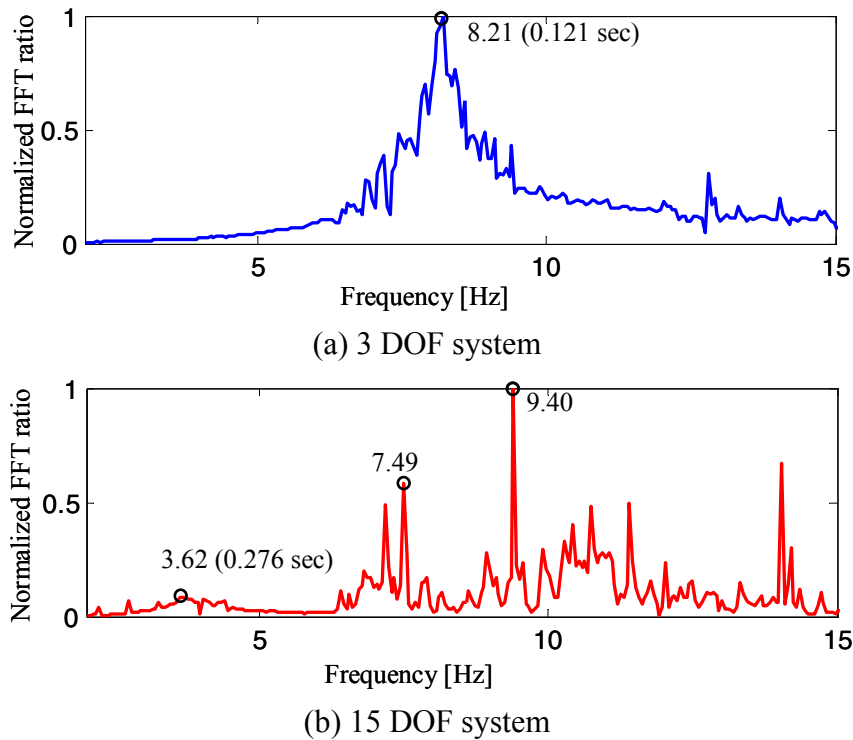


**Fig. 8.31** Evaluated fundamental frequencies of vibration in TAR-2 for different structural systems.

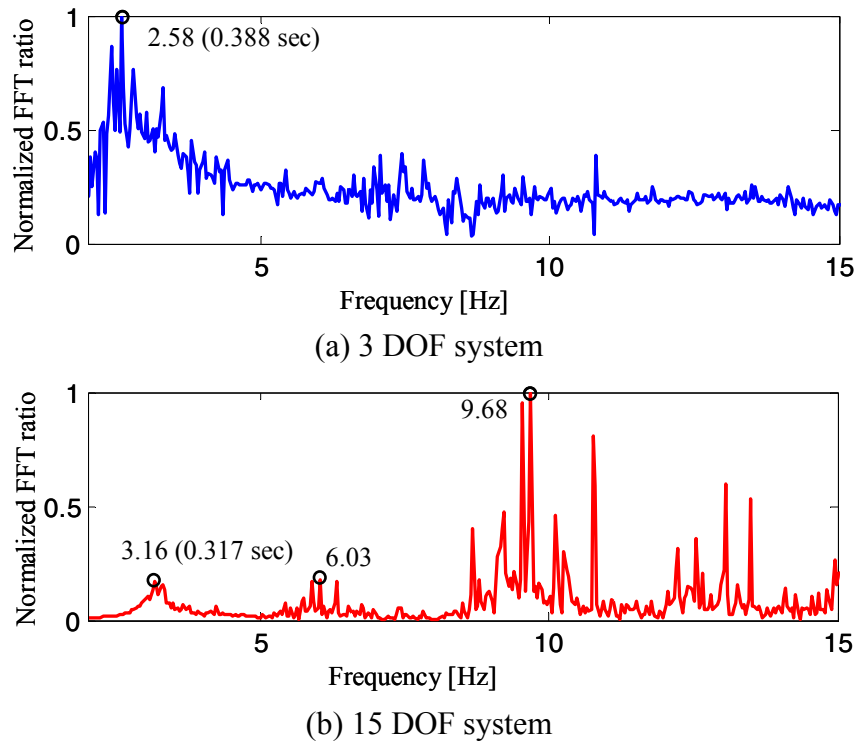


**Fig. 8.32** Evaluated fundamental frequencies of vibration in DUZ-8 for different structural systems.

**Table 8.6** Natural periods  $T_n$  and corresponding spectral accelerations  $S_A$ .

Strong Motion	3 DOF system		15 DOF system		Ratio (15 DOF / 3 DOF)	
	$T_n$ (sec)	$S_A$ (g)	$T_n$ (sec)	$S_A$ (g)	$S_A$	Peak lateral displacement demand
TAR-2	0.121	0.42	0.276	1.02	2.43	1.88
DUZ-8	0.388	2.66	0.317	3.38	1.27	0.79

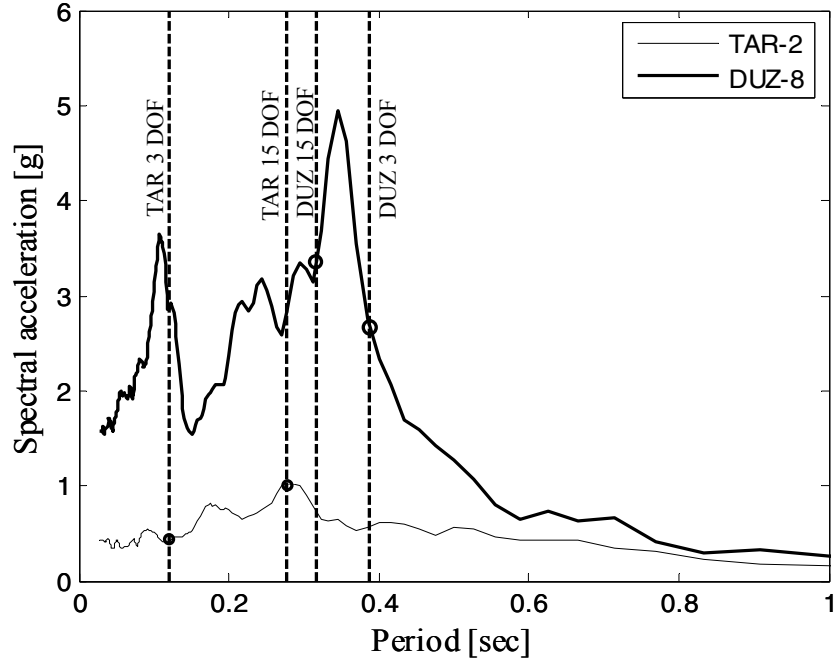


**Fig. 8.33 Spectral acceleration of applied strong motions (5% damping ratio) for quantifying contribution of upper stories.**

## 8.6 TEST STRUCTURE B

The seismic response of test structure B, namely the first-story shear walls of a two-story wood house with a garage opening in the first story is evaluated herein based on its response to three seismic motions applied in sequence. These strong motions are LPG levels 2, 4, and 6, refer to Tables 5.1–5.2, denoted LPG-2, LPG-4, and LPG-6, respectively, in the following discussion. A comparison is finally made between the responses of the HS test structure B and the corresponding ST test structure.

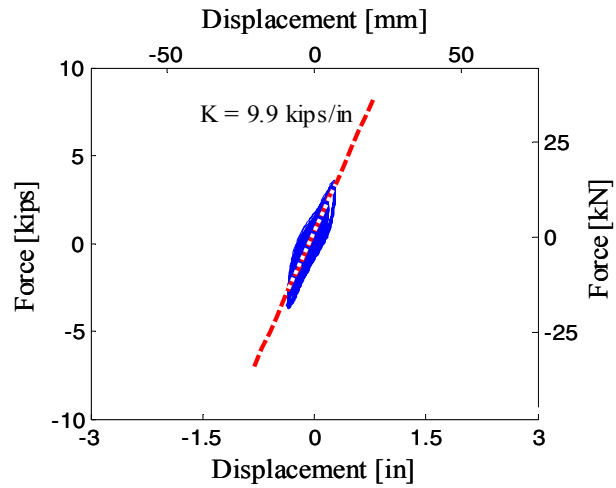
### 8.6.1 Force-Displacement Behavior

The total base shear, as defined in Section 8.1.1, is plotted versus the shear-wall lateral displacement for the three different levels of the applied strong motion LPG. As in the case of test structure A (see Section 8.1.1), the stiffness values in Figure 8.34 are estimated based on the tangent slopes at different stages of the applied strong motion evaluated over a number of lading branches using the least-squares method to obtain a best linear fit. In LPG-2 (Fig. 8.34(a)), the

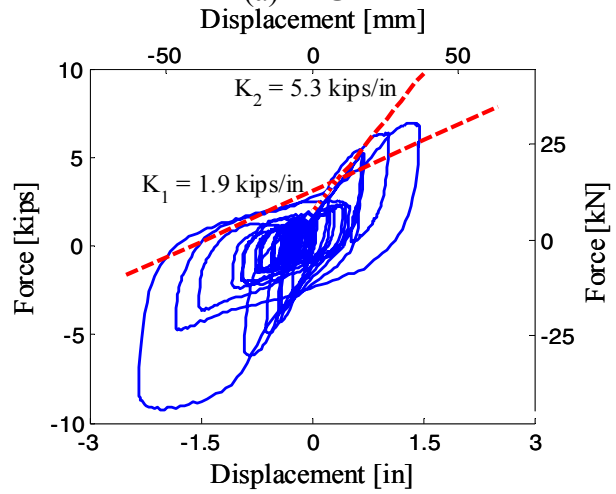
tangent stiffness is estimated as  $K = 9.9$  kips/in. (1.73 kN/mm) where the shear walls are still undamaged and behave almost elastically. As the level of shaking increases to LPG-4, the nails (fasteners) connecting the shiplap siding to the timber shear-wall framing (studs) (Fig. 8.35) are deformed beyond their elastic ranges and induce crushing in the framing, which creates a progressively expanding gap around the nail shank as the shear walls are cycled back and forth (Judd and Fonseca 2005; Dinehart and Shenton 2000; White and Dolan 1995).

A great reduction in stiffness of the shear walls, to  $K_1 = 1.9$  kips/in. (0.33 kN/mm), is observed in the range of shear-wall lateral displacement where the gaps surrounding the nail shanks are formed and the nails are deformed. The stiffness is higher beyond that range at  $K_2 = 5.3$  kips/in. (0.93 kN/mm), resulting in the pinching behavior observed in Figure 8.34(b). Note that at that point, the nails connecting the diagonal struts to the vertical studs are completely pulled out (Fig. 8.36(a)). The diagonal struts are therefore ineffective in shear resistance, contributing to a 46% reduction in stiffness, from 9.9 kips/in. (1.73 kN/mm) in LPG-2 to 5.3 kips/in. (0.93 kN/mm) in LPG-4.

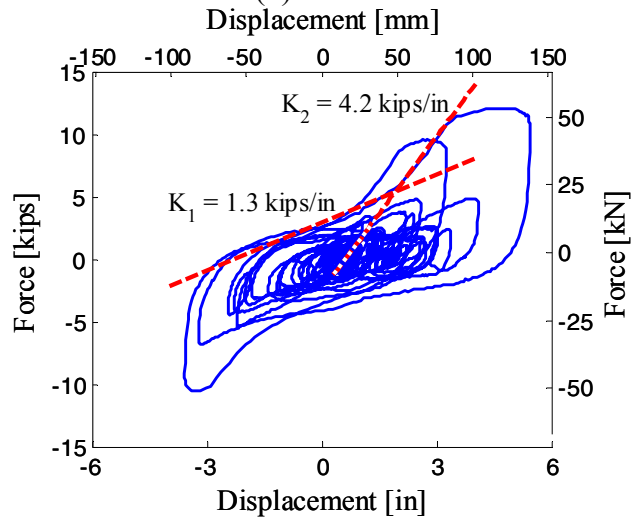
The behavior described above is taken to a greater level of lateral displacement of 5.4 in. (137 mm) in LPG-6, where the total base shear force reaches a maximum of 12.1 kips (53.8 kN) (Fig. 8.34(c)) and slight reductions in  $K_1 = 1.3$  kips/in. (0.23 kN/mm) and  $K_2 = 4.2$  kips/in. (0.74 kN/mm) are observed. The deformation of the shear-wall shiplap siding is characterized by a stair-like form, as shown in Figure 8.36(b), which is sustained for large lateral displacement as observed from the long plateau in the positive large excursion of Figure 8.34(c), along with a slight degradation of stiffness, as long as the nails are not completely pulled out of the framing studs.



(a) LPG-2



(b) LPG-4



(c) LPG-6

**Fig. 8.34 Total base shear versus lateral displacement for HS for test structure B (1 kip/in.=0.175 kN/mm).**

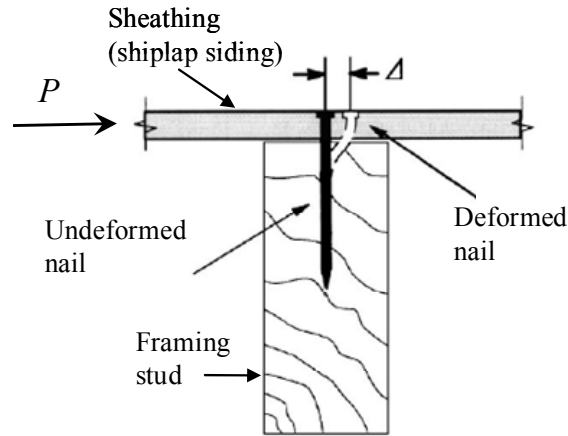


**Fig. 8.35 Framing-to-sheathing connection schematic of local deformation.**



(a) Diagonal strut dislocation (LPG-4)



(b) Stair-like deformed shape of shiplap siding (LPG-6)

**Fig. 8.36 Deformed shape of wood shear walls at peak lateral displacement.**

### 8.6.2 Comparison to ST Experiment

The HS results discussed in Section 8.6.1 are compared to the ST experimental results in this section, where two levels of strong motion are treated, namely, LPG-4 and LPG-6. In LPG-4 (Fig. 8.37), the same pinching behavior is observed in the ST experiment with similar estimated tangent stiffness values as in the HS experiment. The time-history plots for lateral displacement of the first story (Fig. 8.38) and for total base shear (Fig. 8.39) show a good match of behavior between the HS and the ST experiments for LPG-4 motion. Note that the displacement time histories are quite similar up to the peak recorded at 5 sec, where the HS test structure is subjected to a slightly larger lateral displacement (in the absolute sense) compared to the ST test

structure (-2.35 in. (-59.7 mm) in HS versus -1.98 in. (-50.3 mm) in ST). From this point on, a tendency of the HS test structure to deform on the negative side of the plotted displacement is observed resulting in a residual displacement of -0.35 in. (-8.9 mm) at the end of the strong motion.

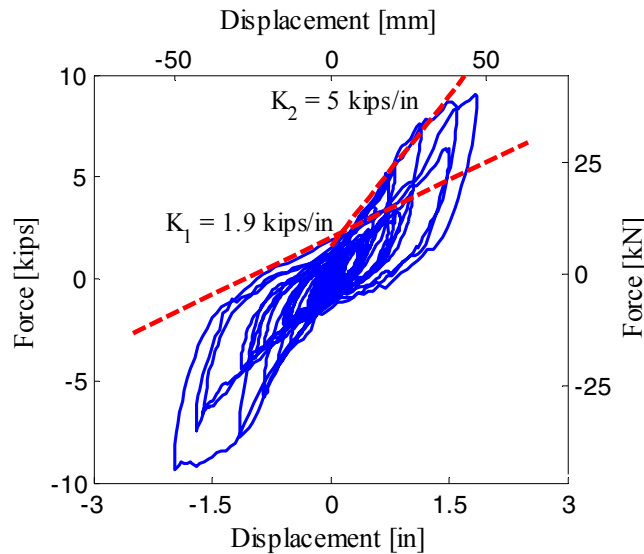


**Fig. 8.37 Total base shear versus first-story lateral displacement for test structure B for LPG-4 (ST experiment).**

In LPG-6, the responses once more show a similarity between the HS and the ST experiments in terms of the lateral displacement pattern of the first story and period of vibration (Fig. 8.40), as well as in the total base shear (Fig. 8.41). In the HS experiment, however, the test structure is left with a larger residual displacement of 1.84 in. (46.7 mm), while the ST test structure almost returns to the zero displacement position as observed in the previous level of LPG-4. Note that in the HS experiment, the actuator is locked at the last reached displacement position in the applied strong motion, while in the ST experiment, the test structure is left to vibrate freely and any tendency of the test structure to return to its original position is not restrained. This tendency may have substantial effects in terms of the recorded residual deformation in both experiments. This observation is particularly amplified, since the stiffness of the damaged test structure at the origin is very low (1.3 kips/in. (0.23 kN/mm)) in the case of LPG-6 in HS (Fig. 8.34(c)), i.e., a small amplitude force of 1 kip (4.45kN) may cause the shear walls to deform more than 0.75 in. (19 mm).

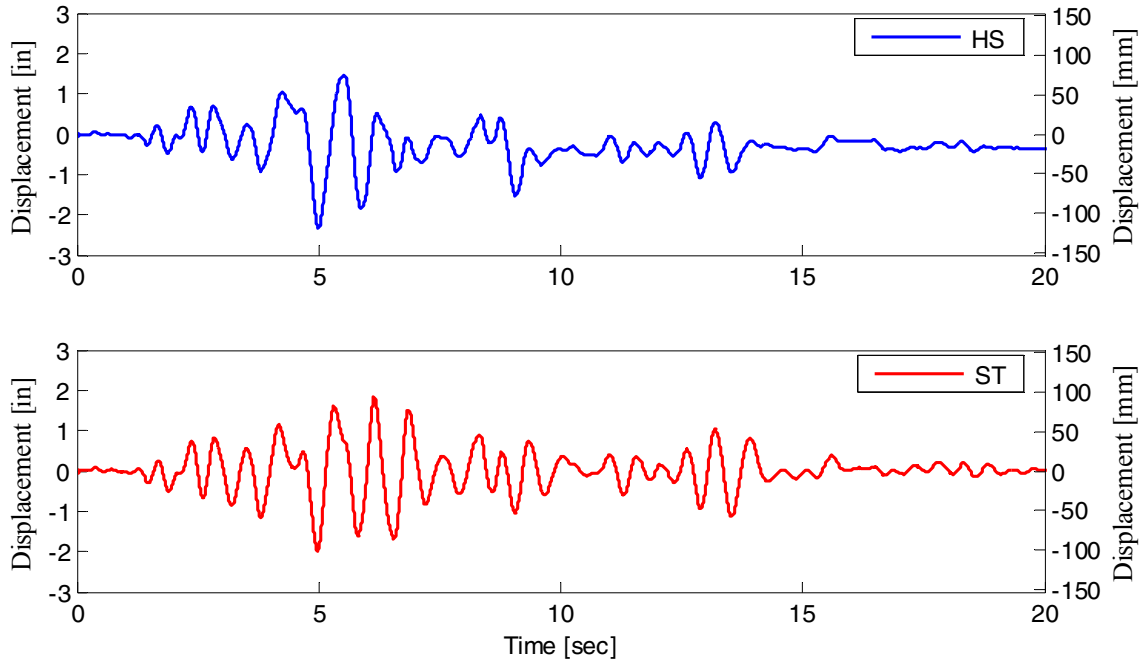


**Fig. 8.38 Displacement time-history comparison for test structure B for LPG-4.**

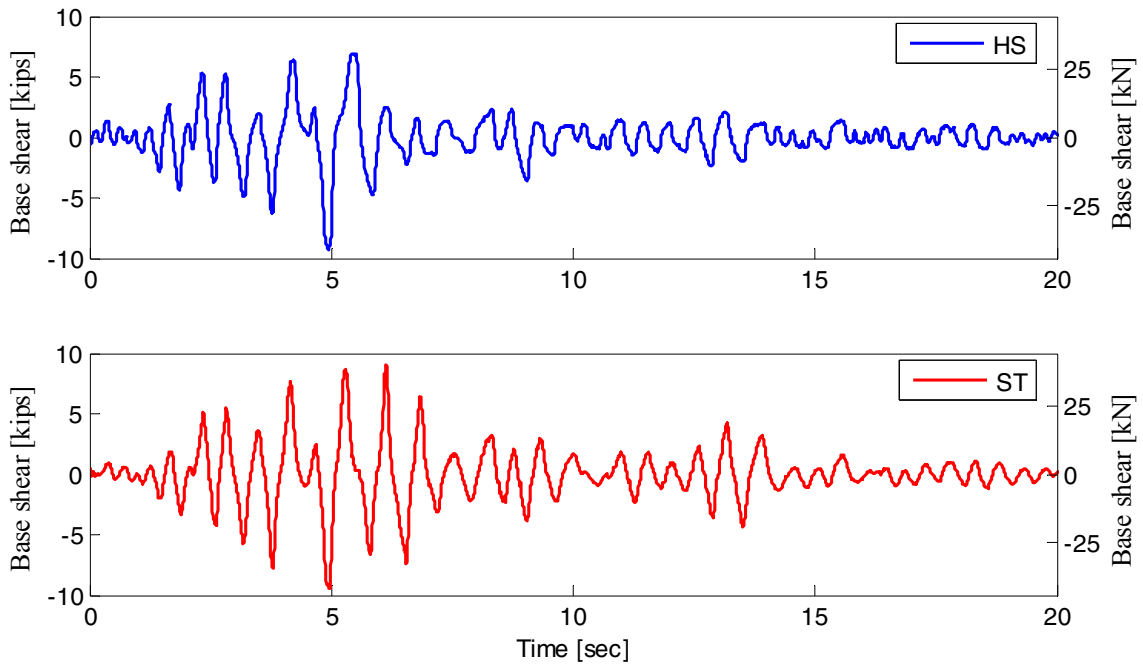


**Fig. 8.39 Total base shear time-history comparison for test structure B for LPG-4.**

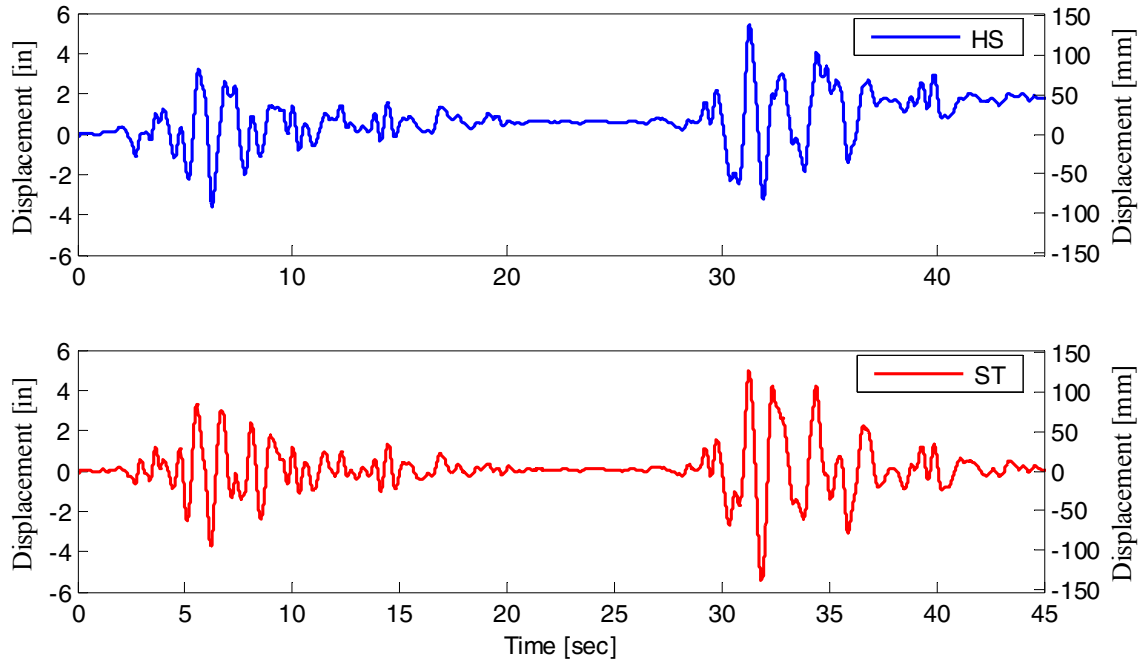


**Fig. 8.40 Displacement time-history comparison for test structure B for LPG-6.**

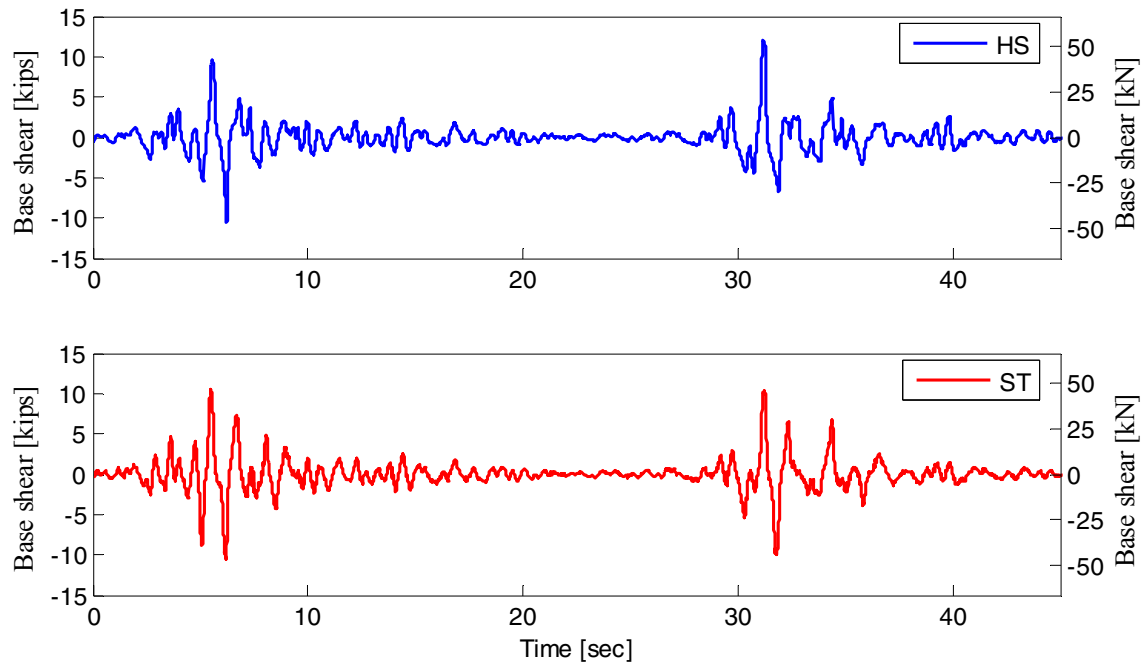


**Fig. 8.41 Total base shear time-history comparison for test structure B for LPG-6.**

Moreover, the HS test structure is simulated as a SDOF system, and the contribution of the higher modes (particularly the second flexural mode of vibration of the two-story ST test structure) to the structural response of the HS test structure are completely neglected. This

contribution, in the case of the ST experiment, is capable of counteracting the fundamental modal response (first flexural mode of vibration of the two-story ST test structure); resulting in minimizing the residual displacement of the test structure. However, after a number of repeated runs (repeating LPG-1, LPG-2, LPG-3, LPG-4, and LPG-6, Tables 5.1–5.2, each three times) applied on the ST test structure, the accumulation of damage results in a modest residual displacement of 0.93 in. (23.6 mm), as shown in Figure 8.42, for the last repeat of LPG-6.

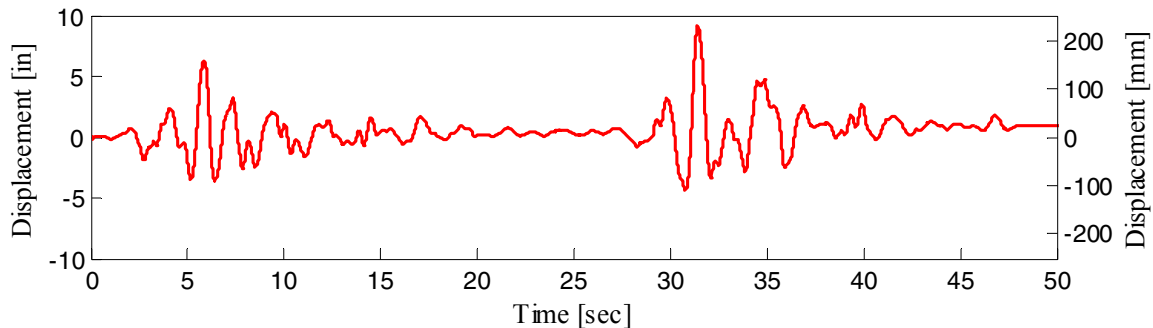


**Fig. 8.42 Displacement time-history for test structure B for third (last) repetition of LPG-6 (ST experiment).**

## 8.7 SUMMARY

This chapter presents the results of phases S-1, S-2, and S-3 of test structure A (see Fig. 1.2), in addition to the structural evaluation of test structure B. Novel comparisons to the corresponding shaking table experiments for each phase are discussed. The main results and inferred conclusions are summarized in the following list:

- In phase S-1, the global response represented by the total base shear of test structure A versus the lateral displacement is illustrated, and the deterioration of the test structure is monitored in terms of its estimated stiffness.
- The URM infill wall contribution to the base shear resistance of test structure A is evaluated, and the degradation of this wall in terms of the reduction of its shear contribution and the formation of the cracking pattern is monitored.
- The results of phase S-1 of test structure A are compared to the shaking table experiment, which is conducted on a similar test structure with the same sequence of applied ground motions.

- The cracking pattern and progressive degradation of test structure A throughout the two experiments using HS and ST are compared and are found to be closely matching.
- Differences due to the rate of load application of the HS and ST experiments are observed leading to a difference in the nature of the sliding mechanism at the interface between the URM infill wall and the surrounding RC frame in test structure A. It is argued that this difference in the sliding mechanism is the cause for the apparent high initial stiffness in the HS experiment, which is absent in the ST experiment.
- Other differences between HS and ST experiments for test structure A are due to the lack of an accurate comprehensive numerical model for the viscous damping in HS. While the damping ratio is estimated in the case of the HS test structure as a constant value based on snap-back test results conducted on the undamaged ST test structure, the results from the ST experiment reveal a changing damping ratio at different states of degradation of the test structure.
- Phases S-2 and S-3 for test structure A are discussed in terms of global behavior, damage observed in the test structure, and local beam-to-column and column-to-footing joint rotations.
- The comparison between the HS experiment and the corresponding ST experiment for test structure A, in phases S-2 and S-3, shows smaller lateral displacement in the HS experiment due to the post-tensioning of the RC beams of the HS test structure leading to limited damage in the beam-to-column joints.
- The effect of the upper stories in a hypothetical five-story test structure on the seismic response of test structure A is examined and the URM infilled RC frame is numerically modeled using the nonlinear hysteretic Bouc-Wen model.
- The difference in the fundamental frequency between the one-story and five-story test structures as well as the participation of higher modes in the case of the five-story structure are found to have a significant effect on the structural response of test structure A.
- The global response of test structure B is evaluated revealing the familiar pinching behavior and stair-like deformation of the timber shear walls with shiplap siding.
- The corresponding ST experimental results, compared to those of the HS of test structure B, reasonably match in terms of the general global response and magnitudes of lateral displacement and total base shear.

- For test structure B, a major difference is observed between the HS and the ST experiments in terms of the residual displacement, which is larger in the case of the HS experiment. This is attributed to the differences in boundary conditions of the HS and ST test structures and to the absence of the higher-mode contribution to the response in the HS experiment where the test structure is simulated as a SDOF system.

## 9 Summary, Conclusions, and Future Work

### 9.1 SUMMARY

The hybrid simulation system (HSS) of the University of California, Berkeley (UCB), namely *nees@berkeley*, is fully utilized and expanded in the present study, which also identifies the main components of the system and the interconnections defining its functionality. A validation experiment is carried out for the purpose of ensuring the proper functionality of the newly installed system. This experiment is developed as two coupled steel cantilevers in which one behaves linearly and the other behaves bilinearly with increasing stiffness by means of a stiffener with an adjustable gap. The experiment is designed with a numerically reproducible structural behavior of the test specimens in which experimental results using the HSS are validated against pure numerical simulation.

Two test structures are used in this study, namely reinforced concrete (RC) frames with and without unreinforced masonry (URM) infill walls, test structure A discussed in Chapter 4, and a two-story wood house including an open first-story garage, test structure B discussed in Chapter 5. The structural performance of the two test structures under seismic loading is examined. These two test structures have the common feature of being large substructures of shaking table (ST) experiments conducted at UCB for different structural systems. Novel comparisons are therefore conducted between the HS results for each of these test structures with the results from its corresponding counterpart on the ST, with the aim of stating the similarities and identifying the sources of discrepancy between the results of the two testing methods.

Two novel procedures, namely feed-forward error compensation and mixed-variables control are developed and implemented in the HSS. The first procedure leads to a more accurate execution of the displacement command signal. The second procedure uses mixed displacement/force control for flexible/stiff (hybrid) structural systems, offering a valuable

solution for testing such hybrid systems pseudo-dynamically. In summary, the study is successful in developing significant steps toward a generalized framework for hybrid simulation to be successfully conducted on structural systems, including hybrid ones, subjected to seismic loading with detailed validations using ST experimentation.

## 9.2 CONCLUSIONS

The following list summarizes the main conclusions inferred from the present study:

- The validation experiment confirms the proper functionality of the HSS used in the present study, including the implementation of the numerical-integration algorithm used in displacement control.
- The structural dynamic response of the one-story RC frame structure with and without URM infill wall, phase S-1 in Figure 1.2, is dominated by the high stiffness offered by the URM infill wall, and therefore such a wall provides more than 80% of the lateral total base shear resistance in the undamaged state. This contribution decreases as the URM infill wall degrades and reaches only 9% of the total base shear resistance at the end of phase S-1 where several levels of ground motion are applied to the test structure up to the in-plane collapse of the URM infill wall with severe shaking.
- In phases S-2 and S-3 in Figure 1.2, for the one-story test structure after the removal of the URM infill wall, the RC frame structure undergoes large lateral displacement, reaching 6.5% lateral story drift at the end of phase S-3. The damage and joint rotations are concentrated in the column-to-footing joints, whereas the beam-to-column joints do not undergo major damage, which is attributed to the post-tensioning of the RC beams for HS loading purposes protecting the top column joints as well as to the seismic detailing of these joints.
- The wood shear walls with shiplap siding in test structure B lose 46% of their initial stiffness after the application of the first strong motion (at 25% upper-bound earthquake, i.e., 10% probability of exceedance in 100 years) due to the dislocation of the diagonal struts between the studs of the shear walls.
- The nails connecting the shiplap siding to the vertical studs of test structure B control the response of the structure after loosening of the diagonal struts. The test structure has a very low lateral stiffness in the lateral displacement range where the framing fibers are

crushed around the nail shanks, while holding most of its stiffness beyond that range resulting in a pinching bilinear behavior with high unloading stiffness. This behavior is maintained throughout the applied sequence of strong motions, justifying the use of a testing approach with force control.

- In test structure A, the comparison of the HS experimental results to its counterpart from the ST experiment reveals that the slow execution of the HS experiment (80 times slower than real time) causes the nature of the sliding mechanism at the interface between the URM infill wall and the surrounding RC frame to differ, leading to higher apparent stiffness in the HS experiment.
- Other differences between the HS and the ST experiments are due to the lack of an accurate comprehensive numerical model for the viscous damping in HS. The damping ratio is estimated as constant in this study based on snap-back test results conducted on the undamaged ST test structure, while results from the ST experiment (Hashemi and Mosalam 2007) reveal a changing damping ratio at different states of degradation of the test structure.
- A study of the upper stories effect in the case of test structure A underlines the importance of considering the higher modes in the dynamic response of the test structure. While it is practically very difficult to consider that effect in the ST experiment, numerical substructuring in HS offers this possibility. This conclusion is also confirmed in the comparison of the HS and ST experiments performed on test structure B.
- The error in executing the displacement command signal in displacement-controlled HS is predicted based on a calibrated hockey-stick model, and a feed-forward error compensation scheme is implemented within the HSS leading to a more accurate execution of the HS experiment.
- A novel implicit force-control algorithm is developed and a parametric study confirms its accuracy.
- A mixed-variables control procedure is implemented within the HSS, and a number of implementation strategies are developed to ensure the smooth functionality of the procedure and to allow the mode switch between displacement and force control to be performed accurately and practically.

- The implementation of the mixed-variables control procedure on test structure A revealed the need for proper actuator tuning in force control for the success of the developed procedure.
- The implementation of the mixed-variables control procedure on test structure B validates its proper implementation and functionality within the HSS.

### 9.3 FUTURE WORK

The following list summarizes the suggested topics based on the conducted study where further research is needed:

- The implementation of the mixed-variables procedure is proven to be useful in the case of flexible/stiff structures. However, actuator control tuning parameters are stiffness dependent; therefore, in order for the HSS to be able to implement force control in a wide range of stiffness of the test structure, it needs to allow online adjustments to these parameters during the experiment, which was not available during this study. The exploration of that option may render mixed-variables control more useful in testing a larger variety of structures over a wider range of their seismic response.
- In the feed-forward error compensation procedure, the online estimation of the hockey-stick model parameters would allow the error prediction and compensation to be implemented during the same test run, which would alleviate the need for a separate run for the purpose of calibration and would also make the procedure suitable for situations where these parameters may change during testing. This is an important endeavor to be pursued in future enhancements of the developed generalized framework for the HS in this report.
- Macro-element modeling allows the numerical modeling of complex structural elements, such as the URM infilled RC frame simulated in this study using the Bouc-Wen model. Such models can be used in parametric studies, within the generalized framework for the HS developed in this report, offering the possibility of studying important problems such as evaluating the effect of the amount of numerical damping and its different modeling assumptions on the dynamic response of complex structural systems.
- In this study, test structure A was excited by unidirectional ground motions parallel to the plane of the RC frames and the URM infill wall. However, the contribution of out-of-

plane excitation forces to the structural performance of the test structure is of great importance. Although a three-dimensional finite element computational model was developed in Hashemi and Mosalam (2007) to study this out-of-plane contribution, an experimental study should be conducted, using the developed generalized framework for HS in this report, to reach a better understanding of this important problem.

- The RC frames in test structure A are seismically detailed and a HS experimental study is needed to evaluate the dynamic response of the very common worldwide non-seismically detailed (gravity-load designed) RC frame structures with and without URM infill walls. Moreover, the developed HSS will offer an excellent platform on which to develop possible retrofit schemes for URM infill walls and their bounding seismically deficient RC frames.

## References

- ACI Committee 318. 2002. *Building code requirements for structural concrete (ACI 318-02) and commentary (ACI 318R-02)*. American Concrete Institute.
- ASTM C837-99. 1999. *Standard test method for compressive strength of concrete cylinders cast-in-place in cylindrical molds*. ASTM, West Conshohocken, PA.
- ASTM C270-03. 2003. *Standard specification for mortar for unit masonry*. ASTM, West Conshohocken, PA.
- ASTM C1314-02a. 2002. *Standard test method for compressive strength of masonry prisms*. ASTM, West Conshohocken, PA.
- Baber, T.T. and Wen, Y.K. 1981. Random vibration of hysteretic, degrading Systems. *Journal of the Engineering Mechanics Division, ASCE* 107(EM6): 1069-1087.
- Baber, T.T. and Noori, M.N. 1986. Modeling general hysteresis behavior and random vibration application. *Journal of Vibration, Acoustics, Stress, and Reliability in Design* 108(October): 411-420.
- Bonelli, A. and Bursi O.S. 2004. Generalized- $\alpha$  methods for seismic structural testing. *Earthquake Engineering and Structural Dynamics* 33(10): 1067-1102.
- Building Seismic Safety Council (BSSC). 2000. *NEHRP recommended provisions for seismic regulations for new buildings and other structures*. Part 1: Provisions (FEMA368) and Part 2: Commentary (FEMA369), Washington D.C.
- Buonopane, S.G. 1997. *Seismic evaluation of a masonry infilled reinforced concrete frame by pseudodynamic testing*. M.Sc. Thesis, School of Civil and Environmental Engineering, Cornell University, Ithaca, New York.
- Chopra, A.K. 2000. *Dynamics of structures: theory and applications to earthquake engineering*. Second Edition, Prentice Hall, Inc., Upper Saddle River, New Jersey.
- Darby, A.P., Blakeborough, A. and Williams, M.S. 2001. Improved control algorithm for real-

- time substructure testing. *Earthquake Engineering and Structural Dynamics* 30(3): 431-448.
- Dermitzakis, S.N. and Mahin, S.A. 1985. *Development of substructuring techniques for on-Line computer controlled seismic performance testing*. UBC/EERC-85/04, Earthquake Engineering Research Center, University of California, Berkeley.
- Dimig, J., Shield, C., French, C., Bailey, F. and Clark, A. 1999. Effective force testing: a method of seismic simulation for structural testing. *Journal of Structural Engineering, ASCE* 125(9): 1028-1037.
- Dinehart, D. W. and Shenton, H.W.III 2000. Model for dynamic analysis of wood frame shear walls. *Journal of Engineering Mechanics, ASCE*, 126(9): 899–908.
- Elkhoraibi, T. and Mosalam, K.M. 2007. Towards error-free hybrid simulation using mixed variables. *Earthquake Engineering and Structural Dynamics* in press.
- Fenves, G.L., McKenna, F., Scott, M.H. and Takahashi, Y. 2004. An object-oriented software environment for collaborative network simulation. *Proceedings, 13th World Conference on Earthquake Engineering, Vancouver, Canada*.
- Gawthrop, P.J., Wallace, M.I. and Wagg, D.J. 2005. Bond-graph based substructuring of dynamical systems. *Earthquake Engineering and Structural Dynamics* 34(6): 687-703.
- Hanson, R.D. and McClamroch, N.H. 1984. Pseudodynamic test method for inelastic building response. *Proceedings of the 8th World Conference in Earthquake Engineering, San Francisco*.
- Hashemi, A. and Mosalam, K.M. 2007. *Seismic evaluation of reinforced concrete buildings including effects of masonry infill walls*. PEER Report 2007/100. Pacific Earthquake Engineering Research Center, Department of Civil and Environmental Engineering, University of California, Berkeley.
- Hashemi, A. and Mosalam, K.M. 2006. Shake-table experiment on reinforced concrete structure containing masonry infill wall. *Earthquake Engineering and Structural Dynamics* 35(14): 1827-1852.
- Hilber, H., Hughes, T. and Taylor, R. 1977. Improved numerical dissipation for time integration algorithms in structural dynamics. *Earthquake Engineering and Structural Dynamics* 5(3): 283-292.
- Hughes T.J.R. 1983. Analysis for transient algorithms with particular reference to stability behavior. *Computational Methods for Transient Analysis* Belyschko, T. and Hughes, T.J.R., Editors, Amsterdam, North-Holland.

- Hughes, T.J.R., Pister, K.S. and Taylor, R.L. 1979 Implicit-explicit finite elements in nonlinear transient analysis. *Computer Methods in Applied Mechanics and Engineering*, 17/18(Part 1): 159-182.
- Judd, J.P. and Fonseca, F.S. 2005. Analytical model for sheathing-to-framing connections in wood shear walls and diaphragms. *Journal of Structural Engineering, ASCE* (131)2: 345-352.
- Kron, G. 1963. Diakoptics; the piecewise solution of large-scale systems. MacDonald, London, UK, pp.166.
- Magonette, G. 2001. Development and application of large-scale continuous pseudo-dynamic testing techniques. *Philosophical Transactions of the Royal Society A: Mathematical, Physical and Engineering Sciences* 359(1786): 1771-1799.
- Mahin, S.A., Shing, P.B., Thewalt, C.R. and Hanson, R.D. 1989. Pseudodynamic test method – current status and future direction. *Journal of Structural Engineering, ASCE* 115(8): 2113-2128.
- Mazzoni, S., McKenna, F., Scott, M.H. and Fenves, G.L. 2006. *Open system for earthquake engineering simulation user command-language manual*. Pacific Earthquake Engineering Research Center, University of California, Berkeley, Version 1.7.3, September.
- McClamroch, N.H., Serakos, J. and Hanson, R.D. 1981. *Design and analysis of the pseudodynamic test method*. UMEE 81R3, University of Michigan, Ann Arbor.
- Menegotto M. and Pinto P.E. 1973. Method of analysis for cyclically loaded R.C. plane frames including change in geometry and non-elastic behavior of elements under combined normal force and bending. *Proceedings of IABSE Symposium on Resistance and Ultimate Deformability of Structures Acted on by Well Defined Repeated Loads, Lisbon* 13: 15-22.
- Mosalam, K.M. 1996a. *Experimental and computational strategies for the seismic behavior evaluation of frames with infill walls*. PhD Dissertation, School of Civil and Environmental Engineering, Cornell University, Ithaca, New York.
- Mosalam, K.M. 1996b. Modeling of the nonlinear seismic behavior of gravity load designed frames. *Earthquake Spectra* 12(3): 479-492.
- Mosalam, K.M., Ayala, G. and White, R.N. 1997a. *Development of fragility curves: masonry infill-concrete frame buildings*. Chapter 7 of Technical Report NCEER-97-0018, Loss Assessment of Memphis Buildings, D.P. Abrams and M. Shinozuka (Eds.).

- Mosalam, K.M., White, R.N. and Gergely, P. 1997b. *The seismic evaluation of frames with infill walls using quasi-static experiments*. Technical Report NCEER-97-0019.
- Mosalam, K.M., White, R.N. and Gergely, P. 1997c. *The seismic evaluation of frames with infill walls using pseudodynamic experiments*. Technical Report NCEER-97-0020.
- Mosalam, K.M., White, R.N. and Gergely, P. 1997d. Static response of infilled frames using quasi-static experimentation. *Journal of Structural Engineering, ASCE* 123(11): 1462-1469.
- Mosalam, K.M., Ayala, G., White, R.N. and Roth, C. 1997e. Seismic fragility of LRC frames with and without masonry infill walls. *Journal of Earthquake Engineering* 1(4): 693-720.
- Mosalam, K.M., White, R.N. and Ayala, G. 1998. Response of infilled frames using pseudodynamic experimentation. *Earthquake Engineering and Structural Dynamics* 27(6): 589-608.
- Mosalam, K.M., Machado, C., Gliniorz, K.-U., Naito, C., Kunkel, E. and Mahin, S. 2002. *Seismic evaluation of asymmetric three-story wood-frame building*. CUREE Publication No. W-19.
- Mosalam, K.M. and Mahin, S.A. 2007. Seismic evaluation and retrofit of asymmetric multi-story wood-frame building. *Journal of Earthquake Engineering*, in press.
- Mosalam, K.M. and Elkhoraibi, T. 2004. *RRW system: specifications, usage and training example* <http://nees.berkeley.edu/Facilities/rrw.shtml>
- Mosqueda G. 2003. *Continuous hybrid simulation with geographically distributed substructures*. PhD Dissertation, Department of Civil and Environmental Engineering, University of California, Berkeley.
- MTS. 2003. Model 793.00 *System software, user information and software reference*. MTS Systems Corporation.
- Nakashima, M. 2001. Development, potential, and limitations of real-time online (pseudo-dynamic) testing. *Philosophical Transactions of the Royal Society A: Mathematical, Physical and Engineering Sciences* 359(1786): 1851–1867.
- Nakashima, M., Kaminosono, T., Ishida, M. and Ando, K. 1990. Integration techniques for substructure pseudodynamic testing. *Proceedings of the 4th U.S. National Conference on Earthquake Engineering, Palm Springs, California II*: 515-524.
- Nakashima, M. and Masaoka, N. 1999. Real-time on-line test for MDOF systems. *Earthquake Engineering and Structural Dynamics* 28(4): 393-420.

- Newmark N.M. 1959. A Method of Computation for structural dynamics. *Journal of Engineering Mechanics Division, ASCE* 85(EM3): 67-94.
- Pacific Instruments. 2004. *PI660-6000, version 8.0, operator's manual*. Pacific Instruments Corporation.
- Pan, P. 2004. *Safety and functionality of base-isolated building structures subjected to vertical ground motions*. PhD Dissertation, Kyoto University, Japan.
- Pan, P., Nakashima, M. and Tomofuji, H. 2005. Online test using displacement–force mixed control. *Earthquake Engineering and Structural Dynamics* 34(8): 869-888.
- Pan P., Tomofuji H., Wang T., Nakashima M., Ohsaki M. and Mosalam, K.M. 2006. Development of peer-to-peer (P2P) internet online hybrid test system. *Earthquake Engineering and Structural Dynamics* 35(7): 867–890.
- Pinto, A., Pegon, P., Magonette, G., Molina, J., Buchet, P. and Tsionis G. 2002. *Pseudodynamic tests on a large-scale model of an existing RC bridge using non-linear substructuring and asynchronous motion*. EUR 20525 EN, European Laboratory for Structural Assessment, Ispra, Italy.
- Schellenberg, A., Mahin, S. and Fenves, G. 2007. A software framework for hybrid simulation of large structural systems. *Proceedings of Structures Congress, ASCE, Reston, VA*, 1269.
- Seible, F., Hegemier, G.A., Igarashi, A. and Kingsley, G.R. 1994a. Simulated seismic-load tests on full-scale five-story masonry building. *Journal of Structural Engineering, ASCE* 120(3): 903-924.
- Seible, F., Priestley, M.J.N., Kingsley, G.R. and K rkch basche, A.G. 1994b. Seismic response of full-scale five story reinforced-masonry building. *Journal of Structural Engineering, ASCE* 120(3): 925-946.
- Seible, F., Hegemier, G.A. and Igarashi, A. 1996. Simulated seismic laboratory load testing of full-scale buildings. *Earthquake Spectra, EERI* 12(1): 57-86.
- Shield, C., French, C. and Timm, J. 2001. Development and implementation of the effective force testing method for seismic simulation of large-scale structures. *Philosophical Transaction of the Royal Society A: Mathematical, Physical and Engineering Sciences* 359(1786): 1911-1929.
- Shing, P.B., Javadian-Gilani, A.S. and Mahin, S.A. 1984. Evaluation of seismic behavior of a braced tubular steel structure by pseudodynamic testing. *Journal of Energy Resources Technology, ASME Transactions* 106(September): 319-328.

- Shing P.B. and Mahin, S.A. 1983. *Experimental error propagation in pseudodynamic testing*. UBC/EERC-83/12, Earthquake Engineering Research Center, University of California, Berkeley.
- Shing P.B. and Mahin, S.A. 1984. *Pseudodynamic test method for seismic performance evaluation: Theory and Implementation*. UBC/EERC-84/01, Earthquake Engineering Research Center, University of California, Berkeley.
- Shing, P.B. and Mahin, S.A. 1985. Computational aspects of a seismic performance test method using on-line computer control. *Earthquake Engineering and Structural Dynamics* 13(4): 507-526.
- Shing, P.B. and Mahin, S.A. 1987a. Cumulative experimental errors in pseudodynamic tests. *Earthquake Engineering and Structural Dynamics* 15(4): 409-424.
- Shing, P.B. and Mahin, S.A. 1987b. Elimination of spurious higher-mode response in pseudodynamic tests. *Earthquake Engineering and Structural Dynamics* 15(4): 425-445.
- Shing, P.B., Vannan, M.T. and Cater, E. 1991. Implicit time integration for pseudodynamic tests. *Earthquake Engineering and Structural Dynamics* 20(6): 551-576.
- Shing, P.B. Nakashima, M. and Bursi, O.S. 1996. Application of pseudodynamic test method to structural research. *Earthquake Spectra* 12(1): 29-56.
- Song, J. and Der Kiureghian, A. 2006. Generalized Bouc-Wen model for highly asymmetric hysteresis. *Journal of Engineering Mechanics, ASCE* 132(6): 610-618.
- Systran. 2000. *ScramNet+ technical description*. Systran Corporation.
- Takahashi, Y. and Fenves, G.L. 2006. Software framework for distributed experimental-computational simulation of structural systems. *Earthquake Engineering and Structural Dynamics* 35(3): 267-291.
- Takanashi, K. and Nakashima, M. 1987. Japanese activities on on-line testing. *Journal of Engineering Mechanics, ASCE* 113(7): 1014-1032.
- Takanashi, K., Udagawa, K., Seki, M., Okada, T. and Tanaka, H. 1975. Nonlinear earthquake response analysis of structures by computer-actuator on-line system. *Bulletin of Earthquake Resistant Structure Research Center, No.8, Institute of Industrial Science, University of Tokyo, Japan*: 1-17.
- Talaat, M., and Mosalam, K.M. *Computational modeling of progressive collapse in reinforced concrete frame structures*. PEER Report 2007/xx (forthcoming). Pacific Earthquake

Engineering Research Center, Department of Civil and Environmental Engineering, University of California, Berkeley.

- Thewalt, C.R. and Mahin, S.A. 1987. *Hybrid solution technique for generalized pseudodynamic testing*. UBC/EERC-87/09, Earthquake Engineering Research Center, University of California, Berkeley.
- Thewalt, C.R. and Mahin, S.A. 1995. An unconditionally stable hybrid pseudodynamic algorithm. *Earthquake Engineering and Structural Dynamics* 24(5): 723-731.
- Wang, Y.P., Lee, C.L. and Yo, T.H. 2001. Modified state-space procedures for pseudodynamic testing. *Earthquake Engineering and Structural Dynamics* 30(1) 59-80.
- Weaver, W.Jr., Timoshenko, S.P. and Young, D.H. 1990. *Vibration problems in engineering*. Fifth edition, John Wiley & Sons.
- Wen, Y.K. 1976. Method for random vibration of hysteretic systems. *Journal of the Engineering Mechanics Division* 102(EM2): 249-265.
- White, M.W. and Dolan, J.D. 1995. Nonlinear shear-wall analysis. *Journal of Structural Engineering, ASCE* 121(11): 1629–1635.
- Wiberg, N.E. 1974. Matrix structural analysis with mixed variables. *International Journal of Numerical Methods in Engineering* 8(11) 167-194.
- Wu, B., Wang, Q., Shing, P.B. and Ou, J. 2007. Equivalent force control method for generalized real-time substructure testing with implicit integration. *Earthquake Engineering and Structural Dynamics* in press.
- Yamazaki, Y., Nakashima, M. and Kaminosono, T. 1989. Reliability of pseudodynamic test in earthquake response simulation. *Journal of Structural Engineering, ASCE* 115(8): 2098-2112.

# Appendix A: Spreadsheet for Configuring the Reaction Wall

## A.1 BACKGROUND

A spreadsheet is developed to estimate the governing parameters of the reconfigurable reaction wall (RRW). A fixed-base condition is assumed throughout the spreadsheet calculations. The user provides a number of inputs to define the RRW configuration and the conditions of its use.

These inputs are:

- Reaction wall height (number of RRW units)
- Number of post-tensioning rods used per reaction wall (typically 10)
- Post-tensioning force applied per rod (typically 100 kips)
- Loading direction with respect to the reaction wall axes (weak or strong axis)

In the case where a second reaction wall is used adjacent to the first reaction wall for increased stiffness and load-carrying capacity, the same four previous inputs are provided for the second reaction wall, in addition to:

- Position of the second reaction wall with respect to the first reaction wall (side by side or back to back)
- The user also provides:
- Deflection limit for the RRW
- Tension stress limit

Material parameters such as unit mass, concrete and steel strength and stiffness (elastic moduli), and the coefficient of friction at the interface of the reaction wall units, are also

considered as input variables and may be modified by the user. The output is in both tabular and graphical forms. Four governing limits are plotted as a function of the load amplitude and application height. These governing limits are:

- Normal stress in tension
- Shear stress
- Deflection
- Sliding

The vibration frequencies of the RRW in all three directions (flexure about strong and weak axes, in addition to torsion) are estimated using Timoshenko beam theory (Weaver 1989). Since the solution is an iterative one, the Euler beam solution is provided as an initial estimate for the fundamental frequency in each direction. Note that the adopted method for estimating the vibration frequencies is validated using vibration testing of the RRW. Further details can be found from the online report (Mosalam and Elkhoraibi 2004).

## **A.2 APPLICATION TO PRESENT TEST SETUP**

The setup used in the present study is seven-units high. The input parameters discussed in the previous section are shown in Figure A.1. The output is shown in Figure A.2. Note that in this particular case, the tension limit governs the RRW design. The vibration properties estimated by the spreadsheet are shown in Figure A.3(a). The frequencies listed are calculated for loading in the strong-axis direction. These frequencies are also estimated for loading that causes bending about the weak-axis direction, by changing the loading direction in the input sheet from “strong” to “weak” in Figure A.3(b).

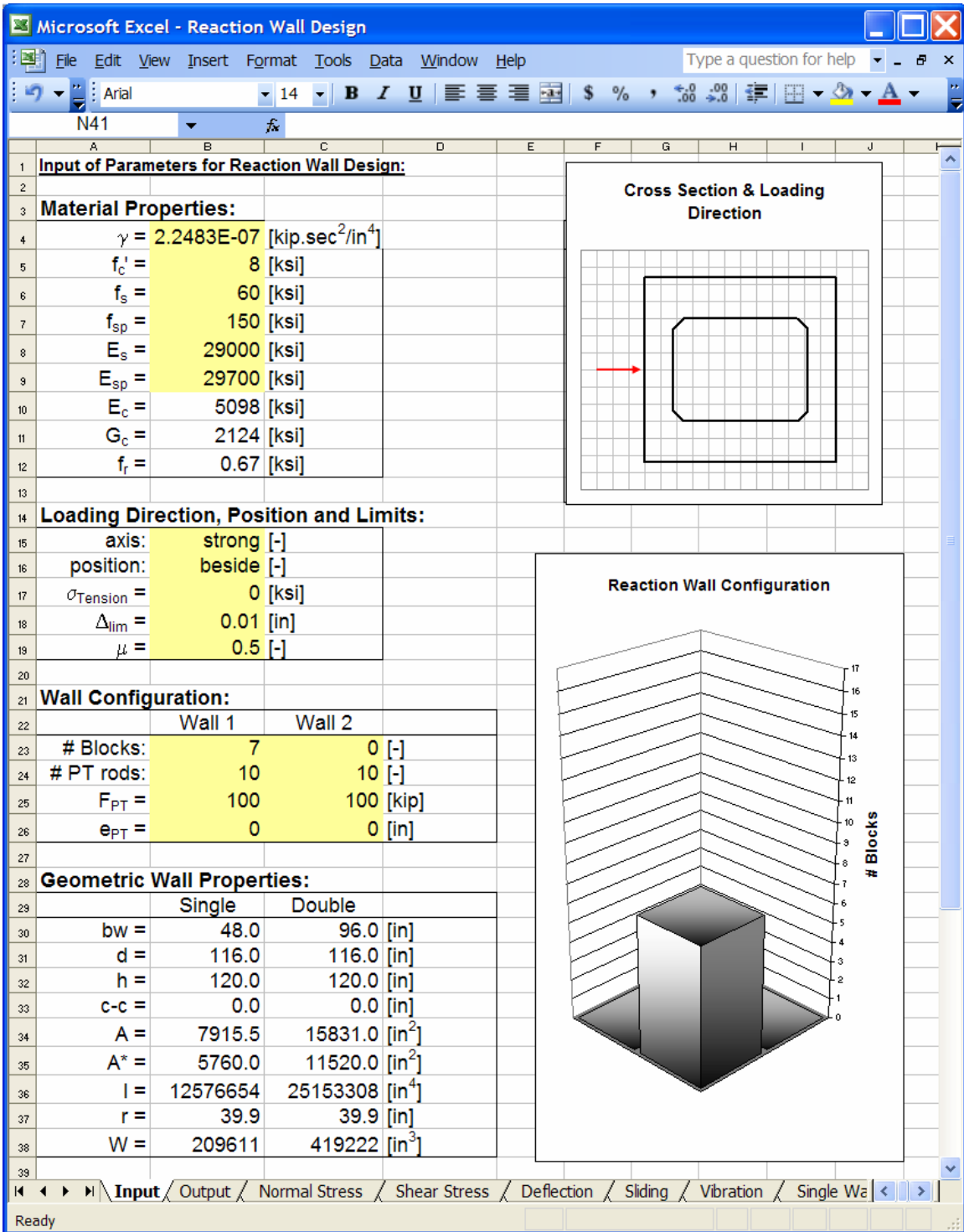
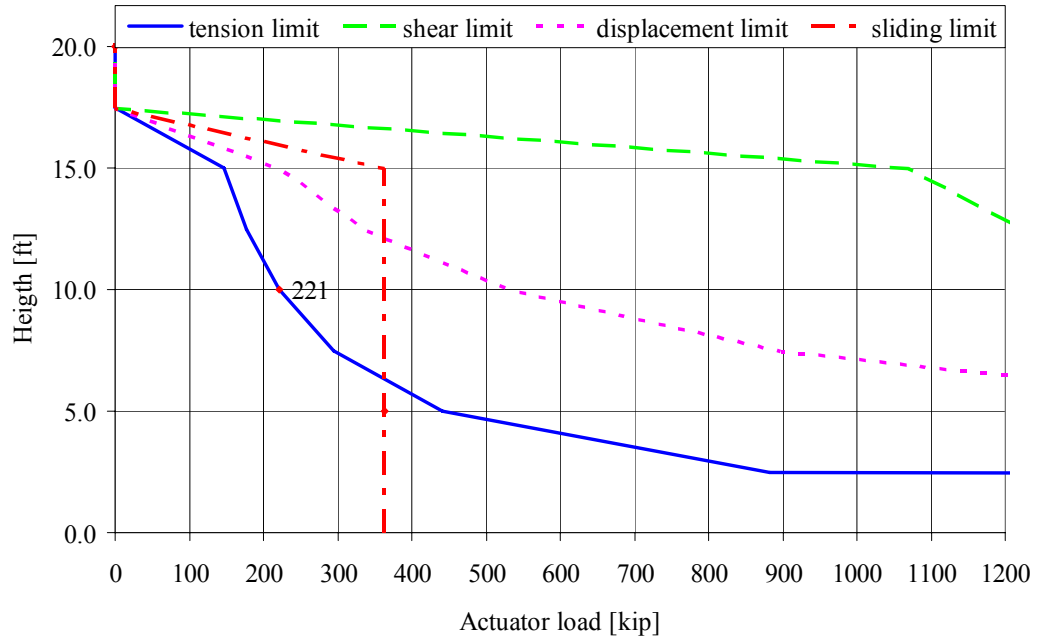
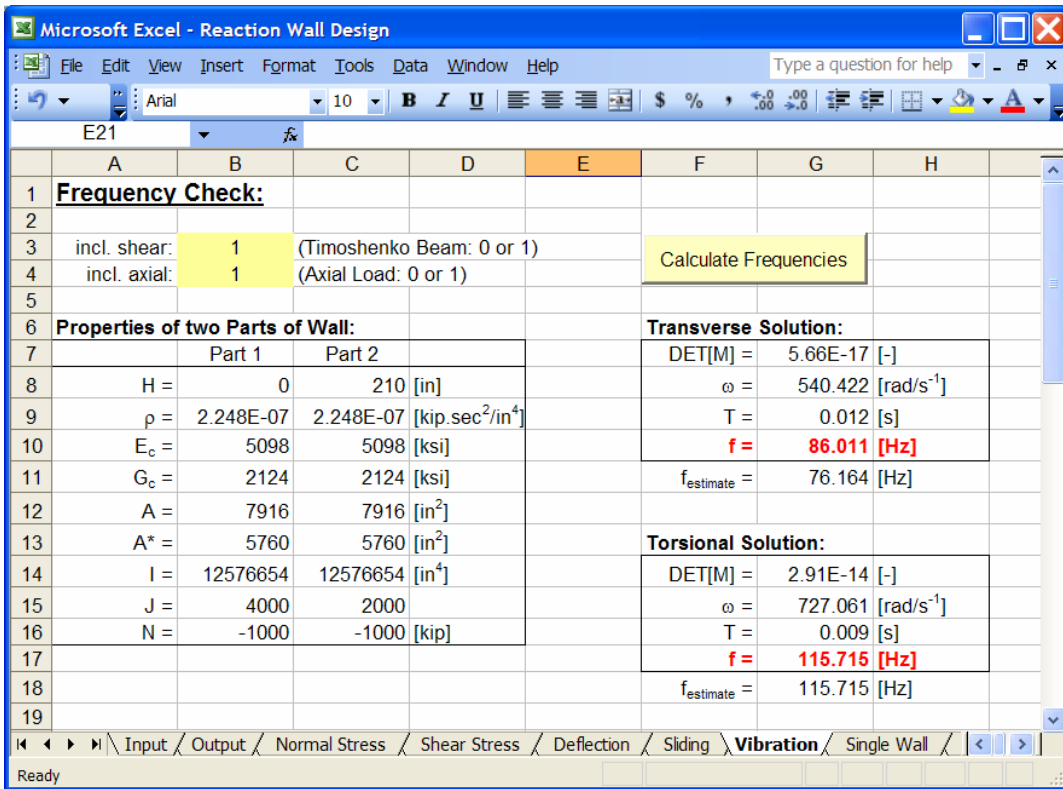


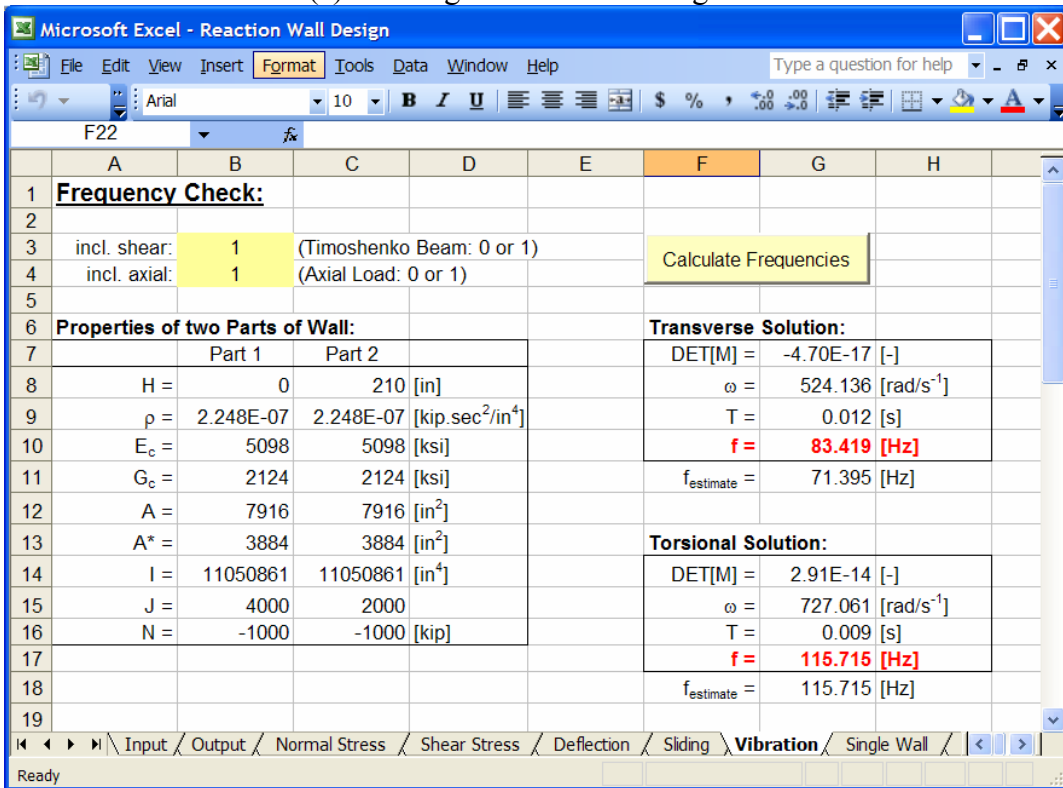
Fig. A.1 Design spreadsheet input for RRW design.



**Fig. A.2 Design spreadsheet output for used RRW (1 kip = 4.448 kN, 1 ft = 30.48 mm).**



(a) Bending about RRW strong axis



(b) Bending about RRW weak axis

Fig. A.3 Frequency calculation of seven-unit high (210 in. (5334 mm)) RRW.

## Appendix B: Exact Solution for a Bilinear Stiffening SDOF

In the numerical study of the mixed-variables control integration algorithm in Section 6.5.3, the response of a bilinear stiffening elastic undamped SDOF system (Fig. B.1 (a)), is considered when subjected to a constant impulse force  $p_o$  (Fig. B.1(b)).

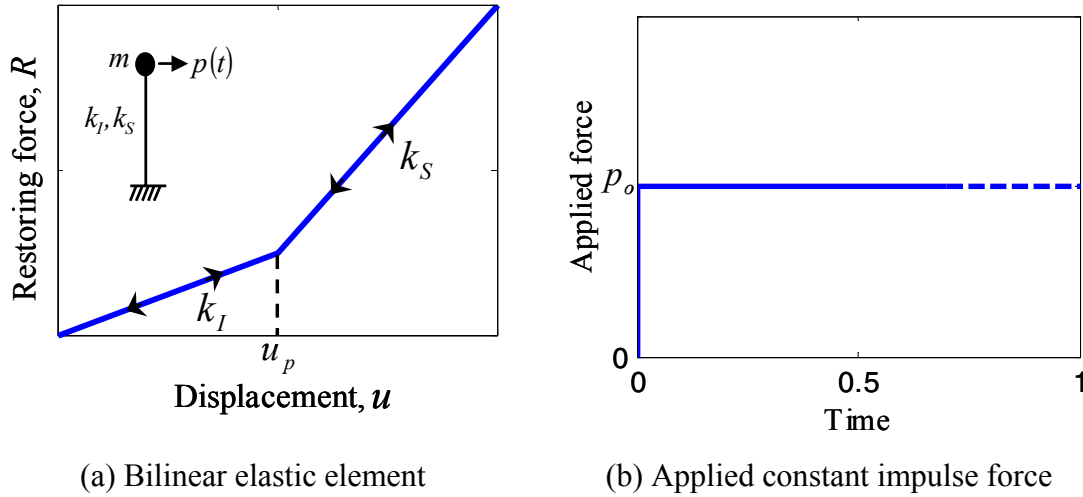


**Fig. B.1** Considered SDOF system.

Given the amplitude of the constant impulse force  $p_o$  (Fig. B.1(b)), and the deformation  $u_p$  (Fig. B.1(a)) at which the stiffness of the bilinear spring element changes from the initial stiffness  $k_I$  to the secondary stiffness  $k_S$ , the displacement of the SDOF system at any time  $t$  can be described by:

$$\begin{aligned}
 u(t) &= (u_{st})_I \left\{ 1 - \cos[\omega_I(t - t_S^{last})] \right\} + u_S^{last} \cos[\omega_I(t - t_S^{last})] + \frac{\dot{u}_S^{last}}{\omega_I} \sin[\omega_I(t - t_S^{last})] & u \leq u_p \\
 u(t) &= (u_{st})_S \left\{ 1 - \cos[\omega_S(t - t_I^{last})] \right\} + u_I^{last} \cos[\omega_S(t - t_I^{last})] + \frac{\dot{u}_I^{last}}{\omega_S} \sin[\omega_S(t - t_I^{last})] & u > u_p
 \end{aligned} \tag{B.1}$$

where the subscripts  $I$  and  $S$  refer to “Initial” and “Secondary,” respectively,  $(u_{st})_I = \frac{p_o}{k_I}$  and  $(u_{st})_S = u_p + (p_o - k_I u_p)/k_S$ ,  $\omega_I = \sqrt{k_I/m}$  and  $\omega_S = \sqrt{k_S/m}$ . The superscript *last* designates the last attained displacement  $u$  or time  $t$  before the change of stiffness occurs. At the beginning of the displacement time history  $u^{last} = 0$  and  $t^{last} = 0$ , while from the point where the displacement reaches  $u_p$  for the first time,  $u_I^{last} = u_S^{last} = u_p$ . The velocity  $\dot{u}$  of the SDOF system at any time  $t$  is governed by:

$$\begin{aligned} \dot{u}(t) &= \omega_I \left\{ (u_{st})_I \sin[\omega_I(t - t_S^{last})] - u_S^{last} \sin[\omega_I(t - t_S^{last})] + \frac{\dot{u}_S^{last}}{\omega_I} \cos[\omega_I(t - t_S^{last})] \right\} & u \leq u_p \\ \dot{u}(t) &= \omega_S \left\{ (u_{st})_S \sin[\omega_S(t - t_I^{last})] - u_I^{last} \sin[\omega_S(t - t_I^{last})] + \frac{\dot{u}_I^{last}}{\omega_S} \cos[\omega_S(t - t_I^{last})] \right\} & u > u_p \end{aligned} \quad (B.2)$$

An example of the resulting displacement time history of this SDOF using the above closed-form solution is illustrated in Figure B.2 with the parameters listed in Table B.1.

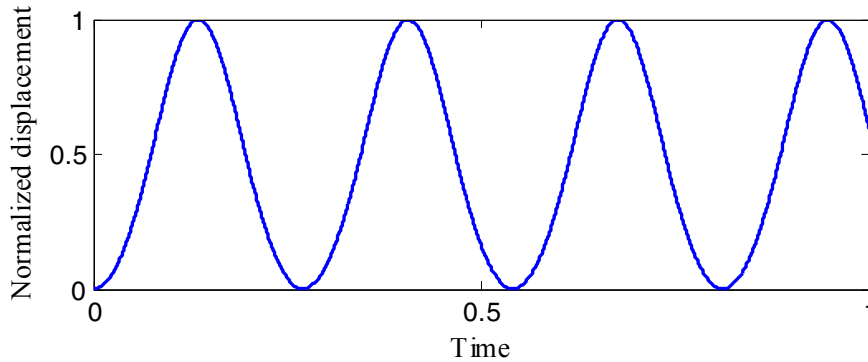


**Fig. B.1 Typical displacement response of bilinear stiffening undamped SDOF system.**

**Table B.1 Parameters for bilinear stiffening undamped SDOF system.**

Parameter	$m$	$k_I$	$k_S = 5k_I$	$p_o$	$u_p$	$T_I = 2\pi\sqrt{m/k_I}$
Example	1	$4\pi^2$	$20\pi^2$	$4\pi$	0.1	1

# Appendix C: Bouc-Wen Model Description and Calibration

The Bouc-Wen numerical model (Wen 1976; Baber and Wen 1981; Baber and Noori 1986) is chosen for its versatility and flexibility in simulating the structural response of nonlinear hysteretic behavior of the type exerted by the URM infilled RC frame (see Section 8.5). The following is a discussion of the model and the parameters that control it. The calibration of these parameters is discussed next with its application on the URM infilled RC frame used in test structure A for two different states of damage.

## C.1 DESCRIPTION

The Bouc-Wen model is governed by a number of parameters each of which controls one or more of its features. These parameters are:

- $\alpha$ : may be regarded as the ratio between the hardening and elastic stiffness of the simulated structure;
- $\beta$  and  $\gamma$ : depending on their numerical sum and difference, the model is softening or hardening;
- $n$ : controls the sharpness of transition from the elastic to the secondary stiffness (hardening or softening);
- $dt$ : is an arbitrary time step and should be chosen to ease any numerical ill-conditioning in the computations;
- $\delta_v$ : is a degradation parameter controlling the hysteretic force without affecting the stiffness; and
- $\delta_\eta$ : is another degradation parameter affecting both the hysteretic force and the stiffness.

Additional parameters are included to introduce pinching in the model as shown in the example in Figure C.1, generated using the parameters in Table C.1. These additional parameters are:

- $\psi_0$ : controls the initial slack, i.e., the range of displacement around the origin with a reduction in stiffness due to pinching;
- $\delta_\psi$ : is a slack growth parameter; and
- $\xi$ : determines the level of pinching, i.e., the amount of stiffness reduction in the slack region.

The model may be described by the differential equations below:

$$\begin{aligned}
 \frac{dy_3}{dt} &= (1 - \alpha) \frac{du}{dt} y_2 \\
 \frac{dy_2}{dt} &= \frac{\frac{du}{dt} - (1 + \delta_v y_3) \left( \beta \left| \frac{du}{dt} \right| |y_2|^{(n-1)y_2} - \gamma \frac{du}{dt} |y_2|^n \right)}{1 + \delta_n y_3} \left( 1 - \xi \exp \left[ \frac{-(y_2)^2}{(\psi_0 + \delta_\psi |A_u|)^2} \right] \right) \\
 \frac{dy_1}{dt} &= \alpha \left( 1 - \exp \left[ \frac{-(y_2)^2}{(\psi_0 + \delta_\psi |A_u|)^2} \right] \right) \frac{du}{dt} + (1 - \alpha) \frac{dy_2}{dt}
 \end{aligned} \tag{C.1}$$

where  $u$  is the total applied displacement where  $\frac{du}{dt} = \frac{u^{\text{current}} - u^{\text{previous}}}{dt}$ ,  $A_u$  is the maximum displacement reached throughout the history,  $y_1$  is the restoring force divided by the initial stiffness  $k_t$ ,  $y_2$  is the hysteretic displacement, and  $y_3$  is the hysteretic energy. At the start of each step,  $\frac{du}{dt}$  is determined and  $\frac{dy_i}{dt}$  where  $i=1, 2, 3$  are subsequently calculated using Equation (C.1). The values of  $y_i$  are subsequently updated as  $y_i^{\text{current}} = y_i^{\text{previous}} + \frac{dy_i}{dt} dt$ . The restoring force is then calculated as  $F = k_t y_1$ .

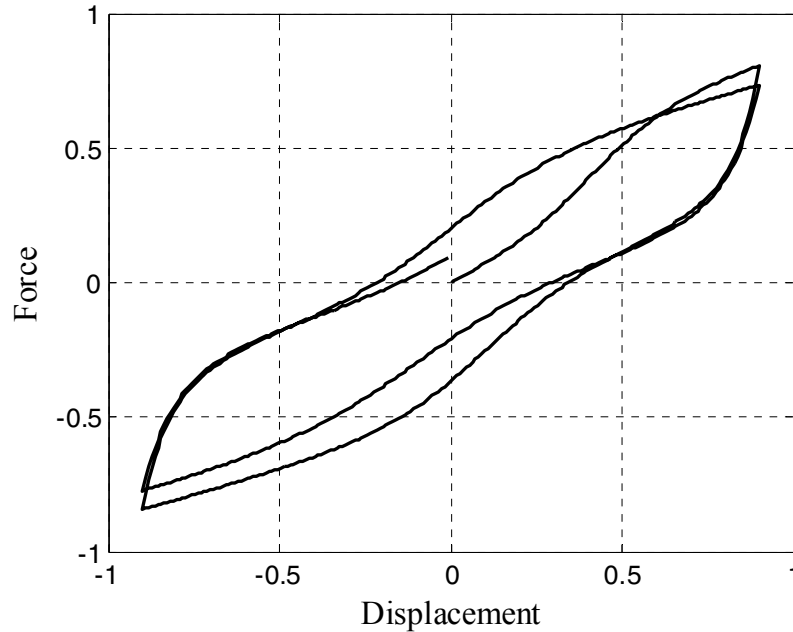


**Fig. C.1 Example of Bouc-Wen model including pinching.**

**Table C.1 Bouc-Wen model calibration parameters.**

Parameter	$\alpha$	$\beta$	$\gamma$	$n$	$\delta_v$	$\delta_\eta$	$\psi_0$	$\delta_\psi$	$\xi$	$dt$
Example	0.1	8	0.6	1.16	0.2	1	0.12	0.82	0.009	0.01
TAR-2 <sup>†</sup>	0.7	12	4	1	0	0	0	0	0	0.01
DUZ-8 <sup>††</sup>	0.1	8	0.6	1.16	0.2	1	0.12	0.82	0.007	0.01

<sup>†</sup> pinching not included

<sup>††</sup> pinching included

## C.2 CALIBRATION

The calibration of the discussed Bouc-Wen model in the previous sections is performed through an understanding of the zone of influence of each parameter, and is judged based on the matching of the peaks of the restoring force generated by the model with the corresponding restoring-force peaks of the experimental results. Two models are calibrated corresponding to two different levels of damage in phase S-1 of test structure A (see Fig. 4.4), namely the pre-cracking (TAR-2) and post-cracking (DUZ-8) phases of the URM infill wall.

Figure C.2 shows the time histories for the recorded HS results and the numerically calibrated model for TAR-2 with the parameters listed in Table C.1. The results show a good

match with respect to the shape of the hysteretic loops. The maximum difference between the numerical model results and the measured HS restoring force is about 9.0% relative to the peak recorded restoring force from the HS.

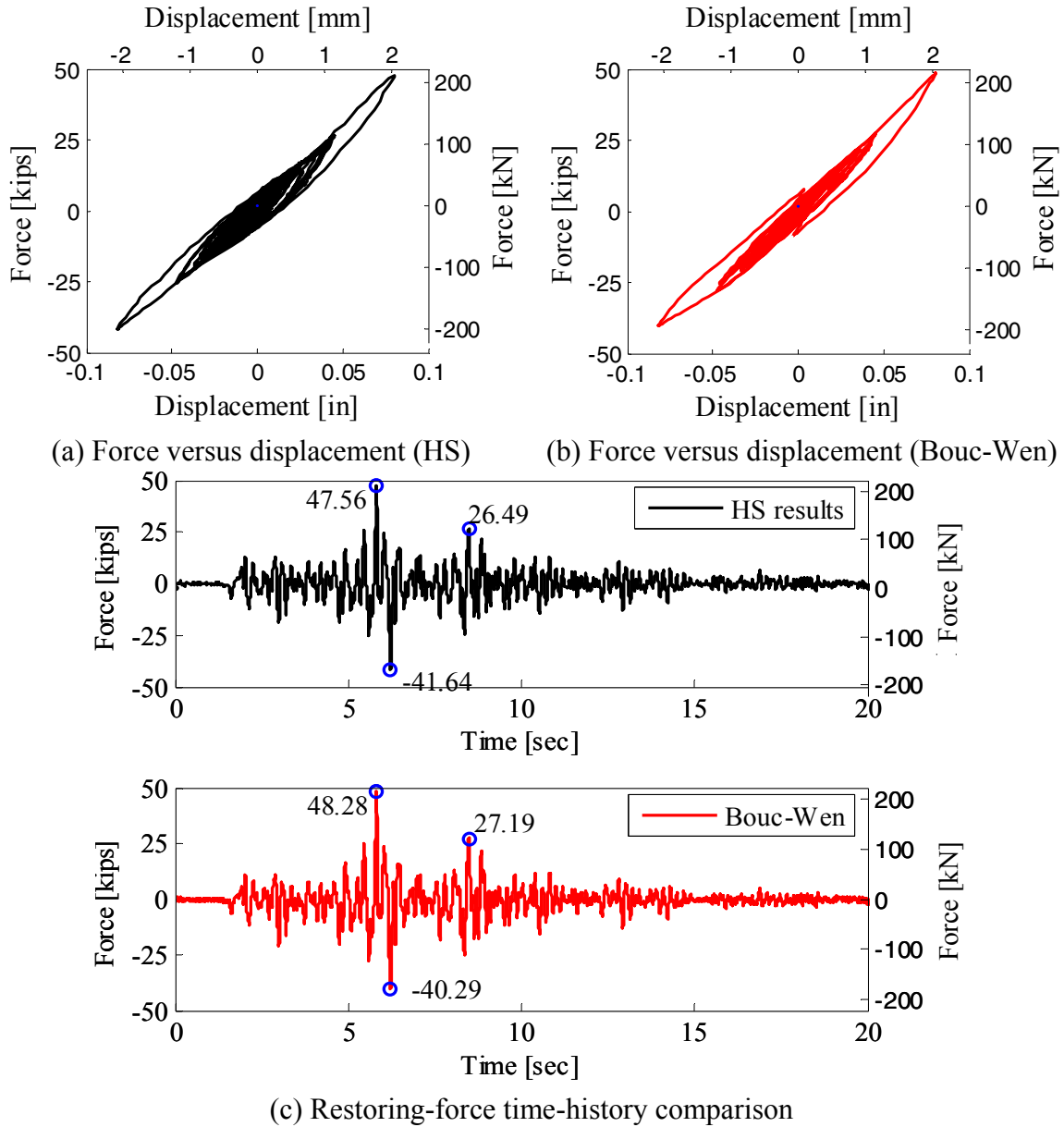
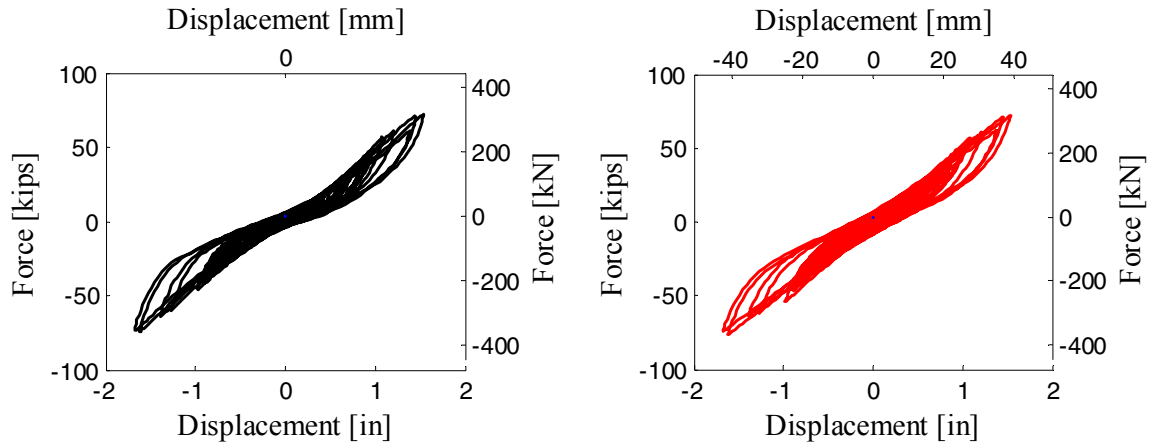


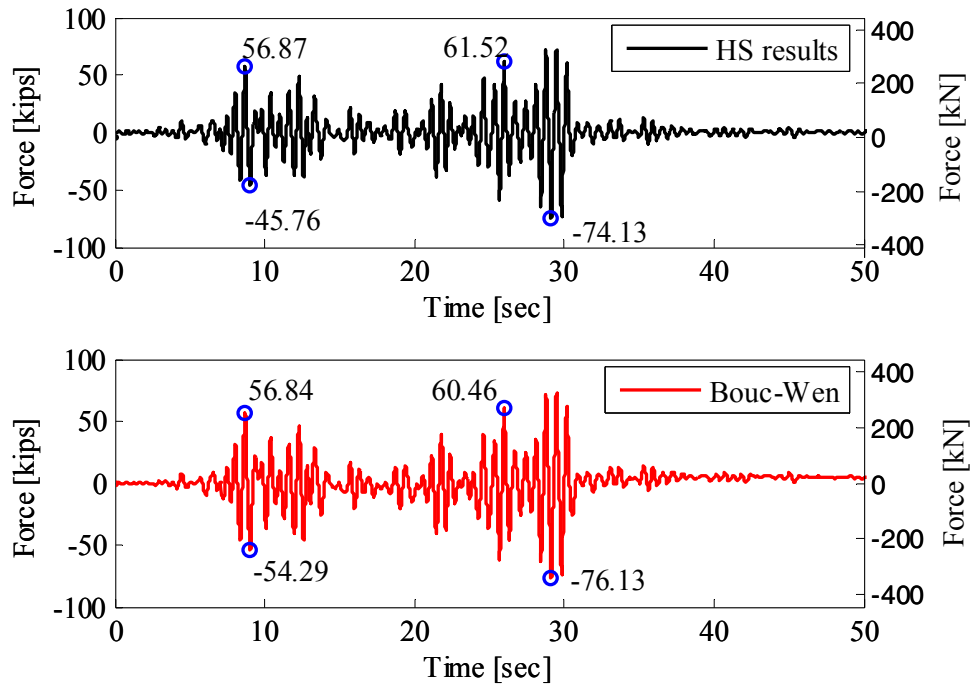
**Fig. C.2 Bouc-Wen model calibration — TAR-2.**

In the case of DUZ-8 (Fig. C.3), with the parameters listed in Table C.1, the maximum difference between the restoring forces in the HS and Bouc-Wen model results is about 14.0%. It is to be noted that an unsymmetrical behavior of the URM infilled RC frame is observed in the

HS results that is not possible to capture using the previously discussed symmetric Bouc-Wen model, resulting in larger differences on the negative side of the plot. For future refinements, an unsymmetrical version of the presented Bouc-Wen (see e.g., Song and Der Kiureghian 2006) model can be used.



(a) Force versus displacement (HS)      (b) Force versus displacement (Bouc-Wen)



(c) Restoring-force time-history comparison

**Fig. C.3 Bouc-Wen model calibration —DUZ-8.**

## PEER REPORTS

PEER reports are available from the National Information Service for Earthquake Engineering (NISEE). To order PEER reports, please contact the Pacific Earthquake Engineering Research Center, 1301 South 46<sup>th</sup> Street, Richmond, California 94804-4698. Tel.: (510) 665-3405; Fax: (510) 665-3420.

- PEER 2007/02** *Campbell-Bozorgnia NGA Ground Motion Relations for the Geometric Mean Horizontal Component of Peak and Spectral Ground Motion Parameters.* Kenneth W. Campbell and Yousef Bozorgnia. May 2007.
- PEER 2007/01** *Boore-Atkinson NGA Ground Motion Relations for the Geometric Mean Horizontal Component of Peak and Spectral Ground Motion Parameters.* David M. Boore and Gail M. Atkinson. May. May 2007.
- PEER 2006/12** *Societal Implications of Performance-Based Earthquake Engineering.* Peter J. May. May 2007.
- PEER 2006/11** *Probabilistic Seismic Demand Analysis Using Advanced Ground Motion Intensity Measures, Attenuation Relationships, and Near-Fault Effects.* Polsak Tothong and C. Allin Cornell. March 2007.
- PEER 2006/10** *Application of the PEER PBEE Methodology to the I-880 Viaduct.* Sashi Kunnath. February 2007.
- PEER 2006/09** *Quantifying Economic Losses from Travel Forgone Following a Large Metropolitan Earthquake.* James Moore, Sungbin Cho, Yue Yue Fan, and Stuart Werner. November 2006.
- PEER 2006/08** *Vector-Valued Ground Motion Intensity Measures for Probabilistic Seismic Demand Analysis.* Jack W. Baker and C. Allin Cornell. October 2006.
- PEER 2006/07** *Analytical Modeling of Reinforced Concrete Walls for Predicting Flexural and Coupled-Shear-Flexural Responses.* Kutay Orakcal, Loenardo M. Massone, and John W. Wallace. October 2006.
- PEER 2006/06** *Nonlinear Analysis of a Soil-Drilled Pier System under Static and Dynamic Axial Loading.* Gang Wang and Nicholas Sitar. November 2006.
- PEER 2006/05** *Advanced Seismic Assessment Guidelines.* Paolo Bazzurro, C. Allin Cornell, Charles Menun, Maziar Motahari, and Nicolas Luco. September 2006.
- PEER 2006/04** *Probabilistic Seismic Evaluation of Reinforced Concrete Structural Components and Systems.* Tae Hyung Lee and Khalid M. Mosalam. August 2006.
- PEER 2006/03** *Performance of Lifelines Subjected to Lateral Spreading.* Scott A. Ashford and Teerawut Juirnarongrit. July 2006.
- PEER 2006/02** *Pacific Earthquake Engineering Research Center Highway Demonstration Project.* Anne Kiremidjian, James Moore, Yue Yue Fan, Nesrin Basoz, Ozgur Yazali, and Meredith Williams. April 2006.
- PEER 2006/01** *Bracing Berkeley. A Guide to Seismic Safety on the UC Berkeley Campus.* Mary C. Comerio, Stephen Tobriner, and Ariane Fehrenkamp. January 2006.
- PEER 2005/16** *Seismic Response and Reliability of Electrical Substation Equipment and Systems.* Junho Song, Armen Der Kiureghian, and Jerome L. Sackman. April 2006.
- PEER 2005/15** *CPT-Based Probabilistic Assessment of Seismic Soil Liquefaction Initiation.* R. E. S. Moss, R. B. Seed, R. E. Kayen, J. P. Stewart, and A. Der Kiureghian. April 2006.
- PEER 2005/14** *Workshop on Modeling of Nonlinear Cyclic Load-Deformation Behavior of Shallow Foundations.* Bruce L. Kutter, Geoffrey Martin, Tara Hutchinson, Chad Harden, Sivapalan Gajan, and Justin Phalen. March 2006.
- PEER 2005/13** *Stochastic Characterization and Decision Bases under Time-Dependent Aftershock Risk in Performance-Based Earthquake Engineering.* Gee Liek Yeo and C. Allin Cornell. July 2005.
- PEER 2005/12** *PEER Testbed Study on a Laboratory Building: Exercising Seismic Performance Assessment.* Mary C. Comerio, editor. November 2005.
- PEER 2005/11** *Van Nuys Hotel Building Testbed Report: Exercising Seismic Performance Assessment.* Helmut Krawinkler, editor. October 2005.
- PEER 2005/10** *First NEES/E-Defense Workshop on Collapse Simulation of Reinforced Concrete Building Structures.* September 2005.
- PEER 2005/09** *Test Applications of Advanced Seismic Assessment Guidelines.* Joe Maffei, Karl Telleen, Danya Mohr, William Holmes, and Yuki Nakayama. August 2006.
- PEER 2005/08** *Damage Accumulation in Lightly Confined Reinforced Concrete Bridge Columns.* R. Tyler Ranf, Jared M. Nelson, Zach Price, Marc O. Eberhard, and John F. Stanton. April 2006.

- PEER 2005/07** *Experimental and Analytical Studies on the Seismic Response of Freestanding and Anchored Laboratory Equipment.* Dimitrios Konstantinidis and Nicos Makris. January 2005.
- PEER 2005/06** *Global Collapse of Frame Structures under Seismic Excitations.* Luis F. Ibarra and Helmut Krawinkler. September 2005.
- PEER 2005/05** *Performance Characterization of Bench- and Shelf-Mounted Equipment.* Samit Ray Chaudhuri and Tara C. Hutchinson. May 2006.
- PEER 2005/04** *Numerical Modeling of the Nonlinear Cyclic Response of Shallow Foundations.* Chad Harden, Tara Hutchinson, Geoffrey R. Martin, and Bruce L. Kutter. August 2005.
- PEER 2005/03** *A Taxonomy of Building Components for Performance-Based Earthquake Engineering.* Keith A. Porter. September 2005.
- PEER 2005/02** *Fragility Basis for California Highway Overpass Bridge Seismic Decision Making.* Kevin R. Mackie and Bozidar Stojadinovic. June 2005.
- PEER 2005/01** *Empirical Characterization of Site Conditions on Strong Ground Motion.* Jonathan P. Stewart, Yoojoong Choi, and Robert W. Graves. June 2005.
- PEER 2004/09** *Electrical Substation Equipment Interaction: Experimental Rigid Conductor Studies.* Christopher Stearns and André Filiatrault. February 2005.
- PEER 2004/08** *Seismic Qualification and Fragility Testing of Line Break 550-kV Disconnect Switches.* Shakhzod M. Takhirov, Gregory L. Fenves, and Eric Fujisaki. January 2005.
- PEER 2004/07** *Ground Motions for Earthquake Simulator Qualification of Electrical Substation Equipment.* Shakhzod M. Takhirov, Gregory L. Fenves, Eric Fujisaki, and Don Clyde. January 2005.
- PEER 2004/06** *Performance-Based Regulation and Regulatory Regimes.* Peter J. May and Chris Koski. September 2004.
- PEER 2004/05** *Performance-Based Seismic Design Concepts and Implementation: Proceedings of an International Workshop.* Peter Fajfar and Helmut Krawinkler, editors. September 2004.
- PEER 2004/04** *Seismic Performance of an Instrumented Tilt-up Wall Building.* James C. Anderson and Vitelmo V. Bertero. July 2004.
- PEER 2004/03** *Evaluation and Application of Concrete Tilt-up Assessment Methodologies.* Timothy Graf and James O. Malley. October 2004.
- PEER 2004/02** *Analytical Investigations of New Methods for Reducing Residual Displacements of Reinforced Concrete Bridge Columns.* Junichi Sakai and Stephen A. Mahin. August 2004.
- PEER 2004/01** *Seismic Performance of Masonry Buildings and Design Implications.* Kerri Anne Taeko Tokoro, James C. Anderson, and Vitelmo V. Bertero. February 2004.
- PEER 2003/18** *Performance Models for Flexural Damage in Reinforced Concrete Columns.* Michael Berry and Marc Eberhard. August 2003.
- PEER 2003/17** *Predicting Earthquake Damage in Older Reinforced Concrete Beam-Column Joints.* Catherine Pagni and Laura Lowes. October 2004.
- PEER 2003/16** *Seismic Demands for Performance-Based Design of Bridges.* Kevin Mackie and Bozidar Stojadinovic. August 2003.
- PEER 2003/15** *Seismic Demands for Nondeteriorating Frame Structures and Their Dependence on Ground Motions.* Ricardo Antonio Medina and Helmut Krawinkler. May 2004.
- PEER 2003/14** *Finite Element Reliability and Sensitivity Methods for Performance-Based Earthquake Engineering.* Terje Haukaas and Armen Der Kiureghian. April 2004.
- PEER 2003/13** *Effects of Connection Hysteretic Degradation on the Seismic Behavior of Steel Moment-Resisting Frames.* Janise E. Rodgers and Stephen A. Mahin. March 2004.
- PEER 2003/12** *Implementation Manual for the Seismic Protection of Laboratory Contents: Format and Case Studies.* William T. Holmes and Mary C. Comerio. October 2003.
- PEER 2003/11** *Fifth U.S.-Japan Workshop on Performance-Based Earthquake Engineering Methodology for Reinforced Concrete Building Structures.* February 2004.
- PEER 2003/10** *A Beam-Column Joint Model for Simulating the Earthquake Response of Reinforced Concrete Frames.* Laura N. Lowes, Nilanjan Mitra, and Arash Altoontash. February 2004.
- PEER 2003/09** *Sequencing Repairs after an Earthquake: An Economic Approach.* Marco Casari and Simon J. Wilkie. April 2004.

- PEER 2003/08** *A Technical Framework for Probability-Based Demand and Capacity Factor Design (DCFD) Seismic Formats.* Fatemeh Jalayer and C. Allin Cornell. November 2003.
- PEER 2003/07** *Uncertainty Specification and Propagation for Loss Estimation Using FOSM Methods.* Jack W. Baker and C. Allin Cornell. September 2003.
- PEER 2003/06** *Performance of Circular Reinforced Concrete Bridge Columns under Bidirectional Earthquake Loading.* Mahmoud M. Hachem, Stephen A. Mahin, and Jack P. Moehle. February 2003.
- PEER 2003/05** *Response Assessment for Building-Specific Loss Estimation.* Eduardo Miranda and Shahram Taghavi. September 2003.
- PEER 2003/04** *Experimental Assessment of Columns with Short Lap Splices Subjected to Cyclic Loads.* Murat Melek, John W. Wallace, and Joel Conte. April 2003.
- PEER 2003/03** *Probabilistic Response Assessment for Building-Specific Loss Estimation.* Eduardo Miranda and Hesameddin Aslani. September 2003.
- PEER 2003/02** *Software Framework for Collaborative Development of Nonlinear Dynamic Analysis Program.* Jun Peng and Kincho H. Law. September 2003.
- PEER 2003/01** *Shake Table Tests and Analytical Studies on the Gravity Load Collapse of Reinforced Concrete Frames.* Kenneth John Elwood and Jack P. Moehle. November 2003.
- PEER 2002/24** *Performance of Beam to Column Bridge Joints Subjected to a Large Velocity Pulse.* Natalie Gibson, André Filiatrault, and Scott A. Ashford. April 2002.
- PEER 2002/23** *Effects of Large Velocity Pulses on Reinforced Concrete Bridge Columns.* Greg L. Orozco and Scott A. Ashford. April 2002.
- PEER 2002/22** *Characterization of Large Velocity Pulses for Laboratory Testing.* Kenneth E. Cox and Scott A. Ashford. April 2002.
- PEER 2002/21** *Fourth U.S.-Japan Workshop on Performance-Based Earthquake Engineering Methodology for Reinforced Concrete Building Structures.* December 2002.
- PEER 2002/20** *Barriers to Adoption and Implementation of PBEE Innovations.* Peter J. May. August 2002.
- PEER 2002/19** *Economic-Engineered Integrated Models for Earthquakes: Socioeconomic Impacts.* Peter Gordon, James E. Moore II, and Harry W. Richardson. July 2002.
- PEER 2002/18** *Assessment of Reinforced Concrete Building Exterior Joints with Substandard Details.* Chris P. Pantelides, Jon Hansen, Justin Nadauld, and Lawrence D. Reaveley. May 2002.
- PEER 2002/17** *Structural Characterization and Seismic Response Analysis of a Highway Overcrossing Equipped with Elastomeric Bearings and Fluid Dampers: A Case Study.* Nicos Makris and Jian Zhang. November 2002.
- PEER 2002/16** *Estimation of Uncertainty in Geotechnical Properties for Performance-Based Earthquake Engineering.* Allen L. Jones, Steven L. Kramer, and Pedro Arduino. December 2002.
- PEER 2002/15** *Seismic Behavior of Bridge Columns Subjected to Various Loading Patterns.* Asadollah Esmaeily-Gh. and Yan Xiao. December 2002.
- PEER 2002/14** *Inelastic Seismic Response of Extended Pile Shaft Supported Bridge Structures.* T.C. Hutchinson, R.W. Boulanger, Y.H. Chai, and I.M. Idriss. December 2002.
- PEER 2002/13** *Probabilistic Models and Fragility Estimates for Bridge Components and Systems.* Paolo Gardoni, Armen Der Kiureghian, and Khalid M. Mosalam. June 2002.
- PEER 2002/12** *Effects of Fault Dip and Slip Rake on Near-Source Ground Motions: Why Chi-Chi Was a Relatively Mild M7.6 Earthquake.* Brad T. Aagaard, John F. Hall, and Thomas H. Heaton. December 2002.
- PEER 2002/11** *Analytical and Experimental Study of Fiber-Reinforced Strip Isolators.* James M. Kelly and Shakhzod M. Takhirov. September 2002.
- PEER 2002/10** *Centrifuge Modeling of Settlement and Lateral Spreading with Comparisons to Numerical Analyses.* Sivapalan Gajan and Bruce L. Kutter. January 2003.
- PEER 2002/09** *Documentation and Analysis of Field Case Histories of Seismic Compression during the 1994 Northridge, California, Earthquake.* Jonathan P. Stewart, Patrick M. Smith, Daniel H. Whang, and Jonathan D. Bray. October 2002.
- PEER 2002/08** *Component Testing, Stability Analysis and Characterization of Buckling-Restrained Unbonded Braces™.* Cameron Black, Nicos Makris, and Ian Aiken. September 2002.

- PEER 2002/07** *Seismic Performance of Pile-Wharf Connections*. Charles W. Roeder, Robert Graff, Jennifer Soderstrom, and Jun Han Yoo. December 2001.
- PEER 2002/06** *The Use of Benefit-Cost Analysis for Evaluation of Performance-Based Earthquake Engineering Decisions*. Richard O. Zerbe and Anthony Falit-Baiamonte. September 2001.
- PEER 2002/05** *Guidelines, Specifications, and Seismic Performance Characterization of Nonstructural Building Components and Equipment*. André Filiatrault, Constantin Christopoulos, and Christopher Stearns. September 2001.
- PEER 2002/04** *Consortium of Organizations for Strong-Motion Observation Systems and the Pacific Earthquake Engineering Research Center Lifelines Program: Invited Workshop on Archiving and Web Dissemination of Geotechnical Data, 4–5 October 2001*. September 2002.
- PEER 2002/03** *Investigation of Sensitivity of Building Loss Estimates to Major Uncertain Variables for the Van Nuys Testbed*. Keith A. Porter, James L. Beck, and Rustem V. Shaikhutdinov. August 2002.
- PEER 2002/02** *The Third U.S.-Japan Workshop on Performance-Based Earthquake Engineering Methodology for Reinforced Concrete Building Structures*. July 2002.
- PEER 2002/01** *Nonstructural Loss Estimation: The UC Berkeley Case Study*. Mary C. Comerio and John C. Stallmeyer. December 2001.
- PEER 2001/16** *Statistics of SDF-System Estimate of Roof Displacement for Pushover Analysis of Buildings*. Anil K. Chopra, Rakesh K. Goel, and Chatpan Chintanapakdee. December 2001.
- PEER 2001/15** *Damage to Bridges during the 2001 Nisqually Earthquake*. R. Tyler Ranf, Marc O. Eberhard, and Michael P. Berry. November 2001.
- PEER 2001/14** *Rocking Response of Equipment Anchored to a Base Foundation*. Nicos Makris and Cameron J. Black. September 2001.
- PEER 2001/13** *Modeling Soil Liquefaction Hazards for Performance-Based Earthquake Engineering*. Steven L. Kramer and Ahmed-W. Elgamal. February 2001.
- PEER 2001/12** *Development of Geotechnical Capabilities in OpenSees*. Boris Jeremi . September 2001.
- PEER 2001/11** *Analytical and Experimental Study of Fiber-Reinforced Elastomeric Isolators*. James M. Kelly and Shakhzod M. Takhirov. September 2001.
- PEER 2001/10** *Amplification Factors for Spectral Acceleration in Active Regions*. Jonathan P. Stewart, Andrew H. Liu, Yoojoong Choi, and Mehmet B. Baturay. December 2001.
- PEER 2001/09** *Ground Motion Evaluation Procedures for Performance-Based Design*. Jonathan P. Stewart, Shyh-Jeng Chiou, Jonathan D. Bray, Robert W. Graves, Paul G. Somerville, and Norman A. Abrahamson. September 2001.
- PEER 2001/08** *Experimental and Computational Evaluation of Reinforced Concrete Bridge Beam-Column Connections for Seismic Performance*. Clay J. Naito, Jack P. Moehle, and Khalid M. Mosalam. November 2001.
- PEER 2001/07** *The Rocking Spectrum and the Shortcomings of Design Guidelines*. Nicos Makris and Dimitrios Konstantinidis. August 2001.
- PEER 2001/06** *Development of an Electrical Substation Equipment Performance Database for Evaluation of Equipment Fragilities*. Thalia Agnanos. April 1999.
- PEER 2001/05** *Stiffness Analysis of Fiber-Reinforced Elastomeric Isolators*. Hsiang-Chuan Tsai and James M. Kelly. May 2001.
- PEER 2001/04** *Organizational and Societal Considerations for Performance-Based Earthquake Engineering*. Peter J. May. April 2001.
- PEER 2001/03** *A Modal Pushover Analysis Procedure to Estimate Seismic Demands for Buildings: Theory and Preliminary Evaluation*. Anil K. Chopra and Rakesh K. Goel. January 2001.
- PEER 2001/02** *Seismic Response Analysis of Highway Overcrossings Including Soil-Structure Interaction*. Jian Zhang and Nicos Makris. March 2001.
- PEER 2001/01** *Experimental Study of Large Seismic Steel Beam-to-Column Connections*. Egor P. Popov and Shakhzod M. Takhirov. November 2000.
- PEER 2000/10** *The Second U.S.-Japan Workshop on Performance-Based Earthquake Engineering Methodology for Reinforced Concrete Building Structures*. March 2000.
- PEER 2000/09** *Structural Engineering Reconnaissance of the August 17, 1999 Earthquake: Kocaeli (Izmit), Turkey*. Halil Sezen, Kenneth J. Elwood, Andrew S. Whittaker, Khalid Mosalam, John J. Wallace, and John F. Stanton. December 2000.

- PEER 2000/08** *Behavior of Reinforced Concrete Bridge Columns Having Varying Aspect Ratios and Varying Lengths of Confinement.* Anthony J. Calderone, Dawn E. Lehman, and Jack P. Moehle. January 2001.
- PEER 2000/07** *Cover-Plate and Flange-Plate Reinforced Steel Moment-Resisting Connections.* Taejin Kim, Andrew S. Whittaker, Amir S. Gilani, Vitelmo V. Bertero, and Shakhzod M. Takhirov. September 2000.
- PEER 2000/06** *Seismic Evaluation and Analysis of 230-kV Disconnect Switches.* Amir S. J. Gilani, Andrew S. Whittaker, Gregory L. Fenves, Chun-Hao Chen, Henry Ho, and Eric Fujisaki. July 2000.
- PEER 2000/05** *Performance-Based Evaluation of Exterior Reinforced Concrete Building Joints for Seismic Excitation.* Chandra Clyde, Chris P. Pantelides, and Lawrence D. Reaveley. July 2000.
- PEER 2000/04** *An Evaluation of Seismic Energy Demand: An Attenuation Approach.* Chung-Che Chou and Chia-Ming Uang. July 1999.
- PEER 2000/03** *Framing Earthquake Retrofitting Decisions: The Case of Hillside Homes in Los Angeles.* Detlof von Winterfeldt, Nels Roselund, and Alicia Kitsuse. March 2000.
- PEER 2000/02** *U.S.-Japan Workshop on the Effects of Near-Field Earthquake Shaking.* Andrew Whittaker, ed. July 2000.
- PEER 2000/01** *Further Studies on Seismic Interaction in Interconnected Electrical Substation Equipment.* Armen Der Kiureghian, Kee-Jeung Hong, and Jerome L. Sackman. November 1999.
- PEER 1999/14** *Seismic Evaluation and Retrofit of 230-kV Porcelain Transformer Bushings.* Amir S. Gilani, Andrew S. Whittaker, Gregory L. Fenves, and Eric Fujisaki. December 1999.
- PEER 1999/13** *Building Vulnerability Studies: Modeling and Evaluation of Tilt-up and Steel Reinforced Concrete Buildings.* John W. Wallace, Jonathan P. Stewart, and Andrew S. Whittaker, editors. December 1999.
- PEER 1999/12** *Rehabilitation of Nonductile RC Frame Building Using Encasement Plates and Energy-Dissipating Devices.* Mehrdad Sasani, Vitelmo V. Bertero, James C. Anderson. December 1999.
- PEER 1999/11** *Performance Evaluation Database for Concrete Bridge Components and Systems under Simulated Seismic Loads.* Yael D. Hose and Frieder Seible. November 1999.
- PEER 1999/10** *U.S.-Japan Workshop on Performance-Based Earthquake Engineering Methodology for Reinforced Concrete Building Structures.* December 1999.
- PEER 1999/09** *Performance Improvement of Long Period Building Structures Subjected to Severe Pulse-Type Ground Motions.* James C. Anderson, Vitelmo V. Bertero, and Raul Bertero. October 1999.
- PEER 1999/08** *Envelopes for Seismic Response Vectors.* Charles Menun and Armen Der Kiureghian. July 1999.
- PEER 1999/07** *Documentation of Strengths and Weaknesses of Current Computer Analysis Methods for Seismic Performance of Reinforced Concrete Members.* William F. Cofer. November 1999.
- PEER 1999/06** *Rocking Response and Overturning of Anchored Equipment under Seismic Excitations.* Nicos Makris and Jian Zhang. November 1999.
- PEER 1999/05** *Seismic Evaluation of 550 kV Porcelain Transformer Bushings.* Amir S. Gilani, Andrew S. Whittaker, Gregory L. Fenves, and Eric Fujisaki. October 1999.
- PEER 1999/04** *Adoption and Enforcement of Earthquake Risk-Reduction Measures.* Peter J. May, Raymond J. Burby, T. Jens Feeley, and Robert Wood.
- PEER 1999/03** *Task 3 Characterization of Site Response General Site Categories.* Adrian Rodriguez-Marek, Jonathan D. Bray, and Norman Abrahamson. February 1999.
- PEER 1999/02** *Capacity-Demand-Diagram Methods for Estimating Seismic Deformation of Inelastic Structures: SDF Systems.* Anil K. Chopra and Rakesh Goel. April 1999.
- PEER 1999/01** *Interaction in Interconnected Electrical Substation Equipment Subjected to Earthquake Ground Motions.* Armen Der Kiureghian, Jerome L. Sackman, and Kee-Jeung Hong. February 1999.
- PEER 1998/08** *Behavior and Failure Analysis of a Multiple-Frame Highway Bridge in the 1994 Northridge Earthquake.* Gregory L. Fenves and Michael Ellery. December 1998.
- PEER 1998/07** *Empirical Evaluation of Inertial Soil-Structure Interaction Effects.* Jonathan P. Stewart, Raymond B. Seed, and Gregory L. Fenves. November 1998.
- PEER 1998/06** *Effect of Damping Mechanisms on the Response of Seismic Isolated Structures.* Nicos Makris and Shih-Po Chang. November 1998.
- PEER 1998/05** *Rocking Response and Overturning of Equipment under Horizontal Pulse-Type Motions.* Nicos Makris and Yiannis Roussos. October 1998.

- PEER 1998/04** *Pacific Earthquake Engineering Research Invitational Workshop Proceedings, May 14–15, 1998: Defining the Links between Planning, Policy Analysis, Economics and Earthquake Engineering.* Mary Comerio and Peter Gordon. September 1998.
- PEER 1998/03** *Repair/Upgrade Procedures for Welded Beam to Column Connections.* James C. Anderson and Xiaojing Duan. May 1998.
- PEER 1998/02** *Seismic Evaluation of 196 kV Porcelain Transformer Bushings.* Amir S. Gilani, Juan W. Chavez, Gregory L. Fennes, and Andrew S. Whittaker. May 1998.
- PEER 1998/01** *Seismic Performance of Well-Confined Concrete Bridge Columns.* Dawn E. Lehman and Jack P. Moehle. December 2000.

## ONLINE REPORTS

The following PEER reports are available by Internet only at [http://peer.berkeley.edu/publications/peer\\_reports.html](http://peer.berkeley.edu/publications/peer_reports.html)

**PEER 2007/101** *Generalized Hybrid Simulation Framework for Structural Systems Subjected to Seismic Loading.* Tarek Elkhoraibi and Khalid M. Mosalam. July 2007.

**PEER 2007/100** *Seismic Evaluation of Reinforced Concrete Buildings Including Effects of Masonry Infill Walls.* Alidad Hashemi and Khalid M. Mosalam. July 2007.